Spincrossover compounds in micro-mesoporous materials and metal-organic frameworks based on adamantyl(tetraphenylcarboxylate) ligands

Inaugural-Dissertation

zur Erlangung des Doktorgrades

der Mathematisch-Naturwissenschaftlichen Fakultät

der Heinrich-Heine-Universität Düsseldorf

vorgelegt von

Tian Zhao

aus China, Hunan

Düsseldorf, July 2015

Aus dem Institut für Anorganische Chemie und Strukturchemie

der Heinrich-Heine-Universität Düsseldorf

Gedruckt mit der Genehmigung der Mathematisch-Naturwissenschaftlichen Fakultät der Heinrich-Heine-Universität Düsseldorf

Referent: Prof. Dr. Ch. Janiak

Korreferent: Prof. Dr. Ch. Ganter

Tag der mündlichen Prüfung: 02.10.2015

Die vorliegende Arbeit wurde in der Zeit von Oktober 2011 bis Juli 2015 am Institut für Anorganische Chemie und Strukturchemie, Abteilung für Bioanorganische Chemie, MOFs, Nanos und Katalyse, der Heinrich-Heine-Universität Düsseldorf im Arbeitskreis von **Prof. Dr. Christoph Janiak** durchgeführt.

Publikationen:

1. **Tian Zhao**, Laure Cuignet, Marinela Maria Dîrtu, Mariusz Wolff, Vojislav Spasojevic, Ishtvan Boldog, Aurelian Rotaru, Yann Garcia*, and Christoph Janiak*, Water effect on the spin-transition behavior of Fe(II) 1,2,4-triazole 1D chains embedded in pores of MCM-41. (Journal of Materials Chemistry C, 2015, **3**, 7802--7812.)
2. **Tian Zhao**, Felix Jeremias, Ishtvan Boldog, Binh Nguyen*, Stefan K. Henninger* and Christoph Janiak*, High-yield, fluoride-free and large-scale synthesis of MIL-101(Cr). (Dalton Transactions, 2015, **44**, 16791 – 16801.)
3. **Tian Zhao**, Ishtvan Boldog, Vojislav Spasojevic and Christoph Janiak*, Solvent-triggered spin-crossover of $[Fe(HB(pz)_3)_2]$ in MOF nano-confinement of NH_2-MIL-101(Al). (Submitted)

Selbstständigkeitserklärung

Hiermit versichere ich an Eides statt, dass die vorgelegte Dissertation (Spincrossover compounds in micro-mesoporous materials and metal-organic frameworks based on adamantyl(tetraphenylcarboxylate) ligands) von mir selbstständig verfasst und unter ausschließlicher Verwendung der angegebenen Literatur und Hilfsmittel gemäß der (Gute wissenschaftliche Praxis für Promovierende) an der Heinrich-Heine-Universität Düsseldorf erstellt wurde.

Bisher habe ich keine erfolglosen Promotionsversuche unternommen und diese Dissertation nicht an einer anderen Fakultät vorgelegt.

Düsseldorf, den 22.07.2015

Tian Zhao

Acknowledgment

The person to thank first and foremost must be Prof. Dr. Christoph Janiak. After all, I did not have much awareness of the excitement that is associated with good science prior to joining his group in the autumn of 2011. During the four years I studied in Düsseldorf, I learnt that ambition, assertion, and pragmatism are a solid basis for exceptional science from him. I gratefully acknowledge the chance he gave me to work in many disciplines in an excellent working environment and to develop independent thinking, which led to the successful completion of this work.

Prof. Dr. Christian Ganter is kindly acknowledged for being the co-examiner.

I sincerely acknowledge to the China Scholarship Council (CSC) for a doctoral fellowship for the financial support during my study in Germany.

I am extremely thankful to Dr. Ishtvan Boldog for his help, inspiring discussions, ideas and encouragement. Especially the first year I arrived Germany, he patiently helped me to solve my problems (both life and study). He found a nice flat for me in Düsseldorf (especially this is not easy in Düsseldorf). He taught me how to operate the Bruker D2 Phaser for powder X-ray diffraction (PXRD) measurements and the Netzsch Tarsus 209 F3 TGA instrument for thermogravimetric (TG) analysis. Although he eventually left the institute to pursue his independent career, he still tried to help me within his capability.

Christian Heering is gratefully thanked for single-crystal XRD measurements and the structure refinement of my samples.

Birgit Tommes is thanked for the FT-IR spectroscopy measurements and technical support on the NOVA-4000e instrument.

Annette Ricken is thanked for technical assistance and atomic absorption spectroscopy (AAS) analysis.

Lei Xing is acknowledged for his help, including helping me to register in the university and to

apply for my bank account.

Annika Herbst is thanked for scanning electron microscopy (SEM) measurements.

Kai Schütte, Susann Wegner and Karsten Klauke are thanked for transmission electron microscopy (TEM) measurements.

I am thankful for my smooth incorporation into the team. I know a lot of friends in Germany in the period of my study. The lunches with Anas Tahli were always very pleasant. I enjoyed very much playing football games with Christian Heering and other people during weekends. I thank Annika Herbst for her help and to become more easily integrated into life in Germany. Also, I thank Gamall Makhloufi for his kind invitation to his BBQ party, usually on Thursday. I also would like to thank all my colleagues for their help and the general good work atmosphere in our group: Dr. Nader de Sousa Amadeu, Martin Wickenheiser, Martin Davi, Roland Thoma, Kai Schütte, Christina Rutz, Hajo Meyer, Raquel Marcos Esteban, Dr. Christian Vollmer, Dr. Dorothea Marquardt, Dr. Asamanjoy Bhunia, Anna Christin Kautz, Sebastian Glomb, Dr. Ines Dumsch, Subarna Dey, Janina Dechnik, Laure Cuignet, Irina Gruber, Maximilian Klopotowski, Sandra Nießing, Susann Wegner and Vasile Lozan.

Importantly, the work in this thesis benefited from a number of fruitful collaborations. The work in collaboration with Institute of Condensed Matter and Nanosciences, Molecules, Solids and Reactivity (IMCN/MOST) (Université Catholique de Louvain) was very successful. I highly appreciate the efforts by Prof. Yann Garcia and Dr. Marinela M. Dîrtu for Mössbauer characterization and discussion in SCO@MCM work (Chapter 4). I also highly appreciate the efforts by Prof. Vojislav Spasojevic (Institute for Nuclear Sciences, Serbia) for DC magnetic measurements both in SCO@MCM (Chapter4) and SCO@MOF (Chapter 3) work. The work on large-scale in MIL-101(Cr) synthesis with Dr. Felix Jeremias (Department of Thermally Active Materials and Solar Cooling, Fraunhofer Institute for Solar Energy Systems (ISE)) was very productive. I am very proud that we were able to prove HNO_3 would lead to a > 30% increase in yield during MIL-101(Cr) synthesis (Chapter 2). Also the efforts performed with Dr. Ishtvan Boldog were of high value. I am very thankful for the novel structure of coordination polymers /MOFs based on carboxyphenyladamantanes (Chapter 5).

Of course, my families have been very supportive of my Ph.D. endeavors, especially my wife. Though every year I have one month vacation to reunion, my wife has to take care of my little daughter herself in the most cases. Because of her understanding and support, I could finish my study in Germany.

Table of Contents

Abstract

Metal-organic frameworks (MOFs) are metal-organic ligand compounds that extend "infinitely" into one, two or three dimensions with coordinative metal-ligand bonds. Their unique properties, e.g. large surface area, tunable pore sizes and topologies, high (hydro)thermal stability, and adsorption selectivity, may lead to promising applications, including host-functions in composite materials.

MIL-101(Cr), one of most important prototypical MOFs, is well investigated and widely used in many scientific fields. The addition of a modifier in the synthesis of MOFs is commonly used to improve the properties of MOFs. Thus, at the start of this thesis, the addition of modifiers in the synthesis of MIL-101(Cr) was thoroughly investigated and HNO_3 was demonstrated to efficiently increase the yield of MIL-101(Cr) by more than 20% compared to traditional synthesis and to improve the porosity by more than 20 % in comparison to traditional synthesis in our laboratory.

In the study of spin crossover (SCO) materials one interest is to modify or tune the transition temperature. One possibility to modify the spin-transition temperature is to embed an SCO compound in a MOF matrix. The spin-crossover compound bis(hydrotris(pyrazolyl)borato)iron(II) ($[Fe(HB(pz)_3)_2]$) was tried to embed in the pores of several prototypical MOFs by various methods. Finally, synthesis of the metal-organic framework (MOF) NH_2-MIL-101(Al) with $[Fe(HB(pz)_3)_2]$ added to the reaction medium yielded the encapsulation product, $[Fe(HB(pz)_3)_2]$@NH_2-MIL101(Al), with a maximum loading of ~11 wt% (0.19 Fe molecules per Al_3OL_3 moiety), and its identity was confirmed by PXRD and spectroscopic evidences. The entrapped complex, which is stable in air, and cannot be removed by vacuum drying (120°C and $<10^{-6}$ Torr) is confined in the cages of the framework. N_2 and CO_2 gas adsorption measurements on the dry S@M composite with different S@M loadings confirm the absence of most of the inital NH_2-MIL-101(Al) porosity. $[Fe(HB(pz)_3)_2]$ is a spin-crossover (SCO) compound with a gradual spin transition at temperature T_c = ~330 K for the relaxed bulk material. When $[Fe(HB(pz)_3)_2]$ is confined in the cages of the MIL framework as S@M composite it is largely in the high-spin (HS) state at RT (light yellow color dominated by the host matrix). Due to confinement the transition temperature of $[Fe(HB(pz)_3)_2]$ in the S@M composite is shifted to

much lower temperature compared to T_c = ~330 K for the relaxed phases of bulk crystalline [Fe(HB(pz)$_3$)$_2$]. At the same time the spin-crossover transition of [Fe(HB(pz)$_3$)$_2$] in the composite could also be triggered at room temperature by immersing the dried compound into polar to non-polar solvents of molecules with small cross sections, (H_2O, MeOH, DMSO, DMF, BuOH, t-BuOH, THF, ethylacetate, CH_2Cl_2, CCl_4, toluene, mesitylene, cyclohexane, hexane). The unusual, albeit not solvent-specific triggered HS→LS spin crossover transition is interpreted as solvent mediated confinement pressure (or matrix effect), effectively similar to pressure induced HS→LS transition.

The spin-crossover compounds [Fe(Htrz)$_3$](BF$_4$)$_2$·H$_2$O (SCO-1) and [Fe(Htrz)$_2$trz]BF$_4$ (SCO-2) (Htrz = 1,2,4-triazole) were embedded in the pores of mesostructured silica MCM-41 to yield SCO@MCM composites as evidenced by electron microscopy, gas sorption studies, powder X-ray diffractometry, atomic absorption and infrared spectrometry. Studies of the temperature-induced spin crossover behavior of the composites by temperature-variable ^{57}Fe Mössbauer spectroscopy, magnetic and differential scanning calorimetry measurements and optical reflectivity indicate that the spin transition of the composites was significantly shifted for SCO-1@MCM to higher temperature in comparison to bulk SCO-1 compounds while the shift for SCO-2 was negligible. These shifts in the transition temperature for SCO-1@MCM [versus bulk SCO-1] amounted to $T_c^{\uparrow}$ = 371/376 K [282/291 K] and $T_c^{\downarrow}$ = 340/345 K [276/286 K] (magnetic/optical reflectivity data) with a broadening of the hysteresis by 25–26 K relative to bulk SCO-1 (varying slightly with the used method). The significant difference in the SCO behavior of the similar materials SCO-1 and SCO-2 when embedded in the MCM-41 matrix is assigned to the hydration of the SCO-1@MCM material. Water is apparently crucial in transmitting the confinement pressure or matrix effect on the spin transition when the SCO compound is embedded between the pore walls.

In the last chapter of this thesis, four coordination polymers / MOFs based on three different carboxyphenyladamantane ligands have been synthesized and their structures were determined by single crystal X-ray diffraction measurements: Co[Ad(COOH)$_2$(COO)$_2$]·xDMF·yH$_2$O (**1**), Mn[Ad(PhCOO)$_4$]·xDMF·yH$_2$O (**2**), Mn[Ad(PhCOO)$_2$·DMF (**3**), Cd[Ad(PhCOO)$_3$·0.5DMF·0.5H$_2$O]·mH$_2$O·nDMF (**4**). These coordination networks were characterized by powder X-ray diffractometry, infrared spectrometry, N_2 sorption measurement

and thermogravimetric analysis. Compound **1** and **2** are 3D frameworks and possess potentially porous structures, but their structures were not very stable under high temperature/vacuum conditions. The dicarboxyphenyladamantane ligand of compound **1** is only singly deprotonated, while the tetracarboxyphenyladamantane ligand of compound **2** is completely deprotonated. Compound **3** and **4** are 2D networks, among them, compound **3** ($Mn[Ad(PhCOO)_2 \cdot DMF$) has paddle wheel nodes in the structure and proved to be nonporous. Compound **4** ($Cd[Ad(PhCOO)_3 \cdot 0.5DMF \cdot 0.5H_2O] \cdot mH_2O \cdot nDMF$) has two kinds of nodes in the structure, $\{Cd(\mu_6\text{-}O) \cdot DMF\}$ and $\{Cd(\mu_6\text{-}O) \cdot H_2O\}$, and proved to be porous in N_2 sorption experiments with a BET surface area of 196 m^2/g and a pore volume of 1.21 cm^3/g.

Zusammenfassung

Metall-organische Gerüstverbindungen (MOFs) sind Verbindungen, die durch koordinative Metall Bindungen mit organischen Liganden ein-, zwei- oder drei-dimensionale koordinationspolymere Netzwerke bilden können. Ihre einzigartigen Eigenschaften, wie z.B. hohe Oberflächen, einstellbare Porengrößen und Formen sowie die hohe (hydro)thermale Stabilität, führen zu vielversprechenden Anwendungen, einschließlich der „Wirt“ Funktion in Kompositmaterialien.

MIL-101(Cr), eines der wichtigsten prototypischen MOFs, ist gut untersucht und wird für viele wissenschaftliche Untersuchungen verwendet. Die Zugabe von Additiven in der Synthese von MOFs wird allgemein angewendet, um die Eigenschaften der MOFs zu verbessern. Daher wurde zu Beginn dieser Arbeit die Zugabe von verschiedenen Additiven zu der Synthese von MIL-101(Cr) gründlich untersucht. Die Zugabe von HNO_3 erwies sich als effiziente Methode um die Ausbeute von MIL-101(Cr) um mehr als 20% im Vergleich zu der üblichen Literatur-Methode nach Férey zu erhöhen. Auch die Porosität konnte um mehr als 20% gesteigert werden, in Bezug auf die besten Ergebnissen die bisher im Arbeitskreis erhalten wurden. Im Bereich der Spin-Crossover (SCO) Materialien ist es von hohem Interesse, die Übergangstemperatur zu verändern bzw. einzustellen. Eine Möglichkeit, die Spin-Übergangstemperatur zu modifizieren ist, das SCO Material in ein MOF einzulagern. Es wurde versucht, das Spin-Crossover Material Bis(hydrotris(pyrazolyl)borato)eisen(II) ($[Fe(HB(pz)_3)_2]$) mit verschiedenen Methoden in verschiedene prototypische MOFs einzulagern. Letztlich resultierte die Synthese des MOFs NH_2-MIL-101(Al) mit $[Fe(HB(pz)_3)_2]$ als $[Fe(HB(pz)_3)_2]$@NH_2-MIL101(Al) (S@M Produkt) undeiner maximalen Beladung von ~11 Gew.% (0.16 Fe Moleküle pro Al_3OL_3-Einheit). Die Struktur des Materials wurde durch Pulver-Röntgen-Diffraktometrie, PXRD und spektroskopische Untersuchungen bestätigt. Der eingeschlossene, luftstabile Komplex kann nicht durch Vakuumtrocknung (120°C and$<10^{-6}$ Torr) aus dem MOF entfernt werden kann, und ist in den Käfigen des MOF-Netzwerks eingeschlossen. Stickstoff und CO_2 Gas-Adsorptionsmessungen der getrockneten S@M Komposite mit unterschiedlichen S@M Beladungen bestätigen die Abnahme der Porosität des Wirtmaterials NH_2-MIL-101(Al). $[Fe(HB(pz)_3)_2]$ ist ein Spin-Crossover Material mit einem stufenweisen Spin-Übergang bei einer

Temperatur von 330 K (T_c) für das im Grundzustand befindliche Volumenmaterial. $[Fe(HB(pz)_3)_2]$, eingeschlossen in den Poren des MIL-Gerüstes als S@M Komposit, liegt bei Raumtemperatur größtenteils in der high-spin (HS) Form vor (hellgelbe Farbe des Wirtmaterials dominiert). Durch die Einlagerung verschiebt sich die Übergangstemperatur von $[Fe(HB(pz)_3)_2]$ im S@M Komposite zu deutlich niedrigerer Temperatur, im Vergleich mit T_c = ~330 K für das im Grundzustand befindliche Volumenmaterial $[Fe(HB(pz)_3)_2]$. Gleichzeitig kann der Spin-Crossover Übergang von $[Fe(HB(pz)_3)_2]$ im Kompositmaterial bei Raumtemperatur ausgelöst werden, indem das getrocknete Material mit verschiedenen polaren bis unpolaren Lösungsmitteln getränkt wird (H_2O, MeOH, DMSO, DMF, BuOH, t-BuOH, THF, Ethylacetat, CH_2Cl_2, CCl_4, Toluol, Mesitylen, Cyclohexan, Hexan). Dieser ungewöhnliche, wenn auch nicht Lösungsmittel-spezifische, HS→LS Spin-Crossover Übergang, wird interpretiert als Lösungsmittel-induzierter Einlagerungsdruck (oder Matrix Effekt), ähnlich zum Druck-induzierten HS→LS Übergang.

Die Spin-Crossover Materialien $[Fe(Htrz)_3](BF_4)_2 \cdot H_2O$ (SCO-1) und $[Fe(Htrz)_2trz]BF_4$ (SCO-2) (Htrz = 1,2,4-Triazol) wurden in die Poren von mesostrukturierter Kieselerde MCM-41 eingelagert. Das resultierende SCO@MCM Material wurde durch Elektronenmikroskopie, Gassorptionsmessungen, Pulverdiffraktometrie, Atomabsorptionsspektrometrie und Infrarotspektroskopie charakterisiert. Untersuchungen des Temperatur-induzierten Spin-Crossover Verhaltens des Kompositmaterials durch Temperatur-variable ^{57}Fe Mössbauer Spektroskopie, magnetische Messungen und dynamische Differenzkalorimetrie, sowie Messung der optischen Reflektivität ergaben, dass der Spin-Übergang des Kompositmaterials SCO@MCM, im Vergleich zum Volumen-SCO-1, deutlich zu höherer Temperatur verschoben ist. Die Verschiebung für SCO-2 hingegen war vernachlässigbar gering.

Die Verschiebung der Übergangstemperatur für SCO-1@MCM [gegenüber Volumen-SCO-1] beträgt $T_c^{\uparrow}$= 371/376 K [282/291 K] und $T_c^{\downarrow}$= 340/345 K [276/286 K] (aus Daten der magnetischen Messungen/optische Reflektivität) mit einer Verbreiterung der Hysterese von 25–26 K relativ zum Volumen-SCO-1 (leichte Abweichungen zwischen den verwendeten Methoden). Der deutliche Unterschied im Verhalten der ähnlichen Materialien SCO-1 und SCO-2, wenn diese in die MCM-Matrix eingebettet werden, wird der Hydratation des SCO-1@MCM Materials zugeschrieben. Wasser scheint dementsprechend eine entscheidene Rolle bei der

Übertragung des Einlagerungsdrucks (oder Matrix-Effekts) auf den Spin-Übergang zu spielen, wenn das SCO-Material in die Poren des porösen Wirts eingelagert wird.

Im letzten Kapitel dieser Arbeit wurden vier Koordinationspolymere/MOFs auf der Basis von drei verschiedenen Carboxyphenyladamantan-Liganden hergestellt. Die Strukturen der Kristalle wurden mit Hilfe von Einkristall-Röntgenstrukturanalyse bestimmt:

$Co[Ad(COOH)_2(COO)_2]\cdot xDMF\cdot yH_2O$ (**1**), $Mn[Ad(PhCOO)_4]\cdot xDMF\cdot yH_2O$ (**2**), $Mn[Ad(PhCOO)_2\cdot DMF$ (**3**), $Cd[Ad(PhCOO)_3\cdot 0.5DMF\cdot 0.5H_2O]\cdot mH_2O\cdot nDMF$(**4**).

Diese Koordinationsnetzwerke wurden mittels Pulverdiffraktometrie, Infrarotspektrometrie, Stickstoff-Sorptionsmessung und thermogravimetrischer Analyse charakterisiert.

Die Materialien **1** und **2** bilden dreidimensionale Gerüste und besitzen potentiell poröse Strukturen. Allerdings erweisen sich diese Verbindungen bei höheren Temperaturen und niedrigen Drücken als nicht stabil. Der Dicarboxyphenyladamantan-Ligand von Verbindung **1** ist nur einfach deprotoniert, während der Tetracarboxyphenyladaman-Ligand von Verbindung **2** vollständig deprotoniert vorliegt. Die Materialien **3** und **4** bilden 2D Netzwerke aus. Verbindung **3** ($Mn[Ad(PhCOO)_2\cdot DMF$), weißt als Knotenpunkte Schaufelrad-Einheiten in der Struktur auf und erwies sich als nicht porös. Verbindung **4** ($Cd[Ad(PhCOO)_3\cdot 0.5DMF\cdot 0.5H_2O]$ $mH_2O\cdot nDMF$) besitzt zwei Arten von Knotenpunkten in der Struktur: $\{Cd(\mu_6\text{-}O)\cdot DMF\}$und $\{Cd(\mu_6\text{-}O)\cdot H_2O\}$, und erwies sich bei Stickstoff-Sorptionsmessungen als porös (BET Oberfläche 196 m^2/g und ein Porenvolumen 1.21 cm^3/g).

Chapter 1
General Introduction

1. Metal organic frameworks (MOFs)

Metal-organic frameworks (MOFs) or metal-organic coordination networks (MOCNs), are crystalline and potentially porous compounds consisting of metal ions or clusters coordinated to often rigid organic ligands to form one-, two-, or three- dimensional structures via coordinative metal-ligand bonding (Scheme 1.1). The ligand should be a bridging organic group. At least in one extended dimension the metal atoms should solely be bridged by this organic ligand. Furthermore, at least one carbon atom should lie between the donor atoms.[1]

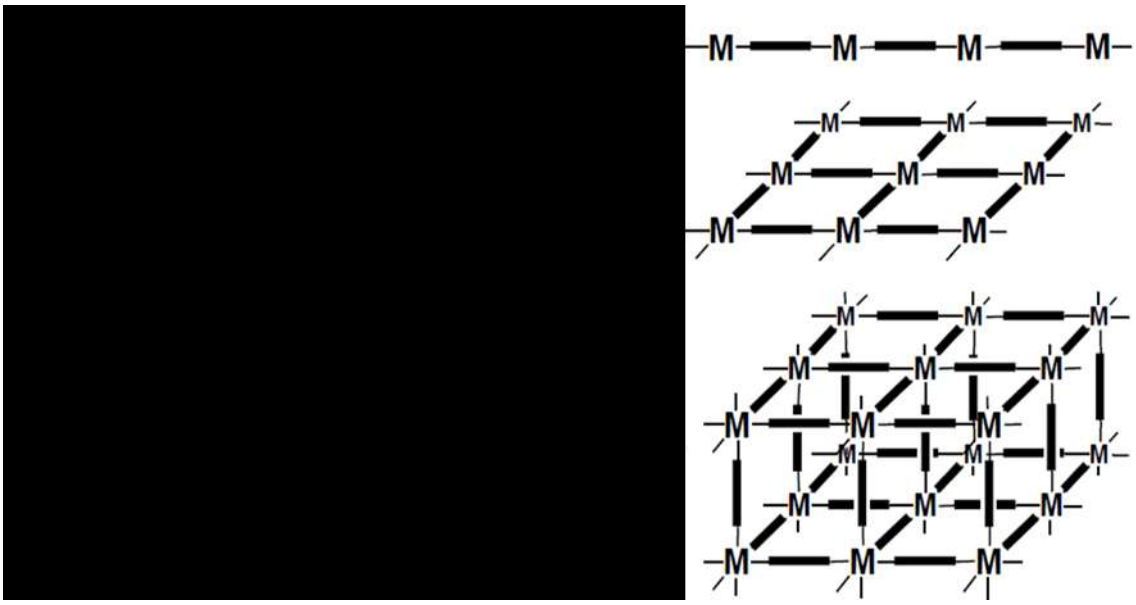

Scheme 1.1. Schematic representation of the definition of 1D, 2D or 3D metal-organic frameworks.(Figure taken with permission from the author of ref 2. Copyright belongs to Christoph Janiak, 2013.)

The preceding class of compounds to MOFs are coordination polymers which can be traced to 1964, but the interest in MOF area started in the early 1990s.[3] Thus, the field has now become mature and but is still fast-growing and timely. The last decade has seen an almost exponential growth in publications on their structural topologies and potential applications (Figure 1.1).

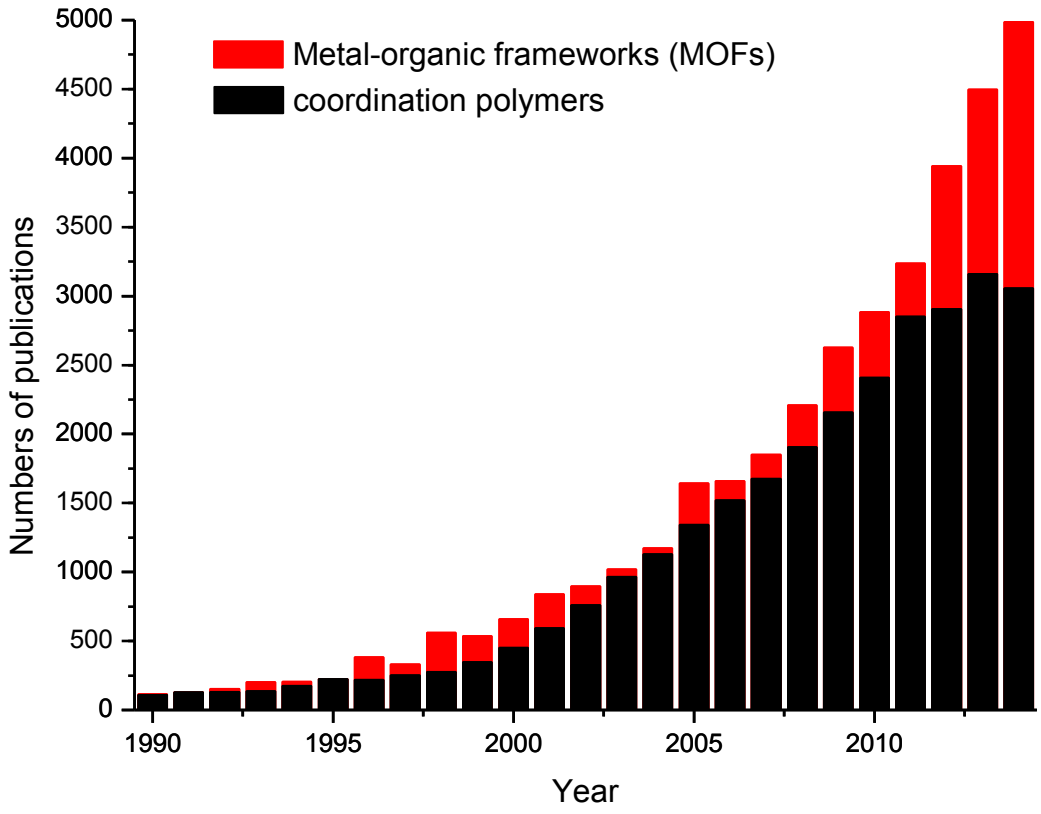

Figure 1.1. Number of papers by year (since 1990) that use the concept (Scifinder) 'metal organic framework', 'MOF' or the term 'coordination polymer'. The numbers are based on a Scifinder search in March 2015 with one of the concepts 'coordination polymer', 'MOF' or 'metal organic framework', but not containing (excluding) the concept 'coordination polymerisation'.

The term metal–organic framework (MOF) was first used by Yaghi et al. in 1995,[4,5] in which MOF can imply a class of compounds with 3D framework structures that exhibit porosity and/or guest exchange properties. In a recent IUPAC definition MOFs are described as coordination networks with organic ligands containing potential voids.[6,7] However many researchers use the term MOF rather freely and refer to a non-porous coordination polymeric structure as a MOF. Furthermore, there are several different MOF terminologies which are commonly used: MIL (Materials Institute Lavoisier/Material of Institute Lavoisier, Férey et al.[8,9]), PCP (porous coordination polymer, Kitagawa et al.[10]), ZIF (zeolitic imidazole frameworks, Park et al.[11]), and

some other MOF terminologies were named with university acronyms, for example HKUST[12] (Hong Kong University of Science and Technology), CAU[13] (Christians-Albrecht-University, in Kiel), NU[14] (Northwestern University, in Michigan), DUT[15] (Dresden University of Technology) and UiO[16] (University of Oslo).

Normally, these metal-organic compounds are synthesized from molecular building units (Scheme 1.1) in solution or by hydro/solvothermal procedures.[17] Anions are essential for the charge balance to the metal cations. The anions can be deprotonated carboxylate ligands. Additonally needed anionic charges are usually functionalized within the metal nodes, e.g, as bridging (μ-) oxido or hydroxido ligands or terminal fluorido or hydroxido ligands.

In most MOFs, the anions donors are negatively charged bridging ligands, for example carboxylates. Multi-carboxylate ligands, especially benzene-multicarboxylato ligands which possess suitable spacer are frequently chosen for metal–organic networks.[18,19,20,21] benzene-1,4-dicarboxylate[22,23,24] (bdc^{2-}, terephthalate), benzene-1,3-dicarboxylate (ip^{2-}, isophthalate)[25,26,27] and benzene-1,3,5-tricarboxylate (btc, trimesate acid)[28,29,30,31] are typical among them (Scheme 1.2). Terephthalate possesses a 180° angle between the two carboxylic groups and it has two ways to form the structure. One is that, it forms short bridges via one carboxylato end, simultaneously connecting four metal ions[32,33,34]; another way is forming long bridges via the benzene ring, leading to a great variety of structures.[35,36] Whereas the two carboxylate moieties of isophthalate are rigidly predisposed at 120°, but it is also a good oxygen donor for building metal–organic networks.[37,38,39] Trimesate has been extensively used as a bridging ligand in the synthesis of multidimensional MOFs. Trimesic acid (benzene-1,3,5-tricarboxylic acid, $btcH_3$) can also be only partly deprotonated in the construction of MOFs as $btcH_n^{(3-n)-}$ (n = 0, 1, 2).[40,41,42,43,44,45]

For neutral bridging ligands, charge balance is accomplished by anions from the original metal salt such as Cl^-, NO_3^-, SO_4^{2-}, and BF_4^-. The ligand 4,4'-bipyridine (4,4'-bipy) is an eminent example for an attractive molecular building block for diverse architectures of metal–organic coordination networks.[46,47,48,49] It can be used to form one- dimensional (1D) chains, two-dimensional (2D) grids and three-dimensional frameworks.[50,51,52] In addition, other similar rigid bridging linkers like 2,4,6-tri(pyridin-4-yl)-1,3,5-triazine (tpt) and bis(pyridin-4-yl)-1,2-ethene (bpe) are also belong to this situation.

Scheme 1.2. Schematic drawings of benzene-1,4-dicarboxylate, benzene-1,3-dicarboxylate and benzene-1,3,5-tricarboxylate.

2. Prototypical MOFs

There are some "famous" prototypical MOFs have been studied intensively, such as HKUST-1[75], MOF-5[53], IR-MOF-n[77], MIL-53[83], MIL-100[88], MIL-101[8], UiO-66[16] and ZIF-8[11]. Due to the fact that they are porous, possess large surface area, tunable pore sizes and topologies, they are considered to have diverse promising applications, such as gas storage,[54,55,56,57] gas separation,[58] drug delivery,[59,60] catalysis,[61,62,63,64,65] container for metal nanoparticles or colloids,[66,67] hosts for polymerization reactions,[68,69,70] luminescence,[71,72,73] and magnetism.[74]

HKUST-1 is a three-dimensional copper-trimesate-based porous material with the empirical formula 3D-$[Cu_3(btc)_2(H_2O)_3]$. It is one of the most studied MOFs because of easy formation, high porosity and known properties associated with this compound.

The $\{Cu_2(btc)_4\}$ building unit of HKUST-1 has $\{Cu_2\}$ units which are coordinated with four carboxylate groups in the well-known paddle-wheel structure of copper acetate (Figure 1.2, Top).[75] The packing diagram with the cubic unit cell of 3D-$[Cu_3(btc)_2(H_2O)_3]$ shows that there is a large square-shaped channel of 9×9 Å along the a-axis (Figure 1.2, Bottom). HKUST-1 can be stable until 240 °C,[75] the crystal water molecules and copper-coordinating aqua ligands can be removed by thermal methods without loss of structure integrity. The BET surface area of HKUST-1 can be up to 1700 m^2/g.[76]

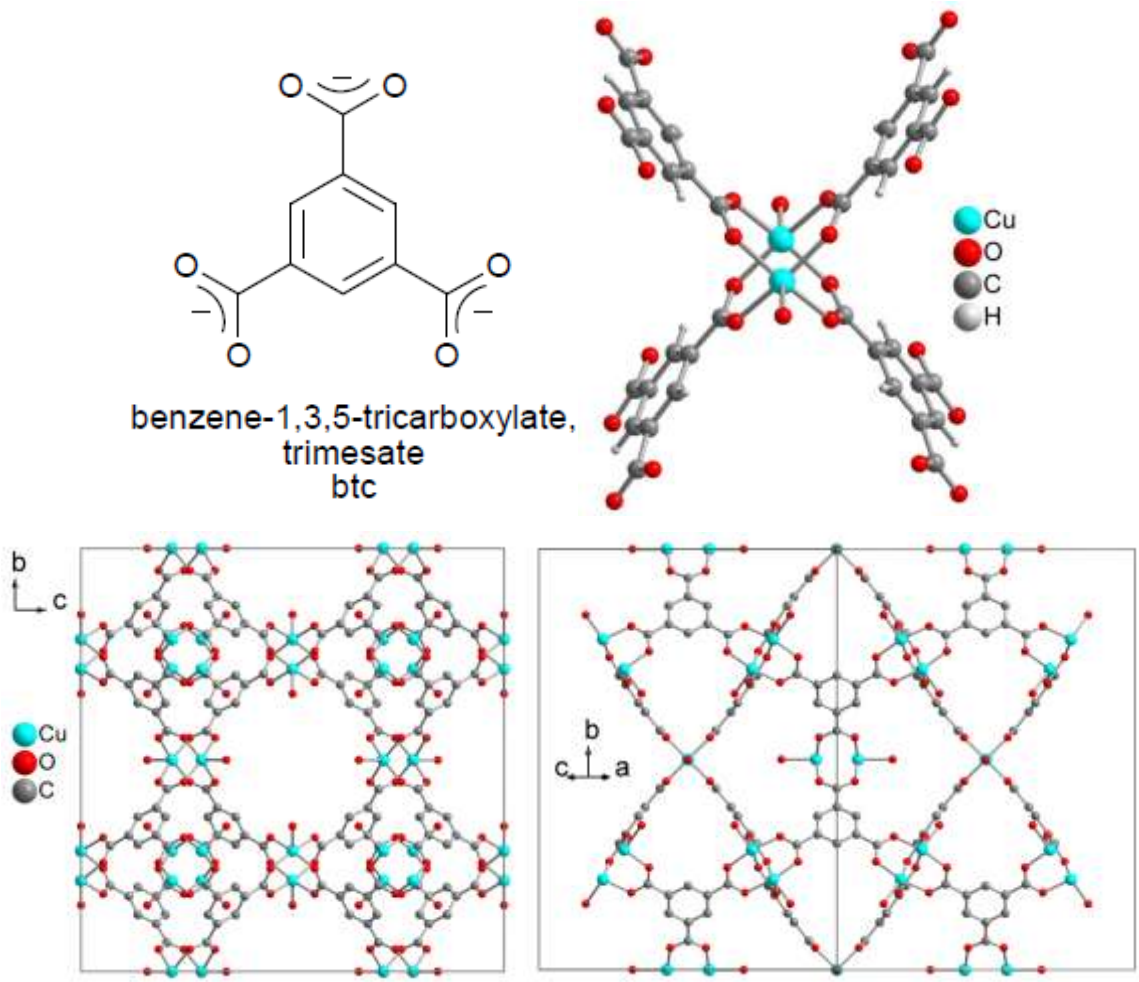

Figure 1.2. The trimesate ligand structure and the {$Cu_2(btc)_4$} building unit of HKUST-1(Top), two views of the packing diagram with the cubic unit cell of 3D-[$Cu_3(btc)_2(H_2O)_3$] (Bottom). Disordered water-guest molecules and the H atoms are not shown; the different objects in this figure are not drawn to scale (CSD-Refcode FIQCEN).[75,97]

IR-MOF-n (n = 1–16) is a series of cubic iso-reticular structure MOFs based on secondary building unit (SBU) {Zn_4O} and the organic carboxylate linkers. These MOFs have large tunable pore sizes, specific pore volumes and high porosity.[77]

IR-MOF-1, which is also named as MOF-5, is one of the best known and prototypical MOFs with the empirical formula [$Zn_4(\mu\text{-}O)(bdc)_3$] (bdc = benzene-1,4-dicarboxylate, terephthalate). The structure of MOF-5 with the terephthalate linker (BDC) is probably one of the most widely recognized. From the section of the crystal packing diagram of MOF-5, each {Zn_4O} secondary building unit coordinates with six carboxylate groups and forms the {Zn_4O} tetrahedron as an octahedrally coordinated node of the framework (Figure 1.3 a). The six edges of the tetrahedron

are spanned by carboxylate groups. The carbon atoms of the $–CO_2$ carboxylate groups are then positioned at the vertices of an octahedron (Figure 1.3 a). Then the $\{Zn_4(\mu_4\text{-}O)(O_2C\text{-})_6\}$ node infinitely extends to a three-dimensional primitive cubic pcu-a or cab network. The structure is shown as ball-and-stick and as space-filling representation (Figure 1.3 b). The yellow sphere which filled in the pore takes into account the van-der-Waals radii of the framework walls with a diameter of 10 Å. The augmented "–a" notation refers to a net where the simple point vertices of the original pcu net are replaced by vertex figures (polyhedron or polygon), here by an octahedron. The B atoms in CaB_6 (cab) form such octahedra which as vertices are connected to a pcu-a net. Hence, cab is an alternative symbol for pcu-a (Figure 1.3 c). Activated MOF-5 possesses a high BET surface area (~2900 m^2/g)[78] and high thermal stability (it can keep its structural integrity up to 400 °C).[79] But MOF-5 is stable only at very low water content and unstable when exposed to ≥4% water. That means that under ambient atmospheric conditions, MOF-5 quickly be decomposes.[80] Thus, high quality MOF-5 can only be obtained when the exposure to water and ambient air was minimized.[81]

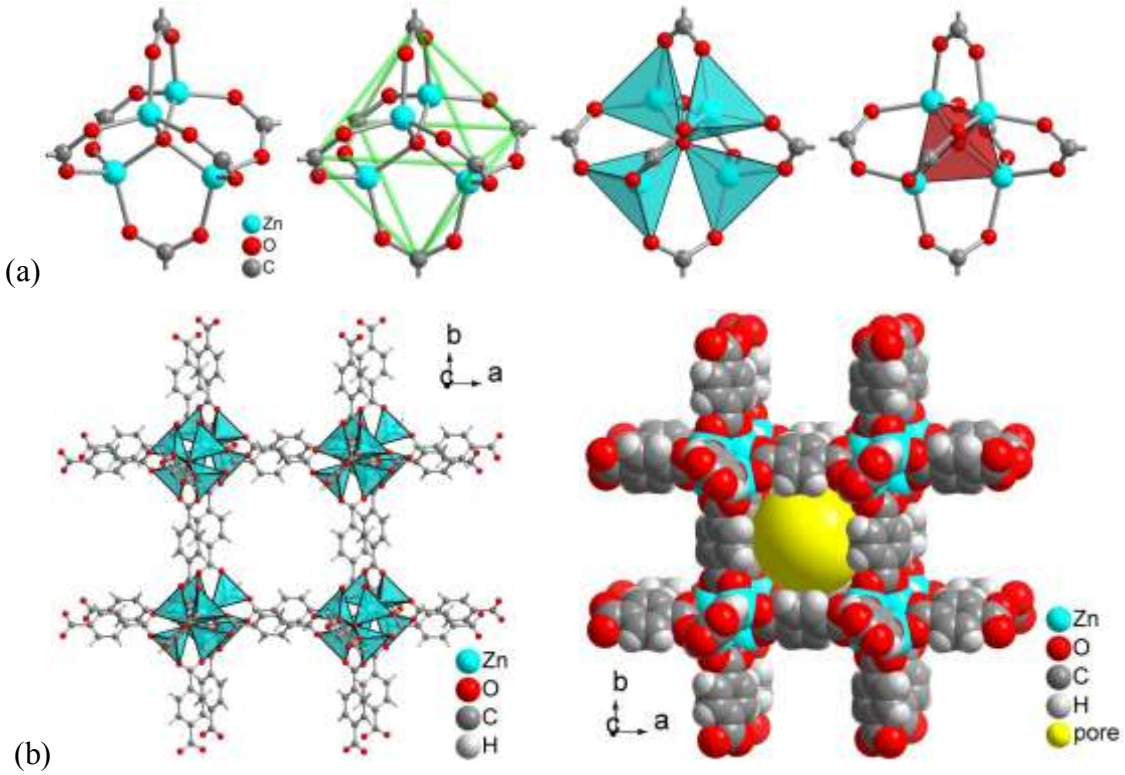

(c)

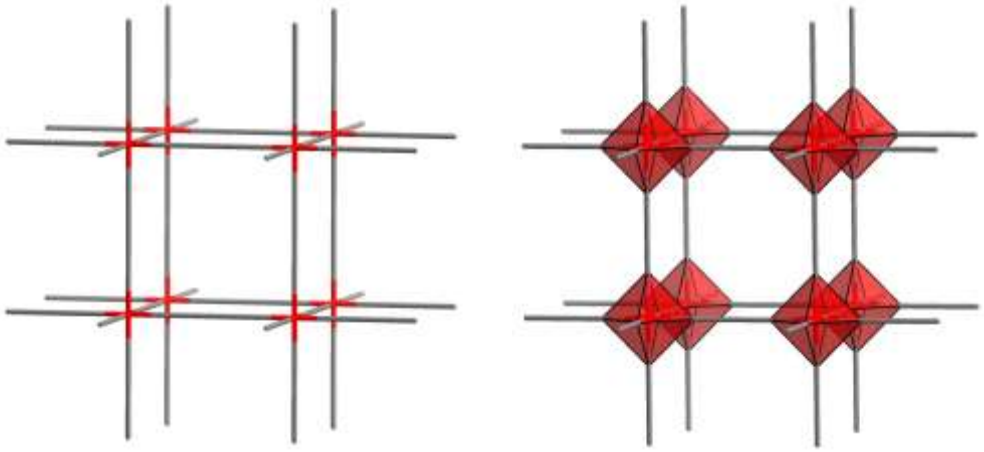

Figure 1.3. (a) ball-and-stick and polyhedral presentations of the tetrahedral {Zn4O} secondary building unit; (b) the crystal packing diagram of MOF-5 with polyhedral {Zn4O} and as space-filling representation (CSD-Refcodes SAHYIK, SAHYOQ, and EDUSIF; disordered solvent-guest molecules are not shown). (c) The three-dimensional primitive cubic pcu-a or cab network of MOF-5. The different objects in this figure are not drawn to scale.

The MIL-n type (for Materials Institute Lavoisier) MOFs are a kind of porous metal carboxylates which are associated with the group of Férey et al.. MILs usually consist of trivalent cations, such as vanadium(III), chromium(III) and iron(III), and also p-elements such as aluminium(III), gallium(III) or indium(III). MILs are 3D, porous framework MOFs with resemblance to zeolite topologies.[82]

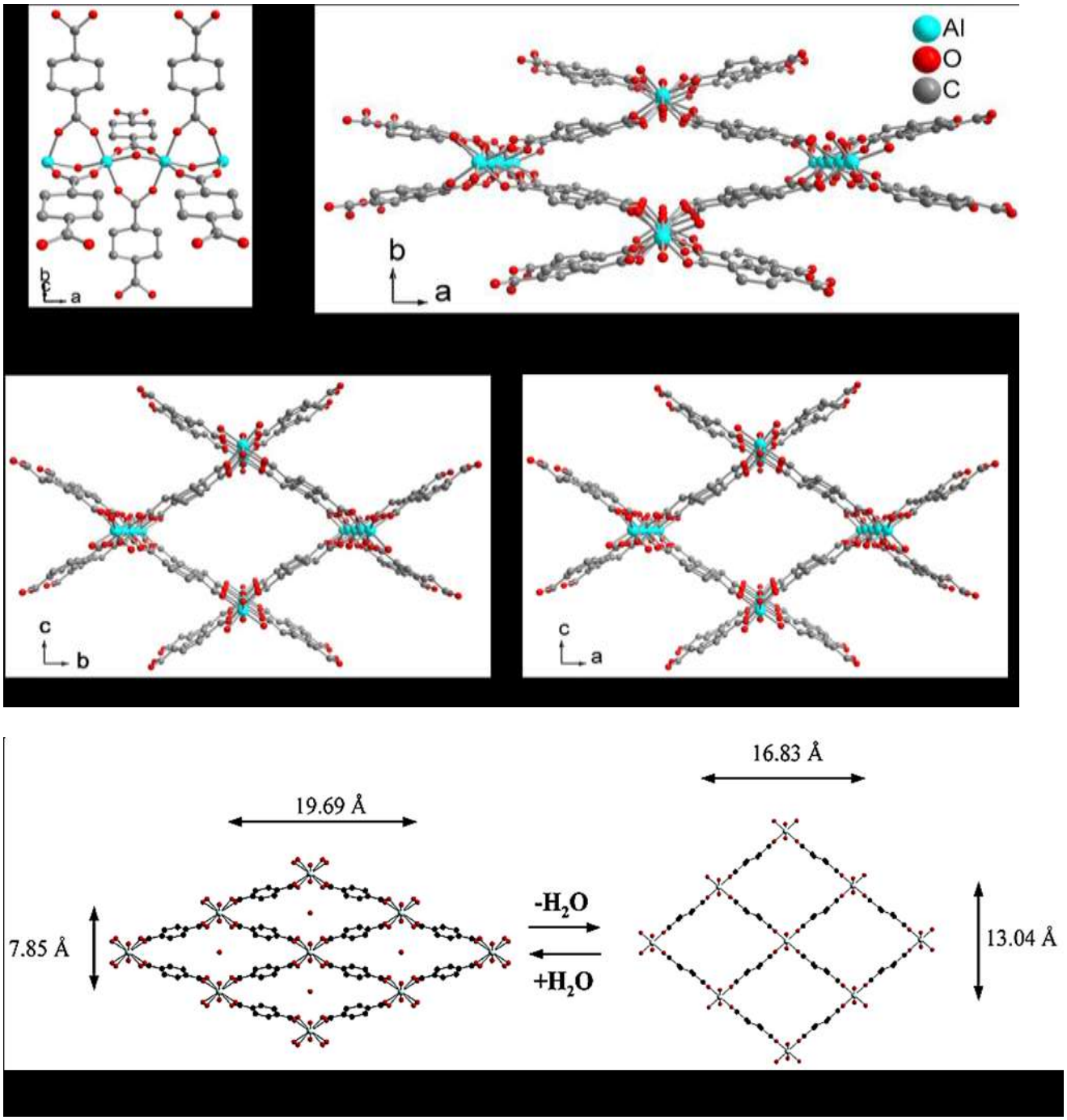

Figure 1.4. (a) Section of the bdc- and OH- bridged Al-strand, (b) narrow pore network form MIL-53(Al)lt, the wide pore network of (c) MIL-53(Al)ht and (d) MIL-53(Al)as; representation of the "breathing" effect between (e) MIL-53(Al)lt and (f) MIL-53(Al)ht through water desorption and adsorption. (CSD-Refcodes QONQEQ and QONOAM; disordered solvent-guest molecules are not shown in b and c, different objects are not drawn to scale.)[83]

MIL-53 is one important MIL-n structure with the empirical formula 3D-[M(μ_4-bdc)(μ-OH)].

It consist of M = Al, Cr or Fe with hydroxido and terephthalate bridges (Figure 1.4).[83,84,85] MIL-53 is well known for its flexible framework structure, that is a 'breathing'-type network, which can assume different shapes and porosities depending on the guest's presence or absence. MIL-53(Al) can be further differentiated as MIL-53(Al)as, MIL-53(Al)ht and MIL-53(Al)lt (with as = as synthesized, ht = high temperature and lt = low temperature).[86] In the section of the packing diagram of [Al(bdc)(μ-OH)] subunit (Figure 1.4 a), each carboxylate of bdc ligand bridges four Al atoms and the channels can contain guest molecules in the MIL-53as and MIL-53ht structure (Figure 1.4 c and d, guest molecules not shown). In MIL-53as (Al), some disordered BDC molecules are trapped in the tunnels with the dimensions 7.3×7.7 $Å^2$. Whereas after heating to 275°C, MIL-53as is turned to be MIL-53ht, which has empty pores and its tunnel dimensions become to 8.5×8.5 $Å^2$ (the Langmuir surface area of MIL-53ht (Al) can be up to 1590 m^2/g).[87] Thus, MIL-53as and MIL-53ht nearly have the same network (Figure 1.4 c, d). MIL-53lt and MIL-53ht can reversibly change the structure via ad/desorption of water (Figure 1.4 e and f). When MIL-53ht is subjected to cooling and exposed to polar molecules, the channels shrink.

MIL-100 is another important MIL-n type MOFs, its empirical formula is 3D-$[M_3O(btc)_2(X)(H_2O)_2] \cdot n\ H_2O$ (M = Cr, Fe, Al or V, X = OH, F, btc = benzene-1,3,5-tricarboxylate, trimesate).[88,89,90,91,92] As an example, the structure of MIL-100(Al) is built up from building units of trinuclear octahedrally coordinated Al atoms, which form a supertetrahedral block (Figure 1.5 a and b). MIL-100(Al) possesses two types of cavities. The larger cage is defined by 12 pentagonal rings and 4 hexagonal rings, and has a pore with a diameter of 29 Å and accessible windows with diameters of 8.8 Å (Figure 1.5 c). The smaller cage is defined by 12 pentagonal rings, and has a pore with a diameter of 25 Å and accessible windows with diameters of 5.2 Å (Figure 1.5 d).[93] Activated MIL-100(Al) possesses relatively high porosity (BET surface area up to 2150 m^2/g), high thermal stability (up to 350 °C) and high water stability. Yet the synthesis condition of MIL-100(Al) is quite harsh (pH = 0.6, T = 210 °C). The other MIL-100(M), M=Cr, Fe or V, are isostructural with other metal atoms instead of Al.

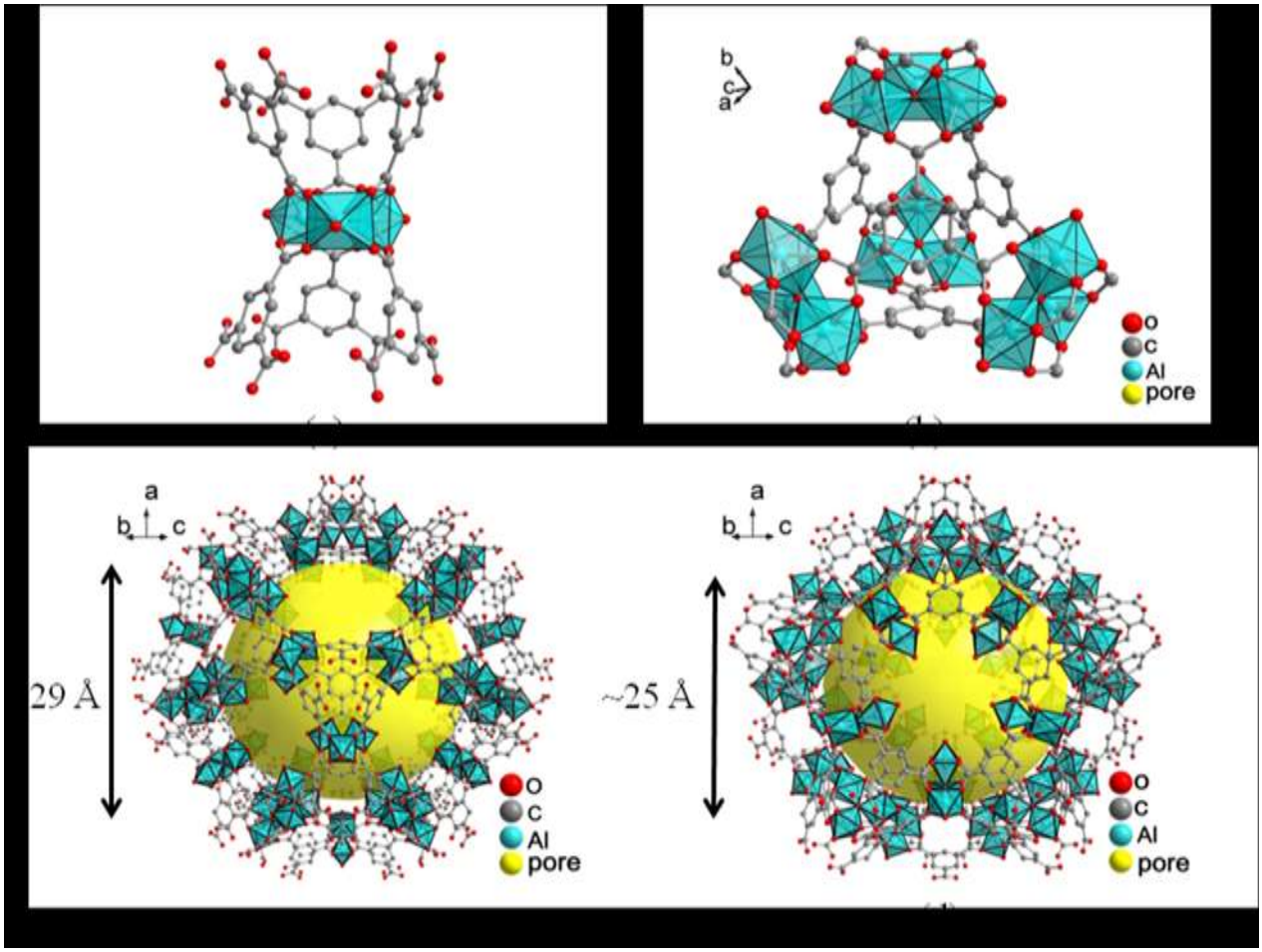

Figure 1.5. (a) The second building unit (SBU), (b) supertetrahedra, (c) large cage and (d) small cage of MIL-100(Al). (CSD-Refcodes BUSPIP, CIGXIA and UDEMEW; hydrogen atoms and solvent molecules of crystallization are not shown, different objects are not drawn to scale.)

MIL-101 is perhaps the most famous MIL-n type MOF. It is well known for its high porosity and hydrothermal stability. The detailed introduction to MIL-101, especially MIL-101(Cr), will be given in Chapter 2.

UiO-n type MOFs (for University of Oslo) are porous zirconium carboxylates frameworks. UiO-66 is a Zr-MOF with bdc linkers and with an empirical formula $Zr_6O_4(OH)_4(bdc)_{12}$. The SBU $\{Zr_6O_4(OH)_4(CO_2)_{12}\}$ in UiO-66 is 12 coordinated, the highest coordination reported for a SBU in a MOF.[94] Coordination number 12 is the coordination of metal atoms in closed packed metal structures. The SBU consists of an inner $Zr_6O_4(OH)_4$ core in which the triangular faces of the Zr_6-octahedron are alternatively capped by μ_3-O and μ_3-OH groups (Figure 1.6 a). All of the polyhedral edges are bridged by carboxylates ($-CO_2$) originating from the dicarboxylic acids

forming a $Zr_6O_4(OH)_4(CO_2)_{12}$ cluster (Figure 1.6 b). Each zirconium atom is eight-coordinated forming a square-antiprismatic coordination consisting of eight oxygen atoms. The packing diagram with the cubic unit cell of 3D-$[Zr_6O_4(OH)_4(CO_2)_{12}]$ is shown in Figure 1.6 c. Up to now, the highest reported BET surface area of UiO-66 is 1580 m^2/g.[16]

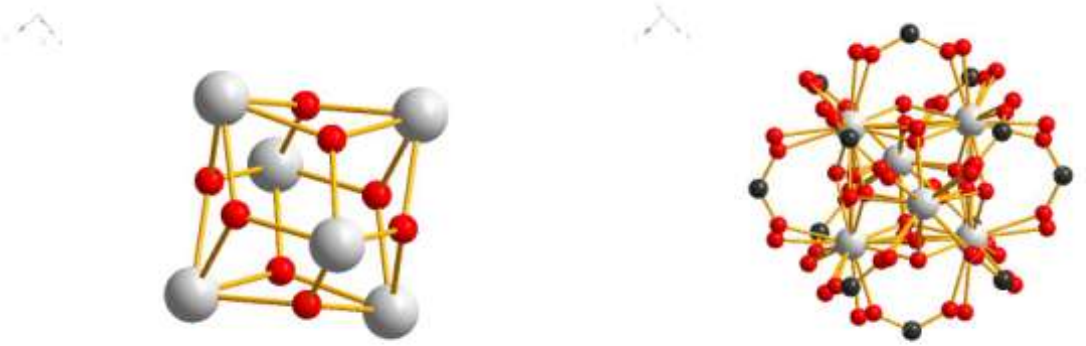

(a) (b)

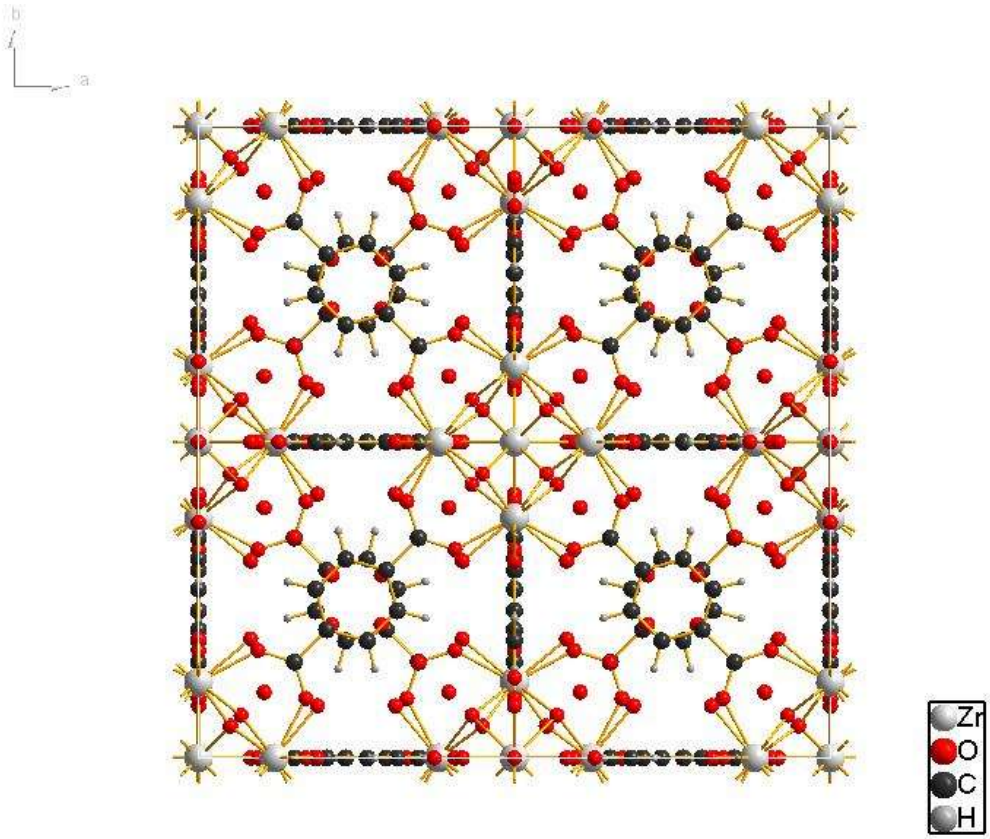

(c)

Figure 1.6. (a) The inner core Zr_6-cluster, (b) the full cluster with the Zr-bridging carboxylate groups and (c) the packing diagram with the cubic unit cell of 3D-$[Zr_6O_4(OH)_4(bdc)_{12}]$ (CSD-Refcodes RUBTAK; solvent molecules of crystallization are not shown, different objects are not drawn to scale.)

Zeolithic imidazolate frameworks or ZIFs are constructed from the bridging action of the anionic imidazolate ligands (or its derivatives) between single zinc atoms. The imidazolate function in ZIFs does not tend to form metal clusters. ZIF-8 is a prototypical ZIF compound, with an empirical formula 3D-[Zn-$(mim)_2$] $\cdot 2H_2O$ (mim = 2-Methylimidazolate). 2-Methylimidazolate ligands bridge between individual zinc atoms and span the edges of the cuboctahedral β-cage in the sodalite network which is depicted by the blue topological lines connecting the Zn atoms (Figure 1.7).[95] ZIF-8 probably is one of the most hydrolytically stable ZIFs, and its BET surface area can be up to 1630 m^2/g.[11]

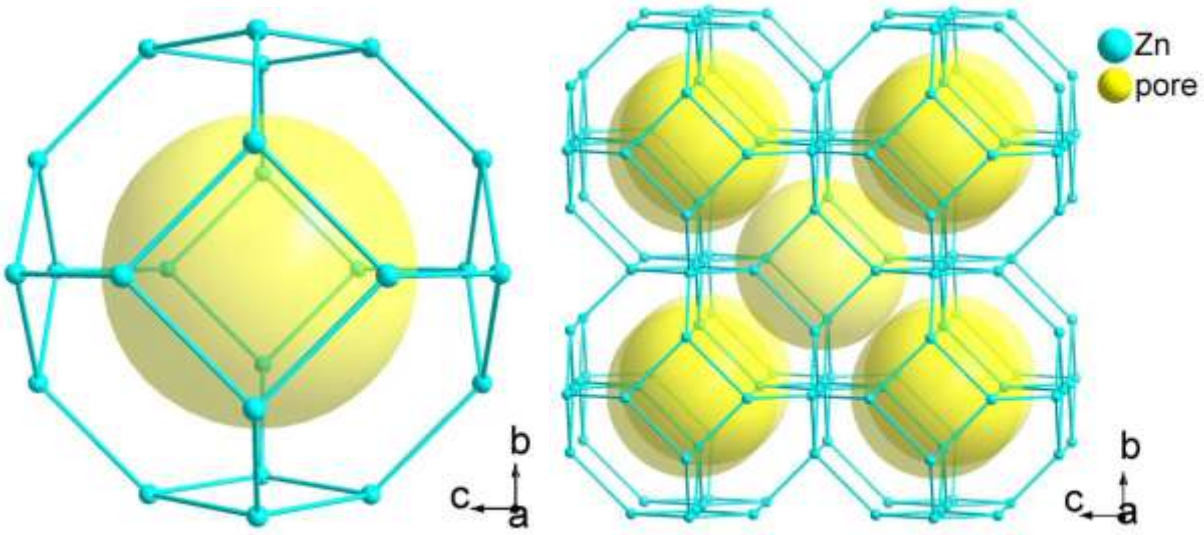

Figure 1.7. One and nine sodalite cages - depicted by the blue topological lines connecting the Zn atoms. The yellow sphere with a radius of 6 Å highlights the inner pore of the sodalite cage and takes into account the van-der-Waals radii of the framework atoms. (CSD-Refcodes VELVOY; solvent molecules of crystallization are not shown, different objects are not drawn to scale.)

3. Application-oriented properties of MOFs

Due to the porous properties of MOFs, they have attracted tremendous attention over the past years.[96] MOFs are assessed in terms of property investigations in the areas of catalysis, chirality, drug-storage/delivery, gas-storage/separation, conductivity, luminescence, magnetism, spin-transition (spin-crossover), non-linear optics (NLO) and zeolitic behavior (Figure 1.8).[97]

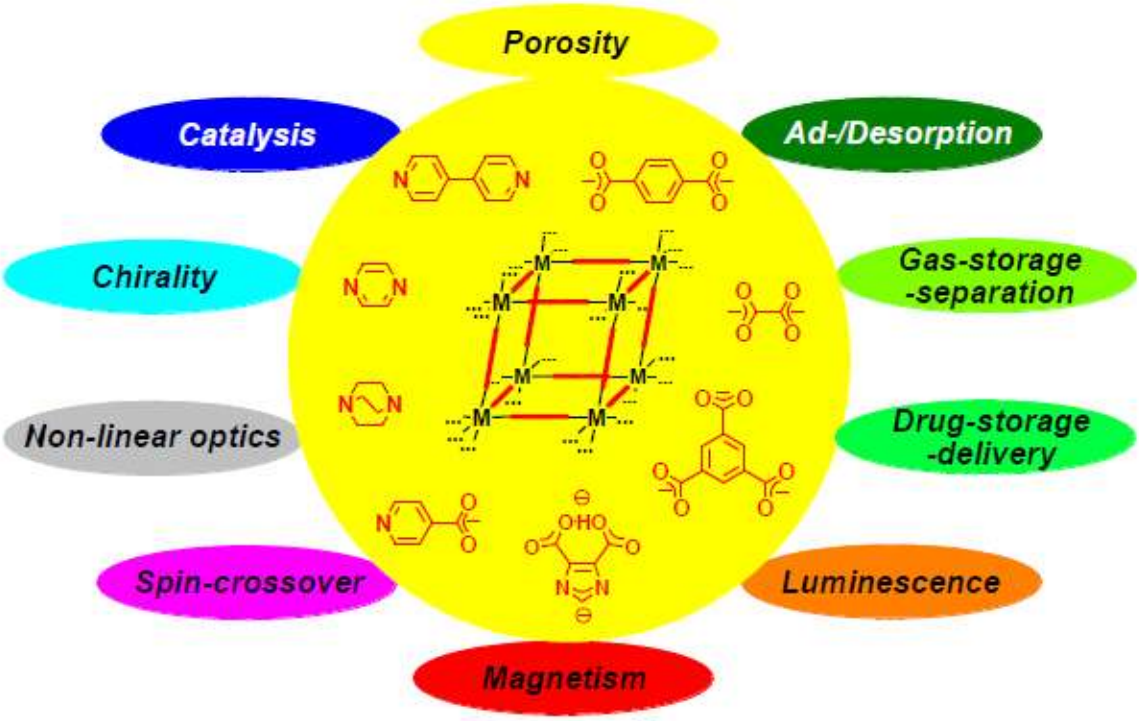

Figure 1.8. Schematic presentation of application-oriented properties of MOFs. (Figure taken with permission from [ref 97]. Copyright 2010, Royal Society of Chemistry.)

The porous nature of some metal-organic frameworks and/or the presence of possibly catalytically active transition-metal centers are seen as the basis of size- and shape-selective catalytic applications of such materials. Generally, a meaningful catalytic study must involve investigation of the liquid phase supernatant over the solid-state catalyst material after a catalytic cycle. This has to make sure that the MOFs does not partly dissolve and degradate so to exclude that it is its components which act as a homogeneous catalyst in solution. For instance, the 2D square network material $^{2}_{\infty}[Cd(NO_3)_2(4,4'\text{-bipy})_2]$ (The notation $^{n}_{\infty}[\text{formula}]$ indicates the dimensionality (n) of an infinite (∞) framework.) was used as catalyst for the cyanosilylation of aldehydes.[98] The homochiral 2D lanthanide phosphonates $^{2}_{\infty}\{[Ln(H_2L)(H_3L)(H_2O)_4]\cdot xH_2O\}$ (Ln = La, Ce, Pr, Nd, Sm, Gd, Tb) had the capability of heterogeneously catalyzing the cyanosilylation of aldehydes and ring opening of mesocarboxylic anhydrides.[99] A 3D coordination polymer of Ru(II) with 1,4-diisocyanobenzene ligands was reported as a heterogeneous hydrogenation catalyst for 1-hexene.[100] Titanium aryldioxide coordination

polymers of one- to three-dimensionality, $^{n}{}_{\infty}[Ti(OArO)_2(py)_2]$ (Ar = p-C_6H_4-, 2,7-naphthyl, 4,4'-biphenyl; py = pyridine and 4-Me- or 4-Phpyridine) were reported as cocatalyst due to their Ziegler–Natta polymerization activity towards ethene or propene with methylalumoxane (MAO).[101]

Chirality is also interested in the formation of chiral MOFs. It is expected that chiral supramolecular architectures could play a role in optical devices. There is a tentative idea that using porous chiral frameworks for enantiomer separation or chiral synthesis.[102] In particularly, the interest for MOFs is focused on the preparation of helices with homochirality. Yet, most helices are formed from achiral ligands which almost always leads to racemic mixtures of P- and M- (right/left-handed) helices.[103,104,105]

Metal-organic frameworks are investigated for luminescence properties due to their higher thermal stability than the pure organic ligand and the capability of affecting the emission wavelength of the organic material by metal coordination. One efficient method to get new types of electroluminescent materials for potential applications as light-emitting diodes (LEDs) is combining organic spacers and transition-metal centers in frameworks.[106] For example, recently, a new yellow phosphor with high quantum yield by immobilizing a preselected chromophore into a rigid framework, which readily generates white light with high luminous efficacy by coating a blue light-emitting diode (LED).[107] Three new layered metal–organic frameworks (MOFs) based on 2-phenylsuccinic acid (H_2psa) and lanthanide ions with the formula $[Ln_2(C_{10}H_8O_4)_3(H_2O)]$ (Ln = Eu, Sm and Eu–Gd) have been reported and show photoluminescence (PL) properties.[108] A lanthanide organic–inorganic hybrid material was reported that has high quantum yield and satisfactory luminescence stability.[109] The luminescence has been observed in the solid state and at room temperature, unless noted otherwise.

Magnetic studies of metal-organic frameworks are mainly focused on embedded in the area of molecular magnetism and the design of light-weight molecular-based magnets.[110, 111] Antiferromagnetism, ferromagnetism and ferrimagnetism are cooperative phenomena of the magnetic spins within a solid. For instance, some Cu(II) metal-organic networks based on triazole ligands were studied by variable temperature magnetic susceptibility measurements, which showed strong antiferromagnetic exchange.[112] A two dimensional metal-organic complex with formula 2D- $[Cu_2(\mu_5\text{-btb})(\mu\text{-OH})(\mu\text{-}H_2O)]$ was synthesized and showed strong ferromagnetic

coupling.[113] The series of homochiral MOFs 2D-[Ln_2(m-H_2mesox)$_3$(H_2O)$_6$] (mesox= mesoxalic) were obtained and reveals that magnetic coupling being noticeable only at very low temperatures.[114]

Non-linear optical (NLO) materials are used in frequency conversion and intensity modulation of light. When MOFs fulfill both requirements of containing organic ligands with large molecular first hyperpolarizabilities, β, and having ordered, non-centrosymmetric structures, it can be used as NLO materials.[115,116] But there is a general problem exist in NLO materials with MOFs, that is their long-term stability in the laser light. Hence, rare NLO properties of metal-organic materials reported for "their solutions".[117,118]

Drug-storage-delivery perhaps is one of the most potential applications for MOFs. Nowadays, one important challenge is that, most existing carrier materials present low drug loading and/or rapid release of the proportion of the drug that is simply adsorbed (or anchored) at the external surface of the nanocarrier. Thus, some non-toxic iron(III) carboxylate MOFs (MIL-53, MIL-88A, MIL 88Bt, MIL-89, MIL-100 and MIL-101-NH_2 could considered as candidate for nanocarrier of drug-storage-delivery.[119]

Gas-storage-separation is also one of the most highlighted and most visible application oriented works in the field of MOFs, ascribe their porosity and zeolitic behavior. MOFs store H_2 mainly by physisorption, and theoretical estimates suggest an optimal condition with binding energy of about 15 kJ/mol to store H_2 at room temperature and pressures between 1.5–20 bar.[120] Mg-MOF-74 is able to filter and retain only the CO_2 out of a mixture of 20% CO_2 and 80% CH_4, which suggest the magnesium ions interact weakly but selectively with the carbon dioxide.[121] The framework 3D-[Cu(m-SiF_6)(4,4'-bipy)$_2$](4,4' -bipy = 4,4'-bipyridine) has the highest methane adsorption capacity of all zeolites.[122]

4. Mobil Composition of Matter (MCM)

Mobil Composition of Matter (MCM) is a series of mesoporous materials which is associated with the group of Beck et al. in 1992.[123] Mobil Composition of Matter No. 41 (MCM-41) and Mobil Composition of Matter No. 48 (MCM-48) are two of the most popular mesoporous silica materials of this family.[124,125,126] Due to their characteristic regular channel structure, high thermal stability, high specific surface area and pore volume, good biocompatibility and ready

surface functionalization,[127,128] they are considered to have new possibilities in many different fields, such as chemical industry,[129,130] environmental protection[131,132] and medical health,[133,134] etc.

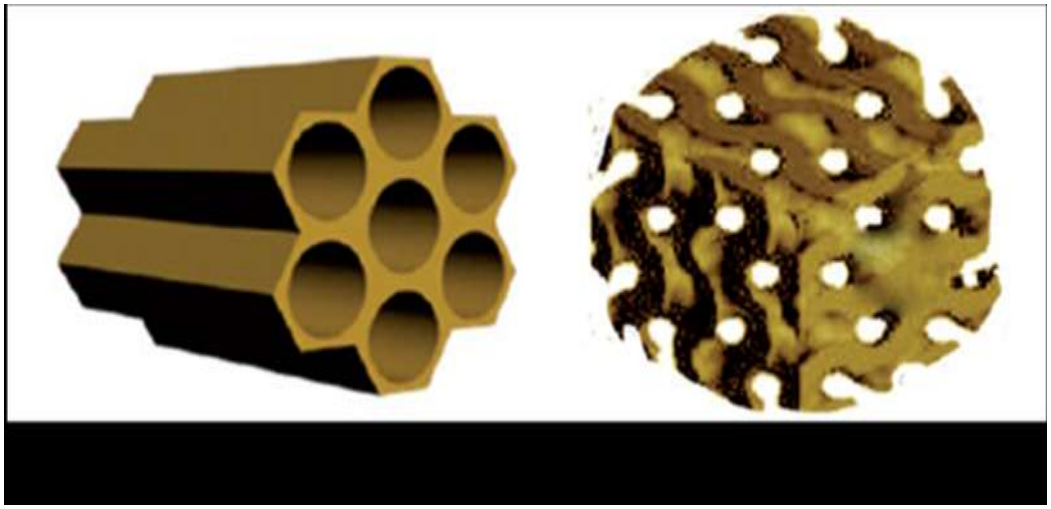

Figure 1.9. Schematic presentation of mesoporous structures of MCM-41 and MCM-48. (Figure taken from [ref .135]. Copyright 2014 Informa Healthcare USA.)

MCM-41 (Figure 1.9, left) presents a regular hexagonal array of cylindrical pores with diameters between 2 and 10 nm, large surface areas (>1000 m^2/g), well-defined mesoporous array and good adsorption properties.[136,137] Due to these properties, MCM-41 is considered to be a suitable materials material that can act as a catalyst or as a catalyst support,[138] and as a host for host–guest nanocomposite materials.[139,140] It has also been used as adsorbent material,[141,142] for electro-chemiluminescence[143] and as electrochemical sensors.[144,145]

MCM-48 (Figure 1.9, right) presents a cubic pore structure with diameters between 2 and 10 nm, large surface areas (>1000 m^2/g) and narrow pore size distribution.[146,147] Due to its large surface area and uniform mesopores, MCM-48 has been applied as catalysts for various chemical reactions,[138] as drug delivery system[148,149] and as adsorbent in waste water treatment.[150]

5. Spin Crossover (SCO) materials

Spin crossover, sometimes referred to as spin transition or spin equilibrium, in molecules refers to a change in the magnetic spin state in response to some external stimulus. The effect was first found by Cambi et al. in the early 1930's,[151,152] but the systematic study of the spin crossover

phenomenon was began in the 1960's with the discovery that $Fe(phen)_2(NCS)_2$ (phen = 1,10-phenanthroline).[153] This phenomenon is commonly observed with some first row transition metal complexes with a d^4-d^7 electron configuration in octahedral ligand geometry. For example, for octahedral iron(II), the diamagnetic low spin (LS) state and the high spin (HS) state with 4 unpaired electrons. The LS state is enthalpically favoured whereas the HS state is entropically favoured. SCO occurs when a perturbation causes a switch in spin state HS←→LS.[154] Hence the spin state is very easily monitored by a magnetometer. There are several characteristic changes which occur on SCO at iron(II) complexes: (a) the Fe–N bond lengths at LS (~1.8–2.0 Å) is about 10% shorter than that in the HS state (~2.0–2.2 Å); (b) the electron density at the nucleus is different between the LS and HS states, which can be observed in the Mössbauer spectra; (c) bond vibrations differ for the two spin states; (d) the LS state is usually strongly coloured (e.g. purple or dark red), whereas the HS state is typically pale; (e) heat is evolved on SCO from the HS to LS state, and taken up when returning to the HS state.[154]

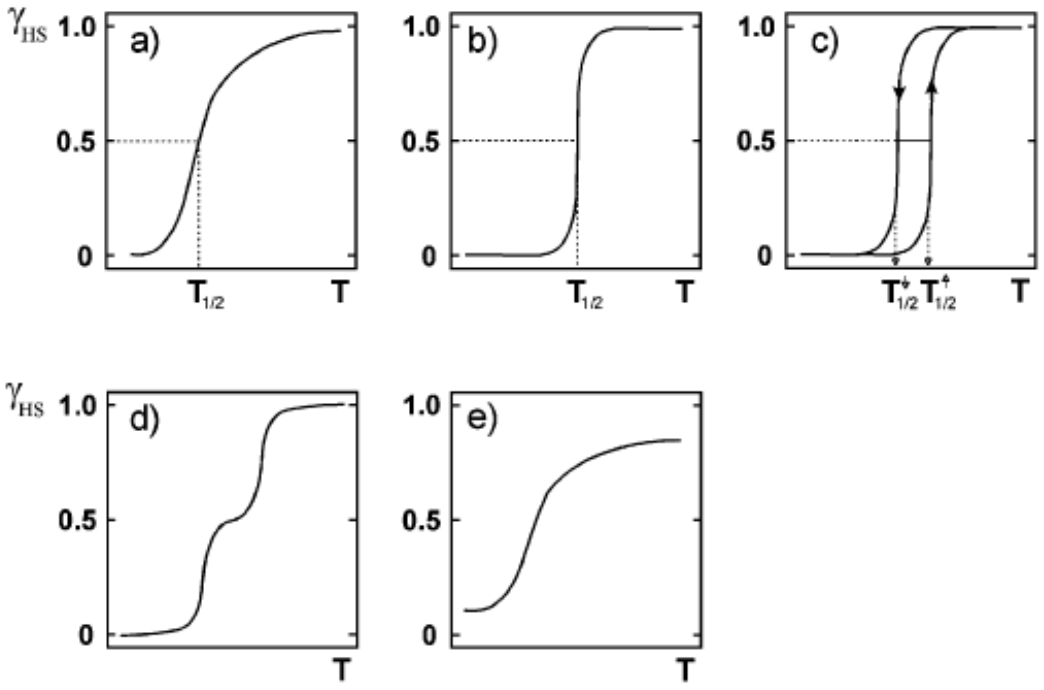

Figure 1.10. Schematic illustrations of themain types of SCO event, where the y axis is fraction HS (g, often shown as x) and the x axis is temperature (T): (a) gradual (b) abrupt (c) abrupt with thermal hysteresis (d) two step and (e) incomplete. (Figure taken with permission from Ref. 154. Copyright 2015 The Royal Society of Chemistry.)

Spin transition curves are a common representation of SCO phenomenon with the most commonly observed types depicted in Figure 1.10. The gradual spin transition (Figure 1.10 a) would be useful for sensing applications,[155,156] the abrupt manner (Figure 1.10 b) would be useful for switching applications.[157,158] When SCO occurs with thermal hysteresis (Figure 1.10 c) it could be useful for memory applications.[159,160] The two-step transition (Figure 1.10 d) is of interest as this moves one from a molecule acting as a binary switch to a ternary (or greater) switch.[161,162] Gradual and incomplete SCO (Figure 1.10 e) is of less interest.

6. Aim of this Thesis

One goal of this thesis is to establish routes to embed spin-cross compounds into metal-organic frameworks or mesostructured silica. Therefore, the choice of host material must take into account the size of the guest molecules. MIL-101(Cr) will be considered as a first MOF candidate MOF. Yet, the available literature synthesis of MIL-101(Cr) gave at the most a yield of 50% (at high temperature of 220 °C in hydrothermal conditions). In order to have an efficient MIL-101 synthesis, a series of additives should be tested for the synthesis of MIL-101(Cr) in order to get high quality products in high yield at lower temperature.

The shape of pores of host materials must also be considered for embedding SCO guests. For example, it is not conceivable to load 1D chain molecules into the pores of MILs. Also, MIL-MOF pores are at the border or micro- and mesopores (2 nm). Such pores are still relatively small when it comes to the inclusion of larger molecules. Hence, in addition to MOFs as hosts, mesoporous MCM-41 with channel-type pores and pore diameters in the range 2.1-2.7 nm will also be investigated as a host towards 1D-SCO chain structures.

In addition the synthesis of new MOFs with adamantyl(tetracarboxylate) and adamantyl(tetraphenylcarboxylate) linkers will be investigated. In the area of MOFs a successful synthesis must include the formation of crystals for single-crystal X-ray studies (or Rietveld refinement from powder X-ray data)

6.1. Outline of this Thesis

The thesis consists out of five chapters, starting with this introduction and the next four chapters present and discuss the results: **Chapter 2** comprises studies of optimization of

MIL-101(Cr) synthesis with various acid additives. **Chapters 3** and **4** involve the studies of embedding three spin-crossover complexes into the pores of a MIL-101 compound and of MCM-41. **Chapter 5** presents the new structures of coordination polymers/MOFs based on carboxyphenyladmantanes ligands.

Chapter 2
Optimization of MIL-101(Cr) synthesis

1. Introduction

Although MIL-101(Cr) with high porosity has already been reported, the development of a high-yield, fluoride-free and large-scale synthesis method of MIL-101(Cr) could help in its commercialization. **Chapter 2** investigates the influence of additive acids to MIL-101(Cr) synthesis, including structure, yields and porosity. MIL-101(Cr) is a three-dimensional chromium−terephthalate-based porous material with the empirical formula $[Cr_3(O)(F,OH)(bdc)_3(H_2O)_2]$ (where bdc = benzene-1,4-dicarboxylate). Its structure resembles the augmented MTN zeolite topology. MIL-101Cr has two types of inner cages with diameters of 29 Å and 34 Å, and pore aperture windows diameter of up to 16 Å (Figure 2.1) with high surface area (BET surface area is over 4000 m^2/g). MIL-101(Cr) has terminal water molecules connected to the octahedral trimeric Cr(III) building units, which can be removed under high vacuum and, thus, create potential Lewis acid sites.[163] MIL-101(Cr) and its ligand-modified derivatives show outstanding stability towards water, which makes it most suitable for applications in the presence of moisture/water.

The smaller cage with only pentagonal windows has a van-der-Waals pore diameter of 2.9 nm, the larger cage with pentagonal and hexagonal windows of 3.4 nm. For further presentations of the pore and window size see Figure 2.2. Building blocks for MIL-101, $[Cr_3(\mu_3\text{-}O)(F,OH)(bdc)_3(H_2O)_2]$, generated from the deposited X-ray data file at the Cambridge Structure Database (CSD-Refcode OCUNAK) using the program DIAMOND.

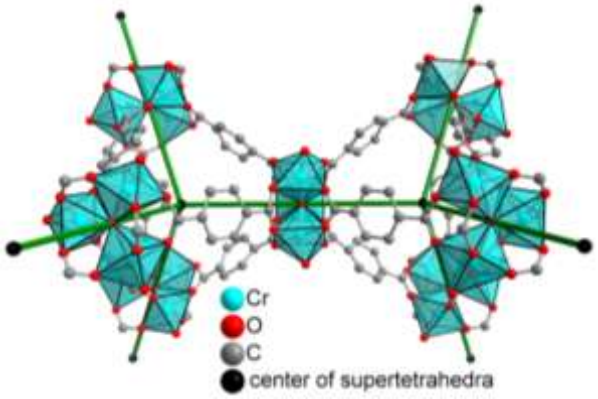

(a)

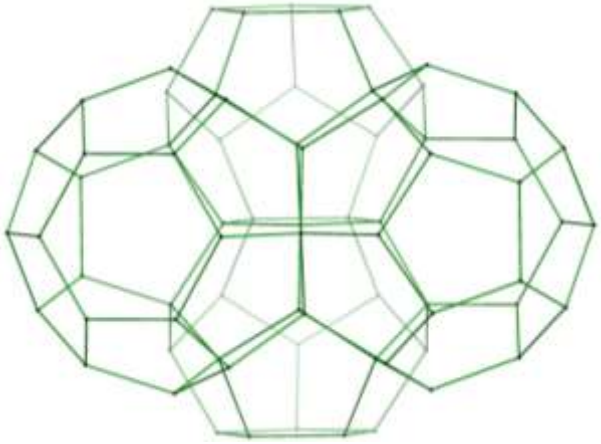

(b)

Figure 2.1. (a) The computational zeolite-type framework presentation of the MIL-101 structure by showing the topological connectivity (in green) of the centers of the vertex-sharing supertetrahedra, (b) with the $[Cr_3(\mu_3\text{-}O)(F,OH)(H_2O)_2(O_2C\text{-})_6]$ secondary building unit at the vertices, from which two types of mesoporous cages with pentagonal and hexagonal windows are formed.[97, 164]

MIL-101(Cr) has evolved into one of the most important prototypical MOFs. Using MIL-101(Cr) or its derivative as catalysts has been introduced in literature for various organic reactions such as oxidation aryl sulfide to corresponding sulfoxide,[165] epoxidation of alkenes[166, 167] in presence of H_2O_2, cyanosilylation of aldehydes,[168] desulfurization of dibenzothiophene.[169] Amine grafted MIL-101(Cr) has been reported to be used as catalyst for Knoevenagel condensation reaction with high yield and high selectivity.[170] Pd loaded on amine grafted MIL-101(Cr) has proven to be useful catalyst for Heck reaction[202] and high activity and strong durability in visible light induced photocatalytic H_2 production.[171] Similarly Cu nanoparticles embedded in MIL-101(Cr) can also work as high performance catalyst for reduction of aromatic nitro compounds.[172] Fe_3O_4 nanoparticles embedded in MIL-101(Cr) can

behave as amagnetic nanocatalyst for the solvent free oxidation of benzyl alcohol in the presence of TBHP.[173] The $CoAl_2O_4$ nanoparticles embedded in MIL-101(Cr) have proved to be efficient catalysts for oxidative catalysis.[174] Recently MIL-101(Cr) and its phospho-tungstic acid (PTA) composite material have been studied as heterogeneous acid catalyst in the reaction of acetalization of aldehydes with alcohols.[175] The functionalized MIL-101(Cr) has been investigated for efficient heterogeneous catalysis in the condensation reaction of aldehydes with alcohols.[209]

MIL-101 (Cr) contained with pyridine has been used for high-performance liquid chromatographic separation of tocopherols.[176] MIL-101 (Cr) was also investigated on the adsorption behavior of 1,2-dichloroethane (DCE), ethyl acetate (EA), and benzene in the presence of water vapor, and the results showed that DCE > EA > benzene.[177]

MIL-101(Cr) contained polysulfone (PSF) mixed-matrix membranes (MMMs) exhibited a remarkable four-fold increase in the permeability of O_2 and CO_2 compared to pure PSF for possible O_2/N_2, CO_2/N_2 or CO_2/CH_4 gas separations. The MMMs for O_2 over N_2 separation with a selectivity of 5–6, and remains constant,[178] for CO_2 over N_2 or CH_4 it increases from about 20 to 25.[179] MIL-101(Cr) loads could up to 24% in PSF, and the MIL-101(Cr) particles showed excellent adhesion with polysulfone in the mixed-matrix membranes and remarkable long term stability.

The post-synthetic modification (PSM) of benzene-1,4-dicarboxylate ligand in MIL-101(Cr) using nitrating acid has been proven can influence, for example, the water uptake behaviour.[180] PSM is a new technique to create suitable functionality into the organic linkers in MOFs.[181,182] Nitro and amino functional groups were introduced in MIL-101(Cr) under extremely strong acidic condition (nitrating acid for nitration and $SnCl_2$/conc. HCl for amination).[178] Moreover, partially functionalized materials (-pNO_2 and -pNH_2) with two different organic ligands in the same framework have been synthesized, which are difficult to obtain through direct synthesis.[183] Mixed-linker MIL-101(Cr) has recently been synthesized with BDC derivatives containing -NH_2, -NO_2, -H, -SO_3H, -Br, -OH, -CH_3, and -COOH.[184]

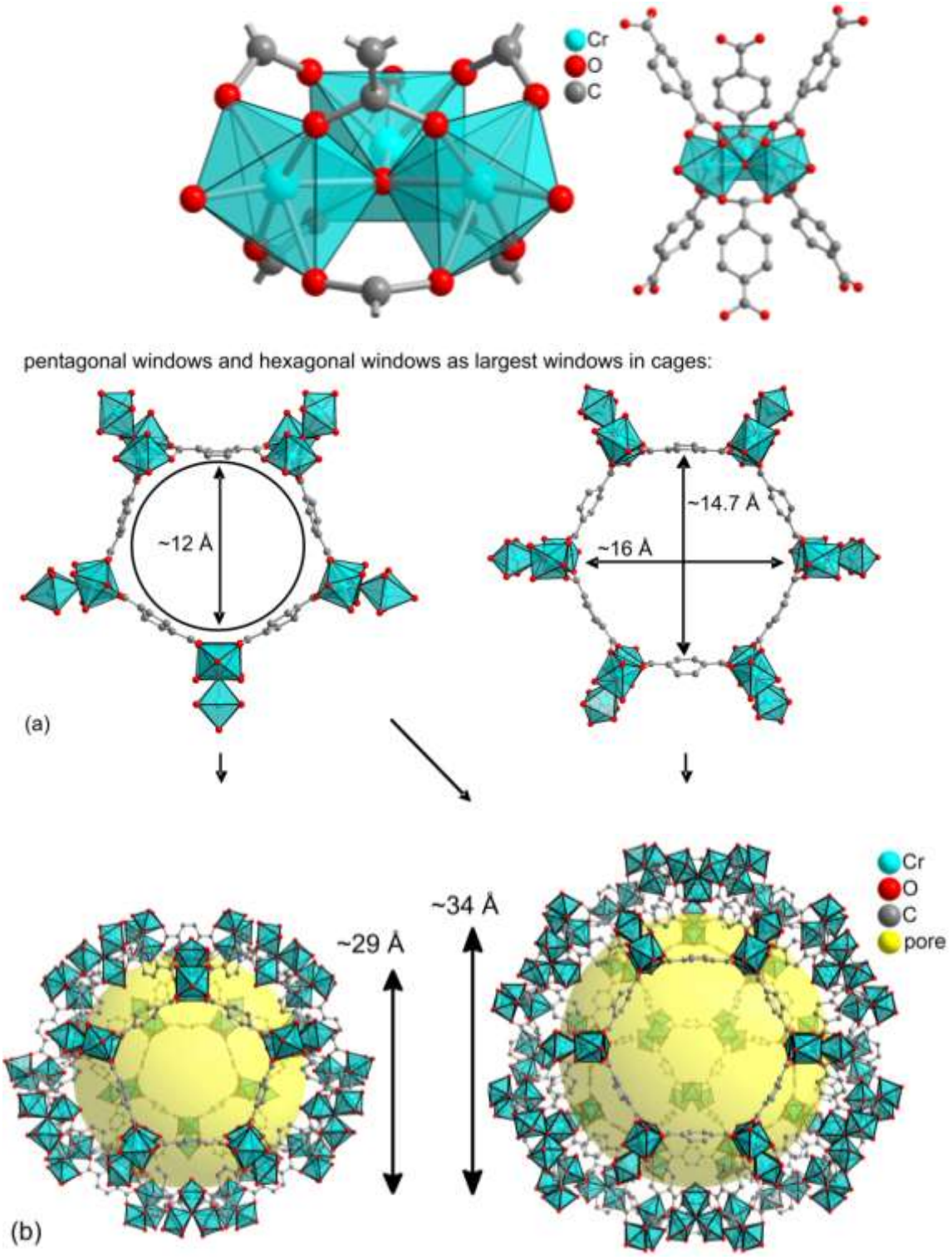

Figure 2.2. Trinuclear$\{Cr_3(\mu_3\text{-}O)(F,OH)(H_2O)_2(O_2C\text{-})_6\}$ building units and bridging benzene-1,4-dicarboxylate ligands form pentagonal and hexagonal rings (a) which are assembled into mesoporous cages. (b) The yellow spheres in the mesoporous cages with diameters of 29 or 34 Å, respectively, take into account the van-der-Waals radii of the framework walls (water-guest molecules are not shown). The different objects in this figure are not drawn to scale.[164,179]

The unique combination of properties highlighted above, as outstanding hydrolytic stability, large surface area and pore sizes, low price of synthetic precursors, presence of functional metal sites and various possibilities for postsynthetic modification makes MIL101(Cr) an excellent candidate for industrial applications.

1.1. Syntheses of MIL-101(Cr)

The initial MIL-101(Cr) synthesis reports a fluorine-free route but also the addition of an equimolar amount of hydrofluoric acid (HF) to chromium and H_2bdc. The obtained products are isostructural.[164] Accordingly, MIL-101(Cr) is given the empirical sum formula $[Cr_3(O)(bdc)_3(F,OH)(H_2O)_2]$ where either F^- or OH^- and two aqua ligands occupy the terminal positions in the three Cr octahedra which form the trinuclear $\{Cr_3(\mu_3\text{-}O)(F,OH)(H_2O)_2(O_2C\text{-})_6\}$ secondary building unit (Figure 2.2). Small scale synthesis involves the use of HF, as a so-called mineralizing agent, which ensure unsurpassed crystallinity and surface area up to 4200 m^2/g.[164] Several small-scale synthesis procedures are reported in the literature (see Table 2.1). Most follow the original synthesis procedure by Férey et al.[164] In this original procedure HF was used and a yield of only "~50%" was stated after filtration of MIL-101 from the free terephthalic acid. A yield of ~50% for MIL-101 is not very satisfying in view of the lengthy synthesis and necessary separation from unused terephthalic acid. Also, the addition of dangerous HF is not helpful for a large-scale synthesis. HF is classified as chemical toxicant, it is a highly corrosive liquid, and also a contact poison. Because of the ability of hydrofluoric acid to penetrate tissue, poisoning can occur readily through exposure of skin or eyes, or when inhaled or swallowed. It should therefore be handled with extreme care, using protective equipment and safety precautions beyond those used with other mineral acids.[185] Beside HF, researchers also try to use other additives in the small scale syntheses of MIL-101 (Cr). For instances, using NaOH instead of HF to get nano-sized (50 nm) MIL-101(Cr) has been reported, and the product possesses relatively good BET surface area (~3200 m^2/g) and fair yield (37%).[200] The particle size of MIL-101(Cr) can be controlled from 19 (4) nm to 84 (12) nm by using a monocarboxylic acid as a mediator, with the BET surface area reaching 2900 m^2/g.[186] The weak alkaline lithium/potassium acetate was employed to assist synthesis of high quality MIL-101(Cr) (BET surface area up to 3400 m^2/g).[187] Hydrofluoric acid and sodium acetate were used as mineralizing agents to obtain

hierarchically mesostructured MIL-101(Cr).[188]

The concomitant drawbacks are the toxicity of hydrofluoric acid especially when it comes to large-scale syntheses, relatively low reported yield at approximately 50%[164] and questionable reproducibility, as there is a large spread of surface area values, with most of them are the interval of 2200-3200 m^2/g (please see Table 2.1). The reported work-up procedures are tedious and could include size-selective / double filtrations for separation of larger crystals of terephthalic acid and prolonged washings, including such environmentally non-benign washing agents as NH_4F.[170] According to the original reference,[170] to obtain the pure crystals, the as-synthesized MIL-101(Cr) was further purified by washing processes using hot water, hot ethanol and hot aqueous NH_4F solutions. Residual terephthalic acid in the as-synthesized MIL-101 (denoted MIL-101A), obtained from the double filtration can be effectively removed by these washing treatments: A first activation treatment was performed using boiling water at 70 °C for 5 h and hot ethanol at 60 °C for 3 h until colored impurities could be detected in the washing solution, resulting in the more purified MIL-101 (denoted MIL-101B). The further purified solid denoted MIL-101C was obtained starting from MIL-101B (200 mg) dispersed in 30 mL of an aqueous solution of 30 mM NH_4F at 60 °C for 10 h. After cooling, the precipitate was filtered and washed five times with 40 mL of hot water (60 °C) to remove traces of NH_4F.[170] The use of fluoride and the necessary washing procedures are mayor obstacles for large-scale manufacturing. Indeed, MIL-101 type compounds are not represented among the Basolite series of MOFs produced by BASF and commercialized by Aldrich, despite recognized importance[189] and the interest towards its production that was announced as early as in 2009.[190]

Stimulated with this background we screened a number of acidic modulators, such as fluorides and H_2O_2,[163,191] in the synthesis of MIL-101 and compared them with fluoride-assisted syntheses under simplified work-up conditions. In this chapter, we report an optimization study which cumulated in development of a high-yielding procedure with proven scalability.

Table 2.1. Synthesis conditions and surface area for MIL-101 (Cr) reported in the literature.[a]

Additive	Time	Temperature	S_{BET} (m^2/g)	V_{pore} (cm^3/g)	Yield (%)[b]	Ref.
HF	8 h	220 °C	~4100(200)	2.02	~50	164

HF	8	220 °C	2231	1.08	not given[b]	192
HF	8	220 °C	2233	1.20	not given[b]	193
HF	8	220 °C	2651	1.29	not given[b]	194
HF	8	220 °C	2846	1.30	not given[b]	195
HF	8	220 °C	2931	1.45	~47	196
HF	8	220 °C	2995	1.31	not given[b]	197
HF	8	220 °C	3007	1.51	~53	198
HF	8	220 °C	3200	2.10	~50	199
NaOH	24 h	210 °C	~3200	1.57	~37	200
--	18 h	218 °C	~3460	not given	~64	201[d]
HF	8 h	220 °C	~3020	1.80	not given[b]	202
HF	8 h	220 °C	~2367	1.46	~57	168
HF	8 h	220 °C	~2693	1.30	not given[b]	203
HF	8 h	220 °C	~2220	1.13	not given[b]	204
HF	8 h	220 °C	~3115	1.58	not given[b]	205
HF	8 h	220 °C	~2059	1.10	not given[b]	206
TMAOH[c]	24 h	180 °C	~3060	1.45	~50	207,208
TMAOH[c]	24 h	180 °C	~3055	1.51	~47	209
HF	8 h	220 °C	~3318	2.02	not given[b]	210
HF	8 h	220 °C	~2800	1.47	not given[b]	183

[a] Follow the original hydrothermal synthesis procedure by Férey et al.164.
[b]The yield is based on Cr, and when no yields were given and the original procedure by Férey et al.[164] was followed a yield of ~50% can be assumed.
[c]TMAOH = tetramethylammonium hydroxide.
[d] However, this is a singular high yield synthesis differing from all other reports.

2. Experimental

2.1. Materials

All reagents were received from commercial sources and used without further purification. Table 2.1 lists the chemicals which are used in chapter 2.

Table 2.2. Chemicals used in this chapter

Reagent	Purity, % / Grade	Commercial Source
Chromium(III) nitrate nonahydrate	98.5%	Alfa Aesar
Terephthalic acid	98%	Sigma-Aldrich
Trifluoroacetic acid	99%	Sigma-Aldrich
Hydrofluoric acid	48 wt. % in H_2O	Sigma-Aldrich
Nitric acid	65 wt. % in H_2O	Fisher Chemical
Sulfuric acid	95.0%-98.0%	Sigma-Aldrich
Hydrochloric acid	36 wt. % in H_2O	Alfa Aesar
Phenylphosphonic acid	98%	Sigma-Aldrich
Acetic acid	99.7+%	Alfa Aesar
Benzoic acid	⩾99.5%	Sigma-Aldrich
Formic acid	97%	Alfa Aesar
Fumaric acid	⩾99.0%	Fluka
Citric acid	⩾99.5%	Sigma-Aldrich
Succinic acid	⩾99.5%	Fluka
N, N-Dimethylformamide	99.9 %	VWR
Ethanol	99.9 %	Merck
Sodium fluoride	⩾99%	Sigma-Aldrich
Ammonium fluoride	⩾98%	Sigma-Aldrich

2.2. Characterization

Powder X-ray diffraction (PXRD) measurements were carried out samples at ambient temperature with a Bruker D2 Phaser using a flat silicon, low background sample holder and Cu-K_α radiation (λ = 1.54184 Å) at 30 kV and 0.04°/s. Diffractograms were obtained on flat layer sample holders where at low angle the beam spot is strongly broadened so that only a fraction of the reflected radiation reaches the detector which leads to the low relative intensities measured at $2\theta < 7°$. Simulated PXRD patterns were calculated from single crystal data with the MERCURY 3.0.1 software suite from CCDC. At the Fraunhofer Institute ISE the PXRD data was recorded on

a Bruker D8 Advance with DaVinci™, using a rotating sample holder, a Cu anode tube at 40kV/40mA, with a Ni filter and constant sample illumination spot size (broadness: 12 mm); step size 0.02°, 0.2 s/step, Cu-Kα radiation.

Nitrogen physisorption isotherms at 77 K were obtained using a NOVA-4000e instrument within a partial pressure range of 10^{-6}~1.0. On the NOVA instrument all samples were activated and vacuum-degassed before nitrogen sorption measurements for 2-4 h at 473 K. The samples were transferred to pre-weighed sample tubes capped with a septum. Then the sample tube was connected to the preparation port of the sorption analyzer and degassed under vacuum for the specified time and temperature. After weighing, the sample tube was then transferred to the analysis port of the sorption analyzer. Helium gas was used for the determination of the cold and warm free space of the sample tubes. DFT calculations for the pore size distribution curves were carried out with the native ASiQWin 1.2 software employing the 'N_2 at 77 K on carbon, slit pore, NLDFT equilibrium' model.[211,212,213] At the Fraunhofer Institute, nitrogen sorption isotherms were measured at 77 K using a QuantachromeAutosorb iQ MP gas sorption analyzer. Ultra high purity (UHP, grade 5.0, 99.999%) nitrogen, and helium gases were used; the latter was used for performing cold and warm free space correction measurements. Samples were degassed for 2 h at 120 °C with the built-in oil-free vacuum system of the instrument (ultimate vacuum $<10^{-8}$ mbar).

Water adsorption isotherms were obtained on a Quantachrome® Hydrosorb, after vac. degassing (120 °C/24 h).

Thermogravimetric (TG) data were collected using a Netzsch Tarsus 209 F3 TGA instrument in a protecting flow of nitrogen (10 mL/min) at 10°C/min heating rate.

Scanning electron microscope (SEM) images and energy dispersive X-ray spectroscopic analysis (EDX) were obtained on a FEI™ QUANTA 400 MK-II (25 kV, ET-detector).

Transmission electron microscope (TEM) images were obtained on a FEI Tecnai G2 f20 with a FEG operated at 200 kV at the Ernst-Ruska center of Forschungszentrum Jülich. TEM samples were prepared as diluted suspensions in water and deposited on carbon coated copper grids.

2.3. Synthesis and Purification

2.3.1. Small-scale MIL-101(Cr) synthesis with additives

By trying to replace HF as an acid additive we tested varies inorganic and organic acids under

otherwise identical conditions. The amount of most acid additives used in MIL-101(Cr) synthesis is 1 mmol equivalent to the molar amount of $Cr(NO_3)_3$.

The general synthesis involves a solution containing chromium(III) nitrate ($Cr(NO_3)_3 \cdot 9H_2O$, 400 mg, 1.0 mmol), the chosen additive acid (1.0 mmol) and benzene-1,4-dicarboxylic acid (H_2bdc, 166 mg, 1.0 mmol) in 5 mL H_2O with stirring for 10 min. Then the mixture is transferred to the Teflon line in a hydrothermal autoclave which is heated for 8 h at 220°C and cooled afterwards slowly to room temperature at a rate of 30 °C /h in 6 h.

2.3.2. Purification of small-scale synthesized MIL-101(Cr)

The contents of autoclave were transferred to two centrifugal tubes and the supernatant solution was carefully removed after centrifugation (4200 U/min for 50 min). Then water (5 mL) was added in each tube and the solid was evenly dispersed in the aqueous phase. After renewed centrifugation and removal of the supernatant solution, DMF (5 mL) was added to each tube which was placed in a hot (80 °C) ultrasonic bath and sonicated for 1 h. Centrifugation was again used to separate MIL-101 and DMF. The precipitate was transferred in a 25 mL beaker where it was stirred with 10 mL of water at 70 °C for 5 h. After separation by centrifugation, the same washing procedure but using ethanol was repeated once more at 70 °C for 5 h. The final product was obtained by centrifugation and dried in a vacuum oven (100 °C, 12 mbar) for 2 h. Yields are listed in Table 2.3-2.6. Analyses of the products were carried out by elemental analysis, powder X-ray diffraction and N_2 sorption, see below.

2.3.3. Large-scale MIL-101(Cr) synthesis and purification (general procedure)

Chromium(III) nitrate nonahydrate (192 g, 0.48 mol) and terephthalic acid (81.3 g, 0.49 mol) were stirred in water (2.4 L) and transferred into a 3 L autoclave. The suspension was heated to 200 °C and left unstirred for 15 h. The mixture was cooled to 20 °C within 24 h. After cooling the suspension was filled into centrifuge vessels. The solid was isolated by centrifugation (4700 U/min for 30 min). The supernatant liquid phase was discarded and the resulting solid was stirred in DMF (4.5 L) for one hour. The suspension was then again centrifuged (4700 U/min for min). The supernatant liquid phase was discarded and the solid stirred in DMF (4.5 L, 16 h). The solid was isolated by centrifugation and the washing step was repeated with ethanol (4.5 L, 1 h and 4.5

L, 16 h of stirring). After the final isolation the resulting wet solid was dried for 2 d in air at room temperature. The dried solid was crushed to a homogenous powder and dried for another 2 d in air at room temperature to produce MIL-101(Cr) as a green powder. Yield 90.2 g (48% with respect to chromium). Analyses of the product were carried out by elemental analysis, powder X-ray diffraction and N_2 sorption, see below.

3. Results and Discussion

During the synthesis experiments with different acid modifiers, two acid additives became noteworthy, nitric acid and acetic acid. Thereby we found that HNO_3 led to a reproducible increase in yield to over 80% with BET surface areas around and over 3200 m^2/g. While the using of acetic acid in MIL-101(Cr) synthesis could significantly decrease the synthesis temperature. Initially a significant amount of terephthalic acid is still present inside the pores and admixed with the MIL crystallites. The residual reactants and eventually the solvent needs to be removed by washing and drying procedures especially from the pores in order to obtain a material with as high porosity as possible (termed activation). All the products of the different synthesis experiments were subjected to the same purification method.

3.1. High-yield, fluoride-free synthesis of MIL-101(Cr) with HNO_3 (small scale)

According to literature, a typical synthesis of MIL-101Cr lasted 8 h at ~220 °C (Table 2.1). Additives are commonly used in the synthesis; especially HF can act as a mineralizing agent to increase the crystallinity of microporous materials and favors the formation of highly crystalline phases in MOFs.[214]

We tried to replace the mineralizer HF by other mineral and also by organic acids. When the addition of HNO_3 showed promising results HNO_3-variable experiments were conducted to reveal the optimal synthetic conditions. The reaction was carried out with addition of 0.25, 0.5, 0.75, 1.0, 1.25 and 1.5 equivalents of nitric acid with respect to chromium nitrate. Products were named as N-0.25, N-0.5, N-0.75, N-1.0, N-1.25 and N-1.5 respectively. The sample without any additives was named N-0. All these experiments were carried out with 1.0 mmol each of chromium(III) nitrate nonahydrate and terephthalic acid in the Teflon liner in an autoclave at 220 °C for 8 hours (see Exp. section). After hydrothermal reaction, the treatment and purification

of products were followed as described in the Exp. section. The analytical results showed that, a considerable improvement of yield and quality could be obtained compared to experiments without addition of nitric acid (Table 2.3).

Nitrogen sorption isotherms of HNO_3-variable MIL-101(Cr) are shown in Figure 2.3, which are typical type I sorption isotherms[215] as reported in the literature for MIL-101(Cr).[164] Obviously, N-1 (red curve) possesses the highest Brunauer Emmett Teller (BET) surface area (3450 m^2/g). N-0.25 (blue curve), N-0.75 (yellow curve), N-1.25 (cyan curve) and N-0.5 (magnenta curve) present lower porosity compared to N-1. While N-0 and N-1.5 (black and green curve) have the lowest BET surface areas with 2410 and 2540 m^2/g, respectively. Figure 2.3 also showed the curve of HNO_3 equivalents versus the corresponded S_{BET} value. It is obvious that the addition of 1.0 equivalent of nitric acid in synthesis produced the best porosity of MIL-101(Cr). In addition, N-1.0 gave an excellent high yield up around 80% after product purification (Table 2.3). Additionally, N-0.25, N-0.5, N-0.75, N-1.25 and N-1.5 also showed a significant increase in yields compared to the original literature yield.[164]

To confirm that the experiment N-1.0 can be reproduced, two repeat experiments had been done. The results are included in Table 2.3. Overall, the synthesis with 1 eq. of HNO_3 is reproducible with yields above 80% and BET surface areas above 3100 m^2/g. The Nitrogen sorption isotherms of each repeated experiment can be found in Figure 2.4. Yields and surface areas are near the high end of syntheses reported in the literature (Table 2.1).

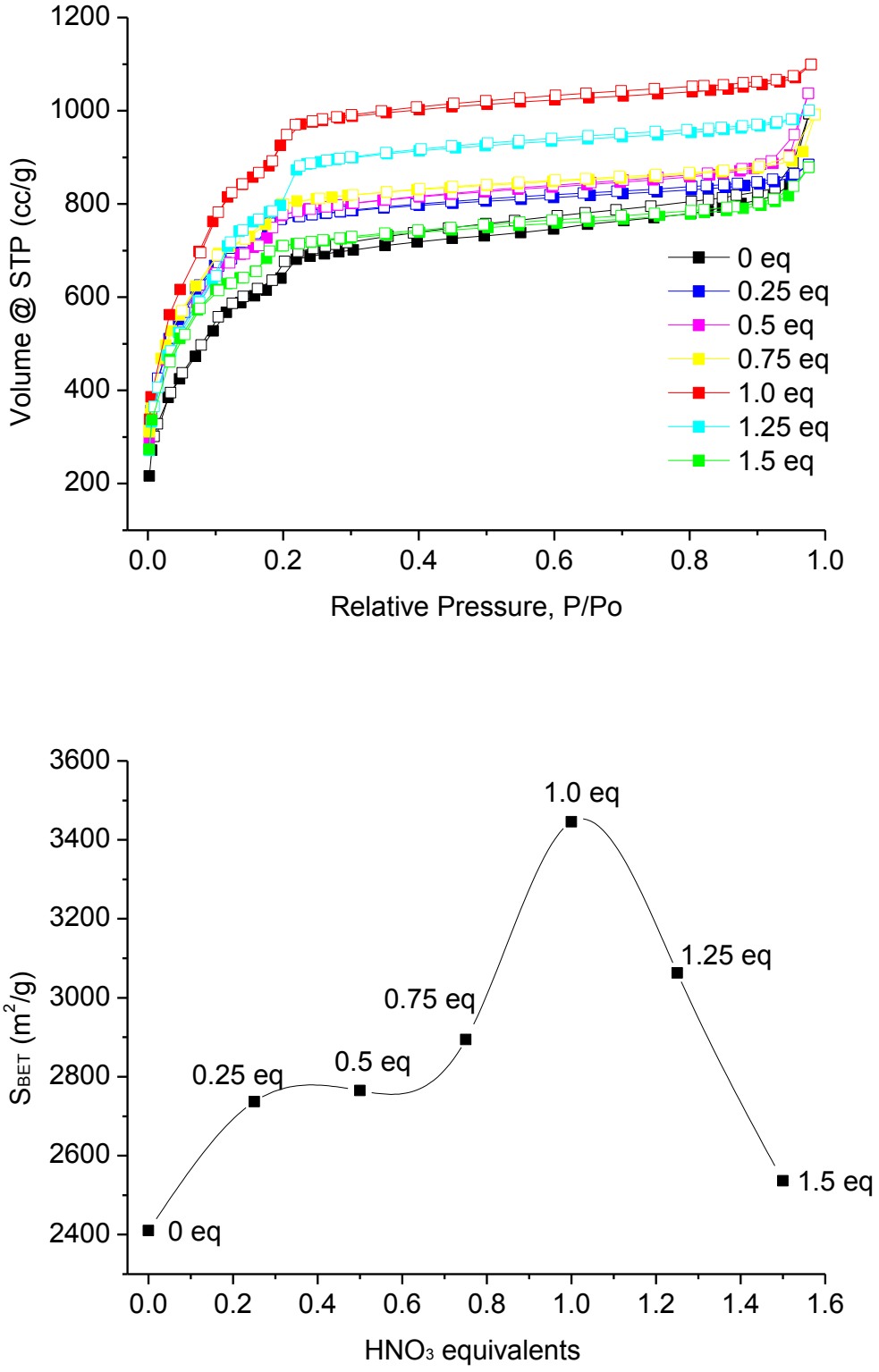

Figure 2.3 N_2 adsorption−desorption isotherms of HNO_3-variable MIL-101(Cr); filled symbols are for adsorption, empty symbols for desorption (top). Plot of S_{BET} values versus HNO_3 equivalents (bottom).

Furthermore, large equivalents of nitric acid (2.0 eq. and 5.0 eq.) were also tested in MIL-101(Cr) synthesis. However, it is found that, under too high nitric acid concentration condition, there is no positive effect anymore for MIL-101(Cr) synthesis. In the 2.0 eq. experiment, S_{BET} had decreased to 1990 m²/g, while 5.0 eq. gave a grey powder product without porosity. Thus, in a small-scale MIL-101(Cr) synthesis (5 mL scale), using 1.0 eq. HNO_3 is the optimum quantity.

Table 2.3. Yield, surface area and pore volume for MIL-101(Cr) with various equivalents of HNO_3 as addition.

Experiment	Yield (%)[a]	S_{BET} (m²/g)[b]	$S_{Langmuir}$ (m²/g)	V_{pore} (cm^3/g)[c]
N-0	56.6	2410	3270	1.30
N-0.25	67.5	2740	3600	1.33
N-0.5	71.7	2765	3690	1.40
N-0.75	73.6	2894	3914	1.38
N-1.0a	82.3	3450	4610	1.66
N-1.0b [d]	81.6	3132	4325	1.58
N-1.0c [d]	80.8	3415	4635	1.69
N-1.25	69.9	3063	4220	1.52
N-1.5	66.2	2540	3320	1.26

[a] The Cr:bdc ratio is always 1:1, and the yield is based on Cr.
[b] Calculated in the pressure range $0.05 < p/p_0 < 0.2$ from N_2 sorption isotherm at 77 K with an estimated standard deviation of ± 50 m^2/g.
[c] Calculated from N_2 sorption isotherm at 77 K ($p/p_0 = 0.95$) for pores ≤ 20 nm.
[d] Repeated experiments to show reproducibility.

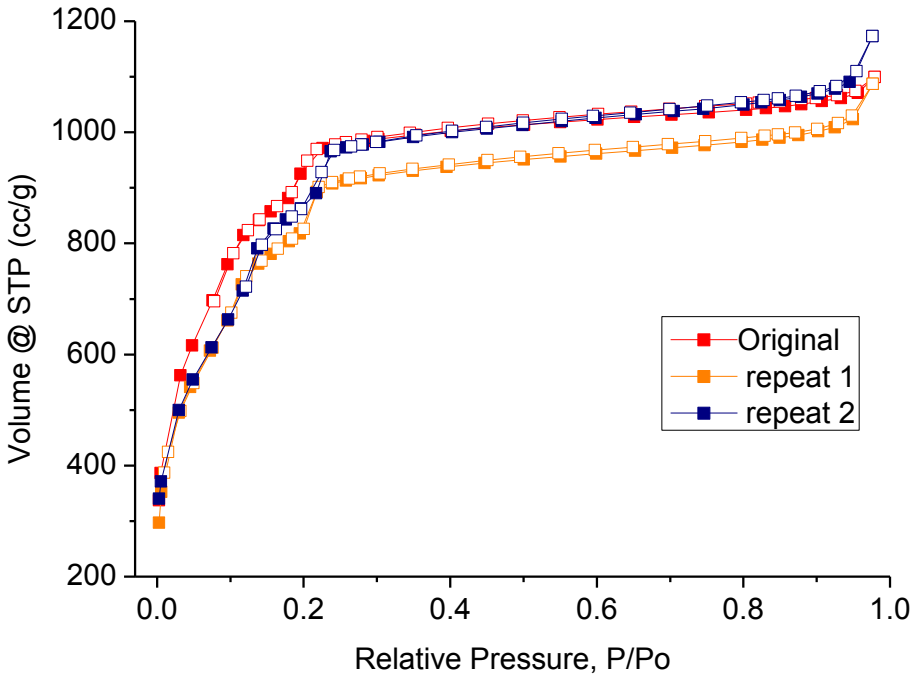

Figure 2.4. N_2 sorption isotherms of repeated MIL-101 synthesis experiments with 1 eq. HNO_3; filled symbols are for adsorption, empty symbols for desorption.

The powder X-ray diffractograms of N-1.0 samples can be positively matched to the simulated XRD pattern which was generated from the deposited X-ray data file at the Cambridge Structure Database (CSD-Refcode OCUNAK) using the program MERCURY (Figure 2.5A). Powder X-ray diffratograms of the samples with other HNO_3 equivalents are shown in Figure 2.5D.

A thermal gravimetric analysis study on N-1.0 (the sample has been stored for several days in ambient air and was investigated without further preconditioning before TG analysis) shows that there are two weight-loss steps: the first step, corresponding to 38%, occurs from 25 °C to 350 °C and relates to the loss of water molecules (adsorbed from air); the second step, corresponding to 40%, is due to the decomposition of the organic moieties and framework between 350 °C and 550 °C. It has to be noticed that the water content of MIL-101 varies considerably, from 20% to 60%, depending on the presence of coordinated solvent, the laboratory temperature, or environment humidity.[164,]

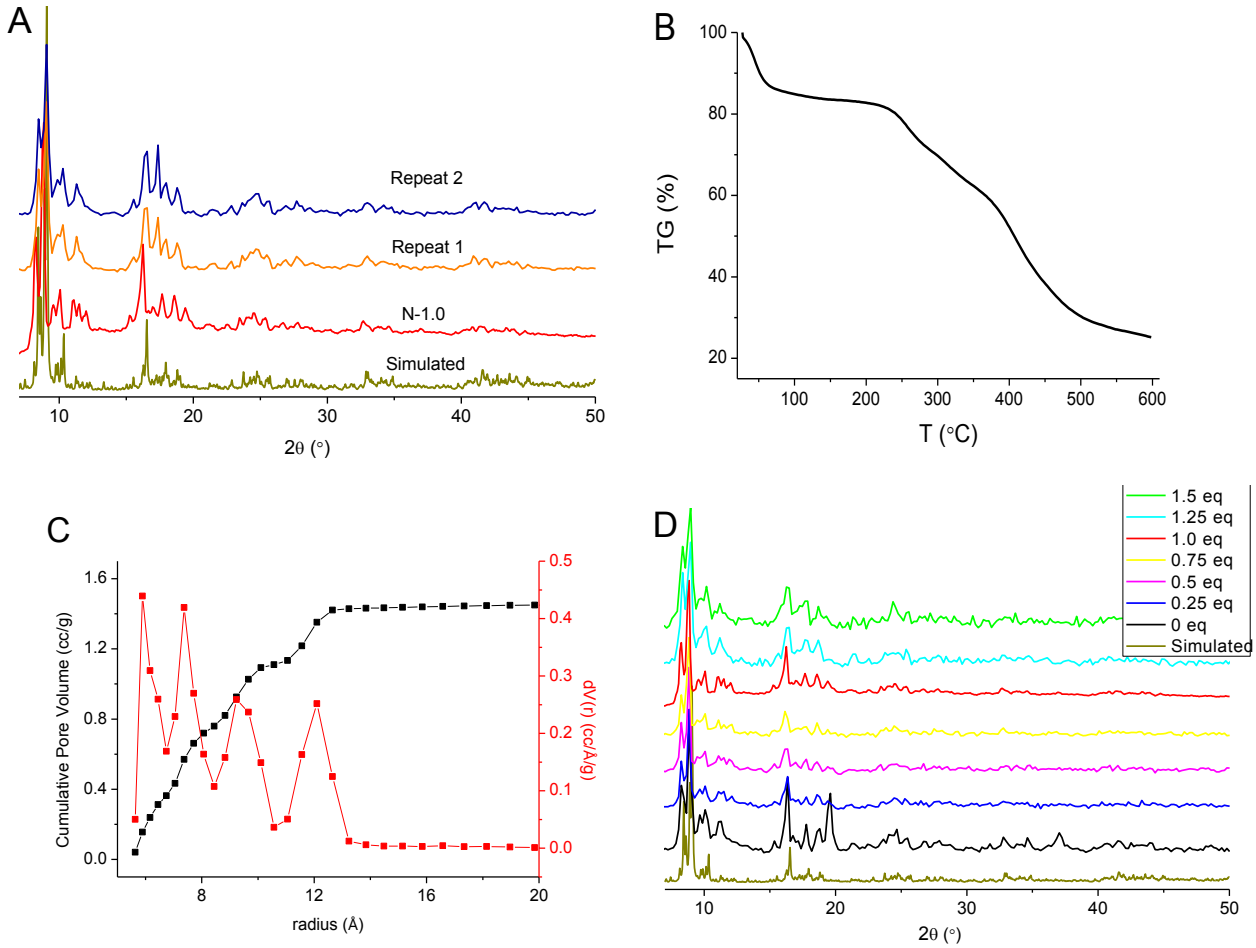

Figure 2.5. Powder X-ray diffractograms (A), TGA curve (B), pore size distribution curve and cumulative volume curve of N-1.0 calculated with 'N_2 at 77 K on carbon, slit pore, NLDFT equilibrium' model (C). PXRD patterns of the samples with other HNO_3 equivalents (D).

The pore size distribution curve and cumulative volume curve for N-1.0 were analyzed by NL-DFT method (Figure 2.5C) and are similar to the reported pore size distribution in MIL-101(Cr).[216,217,218]

3.2. Upscaling of the Synthesis of MIL-101(Cr)

The upscaling work of MIL-101(Cr) synthesis is a collaboration work with Fraunhofer Institute and the company ChemCon in Freiburg. This work was performed by Dr. Felix Jeremias (ISE) and Dr. Binh. Nguyen (ChemCon).

The goal in this work was to transfer the synthesis of MIL-101(Cr) to larger scale of about 100 g product from a single batch. Therefore, the scale-up to a reaction volume of 3 L (the 3 L

autoclave please see Figure 2.6) was successively achieved. According to the resulting analytical data the procedure for the synthesis of MIL-101(Cr) was adapted and optimized as follows to produce the material in good quality and quantity.

Figure 2.6. The picture of 3 L of autoclave used in large-scale MIL-101(Cr) syntheses.

In the literature the MIL-101 synthesis at smaller scales was conducted without stirring.[219,220,221,222] Since the reaction volume was substantially increased, it was interesting to see, whether stirring would be needed in larger scale reactions to maintain homogeneity for the formation of the desired product. The results of the experiments indicate that stirring of the reaction mixture seems not to be necessary to form MIL-101(Cr) in good quality. In fact, stirring leads to a material that showed a lower BET surface area (Figure 2.7).

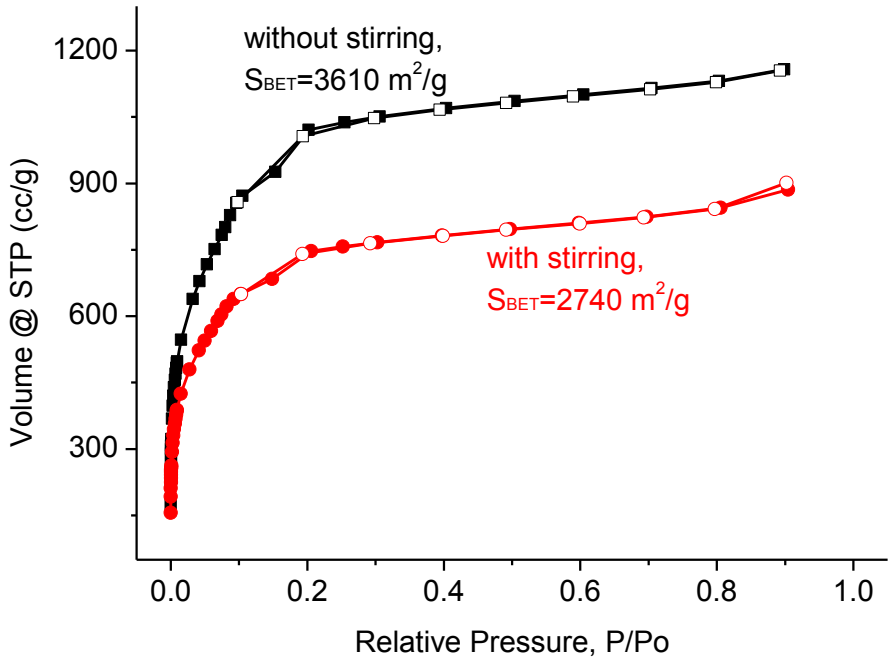

Figure 2.7. Nitrogen sorption isotherms and their corresponding BET surface area for stirring-experiments of large-scale preparations of MIL-101(Cr), filled symbols are for adsorption, empty symbols for desorption. The synthesis and treatment of the experiments both followed the general procedure. The BET surface areas were calculated in the pressure range $0.05 < p/p_0 < 0.2$ from N_2 sorption isotherms at 77 K with an estimated standard deviation of ± 50 m^2/g.

Also, the influence of the reaction temperature on the resulting material was studied. Experiments at smaller scales are usually conducted at 220 °C (Table 2.1). A series of runs were carried out that covered a temperature range from 180–220 °C. The results suggested that a lower reaction temperature also forms the desired product in good quality. Unexpected was the observation, that a reaction temperature of 220 °C at a larger scale seemed to produce an unknown phase instead of the intended MIL-101(Cr) product (Figure 2.8). This result also indicated that in the case of large scale synthesis, the optimized condition can be different from small scale synthesis.

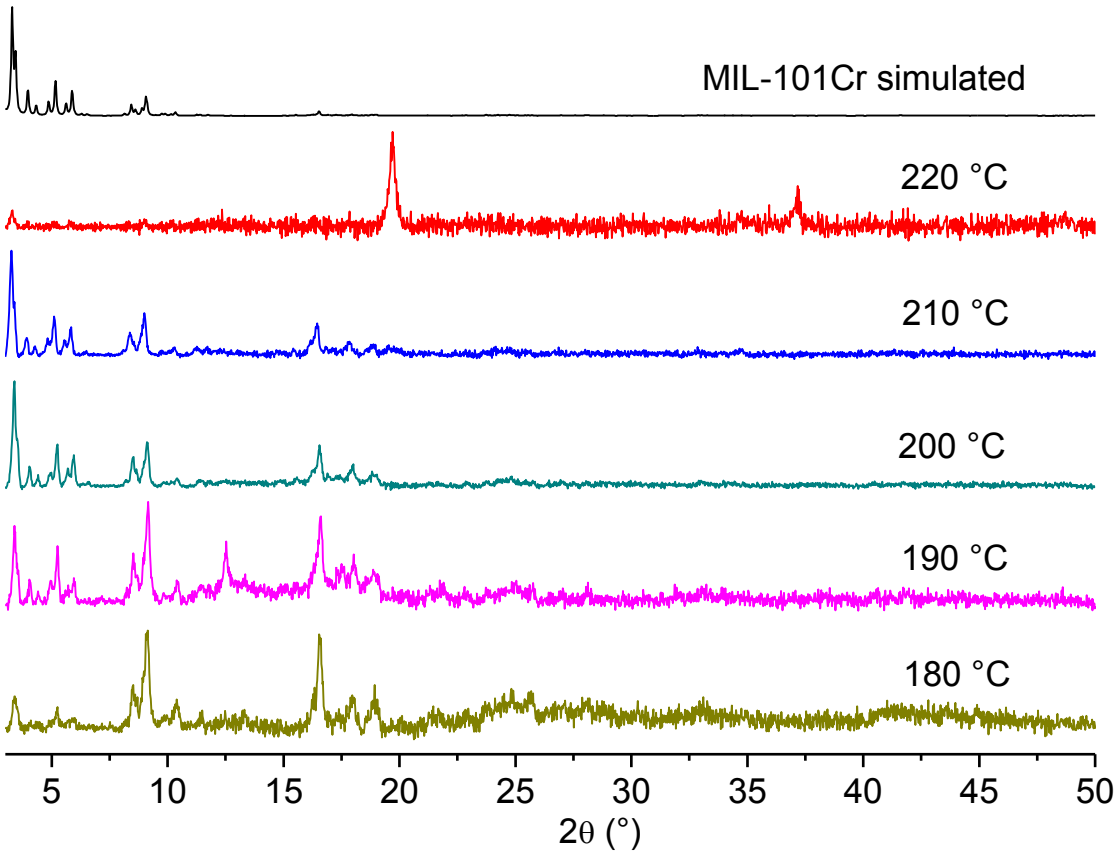

Figure 2.8. PXRD of large-scale preparations of MIL-101Cr at different temperatures. (PXRD data were recorded on a Bruker D8 Advance with DaVinci™)

In addition the reaction time (6-16 h) and cooling time (4-24 h) were extended to study their impacts on the resulting material and yield in the large-scale synthesis. The results indicated no significant effect of reaction and cooling time on quality and quantity of the resulting material. A possible explanation is that crystallization takes place very quickly. Once the material crystallizes, there is only a minor equilibrium process of dissolution and recrystallization.

Also an optimized washing procedure was established for the large-scale synthesis. In the initial procedure the raw product was suspended in DMF by using half the volume of the reaction volume that is 1.5 L, stirred for 15 min. and isolated by centrifugation. This procedure was repeated with ethanol and water. Using this procedure we obtained a material with considerable amounts of impurities remaining in the pores of the product. Hence, we decided to prolong the washing step and to employ solvent volumes 1.5 times of the reaction volume (i.e. 4.5 L) to

ensure the removal of impurities from the pores. The product obtained after washing according to the new procedure (for details see Exp. section) gave materials with higher purity. Consequently, an increase of nitrogen sorption was observed for all materials after using the new washing procedure. The method proved to be very efficient to remove starting material or impurities that remained in the pores of the product (see Figure 2.9). For a large-scale product the BET surface of 3870 m^2/g can be considered remarkable.

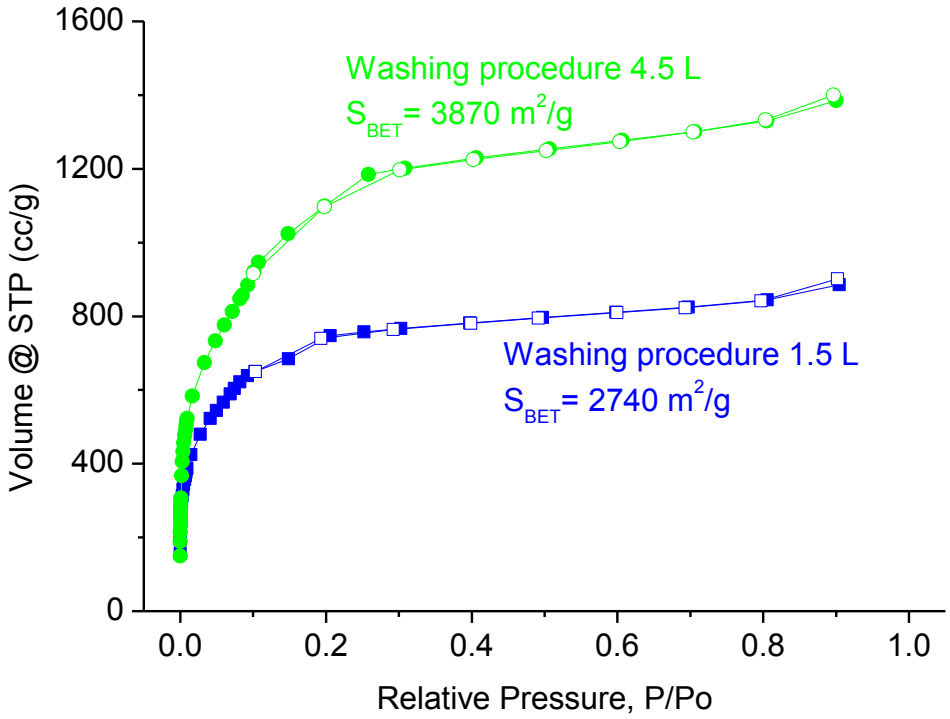

.

Figure 2.9. N_2 sorption isotherms and BET surface area of materals from large scale synthesis and different washing procedures. The given procedure refers to washing with 1.5 L (4.5 L) DMF – separation – 1.5 L (4.5 L) water – separation – 1.5 L (4.5 L) ethanol; see Exp. section for details of the 4.5 L procedure.

Finally, the addition of 0.5, 1.0 and 1.5 HNO_3 equivalents with respect to chromium nitrate was investigated (Figure 2.10). The experiments confirmed the results of the small scale reactions, in which the yield was considerably improved by the addition of nitric acid. The large scale preparations also gave about 20% more material for all conducted experiments with addition of nitric acid (0.5, 1.0 and 1.5 eq) compared to experiments without addition of nitric acid. We

assume that the addition of nitric acid affects the particle growth, yielding material with larger particle size, thus, leading to material that is more efficiently isolated by centrifugation. (Yield around 48% for experiments without addition of nitric acid. Addition of nitric acid yielded around 66% (for 0.5 eq), 68% (for 1.0 eq) and 67% (for 1.5 eq).

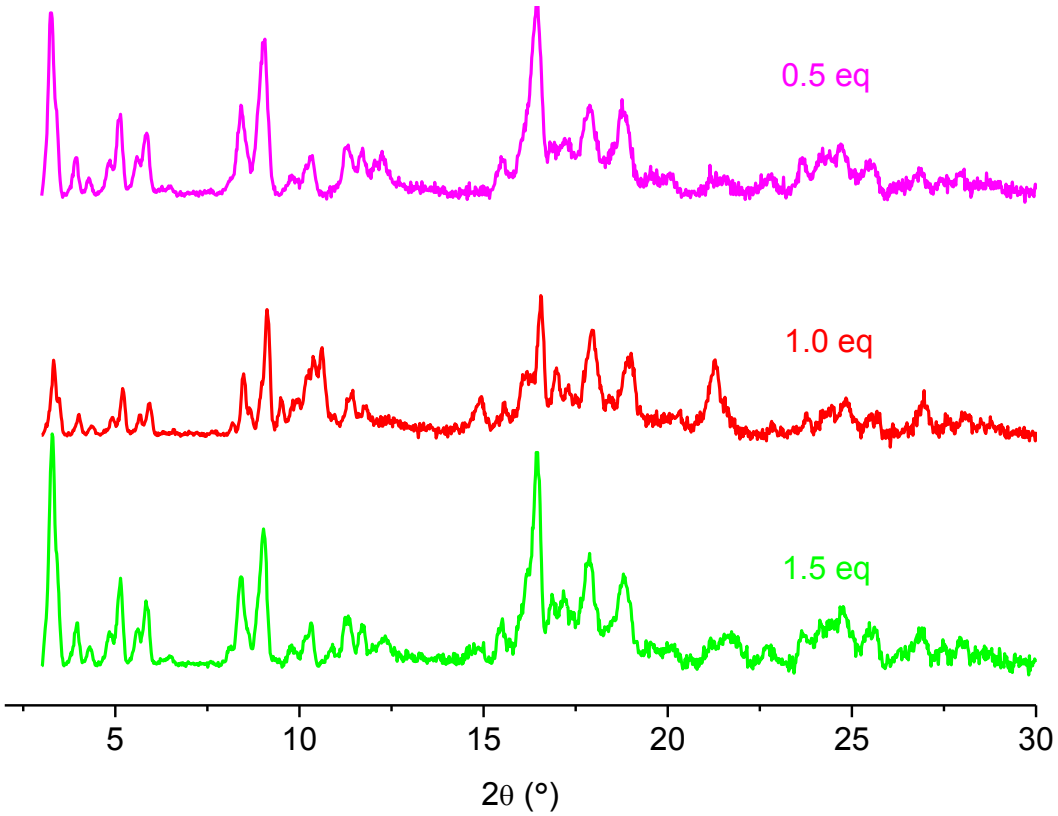

Figure 2.10. PXRD of large-scale preparations of MIL-101(Cr) with different equivalents HNO_3. (PXRD data were recorded on a Bruker D8 Advance with DaVinci™)

3.3. Low temperature synthesis of MIL-101(Cr) with acetic acid

Normally, MIL-101(Cr) syntheses are carried out at 220 °C in a Teflon liner within autoclaves. Using microwave irradiation as heating source one can decrease the reaction temperature to 210 °C.[223] But until now we are not aware of a report to obtain MIL-101(Cr) at a temperature below 180 °C. As previous mentioned the additions of several acids were tested in MIL-101(Cr) synthesis. Among them, acetic acid shows a special effect that it can largely decrease the reaction temperature without significant influence to the material's porosity. A lower synthesis temperature can be desired when, MIL-101(Cr) is intended as a host for guest molecules.[192,193,194,195] In cases, where the S_{BET} of MIL-101(Cr) is only 2000 m²/g, there is still

quite enough space for the storage of guest molecules.[224] In this case, porosity of the MIL-101 material is not the only consideration, but a lower synthesis temperature may allow for the inclusion of temperature-sensitive molecules during the in-situ formation of MIL-101(Cr). For example, one could directly synthesize MIL-101(Cr) in the presence of guest molecules at relatively lower temperature. Here, with the addition of acetic acid, the MIL-101(Cr) synthesis reaction temperature can be decreased to at lowest 160 °C. In some experiments, the addition of several milligram of prepared MIL-101(Cr) powder was necessary as crystal seeds.

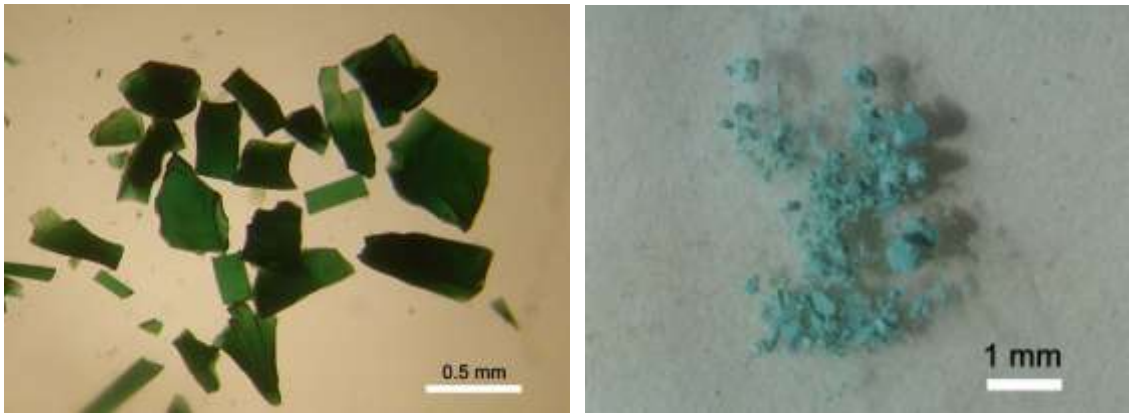

Figure 2.11. The image of MIL-101(Cr) with acetic acid (8.3 equivalents, 220 °C) (left) and HNO_3 (N-1.0) (right) as modifier A-8.3-220ws (left) under optical microscope and picture of N-1.0 (right).

When 1 equivalent of acetic acid with respect to chromium nitrate was added in the MIL-101(Cr) synthesis at 220 °C, the product is of competitive purity, yield and BET surface relative to other MIL-101 product. If the quantity of acetic acid is increased up to 8.3 equivalents with respect to chromium, green glassy-looking material was formed (Figure 2.11, left). When the equivalent of addition of acetic acid with respect to chromium is lower than 8.3, the product is a green powder (similar to Figure 2.11, right). With the addition of more than 8.3 eqivalents of acetic acid with respect to chromium the synthesis reaction would fail. Both, the 1 eq and 8.3 eq acetic acid product of MIL-101 can be positively matched to the simulated pattern of MIL-101(Cr) (Figure 2.12). The yield and porosity information of acetic-variable MIL-101(Cr) are listed in Table 2.4 and their PXRD patterns are shown in Figure 2.12.

Table 2.4. Yield, surface area and pore volume for MIL-101(Cr) with various equivalents of acetic acid as addition.

Experiment	Yield (%)[a]	S_{BET} (m^2/g)[b]	$S_{Langmuir}$ (m^2/g)	V_{pore} (cm^3/g)[c]
1 eq	65.3	2680	3490	1.17
2 eq	52.1	2450	3210	1.28
5 eq	36.4	2660	3480	1.27
8.3 eq	24.4	2750	3620	1.55
10 eq	none	--	--	--

[a] The Cr:bdc ratio is always 1:1, and the yield is based on Cr.
[b] Calculated in the pressure range $0.05 < p/p_0 < 0.2$ from N_2 sorption isotherm at 77 K with an estimated standard deviation of ± 50 m^2/g.
[c] Calculated from N_2 sorption isotherm at 77 K ($p/p_0 = 0.95$) for pores ≤ 20 nm.

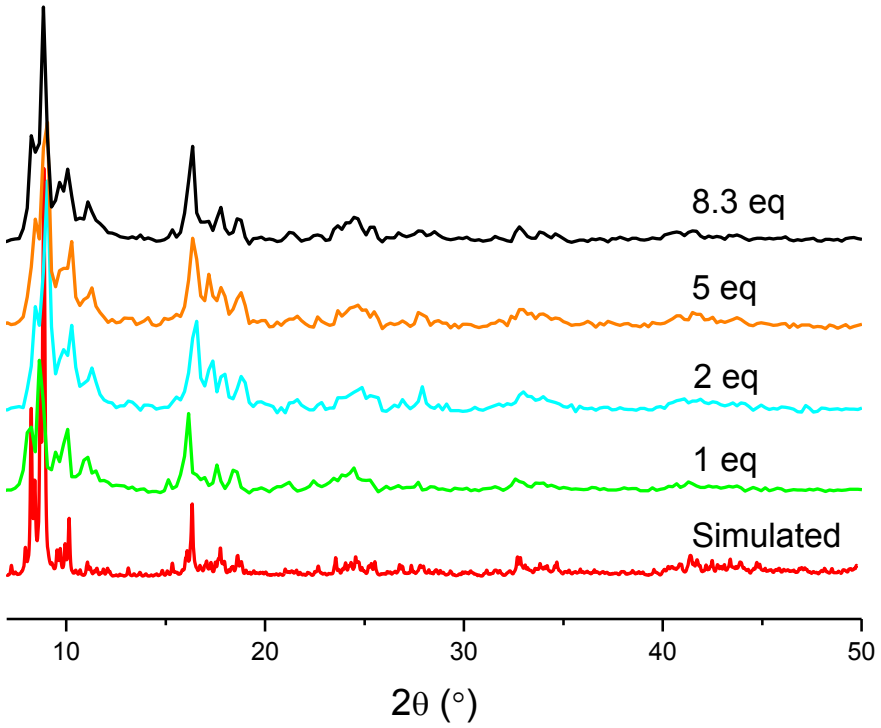

Figure 2.12. The PXRD patterns of 8.3 eq. and 1 eq. acetic-sample compared with simulated pattern.

At the beginning, we thought 8.3 eq. acetic-sample was large single crystal fragment of

MIL-101(Cr), but in the consequent polarized light examination, there were no proofs of existence for large single crystal fragments for 8.3 eq. acetic-sample. And the single-crystal XRD experiment also proved that, these green fragments were not large single crystal. In washing procedure, the product is very hard to separate via centrifugation. We assume that the high concentration (8.3 eq.) of acetic acid affects the particle growth, it dissolved part edge of particles and yielding material with smaller particle size, thus, leading to material that is more difficult isolated by centrifugation. After drying, acetic acid evaporate, these smaller particles stick together and formed this kind of glass-look materials. MIL-101 formed with 1 eq and 8.3 eq acetic acid had BET surface areas of 2680 m²/g and 2750 m²/g respectively. Considering literature reports of MIL-101 with a range of 2000-3000 m²/g (Table 2.1), this value is quite acceptable.

The synthesis of MIL-101Cr with, 8.3 eq of acetic acid was also carried out at temperatures of 220, 200, 180 and 160 °C (Table 2.5). Upon lowering the temperature, the yield decreased considerably. We found, however, that the addition of about 5 milligrams of prepared MIL-101(Cr) powder as seed in the synthesis would significantly raise the yield again (Table 2.5). The PXRD patterns of the "seeded" samples are in very good agreement with the simulated pattern of MIL-101(Cr) (Figure 2.13). The BET results of these "seeded" samples are also better than those of the "non-seeded" samples (Table 2.5).

Noteworthy, the BET and porosity results did not show a clear dependence on temperature. Even at a low yield of a non-seeded sample at 180 °C the BET surface area was determined to 3240 m^2/g (Table 2.5).

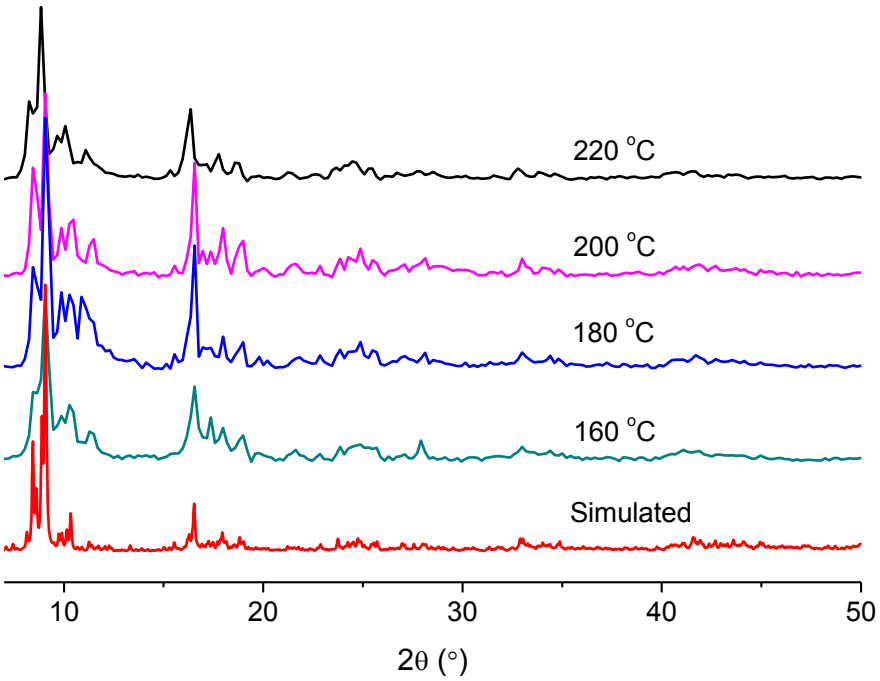

Figure 2.13. Powder X-ray diffractogram of "seeded" samples which with 8.3 eq of acetic acid compared with simulated pattern.

Table 2.5. Yields, surface area and pore volume for acetic-MIL-101(Cr)

Sample Name	Seeds	Temp. (°C)	Yield (%)[a]	S_{BET} (m^2/g)[b]	$S_{Langmuir}$ (m^2/g)	V_{pore} (cm^3/g)[c]
A-8.3-220	Yes	220	48.9	2810	3680	1.85
A-8.3-200	Yes	200	44.5	2790	3600	1.30
A-8.3-180	Yes	180	43.2	2750	3630	1.30
A-8.3-160	Yes	160	33.5	2700	3500	1.38
A-8.3-220ws	No	220	24.4	2750	3620	1.55
A-8.3-200ws	No	200	24.4	2360	3060	1.31
A-8.3-180ws	No	180	13.2	3240	4400	1.61
A-8.3-160ws	No	160	none	—	—	—

[a]The molar Cr:bdc ratio is always 1:1 with 1.0 mmol (400 mg) $Cr(NO_3)_3 \cdot 9H_2O$ and 1.0 mmol (166 mg) of $bdcH_2$, and the yield is based on Cr.

[b]Calculated in the pressure range $0.05 < p/p_0 < 0.2$ from N_2 sorption isotherm at 77 K with an estimated standard deviation of ± 50 m^2/g. Nitrogen sorption isotherms of each sample are presented in Figure 2.13.

[c]Calculated from N_2 sorption isotherm at 77 K ($p/p_0 = 0.95$) for pores ≤ 20 nm.

It is worth to notice that, the presence of seeds in the synthesis of MIL-101(Cr) allowed to achieve a temperature as low as 160 °C at which no product was obtained without seeds. Still, at temperatures below 160 °C no MIL-101(Cr) products could be obtained anymore.

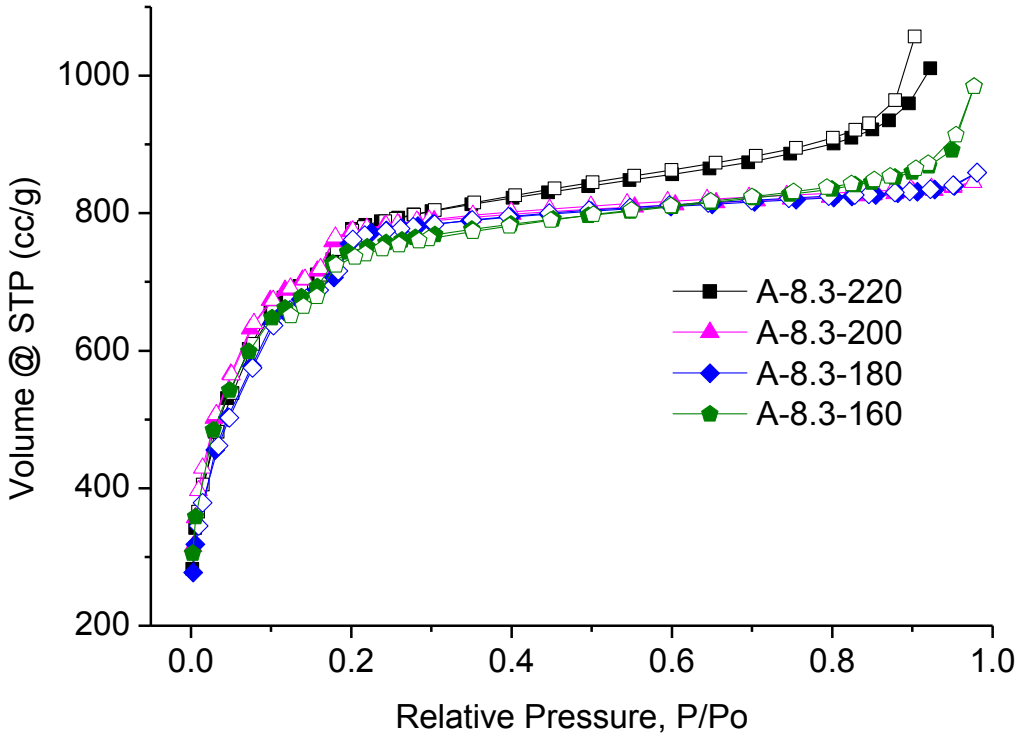

Figure 2.14. Nitrogen sorption isotherms for A-8.3-220, A-8.3-200, A-8.3-180 and A-8.3-160, filled symbols are for adsorption, empty symbols for desorption.

Thermal gravimetric analysis (TGA) study (the activated sample had been stored in ambient air for several days and was used without further preconditioning in the TG analysis) performed on A-8.3-220, A-8.3-200, A-8.3-180 and A-8.3-160 (Figure 2.15). The TG curves of these samples showed three main events between room temperature and 600 °C. As previously observed for MIL-101(Cr), first the departure of the free water molecules occurs in two steps within the range 25-350 °C, which corresponded to the water molecules. The second event, occurs from 350 °C to 550 °C and corresponded to the decomposition of the organic moieties and framework. Because of environment conditions, the water content of MIL-10(Cr) varies considerably from 20% to 60%.[164]

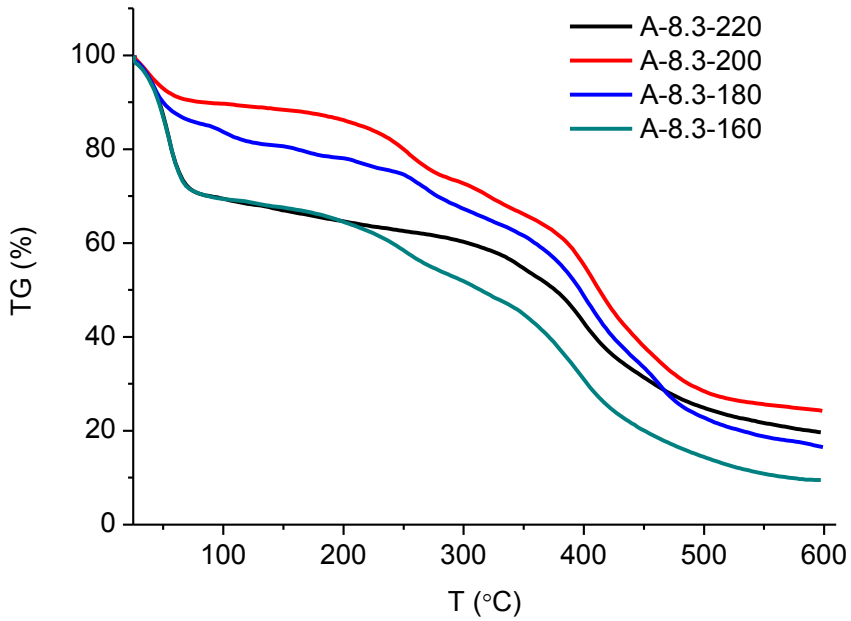

Figure 2.15. TGA curves for A-8.3-220, A-8.3-200, A-8.3-180 and A-8.3-160.

3.4. Other acids as modifiers in MIL-101(Cr) synthesis

We also compared the use of hydrofluoric acid, trifluoroacetic acid, sulfuric acid, hydrochloric acid, phenylphosphonic acid, benzoic acid, formic acid, fumaric acid, citric acid and succinic acid as modifier in MIL-101(Cr) synthesis. According to the general procedure in these experiments, the quantities of all additives were 1.0 equivalent with respect to chromium. All the products were purified in the same way as described in the experimental section. Table 2.6 lists the yields and porosity information with the different modifiers.

Table 2.6. Yields and porosity information of MIL-101(Cr) with different acid modifiers

Modifier	Yield (%)[a]	S_{BET} (m^2/g)[b]	$S_{Langmuir}$ (m^2/g)	V_{pore} (cm^3/g)[c]
Hydrofluoric acid	47.4	3620	4990	1.82
none	56.6	2410	3270	1.30
Trifluoroacetic acid	73.8	2650	3620	1.34
Formic acid	27.1	590	720	0.56
Sulfuric acid	48.2	1750	2200	0.81

Hydrochloric acid	36.3	1560	2030	0.79
Phenylphosphonic acid	51.9	2460	3350	1.49
Benzoic acid	39.4	1760	2290	0.93
Fumaric acid	28.7	760	1040	0.69
Citric acid	37.2	740	1050	0.58
Succinic acid	59.8	2510	3250	1.28

[a] The Cr:bdc ratio is always 1:1, and the yield is based on Cr.
[b] Calculated in the pressure range $0.05 < p/p_0 < 0.2$ from N_2 sorption isotherm at 77 K with an estimated standard deviation of ± 50 m^2/g.
[c] Calculated from N_2 sorption isotherm at 77 K ($p/p_0 = 0.95$) for pores ≤ 20 nm.

The addition of HF was used to repeat the original experiment.[164] Indeed, using HF as additive yielded a MIL-101(Cr) product with the highest BET surface area of all small-scale samples and a yield of around 50%, very near to the values reported in the literature.[164] An additive-free method gave only 2410 m^2/g of BET surface area and the yield was a bit higher than from the HF-experiment. Thus, an additive-free method can be a good choice to use in MIL-101(Cr) synthesis due to its easy operation and its relatively good porosity (compared to other MOFs). Their PXRD patterns showed a high agreement with the simulated pattern (Figure 2.16, top). The nitrogen sorption isotherms as the basis for the BET surface area are presented in Figure 2.16, bottom.

Trifluoroacetic acid (CF_3COOH) also improved the yield of MIL-101(Cr), but not the porosity. From the PXRD pattern of CF_3COOH-MIL-101 it is also evident that unknown phases were produced as byproduct although the shape of the nitrogen sorption isotherm shown in Figure 2.17 (bottom, black curve) still agrees with the typical MIL-101(Cr) nitrogen sorption isotherm.

Formic acid is the simplest monocarboxylic acid, it was used as a modulator in the synthesis of the Zr-fumarate MOF.[225] Here an unknown phase of low yield and porosity was obtained (Figure 2.17).

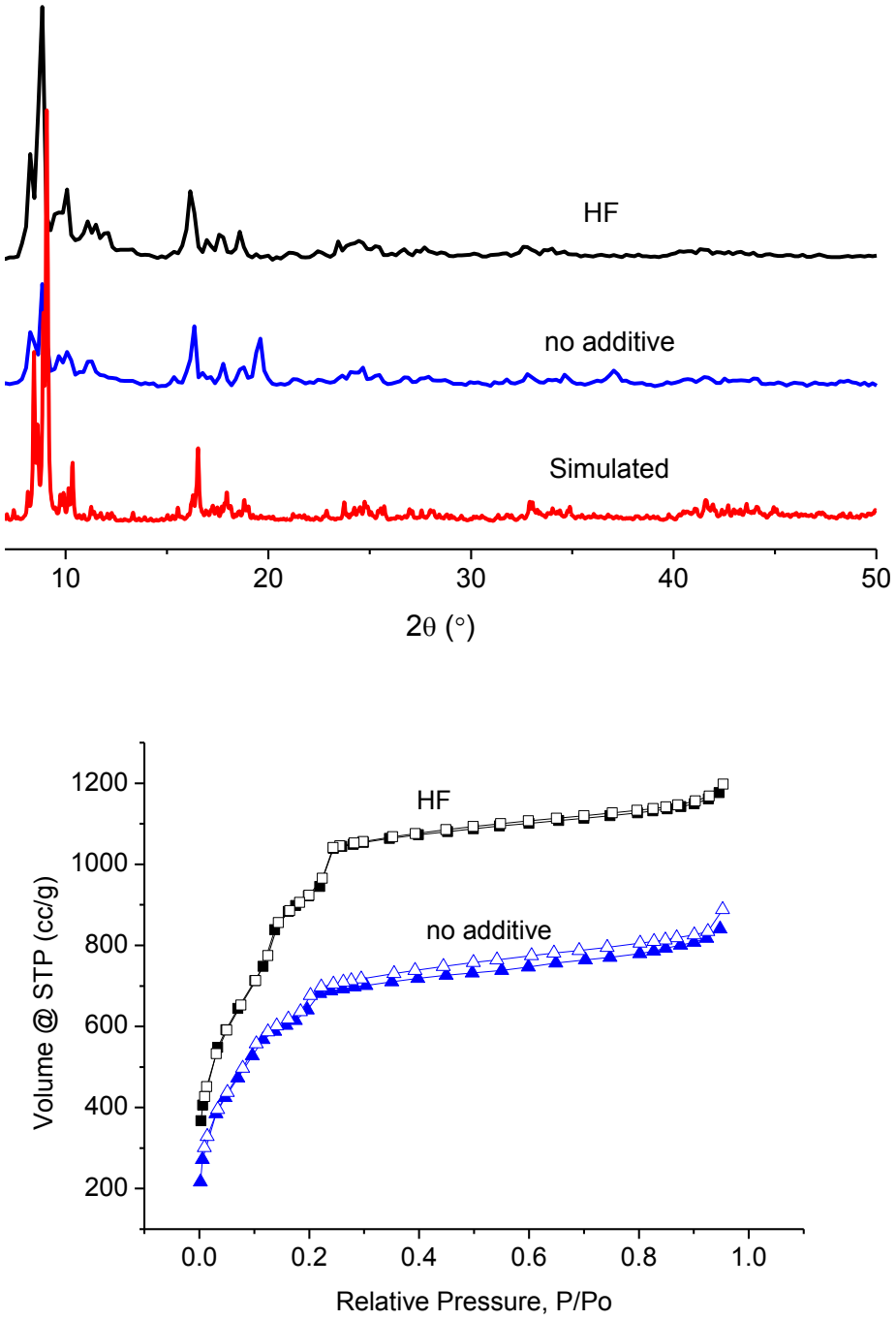

Figure 2.16. PXRD patterns (top) and N_2 sorption isotherms (bottom) for HF-MIL-101 and MIL-101 without additive. Filled symbols are for adsorption, empty symbols for desorption.

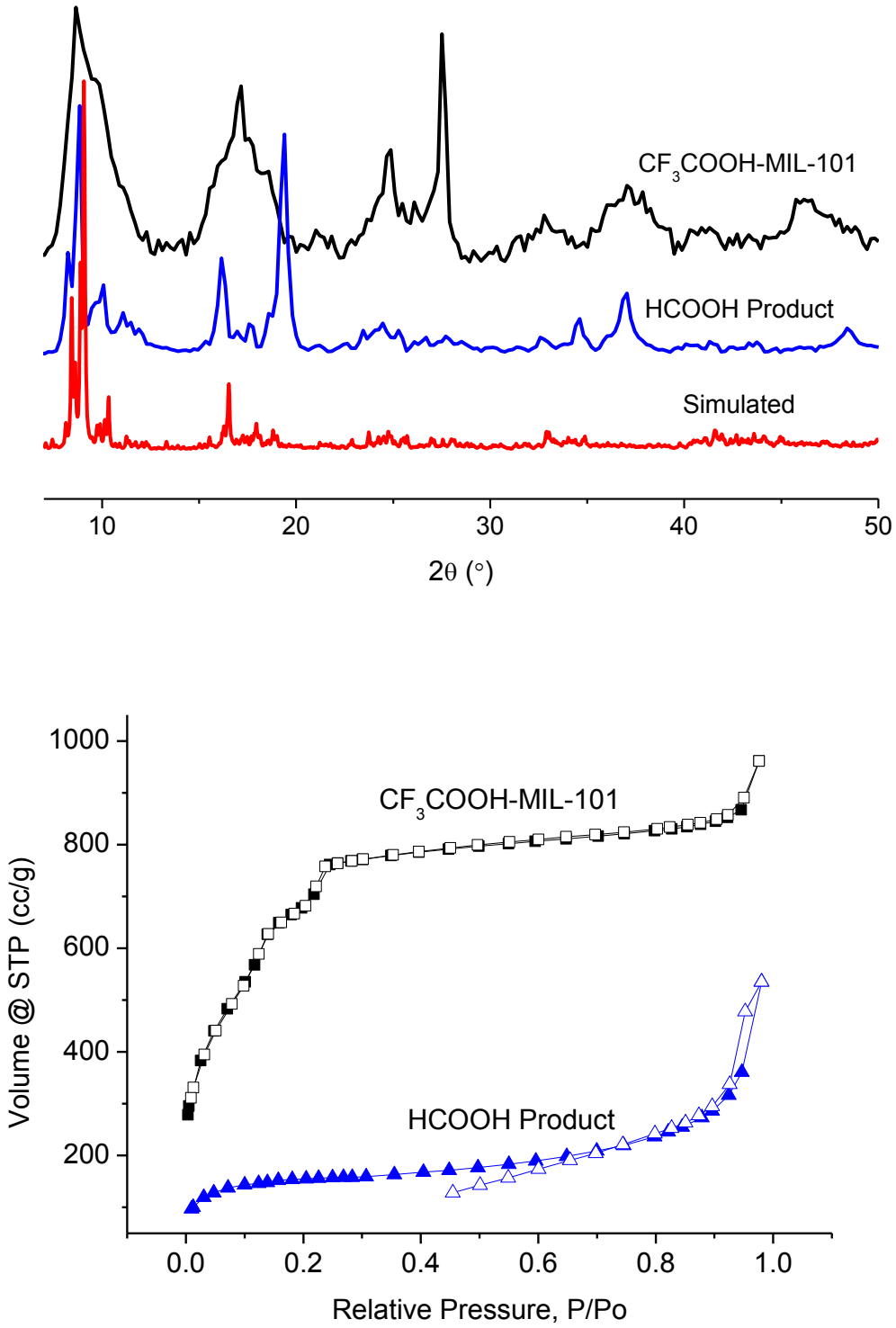

Figure 2.17. Powder X-ray diffractograms (top) and N_2 sorption isotherms (bottom) for CF_3COOH-MIL-101 and HCOOH-unknown material. Filled symbols are for adsorption, empty symbols for desorption.

Sulfuric acid and hydrochloric acid are the two most common inorganic acids. Considering that nitric acid could improve the yield and porosity of MIL-101(Cr), one may expect a similar result for H_2SO_4 and HCl. For sulfuric acid, the product matches the simulated PXRD of MIL-101(Cr) albeit with some additional peaks indicating a byproduct (Figure 2.18, top) Yet, yield and BET surface of the H_2SO_4-material were relatively low. For hydrochloric acid, the PXRD pattern of the product shows enhanced byproduct formation. Still the shape of the N_2 adsorption-desorption isotherms with H_2SO_4 and HCl exhibits the typical MIL-101(Cr) shape (Figure 2.18, bottom).

The products obtained with the acid modifiers phenylphosphonic acid, benzoic acid and succinic acid agreed in their PXRD patterns well with the simulated pattern of MIL-101(Cr) (Figure 2.19, top). For phenylphosphonic acid and succinic acid yields were above 50% and porosities (Figure 2.19, bottom) around 2500 m^2/g. The hysteresis in the N_2 sorption isotherm with phenylphosphonic acid indicates formation of a mesoporous material. For Benzoic acid was used as a modulator in the synthesis of UiO-66 and UiO-67.[226] Here benzoic acid gives only a low yield and low porosity product. None of these three acids can be ascribed with a positive effect on the synthesis of MIL-101(Cr).

Different from the acids used before, fumaric acid and citric acidmay act as bridging ligands themselve because they possess two or three –COOH groups. Thus, the PXRD shows the appearance of some unknown phase product (Figure 2.20, top). Also product yields and porosities (Figure 2.20, bottom) are much lower than with the other acid modifiers.

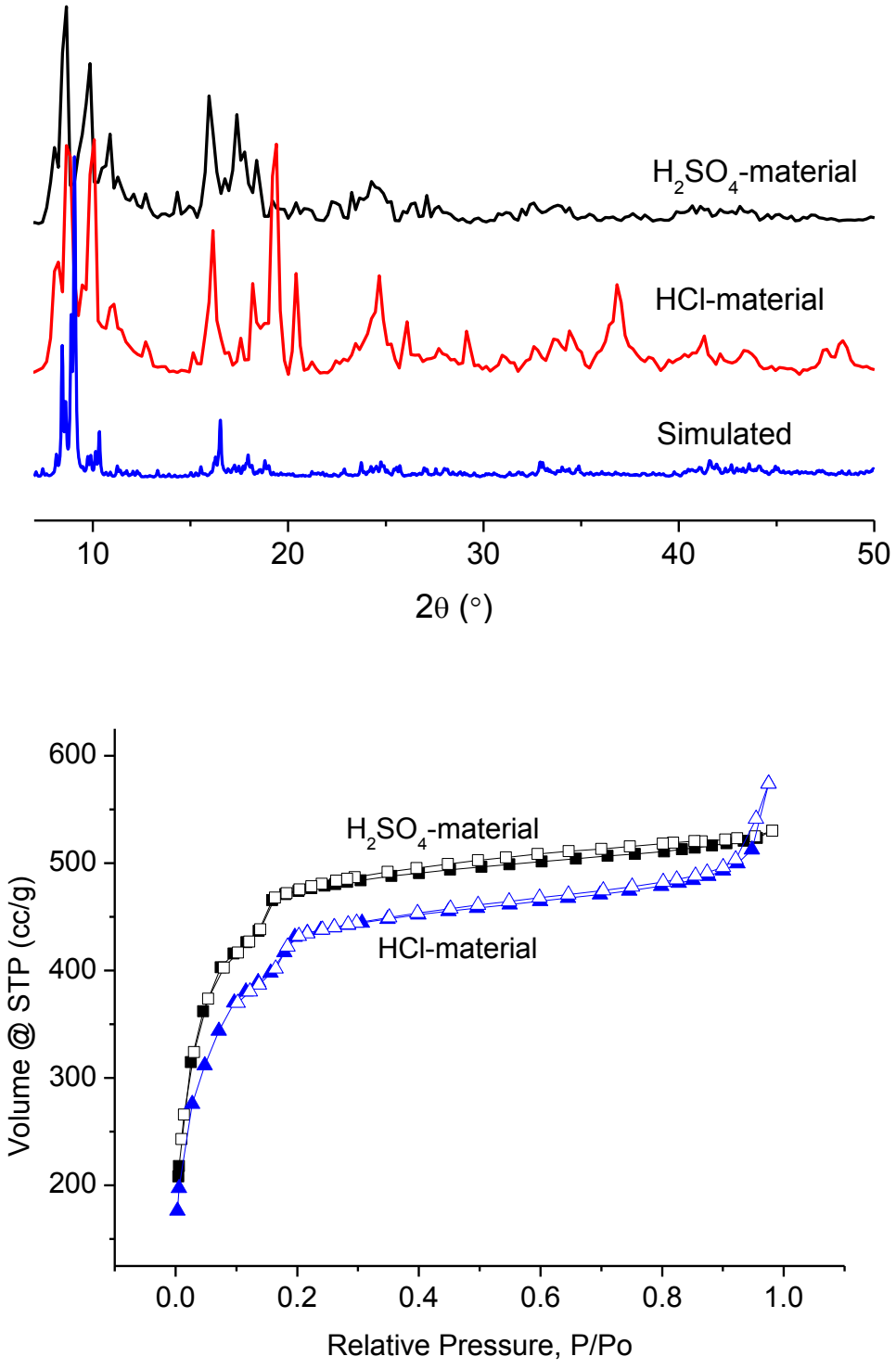

Figure 2.18. Powder X-ray diffractograms (top) and N_2 sorption isotherms (bottom) for H_2SO_4-material and HCl-Material. Filled symbols are for adsorption, empty symbols for desorption.

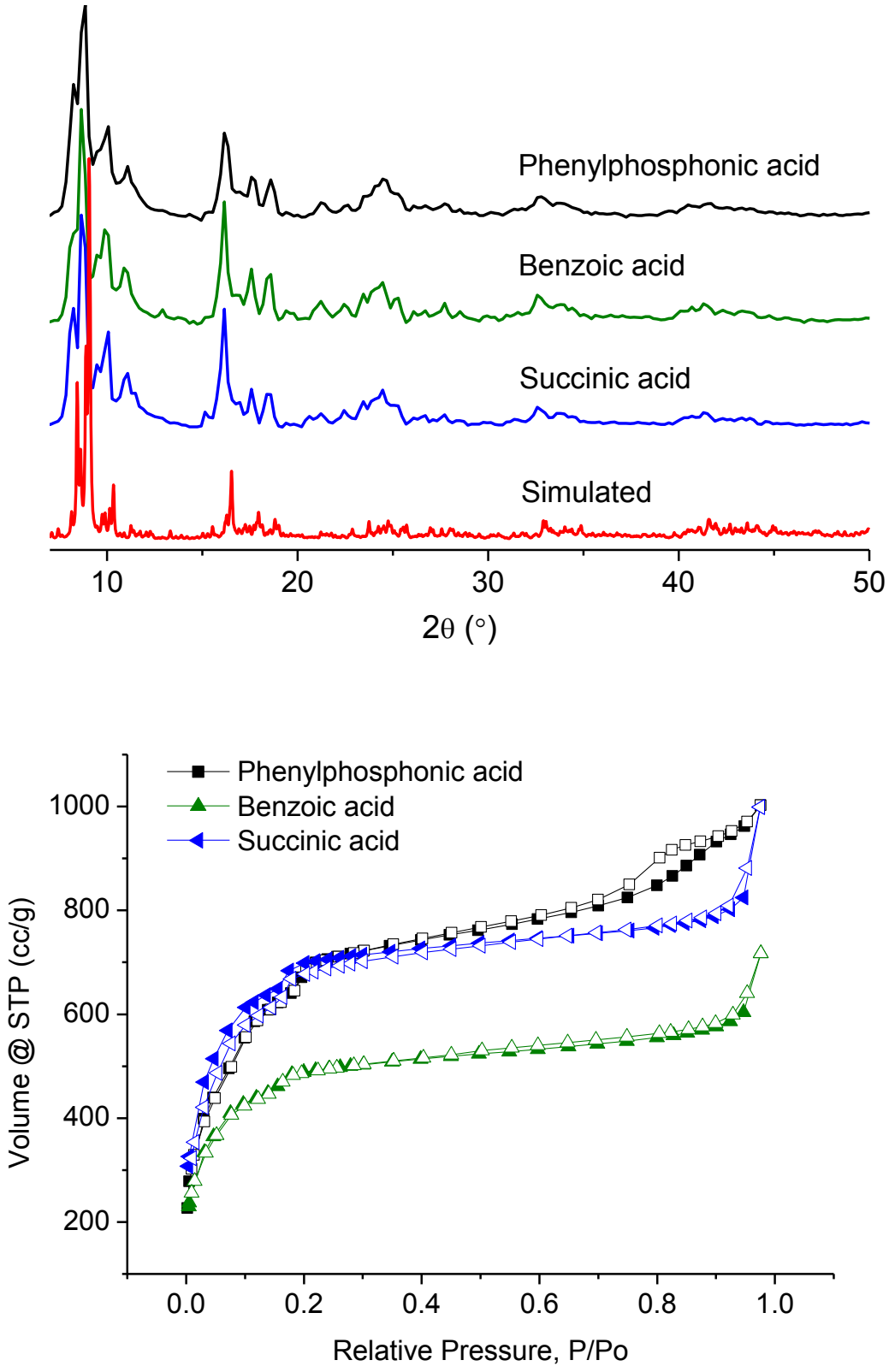

Figure 2.19. Powder X-ray diffractograms (top) and N_2 sorption isotherms (bottom) for MIL-101 with different additives. Filled symbols are for adsorption, empty symbols for desorption.

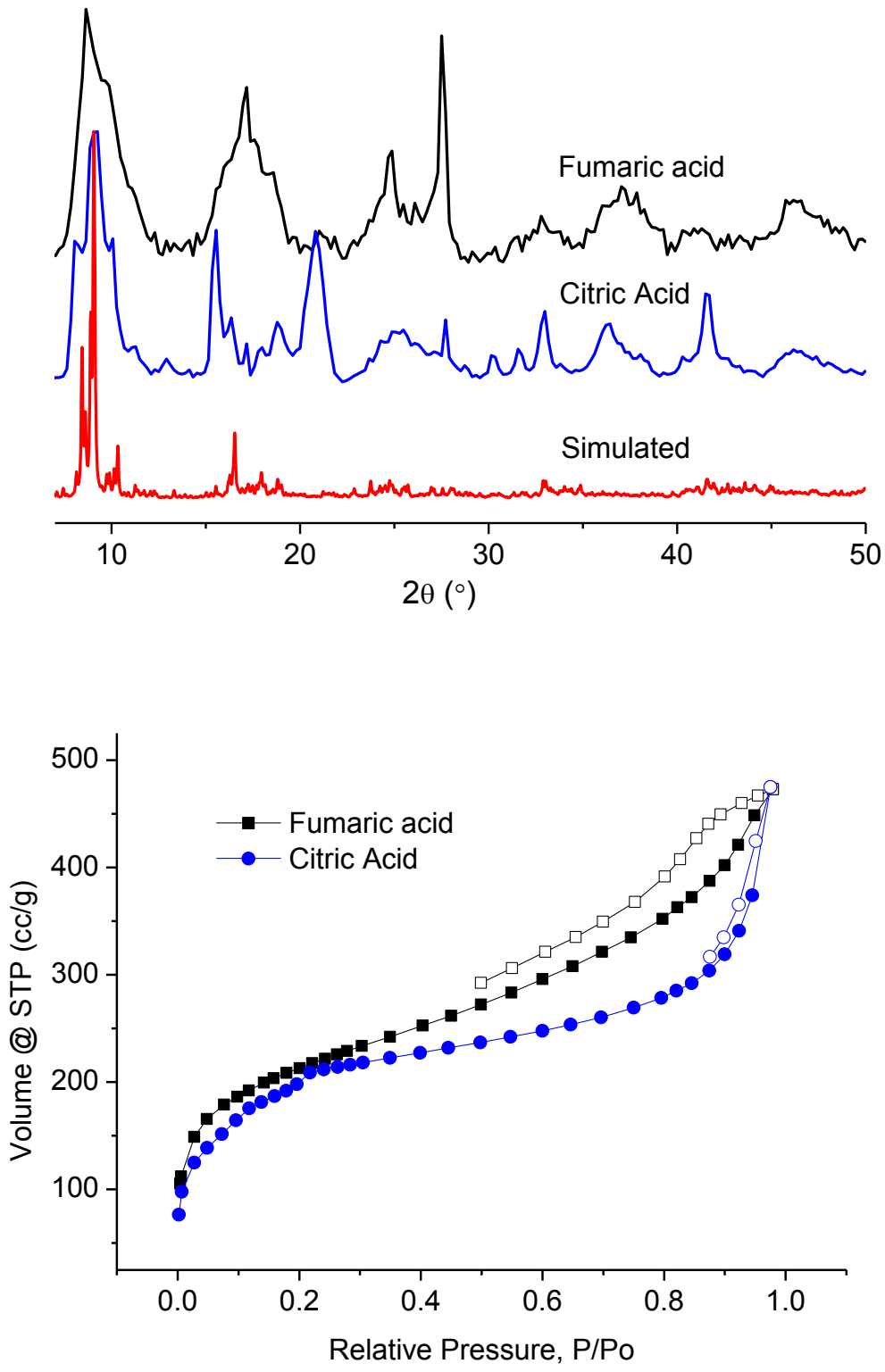

Figure 2.20. Powder X-ray diffractograms (top) and N_2 sorption isotherms (bottom) for fumaric-sample and citric-sample. Filled symbols are for adsorption, empty symbols for desorption.

4. Conclusions

In summary, from a series of tested mineral and organic acid modifiers as alternatives to HF in the synthesis of MIL-101(Cr) only nitric acid (HNO_3) and acetic acid (CH_3COOH) proved advantageous. An advantage of HNO_3 was could provide a > 30% increase in yield with the BET surface area lagging only ~10% behind the use of HF. And it was also proved work well in large-scale MIL-101(Cr) synthesis (3 L). In the synthesis of acetic acid as an additive could largely decrease the reaction temperature, minimum to 160 °C, with the regular laboratory obtained yield (~50%) and BET surface area (2700~2800 m^2/g). Similar to HNO_3, in the synthesis of CF_3COOH as an additive could also provide large increase in yield (>20%), but no outstanding performance on BET surface area. H_2SO_4 and HCl as additives in syntheses were no positive help; they would decrease the yields and porosities of the products. Phenylphosphonic acid succinic acid just like bystanders when they were added to the syntheses, because there was no significant difference found from final results. The presence of benzoic acid would give an inhibition effect to the formation of MIL-101(Cr), this effect would decrease the yield and porosity of the product. In the presence of formic acid、fumaric acid or citric acid would deeply influent the formation of final product, the unknown phases instead of the intended MIL-101(Cr) would be produced.

Acknowledgment

Prof. Christoph Janiak and Dr. Ishtvan Boldog are gratefully acknowledged for the guidance of MIL-101(Cr) synthesis and sample treatment. Dr. Felix Jeremias and Dr. Binh Nguyen are gratefully acknowledged for large-scale MIL-101(Cr) synthesis.

Chapter 3

Embedding spin-crossover compound in the pores of MOFs

1. Introduction

The Spin-Crossover (SCO) phenomenon[227,228] is the switching of spin states occurring in (pseudo) octahedral complexes of some first row transition metals, with iron(II) d^6 complexes being the most studied group. The reversible switching between the low and high spin states (LS $\leftrightarrow$ HS,) is associated with pronounced change of not only the magnetic state from diamagnetic to paramagnetic ($^1A_1$, S=0 $\leftrightarrow$ $^5T_2$, S=2), but many other important physical parameters, including optical, structural and dielectric properties. The simplicity of detection of optical usually LS-red$\leftrightarrow$HS-yellow and magnetic changes, made the iron(II) SCO compounds as early prototypes for information storage[229,230,231,232,233] and sensors[234,235,236,237,238,239].

Triggering of the SCO transition was achieved by change of temperature, pressure, magnetic field, irradiated by light (LIESST), or action of a chemical agent (chemo-switching). Production of functional, individually addressable, SCO units[240,241] as small as possible is an important problem actively researched in the area of SCO nanomaterials.[242,243,244] Various methods for synthesis of SCO nanoparticles[245,246,247] and thin films[248,249] including nanopatterned[250] growth were successfully implemented, also as prototypal functional elements for nanodevices.[251] One of the traditional problematics of such studies is the problem of loss of abruptness in thermal- and pressure- induced SCO, which is associated with loss of cooperativity, i.e. elastic interactions in the solid-state propagating the effect of structural changes during the transition.

An interesting possibility is to sacrifice entirely the traditional cooperativity for the possibility of embedding isolated molecular SCO entities in a regular matrix with a precise spatial placement / addressability. A transparent matrix, penetrable for small molecules, but encapsulating the SCO entities should allow light- and chemo-switching, also providing good mechanical protection. The effect of matrix confinement imposing additional elastic interactions between the host and the embedded object is well known for SCO nanoparticles, represented by, either 'soft' matrices, like

organic polymers, e.g. PVP or chitosan, or 'hard' ones, realized mainly as core-shell particles. In practically all those cases the matrix is firmly adjoined to the surface of the embedded objects, completely isolating them. However, recently we have observed that in $[Fe(Htrz)_3](BF_4)_2 \cdot xH_2O$@MCM-41 (Chapter 4) the mesoporous zeolite matrix loosely surrounding the embedded 1D SCO polymer could transfer the confinement pressure through absorbed water molecules as mediators, significantly altering the SCO parameters.

In this chapter, we try to embed the well studied SCO compound $[Fe(HB(pz)_3)_2]$ (pz = pyrazolyl, Scheme 3.1) into the pores of several large porosity, stable, well investigated MOFs by different methods. The samples were characterized by various analyses to determine whether the $[Fe(HB(pz)_3)_2]$ was successfully embedded.

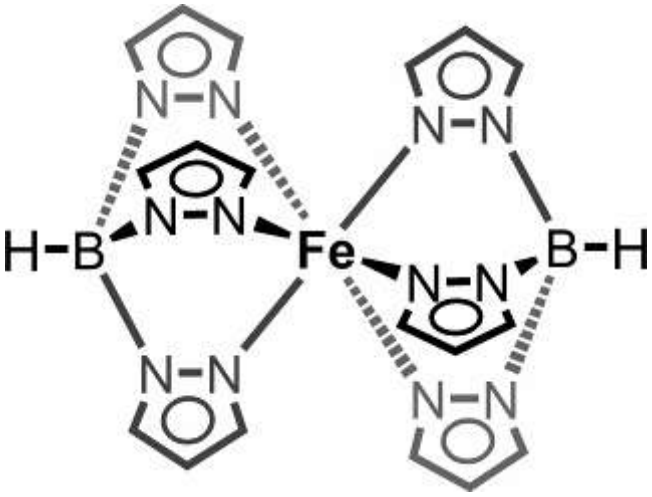

Scheme 3.1. Schematic drawings of SCO material $[Fe(HB(pz)_3)_2]$.

2. Experimental

2.1. Materials

All the reagents were purchased from the following distributors (Table 3.1) and used without further purification.

Table 3.1. The information of chemicals which used in this chapter

Reagent	Purity, % / Grade	Commercial Source
Chromium(III) nitrate nonahydrate	98.5%	Alfa Aesar
Terephthalic acid	98%	Sigma-Aldrich

Aluminum nitrate nonahydrate	⩾98%	Sigma-Aldrich
Trimethyl 1,3,5-benzenetricarboxylate	98%	Sigma-Aldrich
Aluminum chloride hexahydrate	⩾99.0%	Sigma-Aldrich
2-amino terephthalic acid	99%	Alfa Aesar
Ammonium iron(II) sulfate hexahydrate	99%	Sigma-Aldrich
Potassium tri(1-pyrazolyl)borohydride	97%	Sigma-Aldrich
N, N-Dimethylformamide	99.9 %	VWR
Ethanol	99.9 %	Merck
Methanol	99.9 %	Merck
Dichloromethane	>99.9%	Prolabo
Nitric acid	65 wt. % in H_2O	Fisher Chemical
Iron Standard for AAS	1000±4 mg/L	Fluka

2.2. Synthesis and Embedding Procedure

2.2.1. The Synthesis and Purification Procedure

2.2.1.1. The Synthesis and Purification of MIL-101(Cr)

MIL-101(Cr) was synthesized according to the procedure in chapter 2 with 1 equiv HNO_3 with respect to chromium(III) nitrate nonahydrate. A typical synthesis involves a solution containing chromium(III) nitrate nonahydrate ($Cr(NO_3)_3 \cdot 9H_2O$, 400 mg, 1.0 mmol), nitric acid (1.0 mmol) and terephthalic acid (H_2BDC, 166 mg, 1.0 mmol) in 5 mL H_2O with stirring for 10 min. Then the mixture is transferred to the Teflon line in a hydrothermal autoclave which is heated for 8 h at 220°C and cooled afterwards slowly to room temperature at a rate of 30 °C /h in 6 h. The mixture was then isolated from the autoclave and the solid separated from the solution through centrifugation (4200 U/min for 50 min). The contents of autoclave were transferred to two centrifugal tubes and the supernatant solution was carefully removed after centrifugation. Then water (5 mL) was added in each tube and the solid was evenly dispersed in the aqueous phase. After renewed centrifugation and removal of the supernatant solution, DMF (5 mL) was added to each tube which was placed in a hot (80 °C) ultrasonic bath and sonicated for 1 h. Centrifugation was again used to separate MIL-101 and DMF. The precipitate was transferred in

a 25 mL beaker where it was stirred with 10 mL of water at room temperature for 5 h. After separation by centrifugation, the same washing procedure but using ethanol was repeated once more at the same temperature. The final product was obtained by centrifugation and dried in a vacuum oven (100 °C, 12 mbar) for 2 h.

2.2.1.2. The Synthesis and Purification of MIL-100(Al)

Aluminium-based MIL-100 trimesate ($Al_3O(OH)(H_2O)_2[btc]_2 \cdot nH_2O$) was synthesized according to the previously reported procedure.[252] A typical synthesis involves a solution containing aluminium (III) nitrate hexahydrate ($Al(NO_3)_3 \cdot 6H_2O$, 230 mg, 0.61 mmol), nitric acid (0.77 mmol) and trimethyl 1,3,5-benzenetricarboxylate ($btcMe_3$, 104 mg, 0.41 mmol) in 2.8 mL H_2O. Then the mixture is transferred to the Teflon line in a hydrothermal autoclave which is heated for 3.5 h at 210°C (the temperature went up to 210°C in 1 h) and cooled afterwards slowly to room temperature at a rate of 30 °C /h in 6 h. The resulting yellowish powdered sample was collected by filtration, washed with water, and dried at room temperature for overnight. Then the collected solid and 10 mL DMF were transferred to a 20 mL Parr-type Teflon-lined autoclave and heated at 150°C for 4 h. The mixture was then isolated from the autoclave and the solid separated by filtration, washed with water, and dried at room temperature for overnight. After that, the white powdered product was washed with water in reflux at 100°C for 12 h and then collected by filtration at room temperature. The product was placed at ambient condition for 12 h and then stored in a glass bottle.

2.2.1.3. The Synthesis and Purification of NH_2-MIL-100(Al)

Amino Functionalized MIL-101 material based on aluminium (Formula: $Al_3O(DMF)$-$[(COO)C_6H_3NH_2(COO)]_3 \cdot nH_2O$) was synthesized according to the previously reported procedure.[253] A typical synthesis involves a solution containing aluminum chloride hexahydrate ($AlCl \cdot 6H_2O$, 510 mg, 2.11 mmol) and 2-amino terephthalic acid (HO_2C-$C_6H_3NH_2$-CO_2H, 560 mg, 3.09 mmol) in 30 mL DMF. The reactants were placed in a Teflon line in a hydrothermal autoclave which is heated for 72 h at 130°C. The resulting yellowish powdered sample was collected by filtration, washed with acetone, and dried at room temperature for overnight. Then the collected powder was transferred to a bottom-round flask (100mL volume) washed with

boiling methanol (50 mL) in reflux for overnight. The final product was obtained by centrifugation (4200 U/min for 20 min) and dried in a vacuum oven (100 °C, 12 mbar) for 2 h.

2.2.1.4. The Synthesis of spin-crossover compound $[Fe(HB(pz)_3)_2]$

The spin crossover ferrous complex $[Fe(HB(pz)_3)_2]$ was synthesized according to experimental procedures reported in the literature.[254] A typical synthesis was followed: the compound was prepared by adding a solution of 1 equiv of ammonium iron(II) sulfate hexahydrate (392 mg, 1 mmol, in 20 mL H_2O) to a stirred solution of 2 equiv of potassium tri(1-pyrazolyl)borohydride (504 mg, 2 mmol, in 20 mL H_2O), and then the precipitated product was extracted with methylene chloride. The extraction methylene chloride solution was transferred to a beaker and placed in a fume hood at ambient conditions for overnight. After the evaporation of dichloromethane, a kind of wine-red crystals could be obtained.

2.2.2. Embedding Procedure

2.2.2.1. Liquid-Phase Diffusion Procedure

There are many methods to embed guest molecules into the pores of host material. One of the simplest ways is impregnating host material into the solution of spin-crossover compound and let this complex molecules move into the pores by diffusion. To increase the movement of guest molecules, stirring and heating was necessary in this procedure. Here, three well investigated MOFs: MIL-101(Cr), NH_2-MIL-101(Al) and MIL-101(Al) were used as host materials, while as-prepared $Fe(HB(pz)_3)_2$ was guest compound.

A typical liquid phase diffusion experiment was followed: 50 mg of host material was immersed in the dichloromethane solution of $[Fe(HB(pz)_3)_2]$ (0.02 mol/L, 10 mL) with stirring at 40°C for 24 h. Then the solid precipitate was isolated by centrifugation (4200 U/min for 10 min). This precipitate was washed with dichloromethane for three times to remove the residues of $[Fe(HB(pz)_3)_2]$ outside of the pores, and then the sample was dried in the vacuum oven (100 °C, 12 mbar) for 2 h.

2.2.2.2. Gas-Phase Diffusion Procedure

The gas-phase loading of MOF-177(Zn) and MOF-5 with the volatile platinum compounds

known as precursors for metalorganic chemical vapour deposition (MOCVD) had been reported.[255,256] This gas-phase diffusion method avoids some of the deficiencies of liquid-phase diffusion of MOFs with guest molecules that are typically dissolved in organic solvents.[257]

$[Fe(HB(pz)_3)_2]$ could easily sublimate under low pressure when temperature over 100°C. Thus, it was possible that, $[Fe(HB(pz)_3)_2]$ molecules could directly get into the pores of MOFs by gas phase diffusion. A typical gas phase diffusion experiment was followed: 30 mg of host material and 30 mg of $[Fe(HB(pz)_3)_2]$ were mixed and mixture was placed in a sealed vacuum tube (vacuum<10^{-2} Torr). Then the sealed vacuum tube was placed in a rotating device (20 U/min) which also could be heated inside at 170°C for 24 hours and cooled afterwards to room temperature. The sample was washed with dichloromethane for three times to remove the residues of $[Fe(HB(pz)_3)_2]$ outside of the pores. The final product was dried in the vacuum oven (100 °C, 12 mbar) for 2 h.

The key of this experiment was to prepare the sealed vacuum tube. While pumping vacuum of the glass tube, it was melted by oxy-gas flame and then sealed with melted glass (Scheme 3.2).

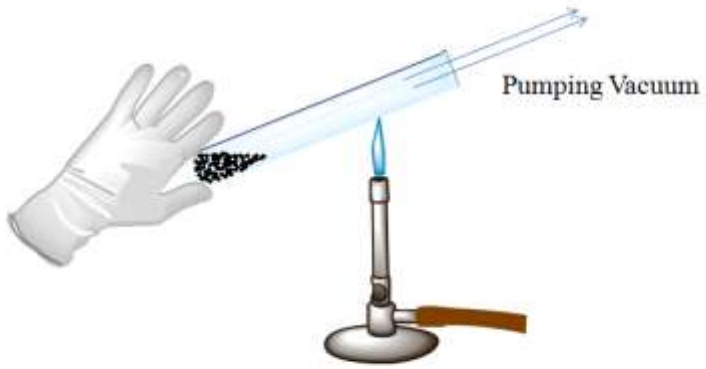

Scheme 3.2. Schematic drawing of preparation of sealed vacuum tube.

2.2.2.3. Synthesis of $[Fe(HB(pz)_3)_2]$ in the pores of MOFs

Some metal particles could be directly formed in the pores of MOFs by reduction of the metal salt. For instance, Pd and Cu particles could be embedded in the pores of MIL-101(Cr) by this method without observed degradation of MOF.[258]

The synthesis of $[Fe(HB(pz)_3)_2]$ is quite simple, just need to mix a solution of Fe(II) ion and a

solution of potassium tri(1-pyrazolyl)borohydride at room temperature. So another available method is to directly synthesize $[Fe(HB(pz)_3)_2]$ with the presence of MOFs. A typical synthesis was followed: 50 mg of host MOF material was added to a solution of potassium tri(1-pyrazolyl) borohydride (126 mg, 0.5 mmol, in 5 mL H_2O) with stirring at room temperature for 12 h. Then a solution of ammonium iron(II) sulfate hexahydrate (98 mg, 0.25 mmol, in 5 mL H_2O) was added to this solution and with stirring at room temperature for another 2 days. The precipitate was isolated by centrifugation (4200 U/min for 10 min) and washed with dichloromethane for three times to remove the residues of $[Fe(HB(pz)_3)_2]$ outside of the pores of MOF. Centrifugation was used to separate solid sample and dichloromethane. The precipitate was transferred in a 25 mL beaker and stirred with 10 mL of water at 70 °C for 5 h. After separation by centrifugation, the final product was dried in the vacuum oven (100 °C, 12 mbar) for 2 h. Worth to notice that, Fe(II) ions would be bonded with $-NH_2$ group, so NH_2-MIL-101(Al) was not suitable to use with this method.

2.2.2.4. Synthesis of NH_2-MIL-101(Al) with the presence of $[Fe(HB(pz)_3)_2]$

It was reported that MOF-199 with encapsulated Keggin polyoxometalate (POM) catalyst was successfully confined in mesoporous SBA-15 by the hydrothermal method.[259] A graphene and copper oxide composites embedded in a Cu-based metal–organic framework was prepared the self-assembly process.[260] Thus, directly synthesize host MOFs with the presence of guest molecules was also an available method.

With this method, NH_2-MIL-100(Al) was the only suitable MOF for host material due to its mild reaction temperature and its non-hydrothermal environment. The synthesis temperature of MIL-101(Cr) and MIL-101(Al) was over 200°C, while $[Fe(HB(pz)_3)_2]$ could not survive under such a high temperature with the presence of water for long time. Second, $[Fe(HB(pz)_3)_2]$ could well dissolved in DMF, and this is also more conductive to the embedding of $[Fe(HB(pz)_3)_2]$. So a typical synthesis involves a solution containing aluminum chloride hexahydrate (57 mg, 0.24 mmol), 2-amino terephthalic acid (61 mg, 0.34 mmol) and some as-prepared $[Fe(HB(pz)_3)_2]$ (50~90 mg) in 3.33 mL DMF. The reactants were placed in a thick-walled glass tube and sealed with a teflon lined screw-cap. The glass tube was placed in a rotating oven (20 U/min), which ensured efficient stirring and heated at 130°C for 72 h. The cooled sample was isolated by

centrifugation, triple washed with acetone and dichloromethane, then transferred to a bottom-round flask (50mL volume) and refluxed in 20 ml of methanol overnight for additional purification. The solid was centrifuged out and dried in a vacuum oven (100 °C, 12 mbar) for 2 h. No inert conditions were imposed at any of the synthetic steps.

2.3. Characterization

Powder X-ray diffraction (PXRD) measurements were carried out with a Bruker D2 Phaser using a flat silicon, low background sample holder and Cu-K_α radiation (λ = 1.54184 Å) at 30 kV and 0.04°/s. Diffractograms were obtained on flat layer sample holders where at low angle the beam spot is strongly broadened so that only a fraction of the reflected radiation reaches the detector which leads to the low relative intensities measured at $2\theta < 7°$.

Nitrogen physisorption isotherms at 77 K were obtained using a NOVA-4000e instrument within a partial pressure range of 10^{-6}~1.0. The samples were degassed under high vacuum (10^{-5}Torr) at 120 °C for at least 2 h, prior to each measurement. The BET surface areas were calculated from adsorption isotherm data points in the pressure range $p/p_0 = 0.05 – 0.2$.

Thermogravimetric (TG) data were collected using a Netzsch Tarsus 209 F3 TGA instrument in a protecting flow of nitrogen (10 mL/min) at 10°C/min heating rate.

Infrared spectra (IR) were measured on a Bruker Tensor 37FT-IR Spectrometer with ATR disks.

Atom absorption spectroscopy (AAS) was conducted with a Perkin Elmer AAnalyst100 instrument (AAS flame: acetylene/air flame, burner head length: 10 cm). The standard solution were prepared with densities 1mg/L、5mg/L and 10mg/L respectively. Carefully weight a few milligrams of each sample and let them completely dissolved in 5 mL HNO_3 (65%) solution. Prepare these solutions into 20 mL using volumetric flask and ready for AAS analysis. The iron content of each sample was determined by the comparison of standard solution.

DC magnetic measurements were performed by using Quantum Design MPMS XL-5 SQUID magnetometer. For both samples, M(T) measurements were carried out in the magnetic field of 1000 Oe, starting from T=70 K up to 400 K (heating), and then while cooling back to 200K.

3. Results and Discussion

3.1. Liquid Phase Diffusion

In liquid phase diffusion experiments, some amount of MOFs were added to the dichloromethane solution of $[Fe(HB(pz)_3)_2]$ with stirring for 24 h at 40°C. The final samples were named as TZ-LD-a, TZ-LD-b and TZ-LD-c, corresponding to different host MOFs, MIL-101(Cr), NH_2-MIL-101(Al) and MIL-100(Al) respectively. One phenomenon of these experiments was the changing of colour; the photos of each sample have been presented as comparison (Figure 3.1).

Figure 3.1. The photos of each sample in comparison to that of free MOFs. The colours of MIL-101(Cr), NH_2-MIL-101(Al) and MIL-100(Al) are green, yellow and white (slight yellowed because of impurities) respectively.

From photos, the colours of TZ-LD-a and TZ-LD-b were deeply changed after diffusion. It was indicated that, $[Fe(HB(pz)_3)_2]$ molecules had covered outside of the MOFs and showed the orange-red colour of spin-crossover compound at LS. The colour of TZ-LD-c was nearly no changing. This is because, compare to MIL-101 structure, MIL-100 structure has much smaller pore size and BET surface area, $[Fe(HB(pz)_3)_2]$ molecules were more difficult to go into the pores of MIl-100(AL) via liquid phase diffusion. Thus, we get the conclusion that, MIL-100(Al) did not work as host material by liquid diffusion method. In consequent analysis, only TZ-LD-a and

TZ-LD-b were conducted.

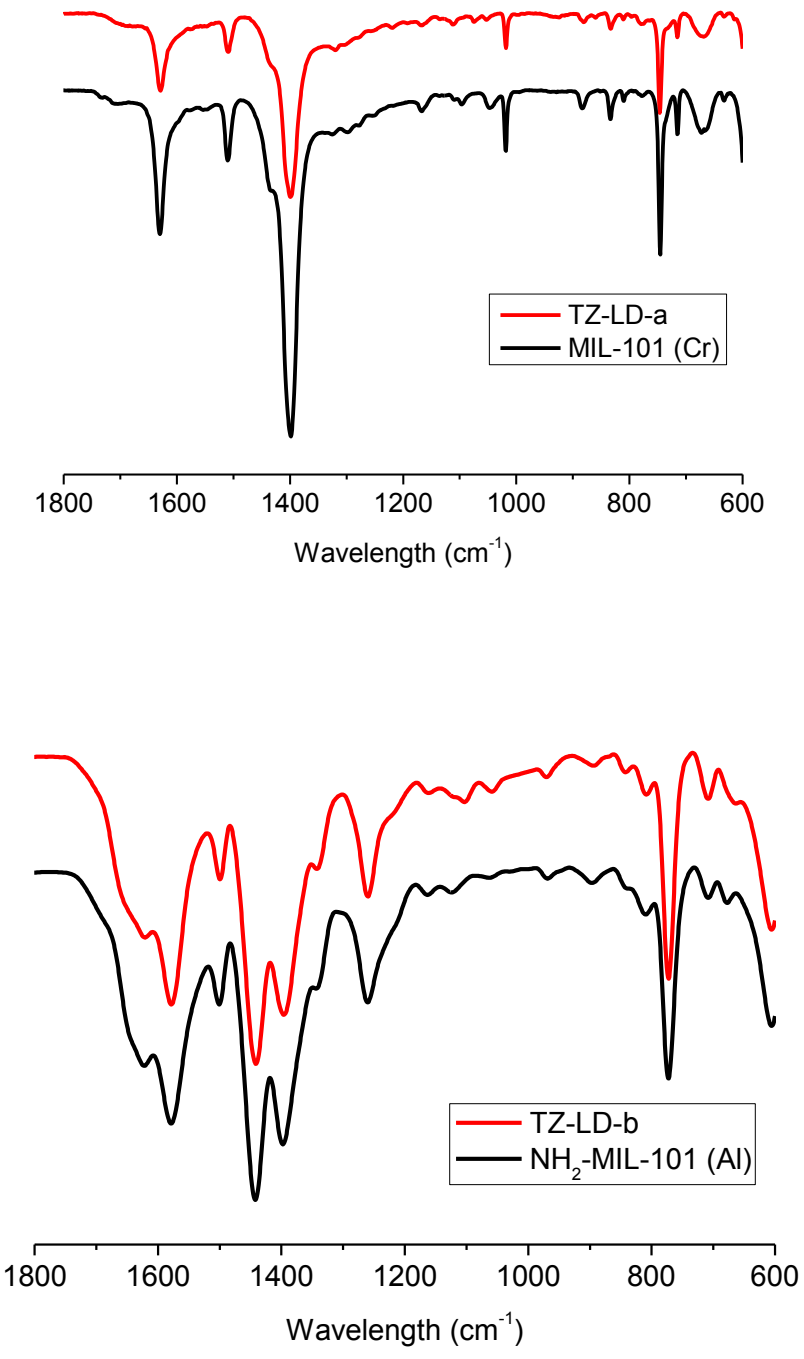

Figure 3.2. IR spectra of TZ-LD-a and TZ-LD-b in comparison to MIL-101(Cr) and NH_2-MIL-101(Al) respectively.

Since the colours of TZ-LD-a and TZ-LD-b were substantially altered, it was interesting to see, whether $[Fe(HB(pz)_3)_2]$ molecules would so simply embedded inside the pores of these two

MOFs. IR spectra were collected on TZ-LD-a and TZ-LD-b (Figure 3.2). Interestingly, the IR spectra of TZ-LD-a and MIL-101(Cr) were almost the same, TZ-LD-b and NH_2-MIL-101(Al) were also presented the same behavior. A possible explanation is that $[Fe(HB(pz)_3)_2]$ molecules just adhere to the surface of MOFs via liquid phase diffusion. Thus, $[Fe(HB(pz)_3)_2]$ molecules formed a layer covered outside and changed the colour of MOFs.

Normally, the loading rate of this kind of surface-embedding would not be high, because the molecules on the surface would block the channel of the pores to prevent the other molecules go through inside. Atom absorption spectroscopy was used to determine the content of iron element in TZ-LD-a and TZ-LD-b, and the content of $[Fe(HB(pz)_3)_2]$ could be obtained by calculation (Table 3.2). The results showed that the weight ratios of $[Fe(HB(pz)_3)_2]$ of TZ-LD-a and TZ-LD-b were only 2.93 wt% and 1.81 wt% respectively. With such a low weight ratios, the influence to IR spectra could be ignored. That's the reason why the IR spectra of TZ-LD-a and TZ-LD-b were almost identical with that of their host MOFs.

Table 3.2. The weight ratios of Fe and $[Fe(HB(pz)_3)_2]$ of each sample

Sample	Fe content (wt%)	$Fe(HB(pz)_3)_2$ content (wt%)
TZ-LD-a	0.34	2.93
TZ-LD-b	0.21	1.81

The structures of TZ-LD-a and TZ-LD-b were determined by powder X-ray diffraction (PXRD) analysis (Figure 3.3). Matching the PXRD patterns of TZ-LD sample and its corresponded MOF host, it was found that, the difference of patterns was very tiny. That because $[Fe(HB(pz)_3)_2]$ only covered the surface of MOFs, and the content of iron(II) compound was low.

As mentioned above, $[Fe(HB(pz)_3)_2]$ can be embedded on the surface of MIL-101(Cr) and NH_2-MIL-101(Al) via liquid phase diffusion, but cannot embedded into the pores of MOFs. Though $[Fe(HB(pz)_3)_2]$ was just adhere to the surface, this embedding effect still relatively strong, washing with dichloromethane couldn't remove those spin-crossover complexes. N_2 sorption studies showed that there were no surface area remained in TZ-LD samples. Because after diffusion, $[Fe(HB(pz)_3)_2]$ would be site on the surface of MOFs and block the channels of pores,

this would stopped outside molecules (like N_2 molecule) go through inside.

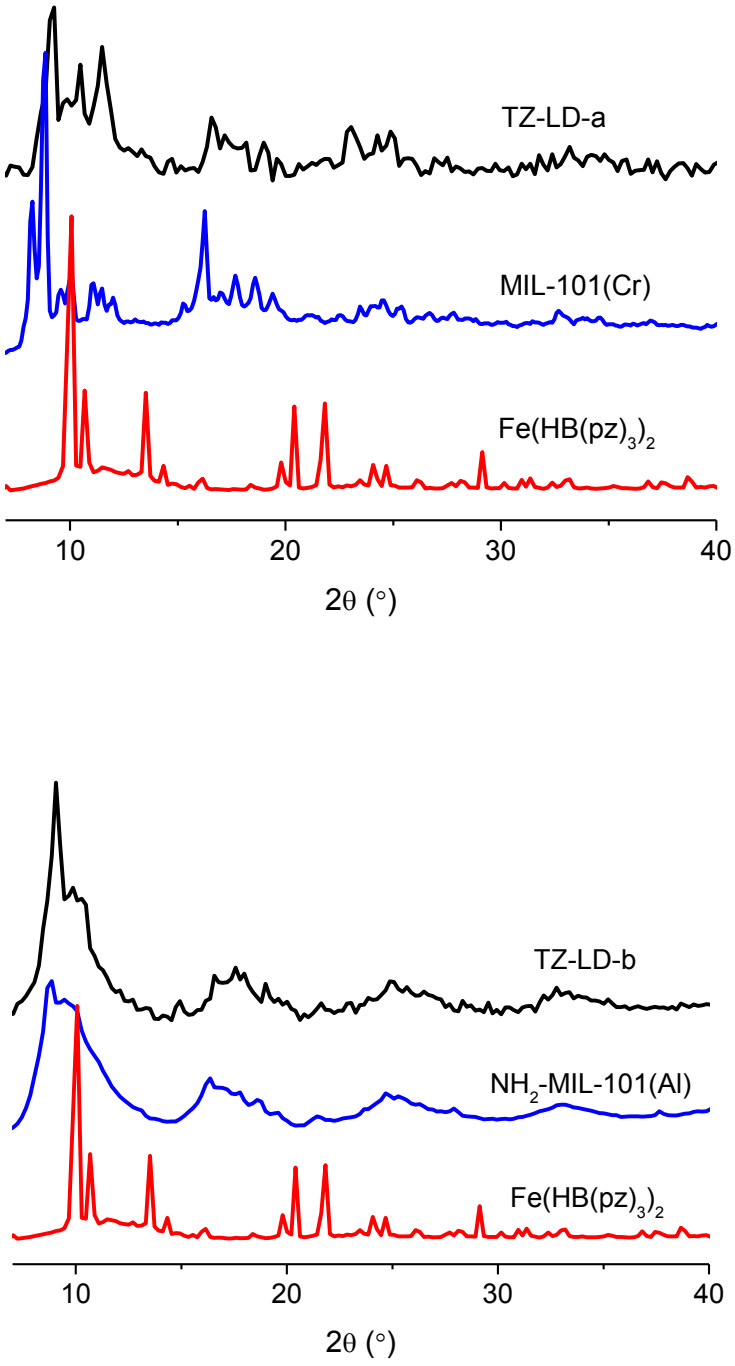

Figure 3.3. Powder X-ray diffractograms of TZ-LD-a and TZ-LD-b, the corresponded MOF host materials and $[Fe(HB(pz)_3)_2]$ were in comparison.

3.2. Gas Phase Diffusion

Similar to liquid phase diffusion, a series of gas phase diffusion experiments were carried out

by using different MOFs. TZ-GD-a, TZ-GD-b and TZ-GD-c were corresponding to MIL-101(Cr), NH_2-MIL-101(Al) and MIL-100(Al) respectively. With the prolonging of diffusion time, it was observed that the reddish $[Fe(HB(pz)_3)_2]$ was gradually disappeared, and then the colour of host materials were slowly turned to orange-red (Figure 3.4). It was disclosed that $[Fe(HB(pz)_3)_2]$ vapour had already slowly diffused into the host MOFs.

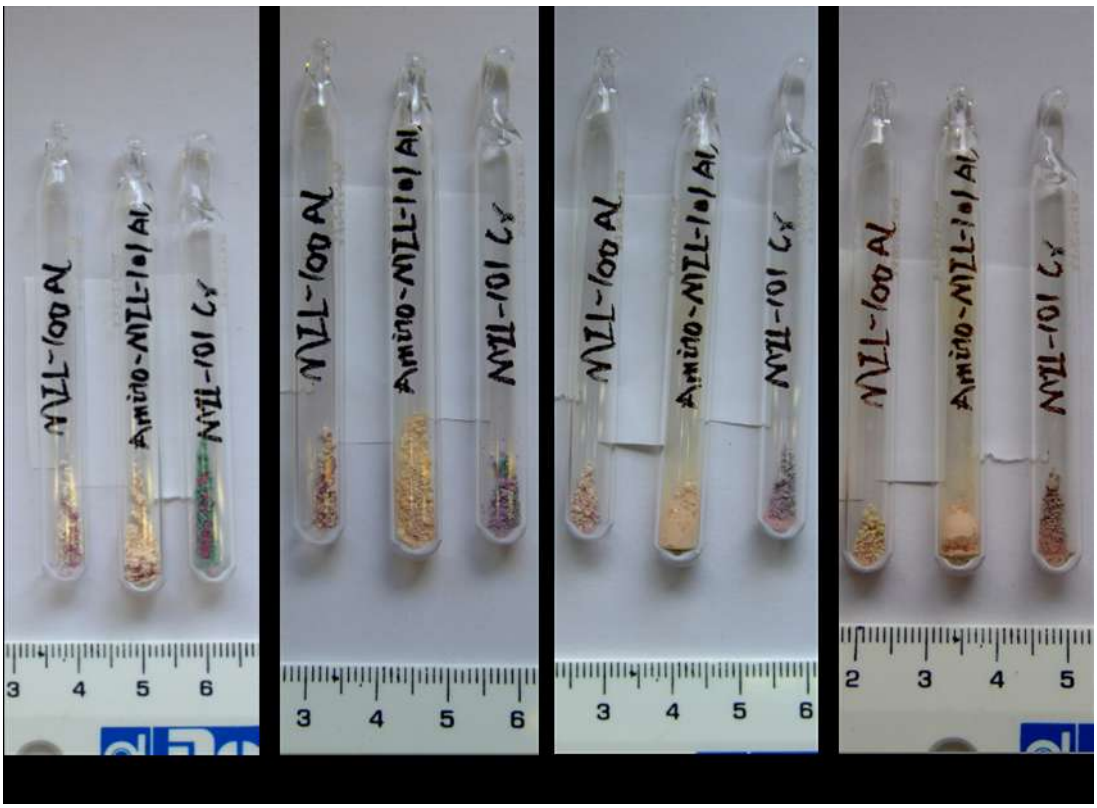

Figure 3.4. The color of each sample at starting, 4 h, 8 h and 24 h.

Unlike liquid phase diffusion, gas phase diffusion had no resistance from solvent molecules; hence, the results of gas phase diffusion experiments seem better. The products were monitored by IR spectra (Figure 3.5); with the comparison of IR spectra, it was found that, within IR 'fingerprint' region from 1000 cm-1 to 1200 cm-1, pure $[Fe(HB(pz)_3)_2]$ possessed two characterized peaks which was at 1041 cm-1 and 1109 cm-1. While on three host MOFs materials, there were no peak exist or with very weak peak in the corresponded region. For TZ-GD samples, these two characterized peaks at 1041 cm-1 and 1109 cm-1 were slight shifted to lower frequencies (typically 1021 and 1098 cm^{-1}).

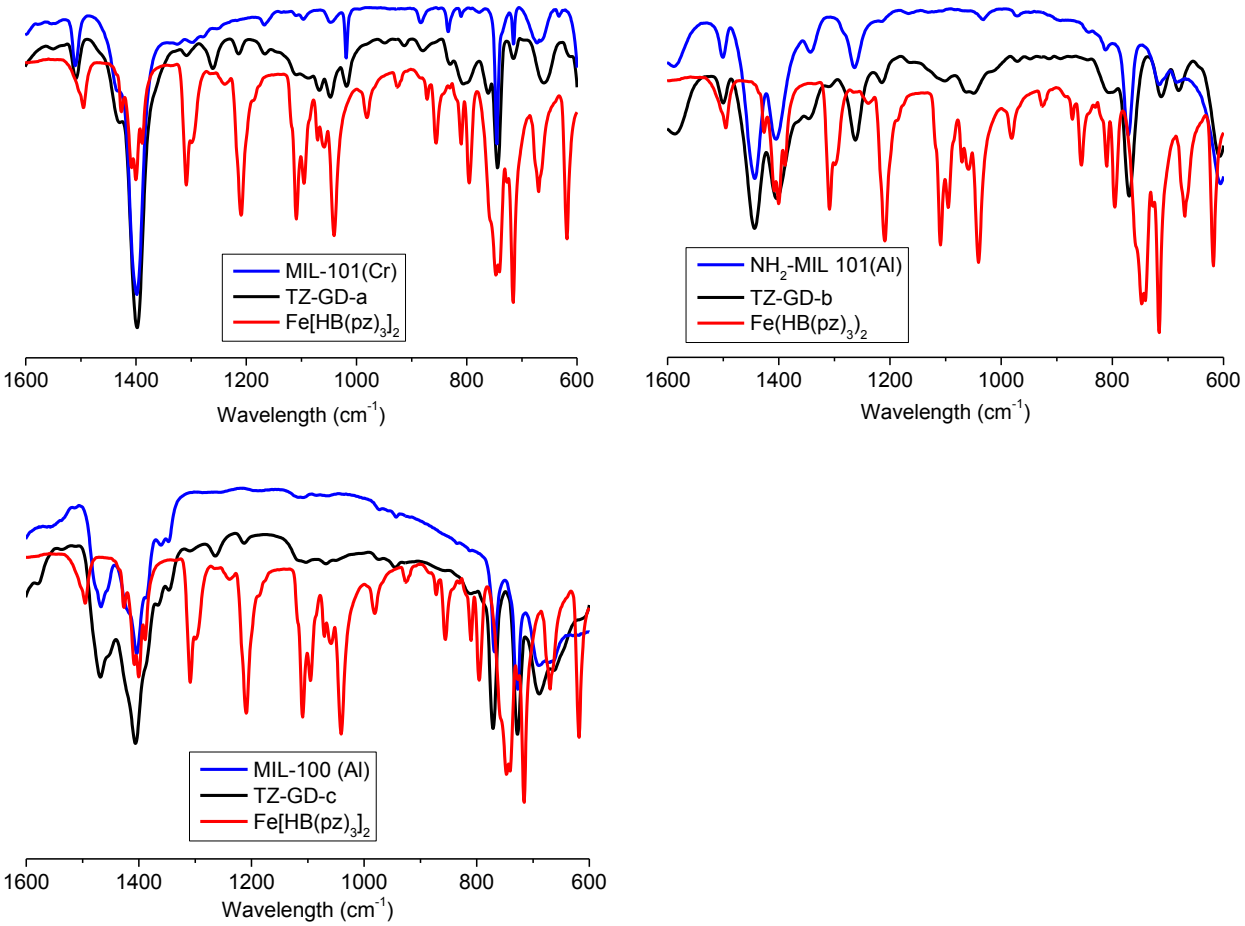

Figure 3.5. IR spectra of each sample in comparison to corresponding host MOFs and $[Fe(HB(pz)_3)_2]$.

The $[Fe(HB(pz)_3)_2]$ amount in the TZ-GD samples were calculated from the iron analysis by atomic absorption spectroscopy to 8.11 wt% for TZ-GD-a, 7.42 wt% for TZ-GD-b and 1.64 wt% for TZ-GD-c (Table 3.3) respectively. So the AAS results also supported that gas phase diffusion method was more efficient than liquid phase diffusion method on loading ratios. But the weight ratios of $[Fe(HB(pz)_3)_2]$ of TZ-GD samples were still not very high. To get higher loading of $[Fe(HB(pz)_3)_2]$, prolonging the diffusion time to 3 days also had investigated, but the AAS results showed that no significant improvement. Thus, we cannot obtain highly loaded samples just by diffusion methods.

Matching powder X-ray diffractograms (PXRD) of the pure $[Fe(HB(pz)_3)_2]$ and the TZ-GD samples confirms the spin crossover compound as a $[Fe(HB(pz)_3)_2]$@MOFs composite for TZ-GD-a and TZ-GD-b. The typical reflection from $[Fe(HB(pz)_3)_2]$ at $2\theta=10.07°$ had been found

both in TZ-GD-a and TZ-GD-b, it exhibited that, $[Fe(HB(pz)_3)_2]$ still had the same crystallized phase (Figure 3.6).

The pore size of MIL-100 (Al) was smaller than that of MIL-101(Cr) and NH_2-MIL-101(Al), therefore, the loading rate of TZ-GD-c was much lower. This perhaps was the reason why the PXRD patterns of TZ-GD-c and MIL-100(Al) were almost the same.

All of these analysis results supported that the gas phase of $[Fe(HB(pz)_3)_2]$ could more easily go through into the pores of MOFs by diffusion in vacuum condition. But the loading rate still not high and it also required skilled operation on glass melting work. Thus, gas phase diffusion is not ideal method to embed $[Fe(HB(pz)_3)_2]$ into MOFs.

N_2 sorption studies showed that there were also no surface area remained in all TZ-GD samples, which indicated that $[Fe(HB(pz)_3)_2]$ blocked the channels of pores.

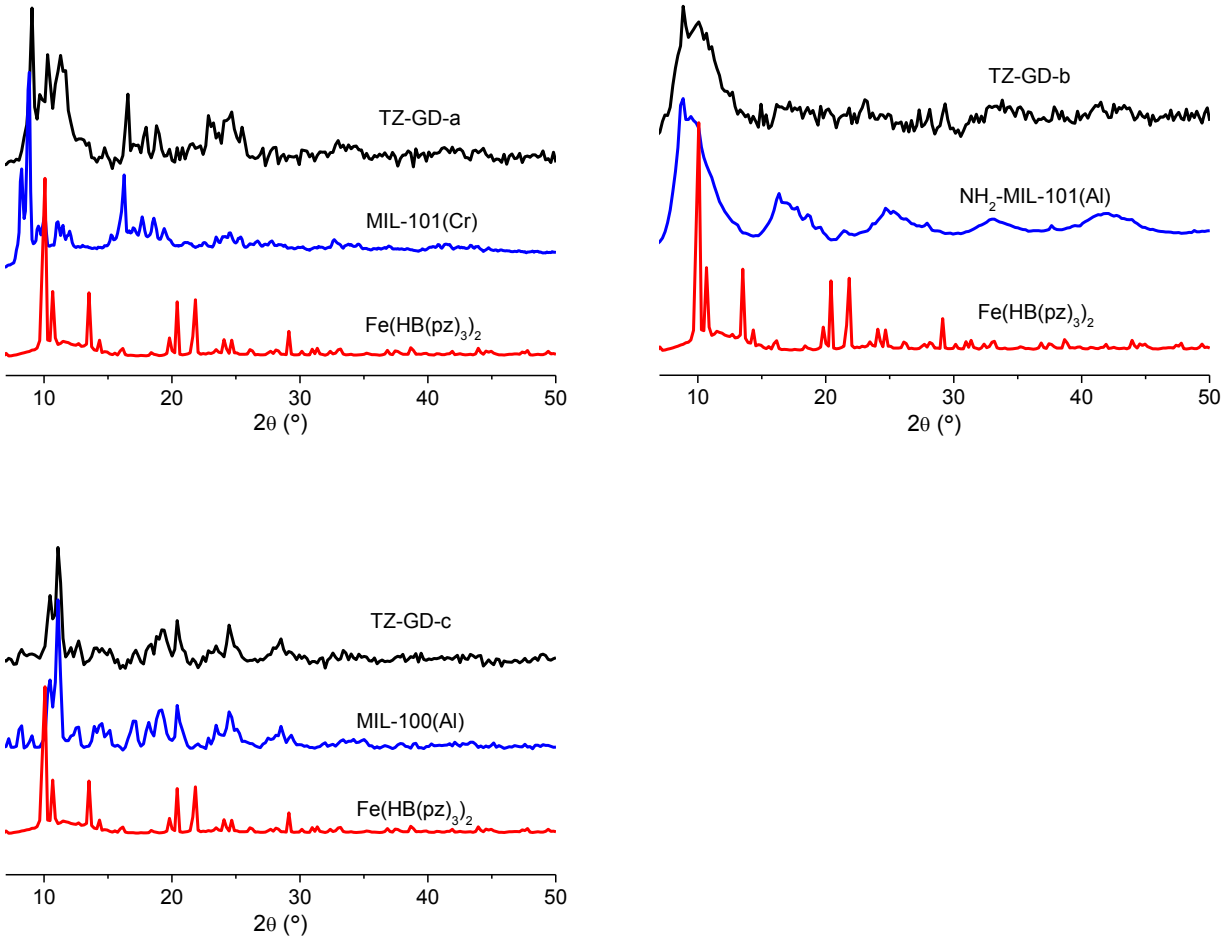

Figure 3.6. Powder X-ray diffractograms of TZ-GD samples, the corresponded MOF host materials and $Fe(HB(pz)_3)_2$ were in comparison.

Table 3.3. The weight ratios of Fe and $[Fe(HB(pz)_3)_2]$ of TZ-GD samples

Sample	Fe content (wt%)	$Fe(HB(pz)_3)_2$ content (wt%)
TZ-GD-a	0.94	8.11
TZ-GD-b	0.86	7.42
TZ-GD-c	0.19	1.64

3.3. Synthesis of $[Fe(HB(pz)_3)_2]$ in the pores of MOFs

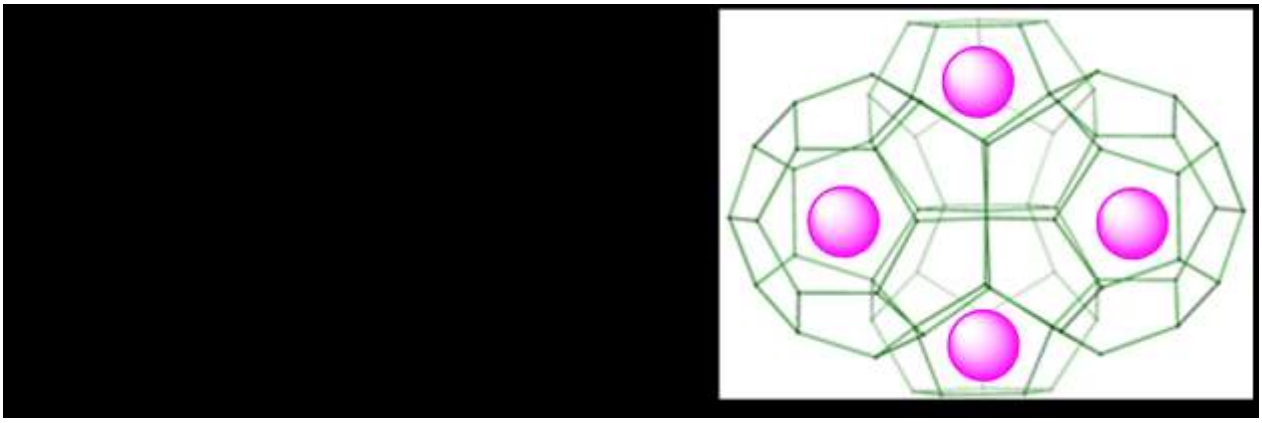

Scheme 3.3. Schematic drawing of synthesis of $[Fe(HB(pz)_3)_2]$ in the pores of MOFs (pink dots stands for $[Fe(HB(pz)_3)_2]$ molecules)

Because Fe(II) ions would be bonded with $-NH_2$ group of NH_2-MIL-101(Al), and then block the channel of NH_2-MIL-101(Al) to prevent the formation of $[Fe(HB(pz)_3)_2]$. Therefore, only MIL-101(Cr) and MIL-100(Al) were used as host materials in this part, the corresponded samples were named as TZ-SP-1and TZ-SP-2 respectively. Due to the presence of $[Fe(HB(pz)_3)_2]$, the changing of colour would be expected. In fact, TZ-SP-1 was a kind of grey powdered solid, while TZ-SP-2 was pale orange powder (Figure 3.7).

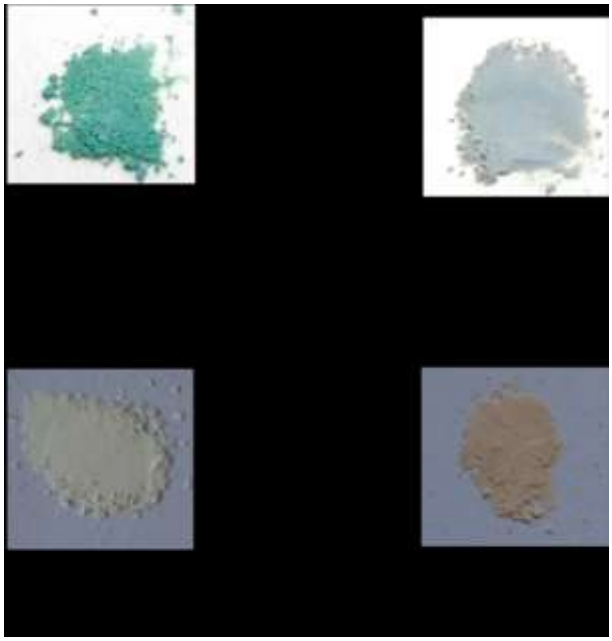

Figure 3.7. The comparison of colour of TZ-SP samples with that of corresponded MOF

The IR spectra in **Section 3.1 and Section 3.2** had already disclosed that, the content of $[Fe(HB(pz)_3)_2]$ would significant influence the IR pattern. If the content was too low, IR spectra of sample and corresponded host MOF would almost no variation, so the IR spectra could directly show the content of $[Fe(HB(pz)_3)_2]$ in samples in some extent. For TZ-SP samples, the main difference of IR patterns fell in the range from 1000 cm-1 to 1200 cm-1. Absolutely, there were several new peaks come out in this region (Figure 3.8, black curves), which indicated that $[Fe(HB(pz)_3)_2]$ was successfully synthesized in the pores of MOFs, and compare the heights of these new peaks with other ones, it was found that they were relatively high and this disclosed a relatively high loading of $[Fe(HB(pz)_3)_2]$. The iron analysis by atomic absorption spectroscopy showed that the spin-crossover compound amounts in the composites were 14.76 wt% for TZ-SP-1 and 10.10 wt% for TZ-SP-2 (see Table 3.4). So this time, the contents of $[Fe(HB(pz)_3)_2]$ were very high, and $[Fe(HB(pz)_3)_2]$ molecules probably successfully embedded in the pores of MOFs. Especially for MIL-100 (Al), in the diffusion experiment, $[Fe(HB(pz)_3)_2]$ cannot go through the pores due to its smaller pore size. But here, the loading is over 10 wt%, which indicate the high efficient of this method.

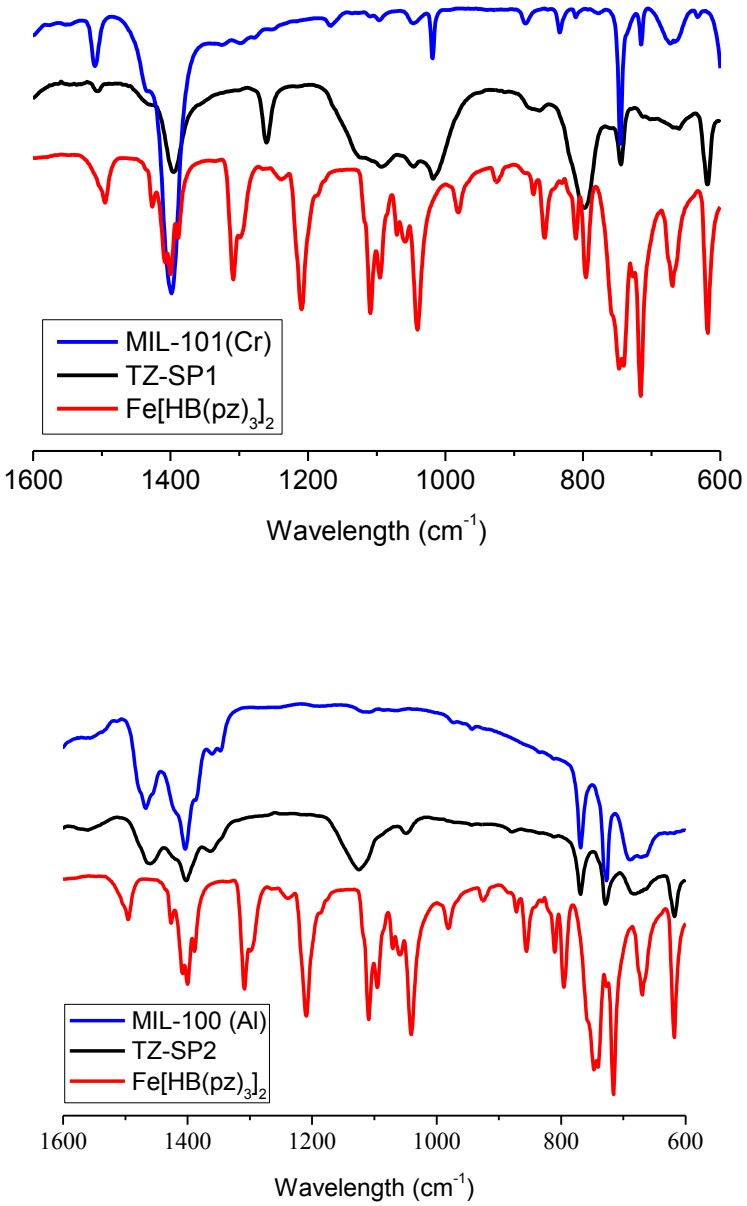

Figure 3.8. IR spectra of TZ-SP samples in comparison to corresponding host MOFs and $[Fe(HB(pz)_3)_2]$.

Table 3.4. The weight ratios of Fe and $[Fe(HB(pz)_3)_2]$ of TZ-SP samples

Sample	Fe content (wt%)	$Fe(HB(pz)_3)_2$ content (wt%)
TZ-SP-1	1.71	14.76
TZ-SP-2	1.17	10.10

$[Fe(HB(pz)_3)_2]$ gives rise to optical transitions from purple in the low-spin state (low temperature) to white in the high-spin state when increasing the temperature. Since the weight ratios of $[Fe(HB(pz)_3)_2]$ of TZ-SP samples were so high, it was interesting to see that, whether they would be change color with the rising of temperature. The samples were heated up to 200°C, but no changing of colour was observed.

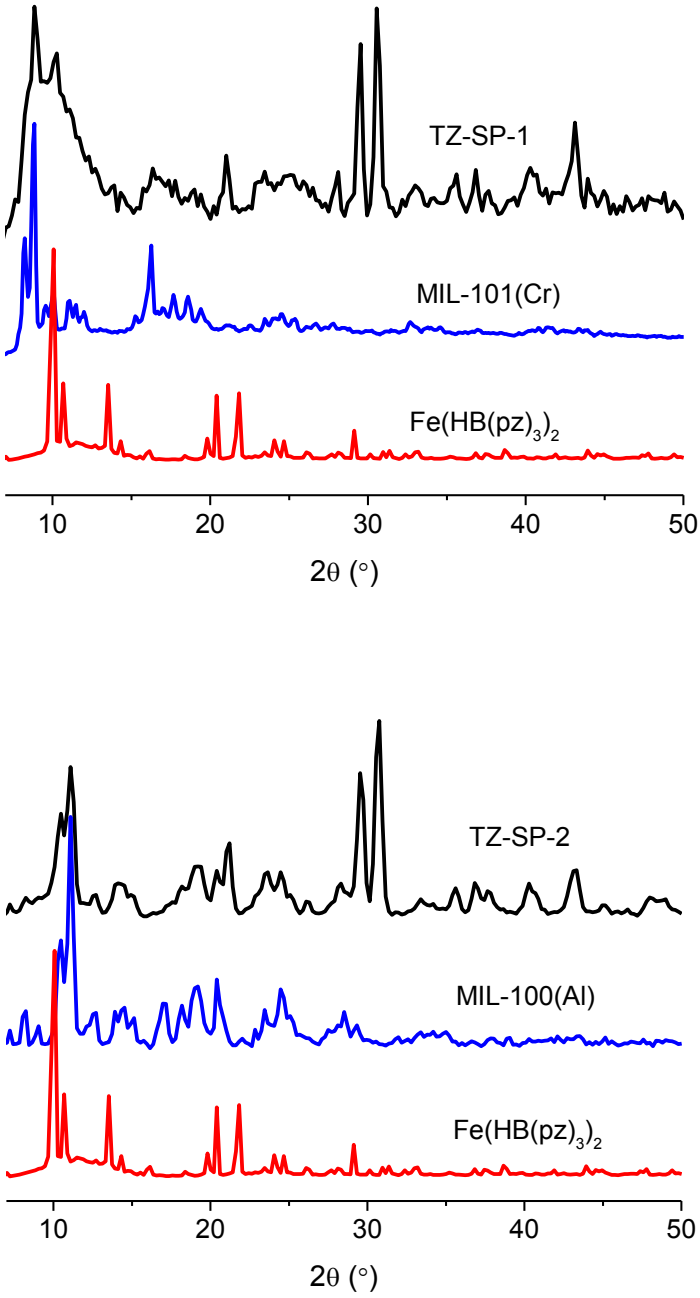

Figure 3.9. Powder X-ray diffractograms of TZ-SP samples, the corresponded MOF host materials and $[Fe(HB(pz)_3)_2]$ were in comparison.

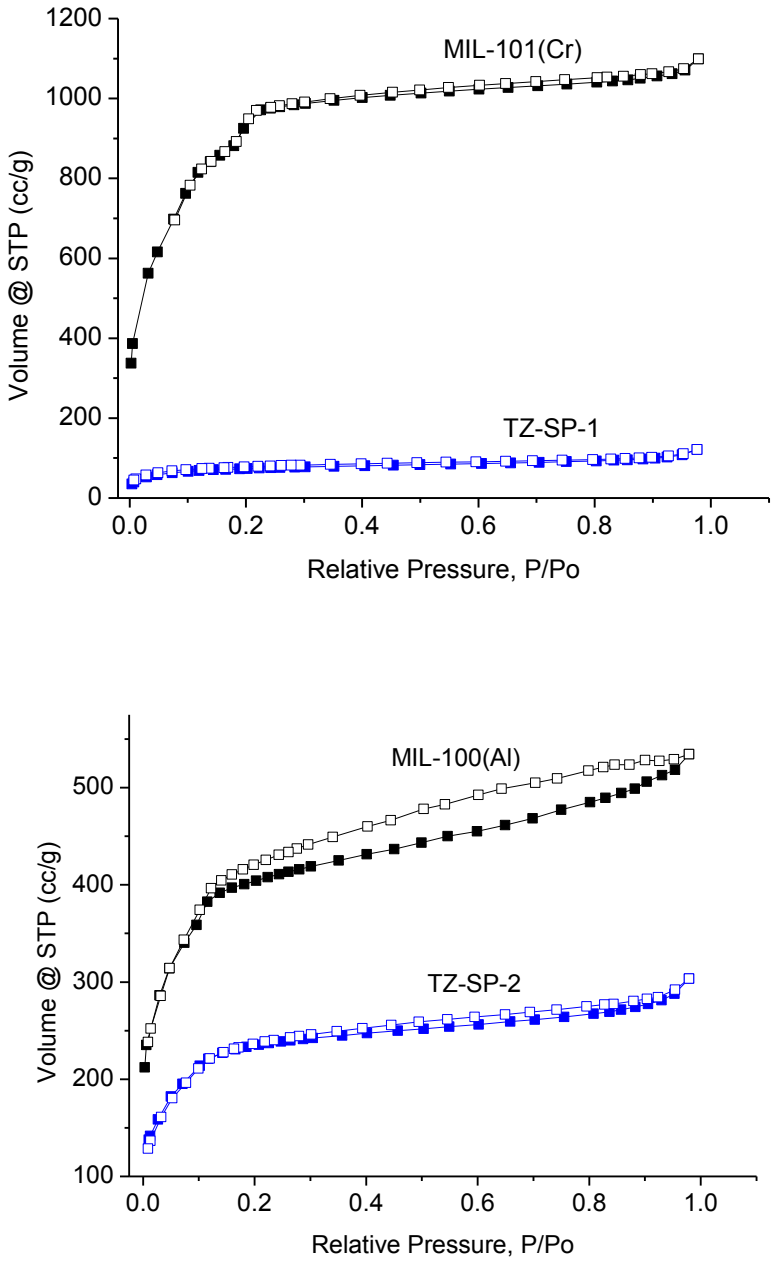

Figure 3.10. N_2 adsorption isotherms of TZ-SP samples in comparison to corresponded MOFs (solid symbols stand for adsorption curve, hollow symbols stand for desorption curve).

Powder X-ray diffraction (PXRD) measurements of TZ-SP samples showed significant change in comparison to their own corresponded MOF host materials (Figure 3.9). First, all the characterized reflection of MOF host materials could be easily observed in TZ-SP sample, it was disclosed that, the MOFs remained structurally robust after the synthesis procedure. Second, the typical reflection from $[Fe(HB(pz)_3)_2]$ at 10.07° also can be easily observed in both samples. But,

there were two new high reflections at 29.54° and 30.55° in both TZ-SP samples, while the corresponded positions of PXRD pattern of bulk-$[Fe(HB(pz)_3)_2]$ only possessed a small peak at 29.13°. Meanwhile, for both TZ-SP samples, there were several other observed reflections at 36.84°, 37.65°, 40.29° and 43.13°. These new reflections were not characteristic for bulk-$[Fe(HB(pz)_3)_2]$, which indicated that, $[Fe(HB(pz)_3)_2]$ were formed another crystalline phase in the pores of MOF host materials. The formation of mechanism of $[Fe(HB(pz)_3)_2]$ in the pores of MOF is to be disclosed in further investigations.

The remaining porosity of the composite materials was analyzed by N_2 sorption studies at 77 K (Figure 3.10). The sample was pre-treated before measurement by outgassing under vacuum at a temperature of 393 K for 2 h. For the composite materials, the Brunauer Emmett Teller (BET) and Langmuir surface areas have largely decreased. To TZ-SP-1, only 260 m²/g of BET surface area had been remained, compared to MIL-101(Cr) it decreased more than 90%. To TZ-SP-2, it still possesses 1009 m²/g of BET surface, which ascribe to the lower loading.

Table 3.5. Texture properties of TZ-SP samples and the corresponded MOFs.

Material	S_{BET} (m²/g)[a]	$S_{Langmuir}$ (m²/g)	V_{pore} (cm^3/g)[b]
MIL-101(Cr)	3450	4610	1.66
TZ-SP-1	260	350	0.167
MIL-100(Al)	1450	1880	0.802
TZ-SP-2	1009	1326	0.446

[a]Calculated in the pressure range $0.05 < p/p_0 < 0.2$ from N_2 sorption isotherm at 77 K with an estimated standard deviation of ± 50 m^2/g.

[b]Calculated from N_2 sorption isotherm at 77 K ($p/p_0 = 0.95$) for pores ≤ 20 nm

So finally, temperature-variable magnetic measurements of both composite materials have been carried out. According to the results, there is no spin transition behavior occurred for both samples. Both TZ-SP-1 and TZ-SP-2 remained in the low-spin state configuration in the whole range of temperature (Figure 3.11). We assume that, the $[Fe(HB(pz)_3)_2]$ was formed another crystalline phase in the pores of MOF material, and there is some unreacted reactant probably still

remained in the pores, which shut down the spin transition of TZ-SP samples. However, the specific reasons of the disappearance of spin transition still need further investigation.

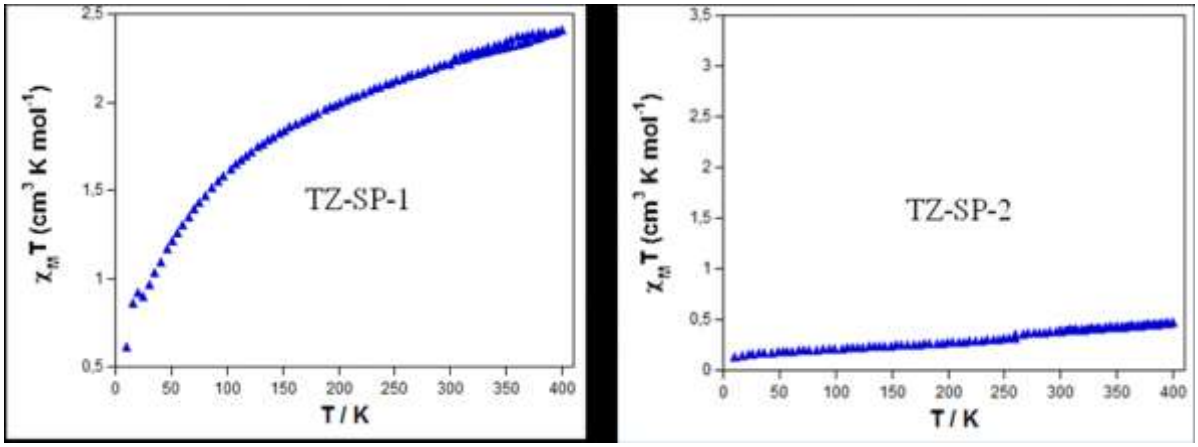

Figure 3.11. Temperature-variable magnetic curves for TZ-SP-1 and TZ-SP-2.

3.4. Synthesis of NH_2-MIL-101(Al) with the presence of $[Fe(HB(pz)_3)_2]$

The goal of the work is to investigate the influence of the confinement on the complex in the pores of a MOF. In the present case the porous material is NH_2-MIL-101(Al), which is a colorless and diamagnetic host, well-suited for optical and magnetic detection of the spin-crossover transition. NH_2-MIL-101(Al) with the empirical formula $[Al_3(\mu_3\text{-}O)(bdc)_3(OH)(H_2O)_2]$ is said to have the same structure as MIL-101(Cr), $[Cr_3(\mu_3\text{-}O)(bdc)_3(F,OH)(H_2O)_2]$.[253,164] NH_2-MIL-101(Al) is characterized by significant thermal (stable up to 650 K) and chemical stability and high porosity (S_{BET} up to 2100 m^2/g).[253] The decrease of the apparent specific surface area as well as total pore volume for the modified NH_2-MIL-101(Al) can be explained by the increased space demand of the amino group.[261]

The SCO-compound $[Fe(HB(pz)_3)_2]$[262,263] was loaded into NH_2-MIL-101(Al) via synthesis of the framework in the presence of the SCO-complex (Scheme 3.4). Three samples, using the same method but different amounts of $[Fe(HB(pz)_3)_2]$ starting material (50, 70 and 90 mg), were synthesized with an aim to check the variation of loading of the SCO compound. The iron complex is soluble in dichloromethane. Washing processes with acetone, dichloromethane and methanol ensured that no iron complex was left on the outside of the MIL crystals at the same time avoiding to remove the incorporated $[Fe(HB(pz)_3)_2]$. The washing procedure of the S@M

samples was different from bulk NH_2-MIL-101(Al) as it intended only to remove the externally adsorbed Fe complex. The approximated cylindrical size of the $[Fe(HB(pz)_3)_2]$ complex (height ~11.6 Å, diameter ~10.6 Å see Scheme 3.5) is probably slightly larger than the pore entrance for NH_2-MIL-101(Al) with the amino groups on the terephthalate ligand (cf. Figure 2.2, in **Chapter 2**). Hence, the Fe-complex molecules could not be washed out, even under the conditions of boiling the samples in MeOH and vacuum drying as part of the analytical sample preparation. The inclusion of the latter in the pores was proven by temperature- and solvent-adsorption induced color change, characteristic for the SCO transition.

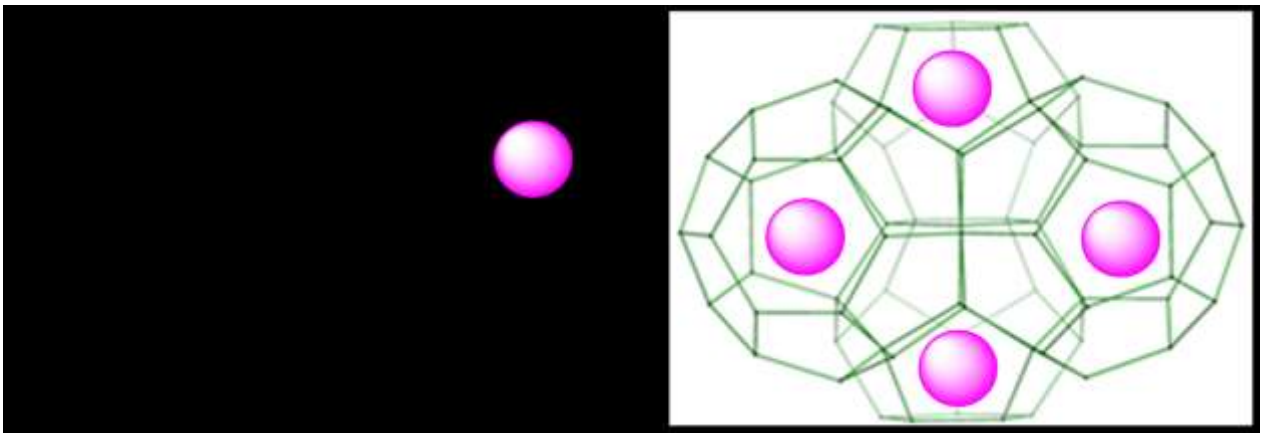

Scheme 3.4. Schematic drawing of synthesis of NH_2-MIL-101(Al) with the irreversible encapsulation of $[Fe(HB(pz)_3)_2]$ (red spheres stands for $[Fe(HB(pz)_3)_2]$ molecules).

At the beginning, after all reagents were dissolved in the DMF, the solution presented the wine-red colour of $[Fe(HB(pz)_3)_2]$. As the reaction proceeded, the red colour faded and the yellowish colour of bulk NH_2-MIL-101(Al) started to dominate (Figure 3.12). From the reaction mixture, the resulting yellowish powdered sample was separated by centrifugation. When the first sample was washed with methanol a surprising change of colour was detected: the yellow sample turned into dark red (Figure 3.12), which gave a serendipitous proof, that a solvent-adsorption spin transition could be triggered or induced. After multiple washings, additional purification in refluxing methanol and drying, the pure $[Fe(HB(pz)_3)_2]$@NH_2-MIL-101(Al) encapsulation product was separated. The addition of a range of polar or medium-to-low polar solvents (H_2O, MeOH, DMSO, DMF, BuOH, t-BuOH, THF, ethylacetate, CH_2Cl_2, CCl_4, toluene, mesitylene,

cyclohexane, hexane) induces an SCO at room temperature, with pronounced yellow to red color change (Figure 3.13). The solvent-adsorption induced color change was fully reversible, i.e., drying of the sample caused the return to yellow. The HS→LS SCO in the dried sample could also be triggered by immersing the sample into liquid nitrogen (Figure 3.13).

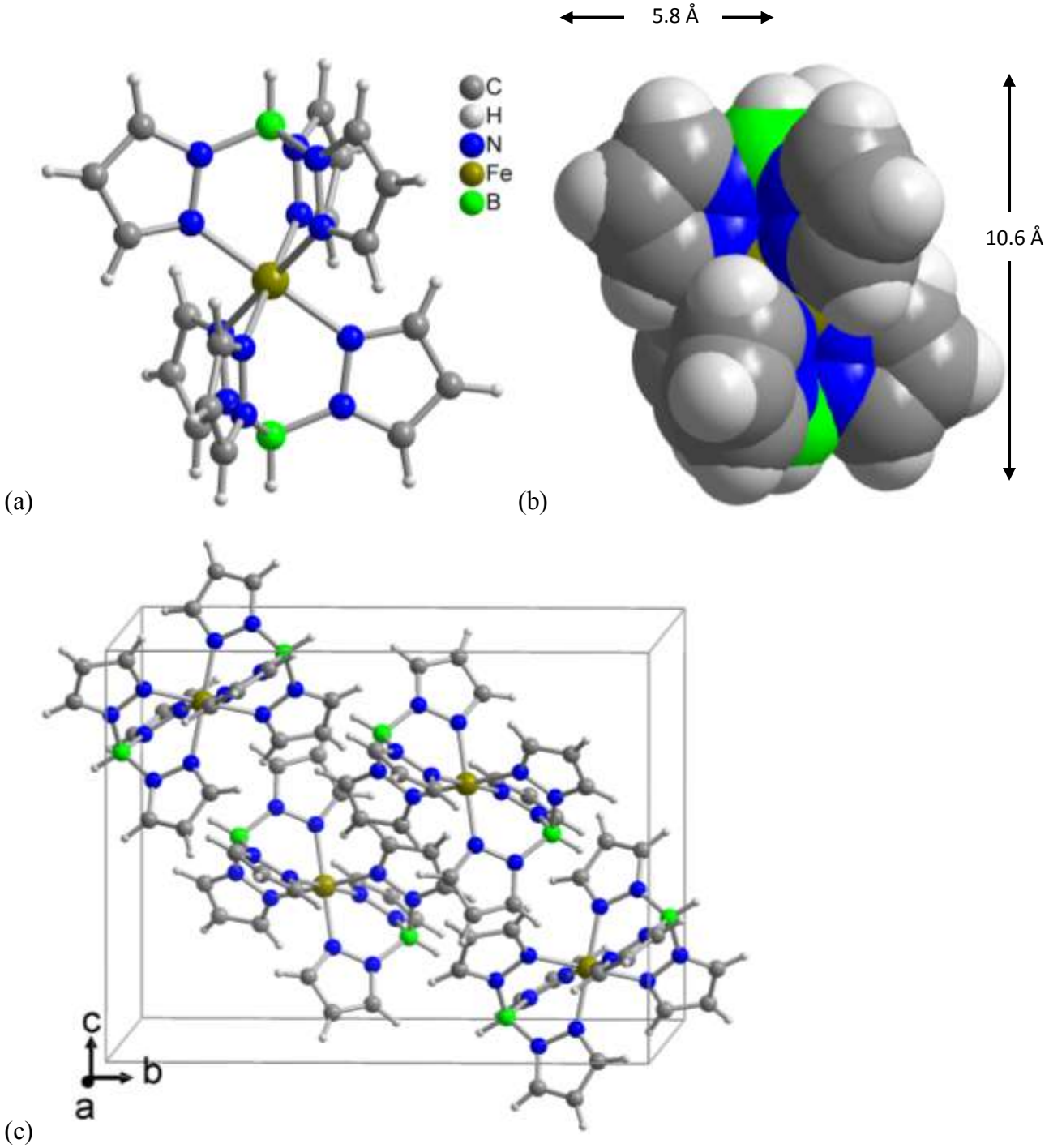

Scheme 3.5. Single-crystal X-ray structure of $[Fe(HB(pz)_3)_2]$ (Refcode HPZBFE03)[263];
(a) ball-and-stick presentation, (b) space-filling presentation of single molecule, (c) unit-cell packing.

Concerning the molecular volume of $[Fe(HB(pz)_3)_2]$ the shape of the molecule can be approximated by a cylinder with height of 10.6 Å and a radius of 5.8 Å (Fig. S1b).

The height is measured as the H(-B)...(B-)H distance of 8.16 Å with twice the van-der-Waals radius of H (2 x 1.2 Å = 2.4 Å) added to give10.6 Å.

The radius is estimated from the 4-H(-C)...B distance of 4.60 Å with the van-der-Waals radius of H (1.2 Å) added to give 5.8 Å.

The volume of this cylinder (π r^2 x h) is then 3.14 x $(5.8)^2$ x 10.6 $Å^3$ = 357 $Å^3$ which is seems less than the molecular volume estimated from the unit cell volume of 2157.85(78) $Å^3$of one of the single-crystal X-ray structures of $[Fe(HB(pz)_3)_2]$with Z = 4: 2158 / 4 = 540 $Å^3$.

Yet, the packing coefficients for the majority of molecular crystals are between 0.65 and 0.77 as for the close-packing of spheres and ellipsoids.[264]

The ratio of 357 / 540 = 0.66 is in the range of typical packing coefficients.

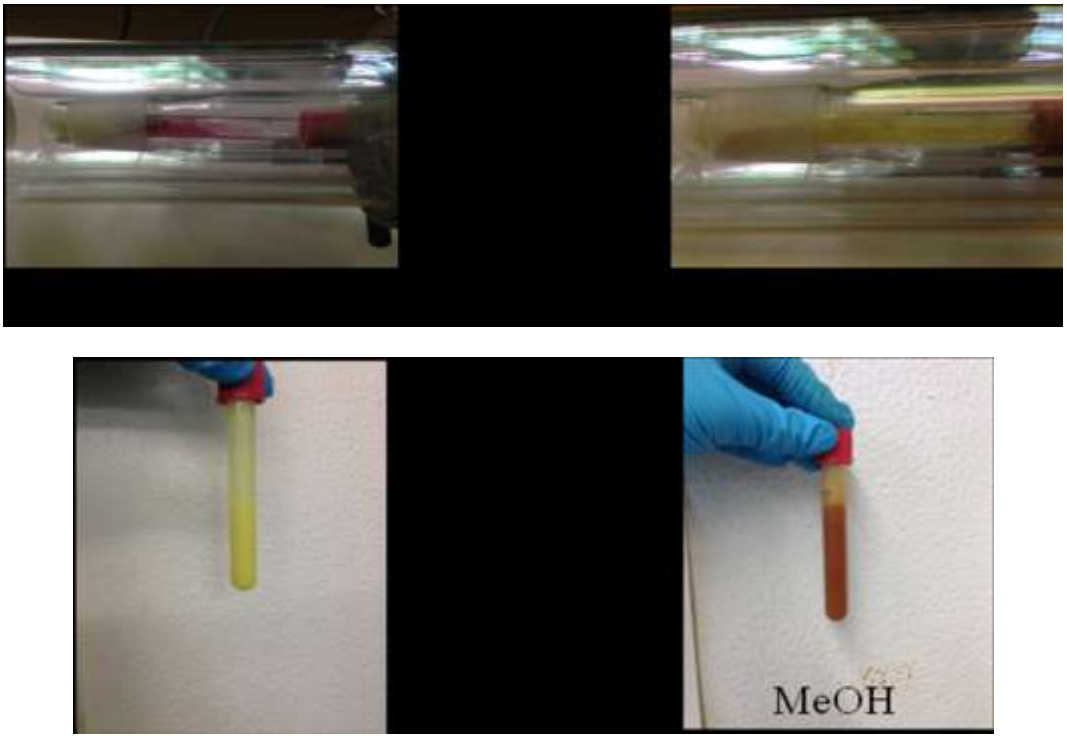

Figure 3.12. The photos of solution with the reaction proceeding for color comparison (Top). Photos of the $[Fe(HB(pz)_3)_2]$@NH_2-MIL-101(Al) sample (Bottom left) with methanol added (Bottom right) for color comparison.

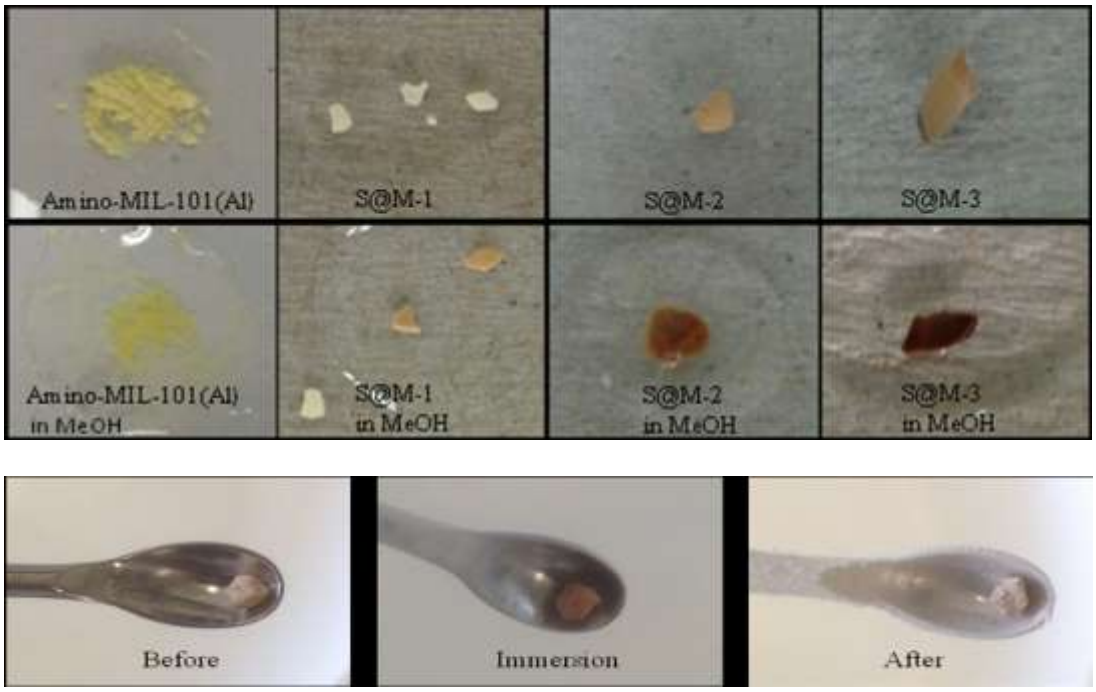

Figure 3.13. The solvent-absorption triggered- (top) *vs* temperature induced (bottom) colour change associated with the SCO transition.

Table 3.6. The content of $[Fe(HB(pz)_3)_2]$ in the samples.[a]

SCO@NH_2-MIL-101(Al)	$[Fe(HB(pz)_3)_2]$[b] (mg)/(mmol)	Al : Fe (molar ratio)[c]	Fe content by AAS (wt%)	calc. $[Fe(HB(pz)_3)_2]$ content (wt%)[d]	Al : Fe (molar ratio)[f]
S@M-1	50/0.10	1 : 0.43	0.61 %	5.26 %	1 : 0.028
S@M-2	70/0.15	1 : 0.61	1.31 %	11.31 %	1 : 0.063
S@M-3	90/0.19	1 : 0.78	1.18 %	10.18 %	1 : 0.056
S@M-1 [e]	50/0.10	1 : 0.43	0.62 %	5.35 %	1 : 0.028
S@M-2 [e]	70/0.15	1 : 0.61	1.29 %	11.13 %	1 : 0.062
S@M-3 [e]	90/0.19	1 : 0.78	1.14 %	9.84 %	1 : 0.054

a - each sample was dried in the vacuume oven (120 °C, 12 mbar) for 2 h before AAS analysis.
b- Amount of $[Fe(HB(pz)_3)_2]$ used in S@M synthesis with 57 mg (0.24 mmol) of aluminum chloride hexahydrate ($AlCl_3 \cdot 6H_2O$) and 61 mg (0.34 mmol) of 2-aminoterephthalic acid.
c - the initial molar ratio of Al : Fe in the synthesis.
d -.Fe content in $[Fe(HB(pz)_3)_2]$, $C_{18}H_{20}B_2N_{12}Fe$ (481.91 g/mol) is 11.59%
e -repeated Fe analysis after the samples were dried at 120°C and $<10^{-6}$ Torr for an additional 4 h.
f - the molar ratio of Al : Fe in the S@M composite.

The iron content of the samples was determined using atomic absorption spectrometry (Table 3.6). Repeated Fe analyses are reproducible within experimental error.

It is evident that from the offered $[Fe(HB(pz)_3)_2]$ amount during synthesis only about 10% or less is incorporated in the formed S@M composite when looking at the possible and the obtained molar Al : Fe ratio. When increasing the starting amount of $[Fe(HB(pz)_3)_2]$ from 50 to 70 mg the incorporated Fe amount more than doubles, that is, S@M-2 contains 2.25-fold the $[Fe(HB(pz)_3)_2]$ amount of S@M-1. A further attempted increase in Fe loading upon increasing the available $[Fe(HB(pz)_3)_2]$ amount to 90 mg did not happen and S@M-3 contains even slightly less encapsulated iron compared to S@M-2. In a molar ratio S@M-2 corresponds to the formula $\{0.19[Fe(HB(pz)_3)_2]°·°[Al_3(\mu_3\text{-}O)(NH_2\text{-}bdc)_3(OH)(H_2O)_2]\}$, S@M-1 and S@M-3 correspond to 0.08 and 0.17 Fe-complex molecules per Al_3OL_3 moiety respectively.

From the dimensions of the cyclindrical-shaped molecular structure (Scheme 3.5b) a molecular volume for the van-der-Waals surface of 357 $Å^3$ can be estimated (see above). Based on the unit cell volume of 2157.85(78) $Å^3$ of one of the single-crystal X-ray structures of $[Fe(HB(pz)_3)_2]$ with Z = 4 (Refcode HPZBFE03)[263] a volume of ~540 $Å^3$ can be estimated for the packing of adjacent single $[Fe(HB(pz)_3)_2]$ molecules (Scheme 3.5). The ratio of 357 / 540 = 0.66 is in the range of typical packing coefficients (0.65-0.77) for molecular structures.[264]

The total pore volume of bulk NH_2-MIL-101(Al) synthesized here was calculated from the N_2 adsorption isotherm to 1.16 cm^3/g (Table 3.7). From the total pore volume we have to deduct the pore volume of ~0.07 cm^3/g for micropores with $d \leq 1$ nm (10 Å) obtained from the CO_2 NL-DFT model (Table 3.7). In view of the molecular dimensions of the iron complex cylinder with diameter ~11.6 Å and height ~10.6 Å these micropores with not be accessible by the complex. This leaves about 1.09 cm^3/g or $1.09·10^{24}$ $Å^3/g$ to be filled by $[Fe(HB(pz)_3)_2]$ molecules.

This corresponds to $1.09·10^{24}$ $Å^3/g$: 540 $Å^3$/molecule = $2·10^{21}$ Fe comples molecules/g(MIL) or when divided by $6.022·10^{23}$ (molecules) mol^{-1} to $3.3·10^{-3}$ mol(Fe complex)/g(MIL). With the molar mass of 481.91 g/mol for $[Fe(HB(pz)_3)_2]$ this gives a maximal possible loading of 1.6 g(Fe complex)/g(MIL) or 1.6/(1.6+1) = 61%.

This value can also be derived by multiplying the pore volume of 1.09 cm^3/g with the crystal density of the Fe complex of 1.483 g/cm^3 to give 1.61 g (Fe complex)/g(MIL).

The achieved highest incorporation of ~0.11 g (Fe complex) / g (MIL) or ~11 wt% (Table 3.6) seems much less than the 61% calculated possible loading.

It must be kept in mind, however, that MOF formation depends also on the templating action of a suitable solvent, such as DMF, which is initially incorporated in the pores. In addition, free ligand or smaller metal-ligand units can be included in the pores. High-boiling solvents like DMF together with residual precursor must be removed by usually tedious washing procedures to activate, that is, achieve a porous material. Here, washing of bulk NH_2-MIL-101(Al) was carried out with DMF followed by drying at 25 °C for 16 h and also under vacuum (10^{-3} Torr) at 120 °C for at least 2 h, prior to the N_2 gas adsorption measurement from which the pore volume is derived.

When forming the S@M samples, the $[Fe(HB(pz)_3)_2]$ complex probably cannot play the role as a sole template for NH_2-MIL-101(Al) and the concomitant inclusion of DMF into the pores is still required. Secondly, together with DMF and the Fe-complex also residual precursor may be included. The presence of minor amounts of terephthalic acid in the pores of $[Fe(HB(pz)_3)_2]$@NH_2-MIL-101(Al) cannot be ruled out even if NH_2-MIL-101(Al) is synthesized in DMF, which is a good solvent for terephthalic acid. The apparently found loading maximum of ~11 wt% included iron complex must be judged against this MOF crystallization process.

Scanning electron microscopy (SEM) images (Figure 3.14) show the morphology of NH_2-MIL-101(Al) with irregular particles, which is highly agreement with the reported literature.[265] And all the morphology of S@M composite is similar to native NH_2-MIL-101(Al). This supports that the SCO compound is inside the pores of NH_2-MIL-101(Al).

The PXRD patterns of all the samples match very well the pattern of the NH_2-MIL-101(Al) reference sample, synthesized under the same conditions, but without the addition of the iron complex (Figure 3.15). The results demonstrated convincingly that the addition of the iron complex does not hinder the crystallization. The absence of additional peaks compared to the reference confirms that there is no crystalline $[Fe(HB(pz)_3)_2]$ phase present, thus, confirming the encapsulation of the $[Fe(HB(pz)_3)_2]$ molecules without crystallization in the pores, as the long-range order is evidently absent. The non-crystalline order in the pores is typical for MOFs with large porosity, e.g., the non-washed MIL-101(Cr) material does not reveal any additional peaks compared to the washed variant. The presence of minor amounts of terephthalic acid in the

pores of $[Fe(HB(pz)_3)_2]$@NH_2-MIL-101(Al) cannot be ruled out but NH_2-MIL-101(Al) is synthesized in DMF, which is a good solvent for terephthalic acid. The adsorption of the apolar $[Fe(HB(pz)_3)_2]$ complex is in accordance with the presence of hydrophobic areas in NH_2-MIL-101(Al) even if the amino groups decreases the difference compared to MIL-101(Cr).

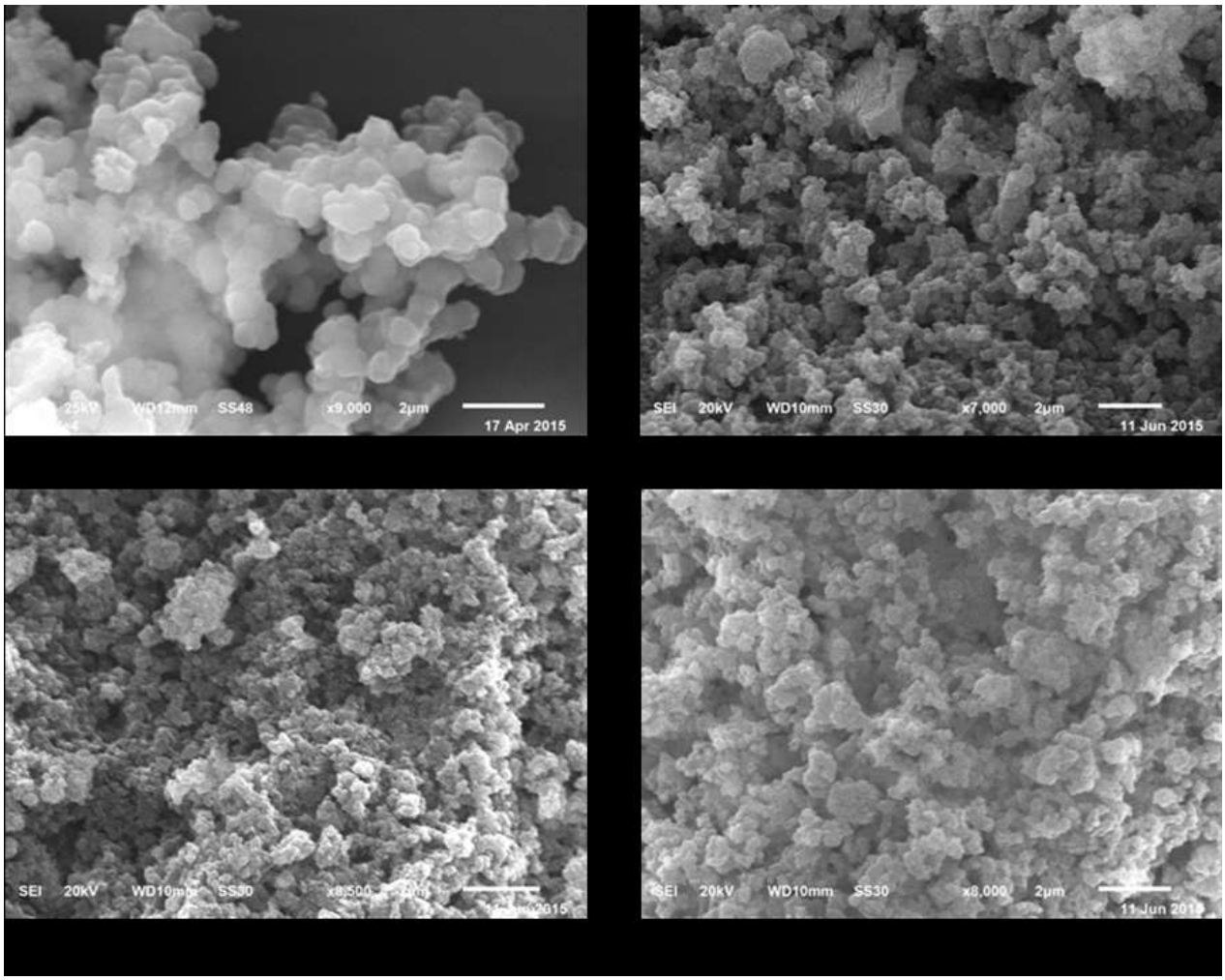

Figure 3.14. The SEM images of S@M materials in comparison with NH_2-MIL-101(Al).

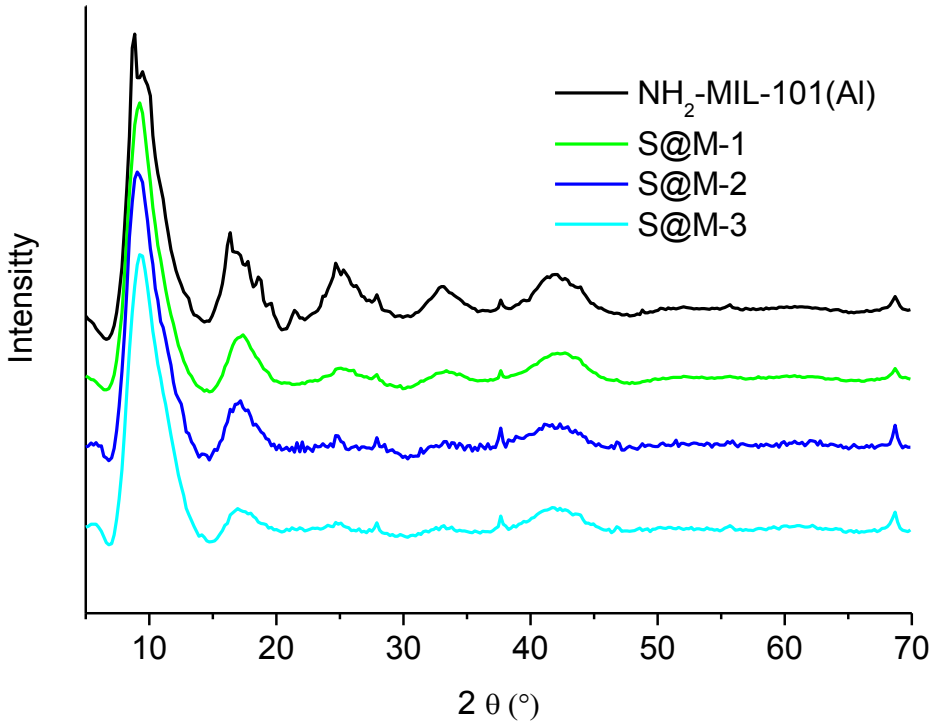

Figure 3.15. PXRD patterns for the three samples of $[Fe(HB(pz)_3)_2]$@NH_2-MIL-101(Al) (differing in Fe-complex loading) in comparison with the NH_2-MIL-101(Al) reference.

Comparison of the IR spectra of the S@M-n samples and $[Fe(HB(pz)_3)_2]$ also confirms encapsulation (Figure 3.16). The 1000-1200 cm^{-1} IR 'fingerprint' region gives clear evidence to a complex profile for the iron complex and is absent for the non-loaded MIL matrix. The two main peaks of the bulk $[Fe(HB(pz)_3)_2]$ in that region at 1041 cm^{-1} and 1109 cm^{-1} are slightly shifted to lower frequencies (typically 1021 and 1098 cm^{-1}) for all products of encapsulation (Figure 3.16, Top). The characteristic peak of BH at 2483 cm^{-1} for bulk $[Fe(HB(pz)_3)_2]$ is also shifted to lower frequency, for S@M-1 is at 2387 cm^{-1}, for S@M-2 is at 2361 cm^{-1}, and for S@M-3 is at 2388 cm^{-1} (Figure 3.16, Bottom). This low-frequency shift may be due to hydrogen bonding to surrounding carboxylate acceptors or DMF molecules

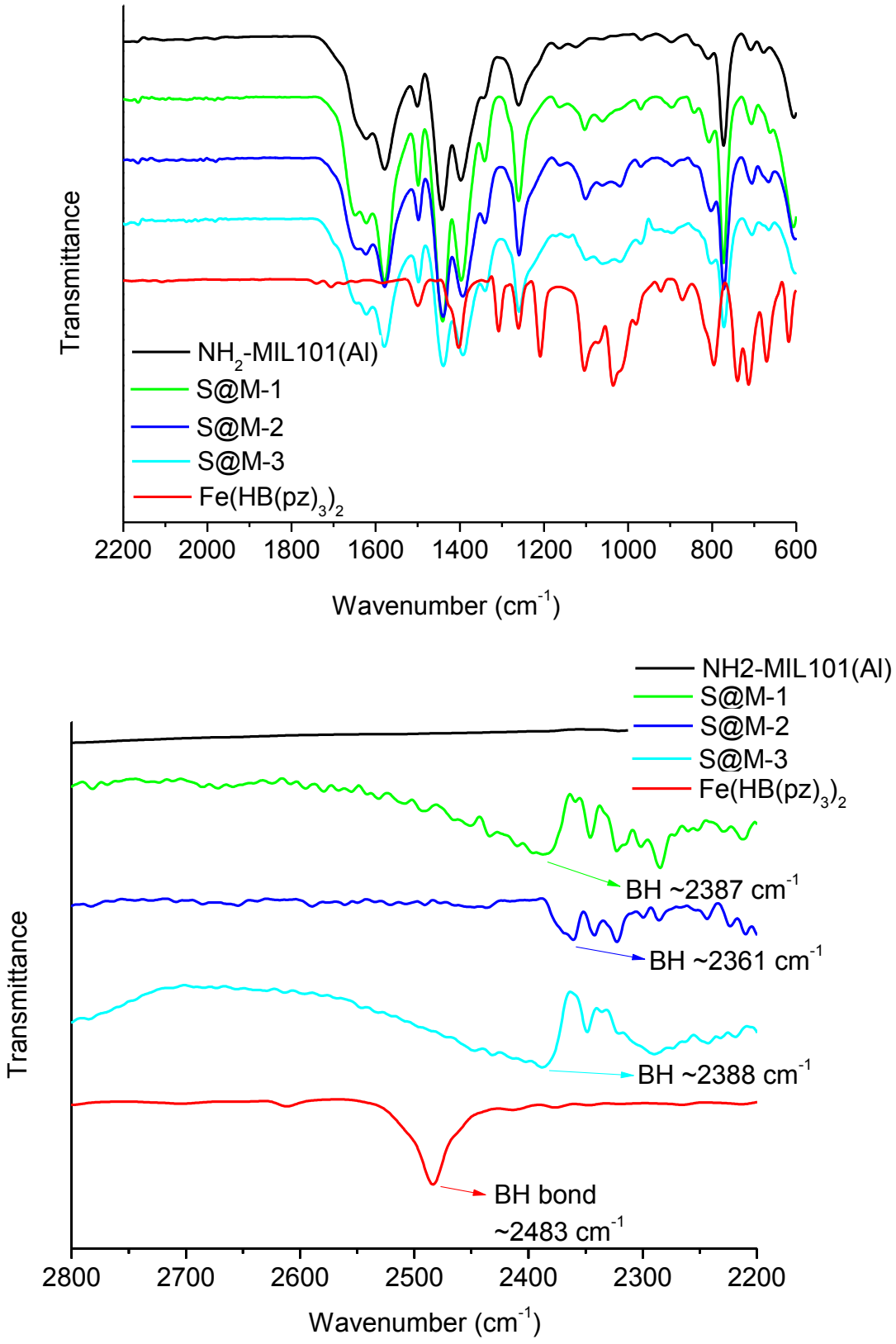

Figure 3.16. IR spectra of S@M samples in comparison with pure NH_2-MIL-101(Al) and $[Fe(HB(pz)_3)_2]$.

The residual porosity of the SCO@NH_2-MIL-101(Al) composite materials was analyzed by means of gas sorption studies. N_2 sorption at 77 K after degassing in vacuum at 393 K for 2 h indicated a very low uptake, of generally less than 10% of the non-loaded NH_2-MIL-101(Al) (Figure 3.17; Table 3.7).

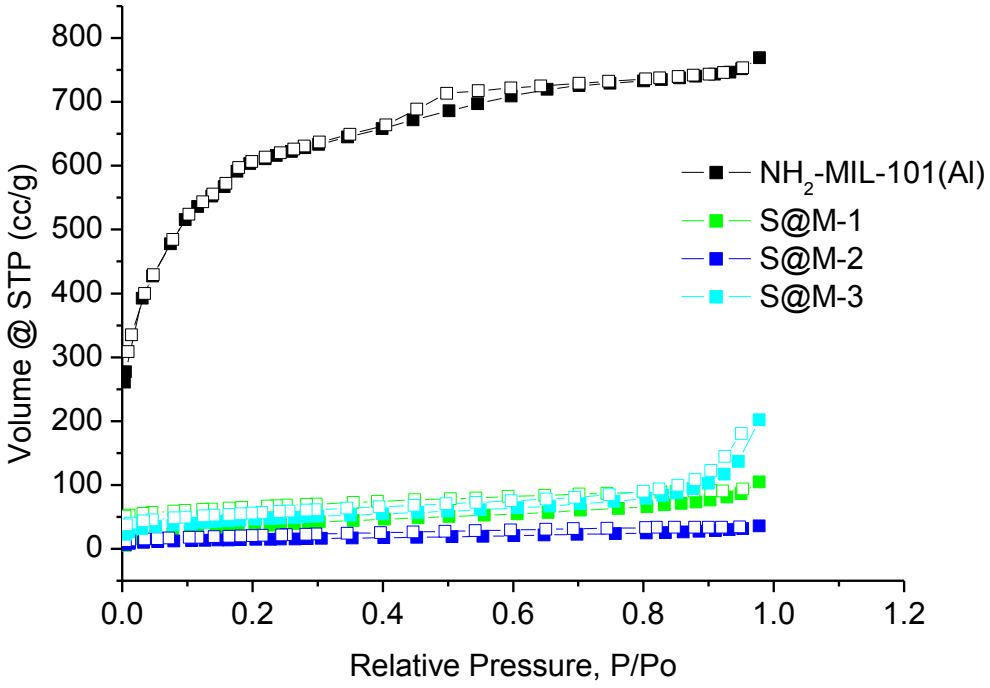

Figure 3.17. N_2 adsorption isotherms of S@M-n samples in comparison with NH_2-MIL-101(Al) (solid symbols stand for adsorption curve, hollow symbols stand for desorption curve).

Table 3.7. Texture properties of NH_2-MIL-101(Al) and SCO@ NH_2-MIL-101(Al) samples

Material	S_{BET} (m^2/g)[a]	$S_{Langmuir}$ (m^2/g)	V_{pore} (cm^3/g)[b]	$V_{micro}(CO_2)$[c] (cm^3/g)
NH_2-MIL-101(Al)	2220	2890	1.16	0.06781
S@M-1	150	210	0.133	0.04366
S@M-2	50	70	0.0488	0.02949
S@M-3	170	230	0.212	0.03323

[a]Calculated in the pressure range $0.05 < p/p_0 < 0.2$ from N_2 sorption isotherm at 77 K with an estimated standard deviation of ± 50 m^2/g.
[b]Calculated from N_2 sorption isotherm at 77 K ($p/p_0 = 0.95$).
[c] Pore volume for pores with d ≤ 1 nm (10 Å, cf. Figure 3.18) from the CO_2 NL-DFT model at 273 K.

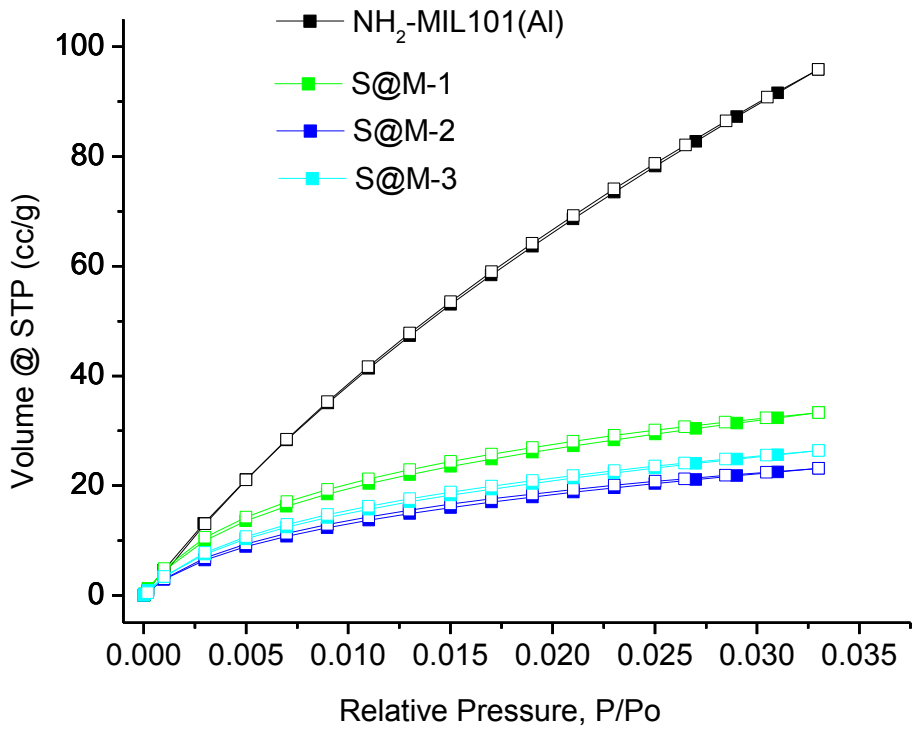

Figure 3.18. CO_2 adsorption isotherms of S@M-n samples in comparison with NH_2-MIL-101(Al) (solid symbols stand for adsorption curve, hollow symbols stand for desorption curve).

Concerning pore size analysis, at the cryogenic temperature of 77 K diffusion of N_2 molecules into micropores and ultramicropores (pores smaller than 7 Å) is very slow and influences adsorption.[311] For porous materials which contain ultramicropores, this would require time-consuming N_2 adsorption measurements and may still lead to under-equilibration of the adsorption isotherms, hence, will give erroneous results of the pore volume and pore size distribution analysis. Such problems can be eliminated by using CO_2 adsorption analysis at 273 K. The saturation pressure of CO_2 at 0 °C is ~26141 Torr and low relative pressure measurements necessary for micropore analysis are achieved in the range of moderate absolute pressures (1–760 Torr).[315] At 273 K and under higher absolute pressures CO_2 molecules can more easily access ultramicropores than N_2 at ~77 K and the kinetic diameter of CO_2 (3.3 Å) is also slightly smaller than for N_2 (3.64 Å). CO_2 micropore analysis at 273 K versus N_2 analysis at 77 K yields (i) faster analysis and (ii) greater confidence that measured adsorption points are equilibrated (both due to higher diffusion rates) and (iii) extension of the range of analysis to pores of smaller sizes that are

accessible to CO_2 molecules but not to N_2.[316]

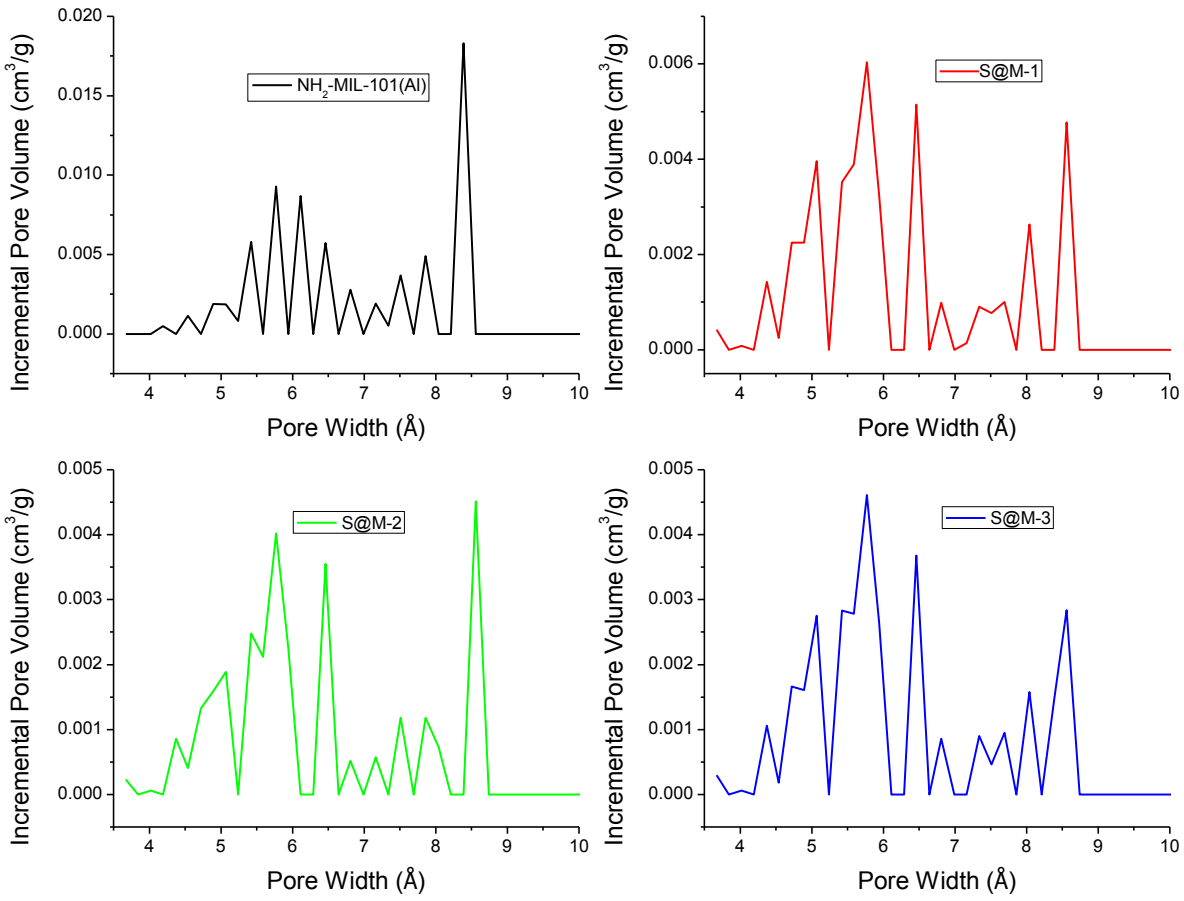

Figure 3.19. NLDFT pore size distribution (PSD) curves of NH_2-MIL-101(Al) and S@M materials from CO_2 adsorption (at 273 K) isotherms

CO_2 adsorption reflects relatively uniform residual free volume for all the samples, with the most porous sample being S@M-1 with the lowest Fe loading (Figure 3.18). The difference of adsorption behavior could be explained by pore clogging of the host matrix by the large molecules of the $[Fe(HB(pz)_3)_2]$ complex, which forms a barrier for the N_2 molecules (3.64 Å kinetic diameter) at 77K,[266] but not for CO_2 molecules (3.3 Å kinetic diameter) at 273K (see above). Aside of size-exclusion and temperature factors, CO_2 has specific affinity to the basic amino groups of the framework, which favors pore 'deblocking'. The comparison of CO_2 adsorption values also confirms the hypothesis that in both S@M-2 and S@M-3 practically full loading is reached, and the slightly higher adsorbed amount in the latter case is consistent with

the lower iron content. From CO_2 adsorption isotherms at 273 K (Figure 3.18), the pore size distribution (PSD) for S@M was derived between 4–10 Å by using nonlocal density functional theory (NLDFT) with a ‘‘slit-pore model’’ (Figure 3.19). CO_2 adsorption with the NLDFT model yields a better resolved PSD towards the ultramicropore end than from N_2 adsorption isotherms for S@M materials (Figure 3.20). From comparison, the larger 8-10 Å pore size of NH_2-MIL-101(Al) has decreased in its relative contribution in the Fe-loaded samples and only the smaller 4-7 nm pores have remained at the same value of the incremental pore volume. Here the three S@M materials give very similar pore size distributions for pores below 10 Å (1 nm).

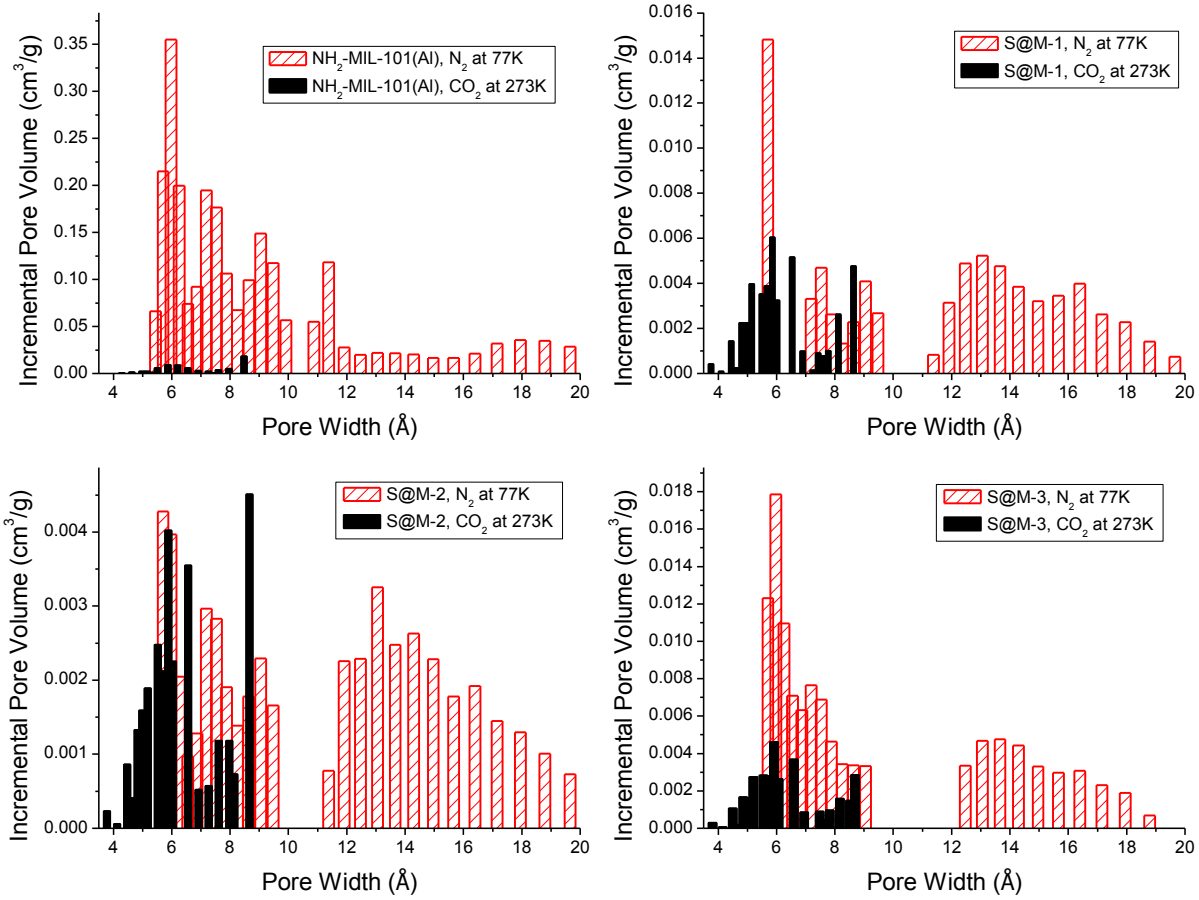

Figure 3.20. Pore size distribution of NH_2-MIL-101(Al) and S@M materials from analysis of N_2 and CO_2 adsorption isotherms.

Thermogravimetric analysis (TGA) indicates that the S@M samples still contain some amount of solvent molecules, which is reflected by weight loss at low temperatures (<150 °C) (Fig. 2), albeit less so than the NH_2-MIL-101(Al) reference. The relatively short washing procedures, mild

and short vacuum drying employed after synthesis (see above) is not enough for complete desolvation due to hindered diffusion. The latter is especially true for the relatively large DMF molecules. For TGA each sample was dried in the vacuum oven for an additional 2 h (120 °C, 12 mbar) before analysis. TGA curves confirm the similarity of the S@M materials. The continuous weight loss without clearly defined inflection points makes it hard to estimate the release point of the iron complex, which certainly happens not before 250 °C (Fig. 2). Visual inspection of S@M samples after heating to 230 °C (503 K) showed no decomposition and SCO could still be triggered by adding methanol solvent. TG analysis on bulk $[Fe(HB(pz)_3)_2]$ indicated that the Fe-compound is stable until ~220 °C at which point the molecular compound starts to sublime under nitrogen gas and ambient pressure.

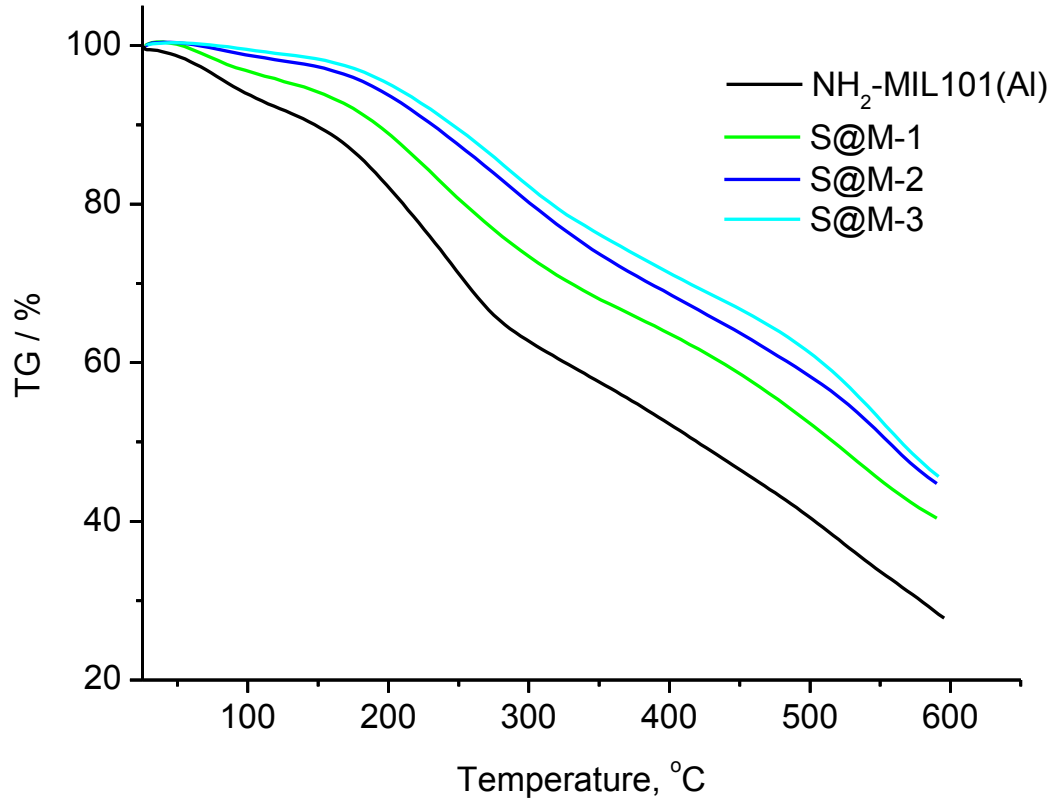

Figure 3.20. TG curves of NH_2-MIL-101(Al) and S@M-n materials.

The spin-crossover behavior of bulk $[Fe(HB(pz)_3)_2]$ is well described in the literature.[263,267,268] Heating a crystalline sample of $[Fe(HB(pz)_3)_2]$, recrystallized from hot toluene[267] or freshly sublimed,[268] from room temperature[267] or 90 K[268] to above 400 K results in an increase of effective magnetic moment from <1.0 to 4.9 μ_B which indicate a change from primarily low-spin

$^1A_{1g}$ to the high-spin $^5T_{2g}$ state. Yet, this increase is slow and very gradual up to 390 K (~2.90 μ_B) at which point a sharp rise in effective magnetic moment to 4.14 μ_B occurs. This sharp increase was assigned to a crystallographic phase transition: the initial well-formed crystals shatter into extremely small fragments. The phase transition is accompanied by a change in the electronic ground state to an essentially high-spin configuration. The magnetic moment reaches the spin-only value of 4.90 μ_B for iron(II) at 461 K.[267,268] Upon cooling the same sample shows no sharp decrease in magnetic moment anymore. The decrease occurs gradual to ~1.38 μ_B at 298 K and to 0.61 μ_B at 90 K. During a second heating of the same sample the magnetic moment follows the gradual preceding cooling curve.[263,267,268] Thus, the change in magnetic moment or susceptibility displayed a hysteresis only for the first thermal cycle. Subsequent heating and cooling cycles follow the first cooling curve and not the first heating curve as the initially metastable crystalline state of $[Fe(HB(pz)_3)_2]$ had relaxed into a stable form.

The temperature variable magnetic susceptibility of the S@M materials and NH_2-MIL-101(Al) reference were monitored using by DC magnetic measurements. Prior to the magnetic measurements the samples were stored under ambient air in a closed glass vessel This way a water and gas uptake could occur.

For the NH_2-MIL-101(Al) reference (Figure 3.21), below 114 K a paramagnetic contribution is visible. Above 150 K the diamagnetic contribution is fitted to the linear equation $\chi_{dia} = -1.1 \cdot 10^{-9} \cdot T - 2.2 \cdot 10^{-7}$. It is apparent from the equation that a small paramagnetic contribution is present also above 150 K. Additionally diamagnetic corrections for the iron complex (Pascal constant) are applied for the S@M composites. This constant amounts to $\chi_{dia} = -3{,}553 \times 10^{-4}$ (emu/molOe) for 1 mol of Fe complex.

Temperature-variable magnetic curves for the S@M composites are presented in Figure 11, taking into account the diamagnetic correction of the matrix. Composite S@M-1 with the lowest Fe content will not be discussed here. The S@M-2 and -3 samples show a similar susceptibility-temperature behavior. The measurement was started at 70 K after cooling the samples to this temperature. At 70 K, the S@M materials are near the LS state. Upon first warming from 70 K to 400 K (127 °C) a gradual increase of χT takes place. The increase in χT corresponds to a LS→HS transition. The slope of the increase is smaller up to 300 K and becomes steeper from 300 K on. This change in slope was also seen during the first heating of

bulk [Fe(HB(pz)$_3$)$_2$], albeit at 390 K.[263,267,268] For the subsequent cooling to 70 K the magnetic moment decreases only to ~80% of the magnetic moment that was reached at 400 K. This indicates that most Fe(II) in the composites remains in the high-spin state. From 150 K to 70 K the paramagnetic contribution of NH_2-MIL-101(Al) (Figure 3.21) becomes more visible, thus, χT slightly increases with the temperature decrease in Figure 3.22. A full second cycle with warming to 400 K and cooling to 70 K just retraces the previous cooling and remains above 80% of the maximum χT value. Thus, most of the Fe(II) in the S@M materials is kept in the high-spin state during second cycle measurements. The loss of apparent hysteresis from the first heating and cooling cycle was also seen for bulk [Fe(HB(pz)$_3$)$_2$] where it was explained with a crystallographic phase transition upon first heating.[263,267,268]

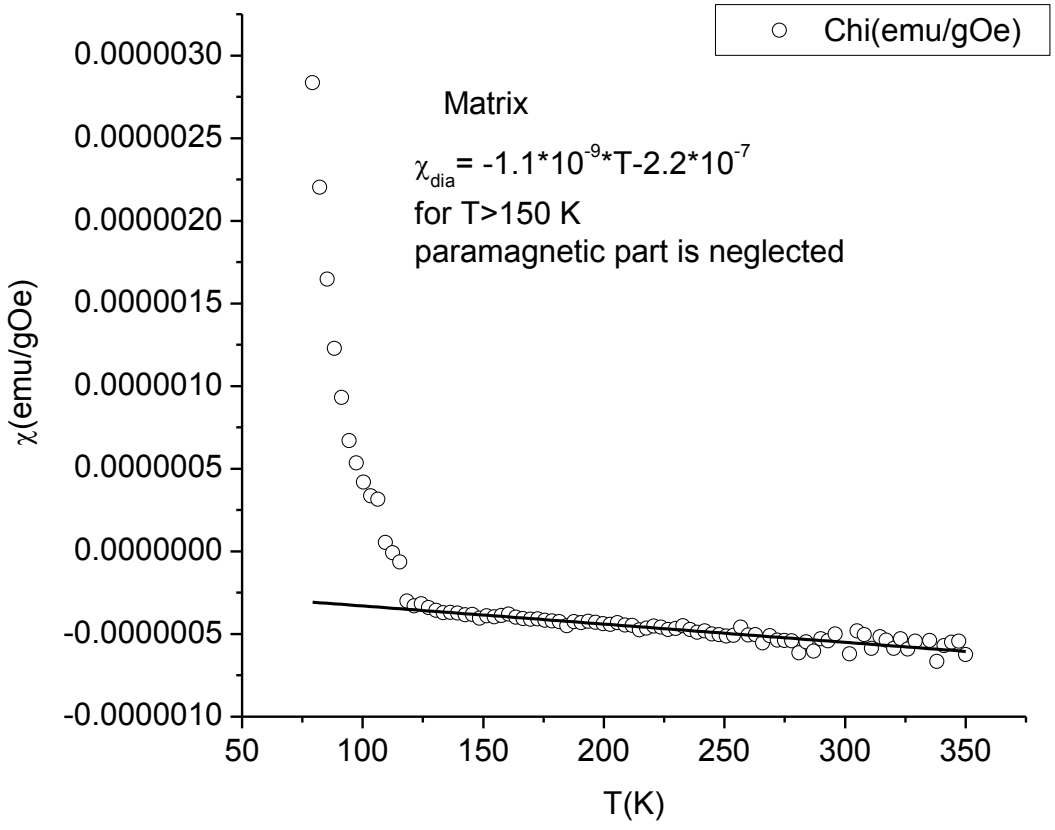

Figure 3.21. Temperature-variable magnetic curve for NH_2-MIL-101(Al) reference.

We explain the initial strong increase in χT when first heating from 70 to 400 K by either a crystallographic phase transition, akin to bulk [Fe(HB(pz)$_3$)$_2$] (see below) or the presence of small amounts of adsorbed water that is desorbed towards 400 K. The second cycle then reflects the spin-crossover behavior of single [Fe(HB(pz)$_3$)$_2$] molecules or small complex nanoparticles in the

NH_2-MIL-101(Al) host matrix. After the loss of solvent molecules the $[Fe(HB(pz)_3)_2]$ molecules are in a low-pressure situation in the matrix. A lower pressure favors the high-spin state with its larger molecular volume.[227,273,276]

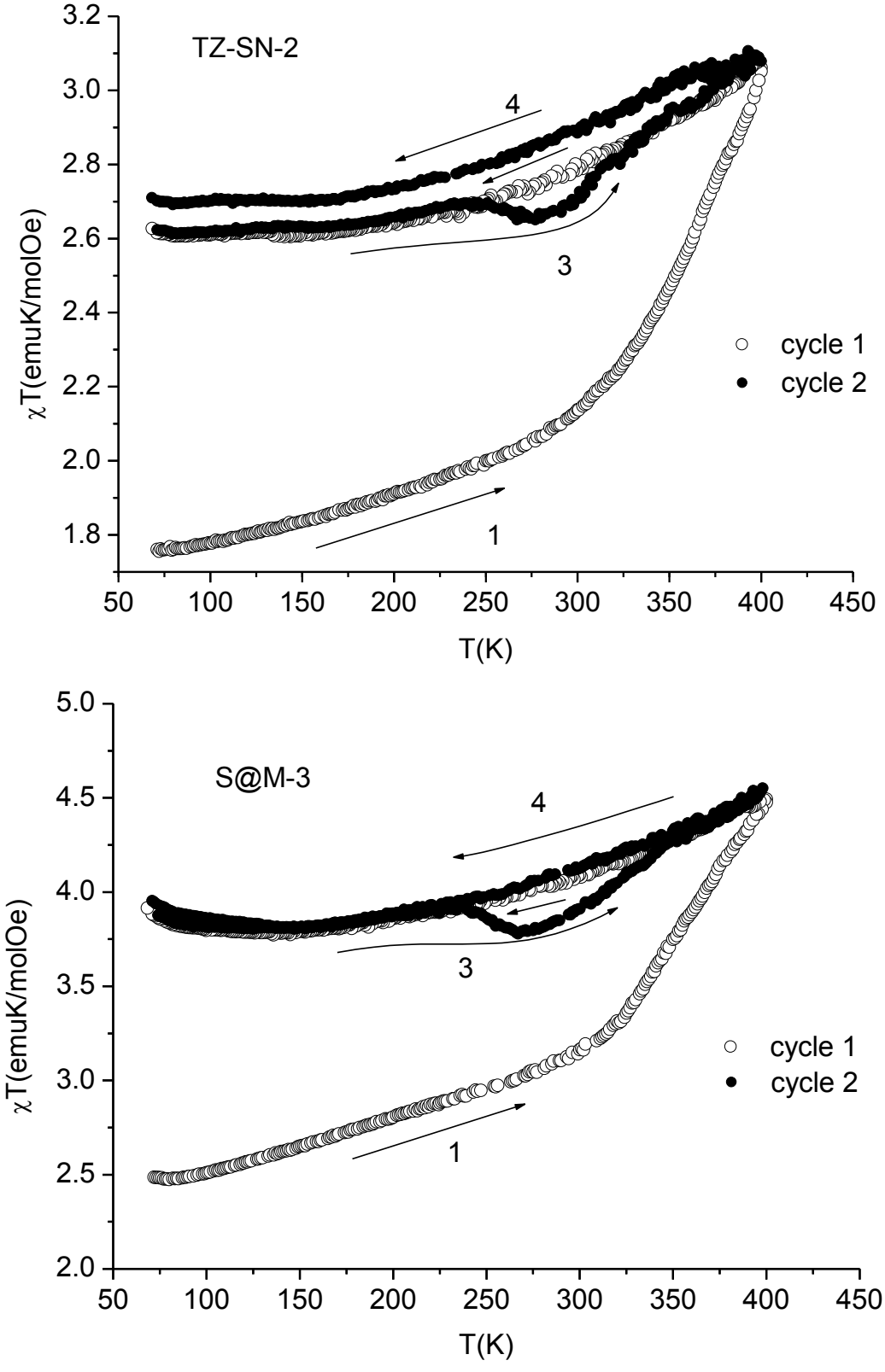

Figure 3.22. Temperature-variable magnetic curves for S@M-2 (top) and for S@M-3 (bottom).

The transition temperature for $[Fe(HB(pz)_3)_2]$ has been shifted to much lower values in the S@M composite compared to the bulk form. Even at 70 K the low-spin state has not come close. This can also be explained by having nano-sized $[Fe(HB(pz)_3)_2]$ particles in the composite. The smaller the particles of an SCO material has the more gradual the transition and the lower the transition temperature T_c. The spin transition of microcrystalline $[Fe(pz)Pt(CN)_4]\cdot 2.6H_2O$ (pz=pyrazine) is much more gradual than bulk material.[269] $[Fe(H_2Bpz)_2(phen)]$ and $[Fe(H_2Bpz)_2(bipy)]$, which prepared in thin films, presented a more gradual spin transitions than in the powder samples and shifted to lower transition temperature.[270] Though microcrystals of the spin-crossover coordination polymer [FeL(bipy)] (L=[3,3′]-[1,2-phenylenebis(iminoethylidyne)] bis-(2,4-pentanedionato)(2-), bipy=4,4′-bipyridine), which prepared in a poly(4-vinylpyridine) (P4VP) matrix, showed the same cooperative spin transition as the bulk material. But the remaining iron centers are either high-spin or low-spin depending on the coordination environment.[271]

4. Conclusions

To obtain $[Fe(HB(pz)_3)_2]$@MOF composites, several methods were tested in this chapter. The $[Fe(HB(pz)_3)_2]$ would cover and form a layer on the surface of MOFs via diffusion method (both liquid phase and gas phase diffusion). The loading of outside covered SCO@MOF materials were fairly low, but the 'adhesion effect' of $[Fe(HB(pz)_3)_2]$ still very strong. $[Fe(HB(pz)_3)_2]$ molecules would not removed by solvent washing or vacuum heating (100 °C, 12 mbar). The TZ-SP materials which get by 'direct synthesis in the pores' method present an outstanding high loading performance, but the $[Fe(HB(pz)_3)_2]$ inside the pores seems formed an unknown crystalline phase and showed silence on SCO behaviour. The specific reasons of the disappearance of spin transition of TZ-SP materials still need further investigation.

A composite from $[Fe(HB(pz)_3)_2]$ inside a metal-organic framework $[Fe(HB(pz)_3)_2]$@ NH_2-MIL-101(Al) (S@M) was synthesized by formation of the host NH_2-MIL-101(Al) in the presence of pre-formed $[Fe(HB(pz)_3)_2]$. S@M materials had a maximum loading of ~11.3 wt% (0.19 Fe molecules per Al_3O SBU). Gas adsorption measurements on the dry compounds with different loadings confirm the absence of appreciable accessible porosity in the S@M composite materials. The entrapped complex, which is stable in air and cannot be removed by vacuum

drying (120 °C and $<10^{-6}$ Torr), is confined in the high-spin state at room temperature and this state is retained for 80% upon cooling to 70 K. Temperature-variable magnetic measurements show that S@M composites approaches the low-spin state only upon first cooling to 70 K. Upon warming to 400 K a gradual low- to high-spin transition occurs. Subsequent cooling to 70 K preserves over 80% of the magnetic moment previously achieved at 400 K. This is explained by the presence of adsorbed water during the first cooling and the loss of this incorporated water from the sample upon first heating to 400 K. Prior to the magnetic measurements the sample was stored under ambient air.

Interestingly, the spin-crossover (SCO) could be triggered at room temperature by immersing the dried compound into various solvents composed of molecules with small cross sections: H_2O, MeOH, DMSO, DMF, BuOH, t-BuOH, THF, ethylacetate, CH_2Cl_2, CCl_4, toluene, mesitylene, cyclohexane, hexane. The unusual triggered SCO is interpreted as solvent mediated pressure in the confinement, effectively similar to pressure induced SCO. For an SCO compound the low-spin state with its smaller volume is favored at higher pressure.

Acknowledgment

Prof. Christoph Janiak and Dr. Ishtvan Boldog are gratefully acknowledged for the guidance of SCO@MOF composites work in this chapter. Prof. Vojislav Spasojevic is thanked for DC magnetic measurements.

Chapter 4

Spin-crossover (SCO) behavior of Fe(II) 1,2,4-triazole complexes embedded in pores of MCM-41

1. Introduction

The spin crossover (SCO) phenomenon is the ability of a transition metal complex to exist in two different stable ground states: the low-spin state and the high-spin state.[272,273] The switching between the high-spin and the low-spin states may be caused by different external stimuli such as light, temperature or pressure[274,275,276].The spin crossover of iron(II) complexes has been thoroughly studied and not only leads to a change in magnetic moment but usually gives rise to optical transitions from purple in the low-spin state (low temperature) to white in the high-spin state when increasing the temperature.[277,278,279,280,281,282,283] One interesting aspect in this area concerns the case of SCO hybrid materials where a given complex can feel the constraint of a given matrix.[284,285,286]Several SCO nanoparticles based on Fe(II) complexes were prepared and embedded in matrices, such as SiO_2,[287] Ni,[288] and $CsFe[Cr(CN)_6]$, to name a few.[289] Theoretical studies of such nanoparticles were recently proposed.[290,291]

In this chapter, two iron(II) SCO compounds were embedded in the mesostructured silica MCM-41. The selected materials are the 1D chains $[Fe(Htrz)_3](BF_4)_2{\cdot}H_2O$ (SCO-1) and $[Fe(Htrz)_2trz]BF_4$ (SCO-2) with Htrz = 4*H*-1,2,4-triazole and trz = 1,2,4-triazolato) (Scheme 1).[292,293,294] Both are known to exhibit a hysteretic SCO behaviour with sharp spin transition (ST) above room temperature. SCO-2 which displays a reproducible hysteresis loop of ~40 K has been selected for numerous studies, because it does not contain any water molecules which can give rise to unstable hysteresis loops due to solvent release. In particular, hybrid materials including SCO-2 were recently prepared with a mesoporous silica monolith,[295,296] graphene,[297] and with silica–gold nanocomposites.[298] Yet, the matrix effect with MCM-41 has not yet been investigated although this material is well known for its potentiality to accommodate various sort of guests.[299]

The MCM-41 matrix effect, that is, the change in SCO behaviour under the constraints of surrounding silicate walls has been studied herein by temperature variable ^{57}Fe Mössbauer spectroscopy, magnetic measurements and optical reflectivity.

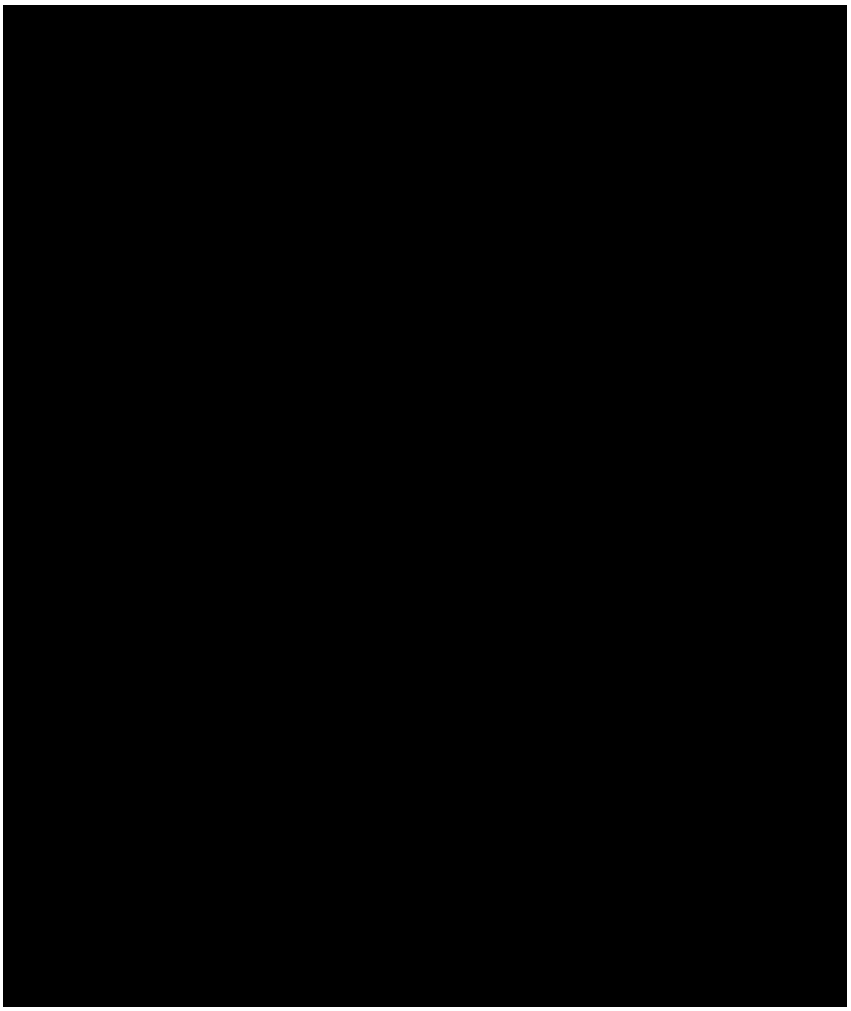

Scheme 4.1. Schematic drawings of 1D SCO materials inserted into MCM-41.

2. Experimental

2.1. Materials

All the reagents were purchased from the following distributors (Table 4.1) and used without further purification.

Table 4.1. The information of chemicals which used in this chapter

Reagent	Purity, % / Grade	Commercial Source
Mesostructured Silica	MCM-41 type	Sigma-Aldrich

Iron(II) tetrafluoroborate hexahydrate	97%	Sigma-Aldrich
1,2,4-4H-triazole	99%	Alfa Aesar
Methanol	99.9 %	Merck
Ethanol	99.9 %	Merck
Iron standard for AAS	1000 mg/L	Sigma-Aldrich

2.2. Synthesis of SCO@MCM materials

MCM-41 host matrices were used as received. Fe(II) 1,2,4-triazole compounds in MCM-41 host matrices were synthesized by first impregnating the MCM-41 material with an alcoholic solution of the 1,2,4-triazole ligand over a time of at least 12 h. Then an alcoholic solution of the appropriate molar amount of the iron(II) salt, $Fe(BF_4)_2 \cdot 6H_2O$, was added to form the composite SCO@MCM materials. For the subsequent investigations it was crucial to only have SCO inside the cylindrical pores of MCM-41. So, careful washing with water was done to remove any SCO precipitate outside of the pores. Both compounds SCO-1 and -2 are readily soluble in water.

SCO-1@MCM was prepared by follows: 1,2,4-4H-triazole (208 mg, 3.0 mmol) and MCM-41 (100 mg) were stirred in 100 mL of methanol for 12 h. A solution of 337.5 mg (1.0 mmol) of $Fe(BF_4)_2 \cdot 6H_2O$ in 60 mL of methanol was added to the slurry and the solvent was removed rapidly at 70°C using a rotary evaporator. The formed product was collected and thoroughly washed with water 3 times and 10 mL each. The product was dried in an evacuated desiccator over silica gel. Yield ~253 mg of a red-pink powder. (Scheme 4.2)

The pure SCO-1 was synthesized according to ref. 300. Calcd for $C_6H_{11}N_9OB_2F_8Fe$: C 15.85; H 2.44; N 27.73. Found: C 16.26; H 2.64; 28.06.

SCO-2@MCM was prepared by follows: To a solution of 416 mg (6 mmol) of 1,2,4-4H-triazole in 2 mL ethanol,100 mg of MCM-41 powder was added and the slurry was stirred for 12 h. The formed suspension was transferred to a solution of 675 (2 mmol) of $Fe(BF_4)_2 \cdot 6H_2O$ in 4 mL of water and the mixture was stirred for 24 h at room temperature. The solid product was filtered, washed with ethanol and water for 3 times (10 mL each), and dried in an evacuated desiccator over silica gel. Yield ~235 mg of a light-pink powder. (Scheme 4.2)

Nanoparticles of SCO-2 were prepared as a purple solution following a procedure described in

ref.301. Calcd for $C_6H_8N_9BF_4Fe$: C 20.66; H 2.33; N 36.14. Found: C 20.33; H 2.27; N 35. 46.

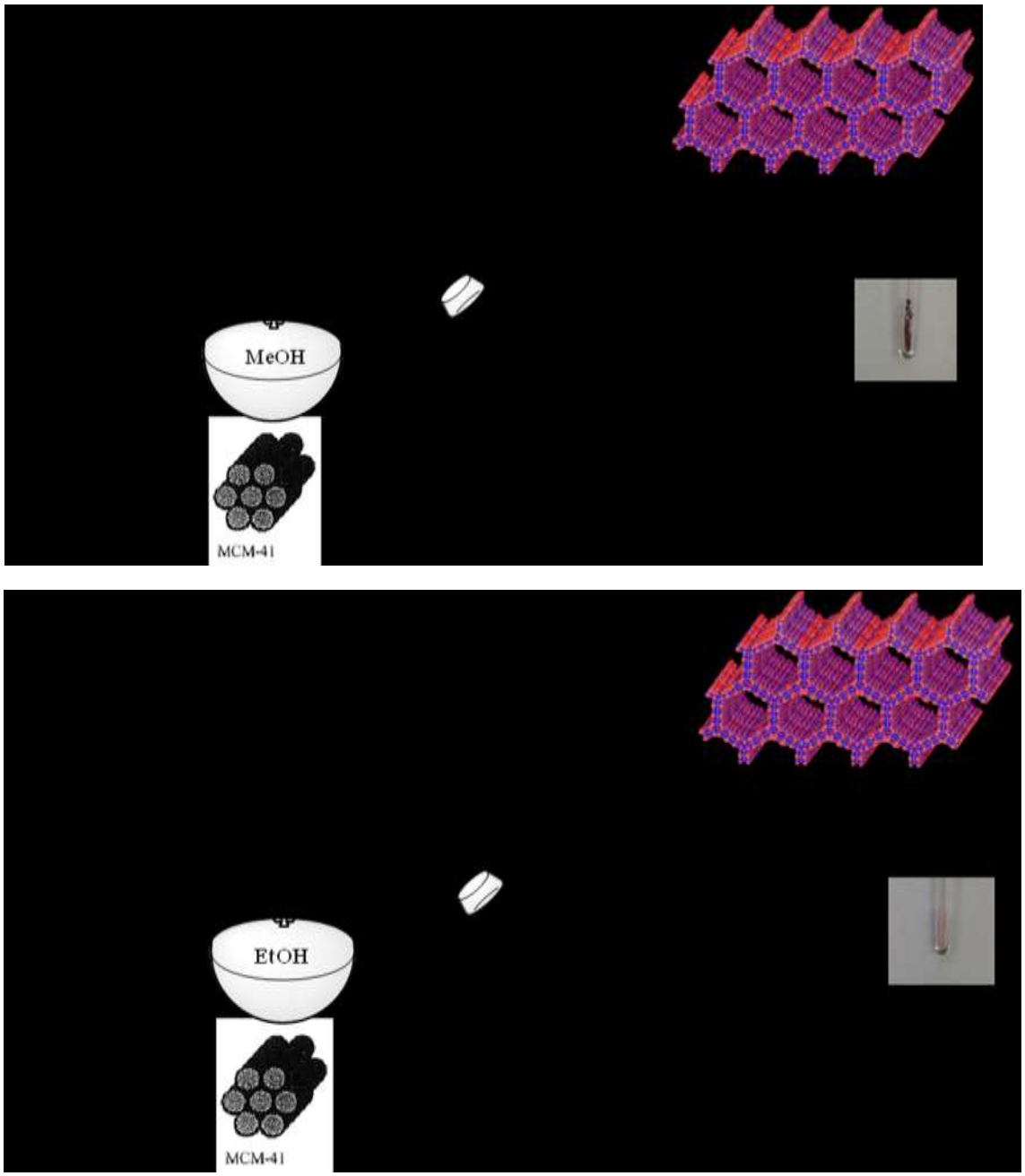

Scheme 4.2. The Schematic synthesis of SCO-1@MCM and SCO-2@MCM.

Washing procedure: any SCO precipitate which formed on the outer MCM surface was removed by washing procedures. SCO-1@MCM was washed three times with water, because SCO-1 is very easy dissolved in water. For SCO-2@MCM, the solid product was first placed in a beaker, stirred for 2 h with water and separated by centrifugation. This step was repeated 3 times. Then the solvent was changed to ethanol, stirred for 2 h again and centrifuged. The ethanol

washing was repeated until no pink color appeared in the supernatant.

2.3. Characterization

Powder X-ray diffractograms were acquired at ambient temperature on a Bruker D2 Phaser using a flat low background sample holder and Cu-Kα radiation (λ = 1.54182 Å) at 30 kV covering 2 theta angles 5-70° over a time of 2 h.

Nitrogen adsorption isotherms were acquired on a Quantachrome Nova®, 2 h degassing at a temperature of 120°C in vacuum prior to each measurement.

CO_2 sorption isotherms were measured using a Micromeritics ASAP 2020 automatic gas sorption analyzer at 0°C,4 h degassing at a temperature of 120°C in vacuum prior to each measurement.

Thermo gravimetric analysis (TGA) was measured on a Netzsch TG 209 F3 at 5 °C/min heating rate using aluminum sample holders and nitrogen as carrier gas.

FT-IR measurements were carried out on a Bruker TENSOR 37 IR spectrometer at ambient temperature in the range of 4000 to 500 cm^{-1} with an ATR unit (Platinum ATR-QL, Diamond).

Atom absorption spectroscopy (AAS) was conducted with a Perkin Elmer AAnalyst100 instrument (flame AAS, acetylene/air as firing gas, burner head length: 10 cm). The standard solution were prepared with densities 5mg/L、10mg/L and 20mg/L respectively.

Scanning electron microscopy, SEM images were obtained with an ESEM Quanta 400 FEG (University of Essen, Dipl.-Ing. S. Boukercha).

Transmission electron microscopy, TEM measurements were conducted with a FEI Tecnai G2 f20 with a FEG operated at 200 kVat the Ernst-Rusca centrum of Forschungszentrum Jülich. TEM samples were prepared as diluted suspensions in water and deposited on carbon coated copper grids.

Mössbauer spectra were recorded in transmission geometry using a Wissel spectrometer, equipped with a $^{57}Co(Rh)$ source and fitted to an Oxford Instruments bath cryostat. Samples were inserted into aluminium foils. Measurements above room temperature were carried out with a Wissel Furnace MBF-1100. The sample was fixed between two round plates of B_4C, made of heat- and corrosion-resistant steel with high nickel content. The sample holder and heat screens were positioned in quartz tubes, in air atmosphere. Spectra were fitted to a sum of

Lorentzianlineshapes by least-squares refinement using Recoil 1.05 Mössbauer Analysis Software.[302]

The optical reflectivity was measured via a Multizoom AZ100 microscope system (Nikon) at 5°C heating rate and cooling rate. The data was treated using ImageJ software (Wayne Rasband, National Institute of Mental Health, Bethesda, Maryland, USA).

DC magnetic measurements were performed by using Quantum Design MPMS XL-5 SQUID magnetometer. For both samples, M(T) measurements were carried out in the magnetic field of 1000 Oe, starting from T=200 K up to 400 K (heating), and then while cooling back to 200K.

DSC were carried out in a $He_{(g)}$ atmosphere using a Perkin-Elmer DSC Pyris 1 instrument equipped with a cryostat and operating down to 98 K. Aluminum capsules were loaded with 20-50 mg of sample and sealed. The heating and cooling rates were fixed at 10 K min^{-1}. Temperatures and enthalpies were calibrated over the temperature range of interest (298 K- 400 K) using the solid-liquid transitions of pure Indium (99.99%)[303], over the range 78 K – 298 K.

3. Results and Discussion

Scheme 4.3. Preparation of SCO hybrid materials used in this work

Fe(II) 1,2,4-triazole compounds were embedded in MCM-41 host matrices by first impregnating the MCM-41 material with an alcoholic solution of the 1,2,4-triazole ligand over a time of at least 12 h. Then an alcoholic solution or an aqueous solution of the appropriate amount of the iron(II) salt, $Fe(BF_4)_2 \cdot 6H_2O$, was added to form the composite SCO@MCM materials (Scheme 4.3, 1 and 2). For the subsequent investigations it was crucial to only have the SCO material only inside the cylindrical pores of MCM-41. So, careful washing with water was done to remove any SCO precipitate outside of the pores. Both compounds SCO-1 and -2 readily dissolve in water with plausible fragmentation of the 1D chain (according to ref. 293 SCO-2 dissolves with decomposition).

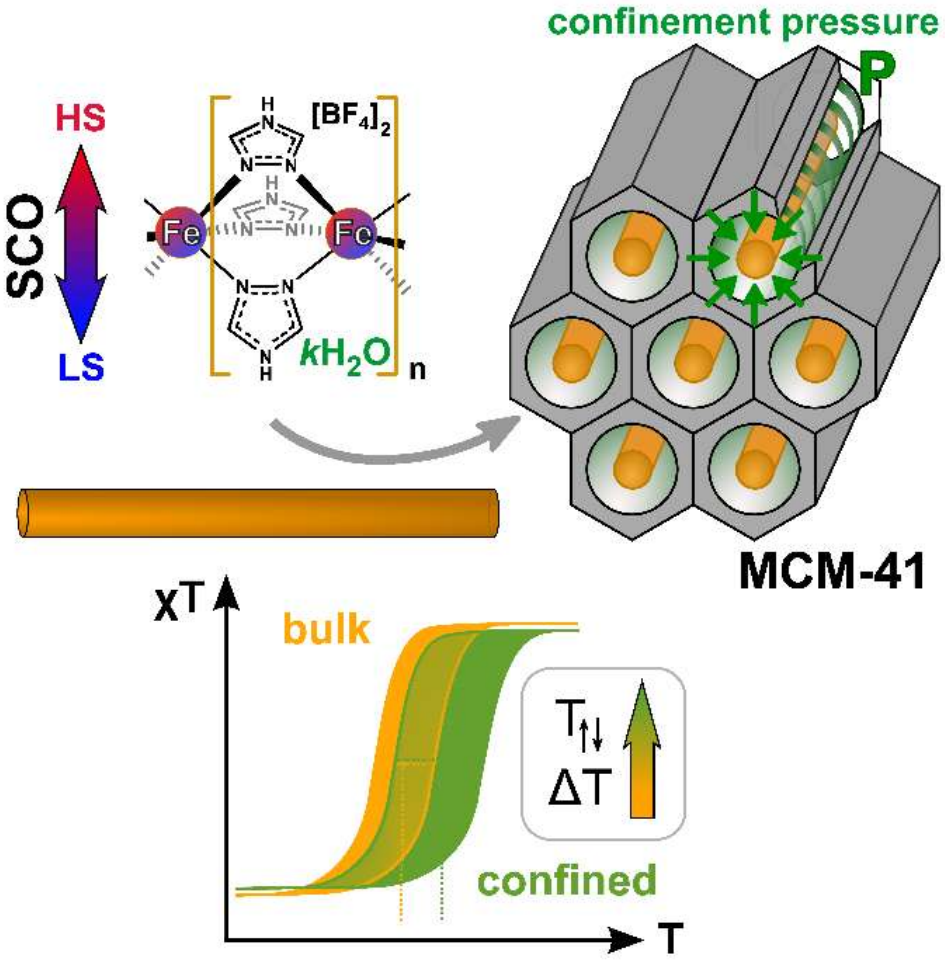

Scheme 4.4. Schematic presentation of the confinement pressure on the SCO-1 material mediated by water.

The spin-crossover (SCO) compounds $[Fe(Htrz)_3](BF_4)_2 \cdot H_2O$ (SCO-1) and $[Fe(Htrz)_2trz](BF_4)$ (SCO-2) (Htrz = 1,2,4-triazole)were embedded in the pores of mesostructured silica MCM-41 to yield SCO@MCM composites as evidenced by electron microscopy, gas sorption studies, powder X-ray diffractometry, atomic absorption and infrared spectrometry. Studies of the temperature-induced spin crossover behavior of the composites by temperature-variable ^{57}Fe Mössbauer spectroscopy, magnetic and differential scanning calorimetry measurements and optical reflectivity indicate that the spin transition of the composites was significantly shifted for SCO-1@MCM to higher temperature in comparison to bulk SCO-1 compounds while the shift for SCO-2 was negligible. These shifts in the transition temperature for SCO-1@MCM [versus bulk SCO-1] amounted to $T_c^{\uparrow}$ = 371 / 376 K [282 / 291 K] and $T_c^{\downarrow}$ = 340 / 345 K [276 / 286 K] (magnetic / optical reflectivity data) with a broadening of the hysteresis by 25-26 K relative to bulk SCO-1(varying slightly with the used method). The significant difference in the SCO behavior of the similar materials SCO-1 and SCO-2 when embedded in the MCM-41 matrix is assigned to the hydration of the SCO-1@MCM material (Scheme 4.4). Water is apparently crucial in transmitting the confinement pressure or matrix effect on the spin transition when the SCO compound is embedded between the pore walls.

3.1. IR, PXRD and AAS

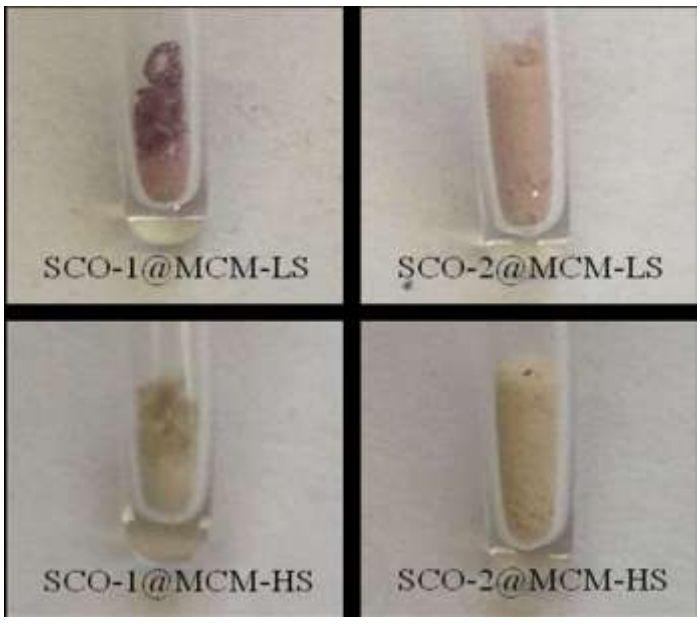

Figure 4.1. Photographs showing the color change from LS (room temperature) to HS (~100 °C) for each sample.

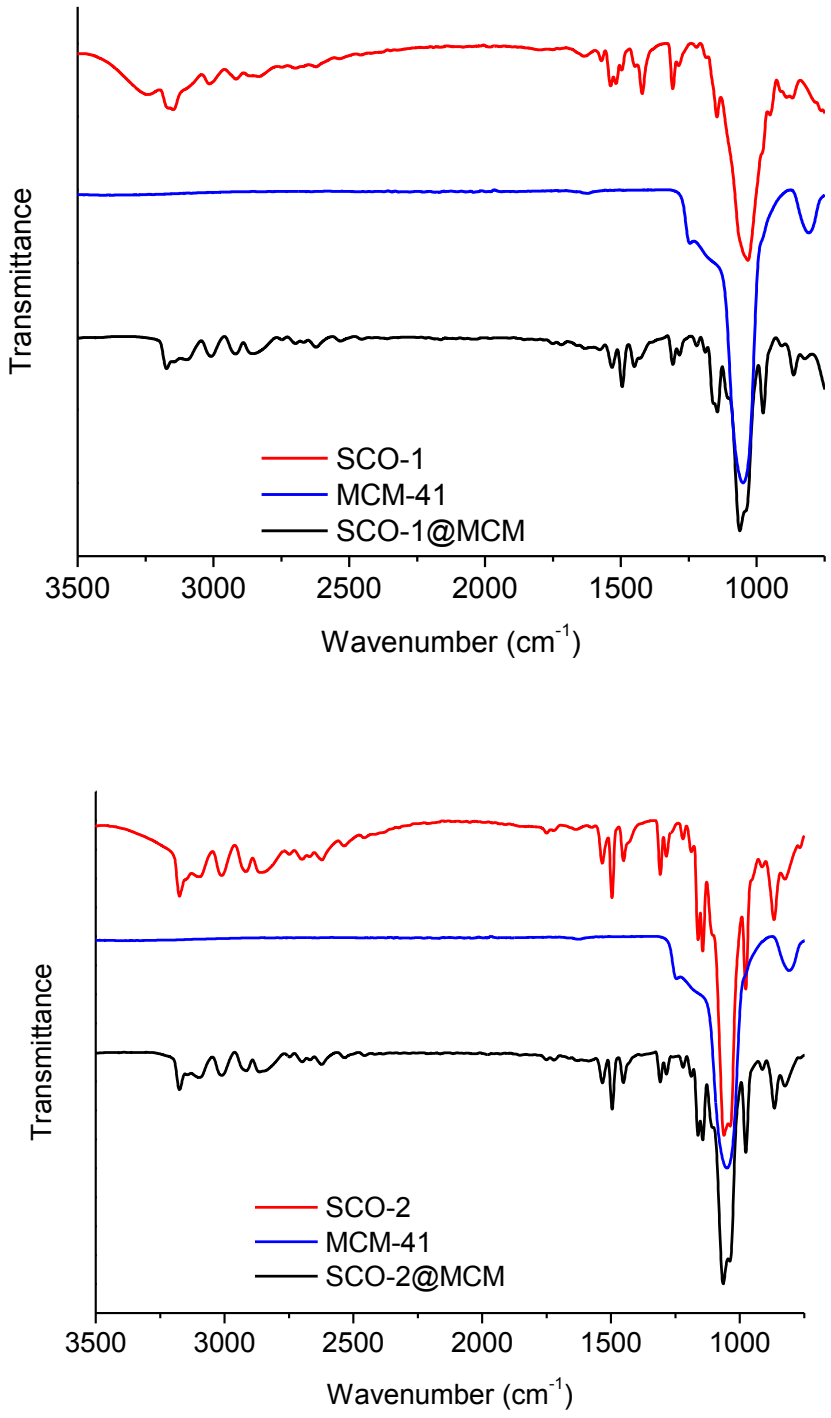

Figure 4.2. IR spectra of SCO@MCM samples in comparison to the bulk SCO compound and MCM-41.

The IR spectra of the composite materials SCO@MCM compared to the IR spectra of bulk SCO and MCM-41showed the presence of both components in the composite (Figure 4.2).

Matching powder X-ray diffractograms (PXRD) of the pure SCO and the SCO@MCM materials confirms the identity of the SCO materials formed in bulk and as a SCO@MCM composite for SCO-1 and SCO-2 (Figure 4.3).

The SCO amount in the composite was calculated from the iron analysis by atomic absorption spectroscopy to 56.39 wt% for SCO-1@MCM and 43.81 wt% for SCO-2@MCM (see Table 4.2 for details). The standard solution were prepared with densities 1mg/L、5mg/L and 10mg/L respectively.

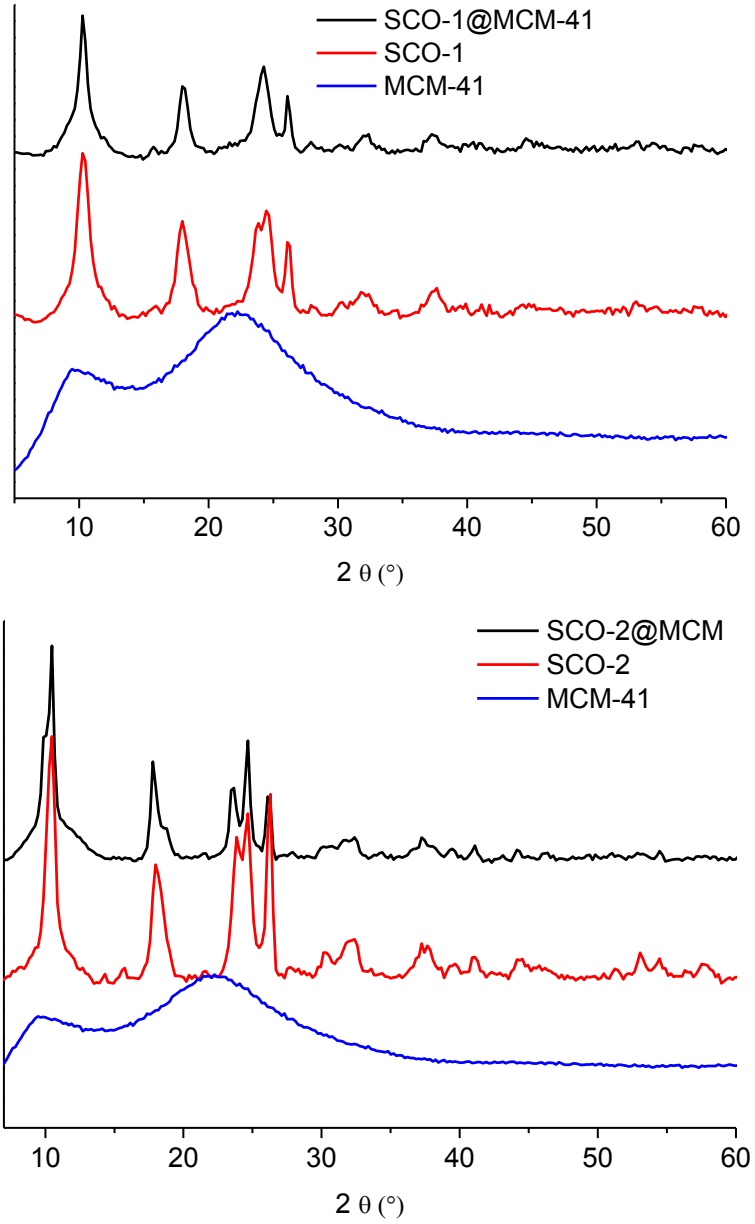

Figure 4.3. Powder X-ray diffractograms of pure SCO complexes, and SCO@MCM composite materials. The MCM host matrix is amorphous.

Table 4.2 The weight ratios of Fe and SCO of SCO@MCM samples

Code	c(Fe), mg/L	Fe content (wt%)	SCO content (wt %)
SCO-1@MCM	4.076	7.21	56.39
SCO-2@MCM	4.119	7.01	43.81

3.2. Porosity measurements

IR spectroscopy, elemental analysis and PXRD cannot distinguish between bulk and embedded SCO material and, hence, prove the presence of SCO inside the pores of MCM. However, with the pores of MCM filled by the SCO compound the porosity should decrease. The remaining porosity of the SCO@MCM composite materials was analyzed by N_2 sorption studies at 77 K (Figure 4.4). The sample was degassed in vacuum before measurement at a temperature of 393 K for 2 h. In the composite materials the Brunauer-Emmett-Teller (BET) and Langmuir surface areas for SCO-1 have decreased considerably to less than 25% of the value found in MCM-41 (Table 4.3).

The adsorption isotherm of SCO-1@MCM is of type-IV, which is typical for many mesoporous adsorbents[304,305,306], with an H2hysteresis loop which may be associated with pores with narrow necks and wide bodies ("bottle-neck" pores).[215] Such pore structures can result from the formation of SCO-1 microcrystals inside the MCM mesopores. The N_2 sorption isotherm for MCM-41 with its S-shape matches the literature reports.[307,308,309,310] In summary, the decrease of surface area and porosity is a good indication that the MCM-41 matrix was filled by SCO materials as intended.

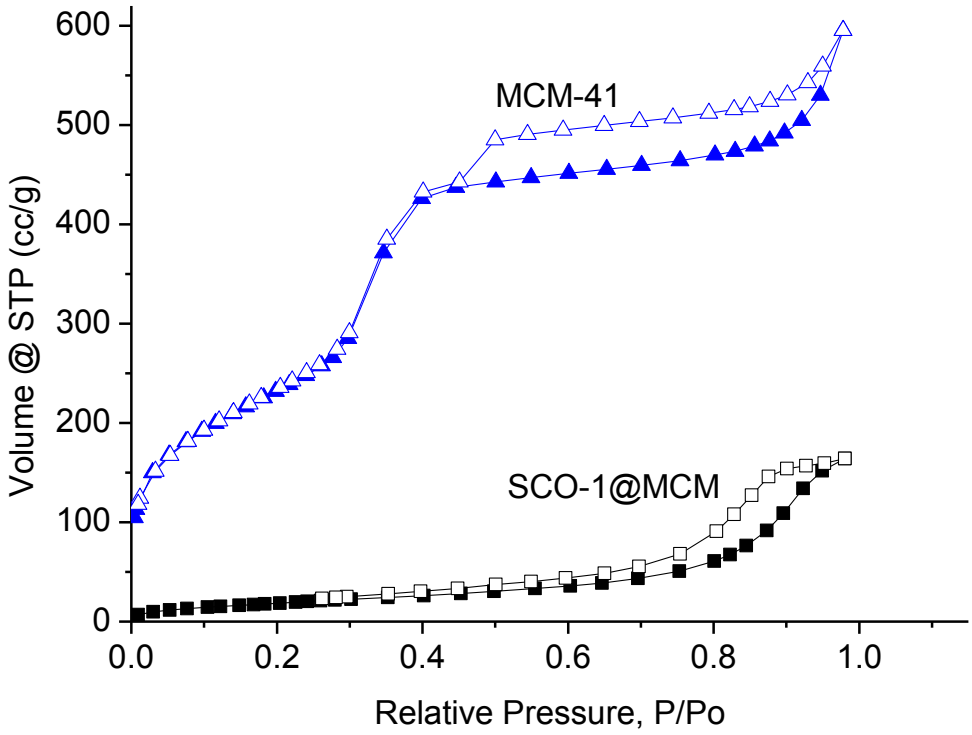

Figure 4.4. N_2 sorption isotherms of MCM-41 and SCO@ MCM samples; closed and open symbols refer to adsorption and desorption, respectively.

No surface area was found by N_2 sorption for SCO-2@MCM. However, that at the cryogenic temperature of 77 K diffusion of N_2 molecules into micropores is very slow. Diffusion limitations at this temperature influences adsorption in ultramicropores (pores smaller than 7 Å).[311] For porous materials which usually contain a wide range of pore sizes including ultramicropores, this would require time-consuming N_2 adsorption measurements and may still lead to under-equilibration of the adsorption isotherms, hence, will give erroneous results of the pore volume and pore size distribution analysis. Problem of this type can be eliminated by using CO_2 adsorption analysis at 273 K.[312,313,314] The saturation pressure of CO_2 at 0°C is very high (~26141 Torr), therefore low relative pressure measurements necessary for micropore analysis are achieved in the range of moderate absolute pressures (1–760 Torr).[315] At 273 K and under higher absolute pressures CO_2 molecules can more easily access ultramicropores than N_2 at ~77 K and the kinetic diameter of CO_2 (3.3 Å) is also slightly smaller than for N_2 (3.64 Å). CO_2micropore analysis at 273 K versus N_2 analysis at 77 K is advantageous because of (i) faster

analysis and (ii) greater confidence that measured adsorption points are equilibrated (both due to higher diffusion rates) and (iii) extension of the range of analysis to pores of smaller sizes that are accessible to CO_2 molecules but not to N_2.[316]

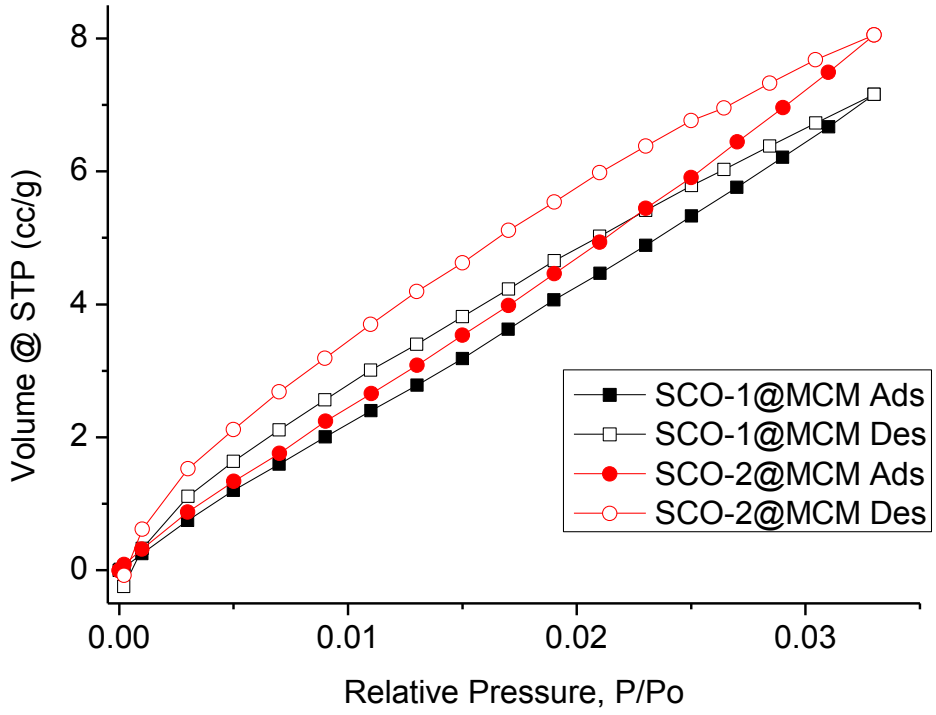

Figure 4.5. CO_2 sorption isotherms for SCO-1@MCM and SCO-2@MCM at 273 K.

CO_2 sorption at 273 K show that, SCO-2@MCM still possesses higher porosity than SCO-1@MCM (Figure 4.5). This indicates that pores or pore mouths of SCO-2@MCM are narrower than that of SCO-1@MCM. Thus, from CO_2 adsorption isotherms at 273 K (Figure 4.5), the pore size distribution for SCO@MCM was derived between 4-10 Å by using NLDFT with a "slit-pore model" model (Figure 4.6). CO_2 adsorption with the NLDFT model yields a better resolved PSD towards the ultramicropore end than from N_2 adsorption isotherms for SCO-1@MCM (Figure 4.6 to 4.8). Here the two SCO@MCM materials give very similar pore size distributions for pores below 10 Å (1 nm)

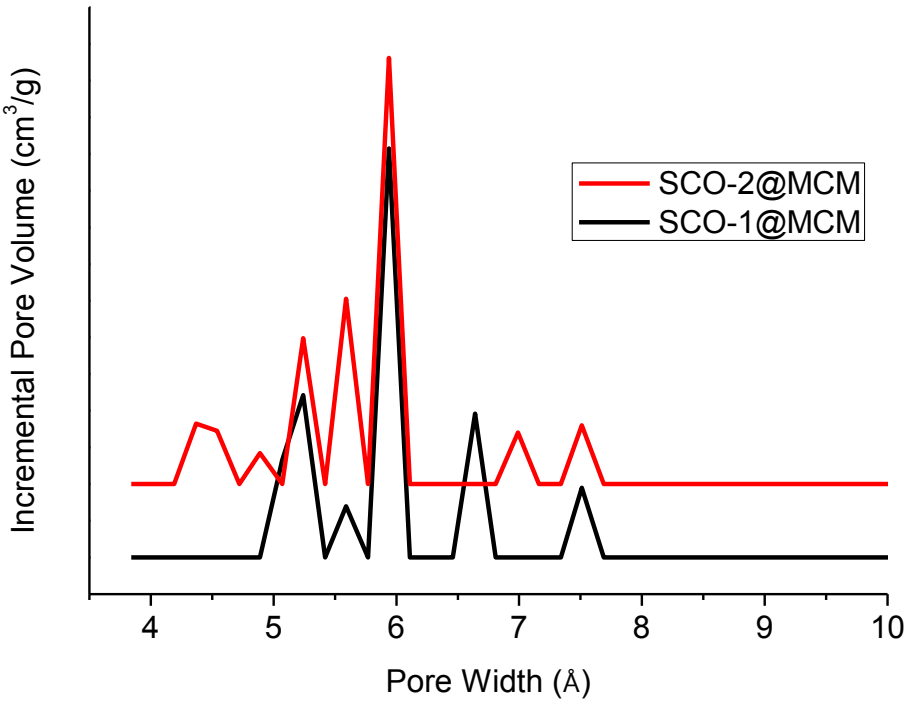

Figure 4.6. NLDFT pore size distribution (PSD) curves of SCO@MCM from CO_2 adsorption (at 273 K) isotherms.

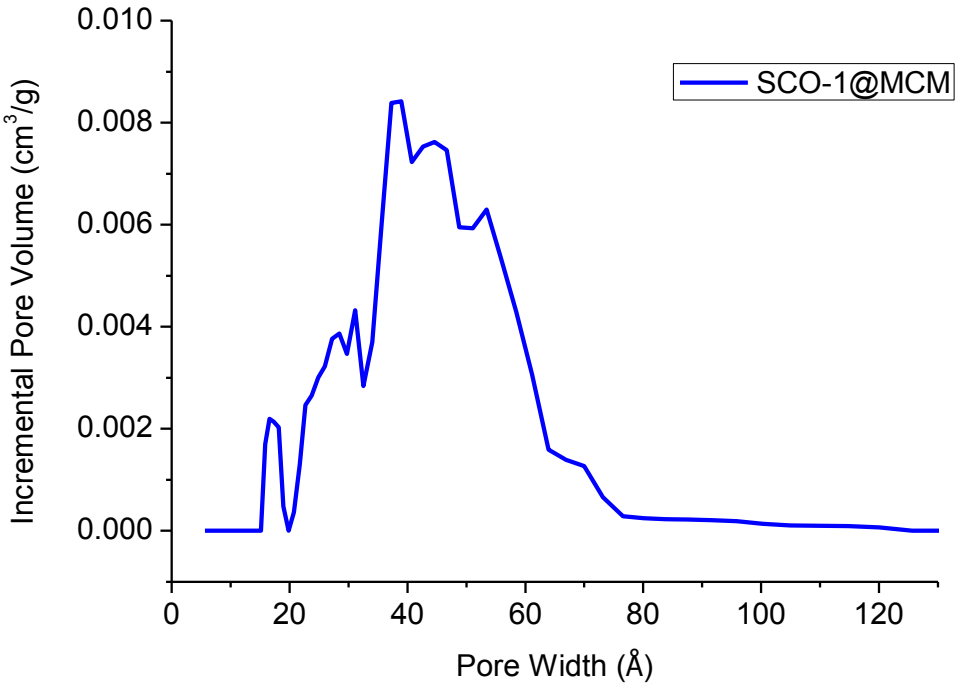

Figure 4.7. Pore size distribution of SCO-1@MCM from N_2 adsorption isotherm (at 77 K) analysis.

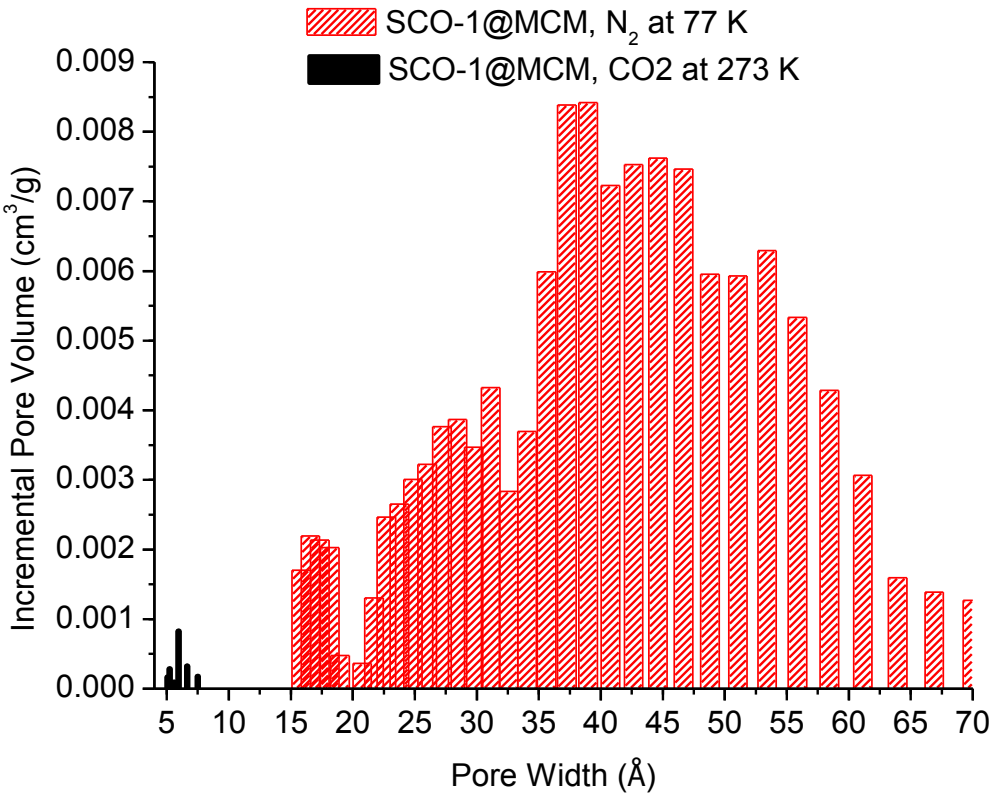

Figure 4.8. Pore size distribution of SCO-1@MCM from analysis of N_2 and CO_2 adsorption isotherm.

Table 4.3 Porosity data for SCO@MCM from N_2 isotherms at 77 K and CO_2 isotherms at 273 K.

Composite	S_{BET}[a] (m^2g^{-1})	S_{Lang}[b] ($m^2\ g^{-1}$)	$V_{0.1}$[c] (cm^3g^{-1})	V_{tot}[d] (cm^3g^{-1})	$V_{0.1}/V_{tot}$	$V_{micro}(CO_2)$[e] (cm^3g^{-1})
MCM-41	857	1238	0.297	0.82	0.36	0.0175
SCO-1@MCM	70	104	0.0222	0.235	0.09	0.00189
SCO-2@MCM	0	0	n.a.	n.a.	n.a.	0.00197

[a] BET surface area calculated at 0.05 <$p/p0$< 0.2 from N_2 sorption isotherm at 77 K with a standard deviation of ± 50 m^2/g.

[b] Langmuir surface area over the pressure range 0-110 Torr.

[c] Micropore volume calculated from N_2 adsorption isotherm at $p/p0 = 0.1$ for pores with d ≤ 2 nm (20 Å).

[d] Calculated from N2 sorption isotherm at 77 K ($p/p0 = 0.95$) for pores ≤ 20 nm.

[e] Pore volume for pores with d ≤ 1 nm (10 Å, *cf.* Figure 4.6) from the CO_2 NL-DFT model at 273 K.

3.3. Electron microscope

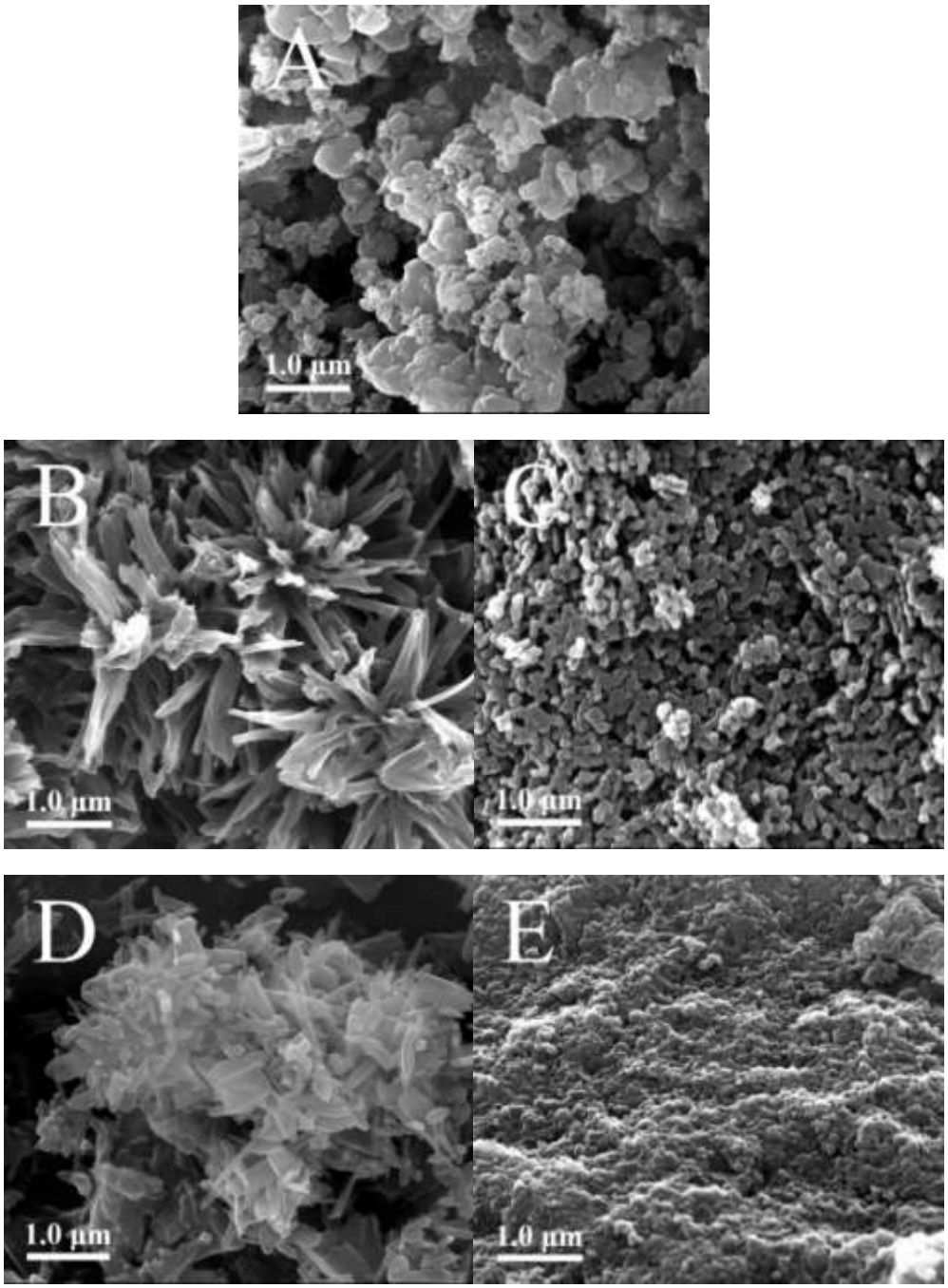

Figure 4.9. SEM images of (a) MCM-41, (b) SCO-1, (c) SCO-1@MCM, (d) SCO-2 and (e) SCO-2@MCM.

Scanning electron microscopy (SEM) images (Figure 4.9) showed a morphology of the SCO@MCM composite materials which was similar to native MCM. The morphology of MCM-41 was typical irregular particles with the size around 50 nm to 2 μm. While pure SCO-1 and SCO-2 were rod-like crystals under SEM. But there was no characteristic SCO crystallites

can be seen in the picture C and E. This supported the formation of SCO inside the MCM mesopores and the removal of any SCO formed outside through the washing procedures. Due to the long time stirring in washing procedure, SCO@MCM composite possessed smaller particle size compare to MCM-41.

Transmission electron microscopy (TEM) images reveal the formation of nanocrystals of SCO-1 and -2 inside the MCM matrix (Figure 4.10). The dark spots which are ~2 nm in diameter contain iron and the "5 nm" resolutions (Figure 4.10 b, d) show that the dark spots consist of lattices planes which are indicative of crystalline material. The crystallinity of the SCO materials inside MCM is in agreement with the observation of PXRD patterns for the SCO@MCM composites (see Figure 4.3).

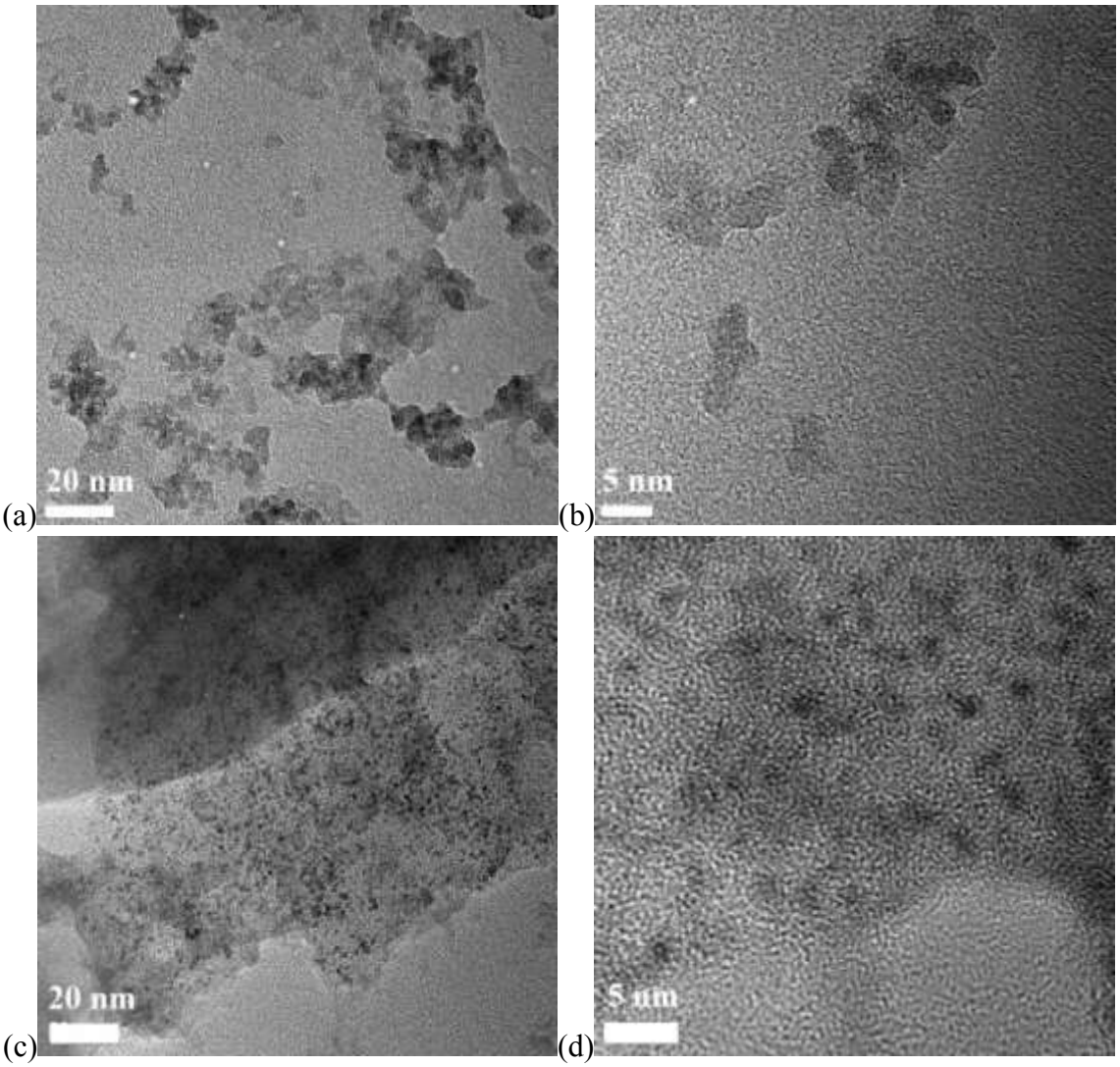

Figure 4.10. TEM images of SCO-1@MCM (a,b) and SCO-2@MCM (c,d) at different magnifications.

3.4. Spin transition behaviour

In this work, the ST behaviour of the composites was investigated and compared to those of the guest materials using the same set of physical techniques. Such a careful comparison is important because of the diversity of techniques presented which can provide a different set of transition temperatures. Bulk techniques: Mössbauer measurements (run in static mode with long acquisition times) and DC magnetic measurements (in settle mode) and a surface technique: optical reflectivity (in scanning mode). Mössbauer spectroscopy is the only method which provides a careful evaluation of the spin population given that by reflectivity, only the surface of the sample is probed.

3.4.1. ^{57}Fe Mössbauer studies

SCO-1@MCM was investigated over the temperature range 78-358 K. The associated Mössbauer parameters are gathered in Table 4.5. At 78 K, the spectrum of SCO-1@MCM consists of one quadrupole doublet, with an isomer shift of δ^{LS} = 0.43(1) mm·s^{-1} and aquadrupole splitting of ΔE_Q^{LS} = 0.26(2)mm·s^{-1} characteristic for the LS state of iron(II) ions (Figure 4.11). The composite remains in the LS state on warming up to 328 K, showing no influence of the matrix on the spin state. SCO-1 was only partly investigated by Lavrenova et al by Mössbauer spectroscopy.[292] Nevertheless, the isomer shift δ^{LS} of SCO-1@MCM at room temperature nicely corresponds to the one reported for SCO-1 (δ = 0.43 mm/s),[292] indicating that the coordination polymer structure is not affected by the matrix environment, *i.e.*, the 1D chain is not located nearby the walls of the MCM-41. No decomposition of the sample is noticed within the composite as seen by the absence of oxidation products, which was however clearly observed when studying a less stable derivative, $[Fe(NH_2trz)_3](NO_3)_2$ (NH_2trz = 4-amino-1,2,4-triazole) within the same matrix. On warming to 333 K, a major signal is detected for the composite with larger parameters (δ^{HS} = 0.97(1) mm·s^{-1} and ΔE_Q^{HS} = 2.30(1) mm·s^{-1}) which are characteristic for the HS state of iron(II) ions. The major signal is present in 80% population compared to the LS state. On warming further to 358 K, this population grows up to 87% indicating an incomplete spin transition. An asymmetric quadrupole doublet is noticed for the HS state at this temperature which is attributed to a texture effect. On cooling, a slight decrease of the HS population is observed down to 318 K after which a sharp transition to the LS state is observed. Interestingly,

the ST is also incomplete at room temperature with 5% of ions remaining in the HS state. The temperature dependence of the HS molar fraction assuming equal Debye Waller factors for HS and LS states, which is justified taking into account the sharpness of the ST,[317] is shown in Figure 4.12. A hysteresis loop of 20 K width is delineated with transition temperatures $T_c^{\uparrow}$ = 330 K and $T_c^{\downarrow}$ = 310 K. The ST is not complete in both HS and LS states.

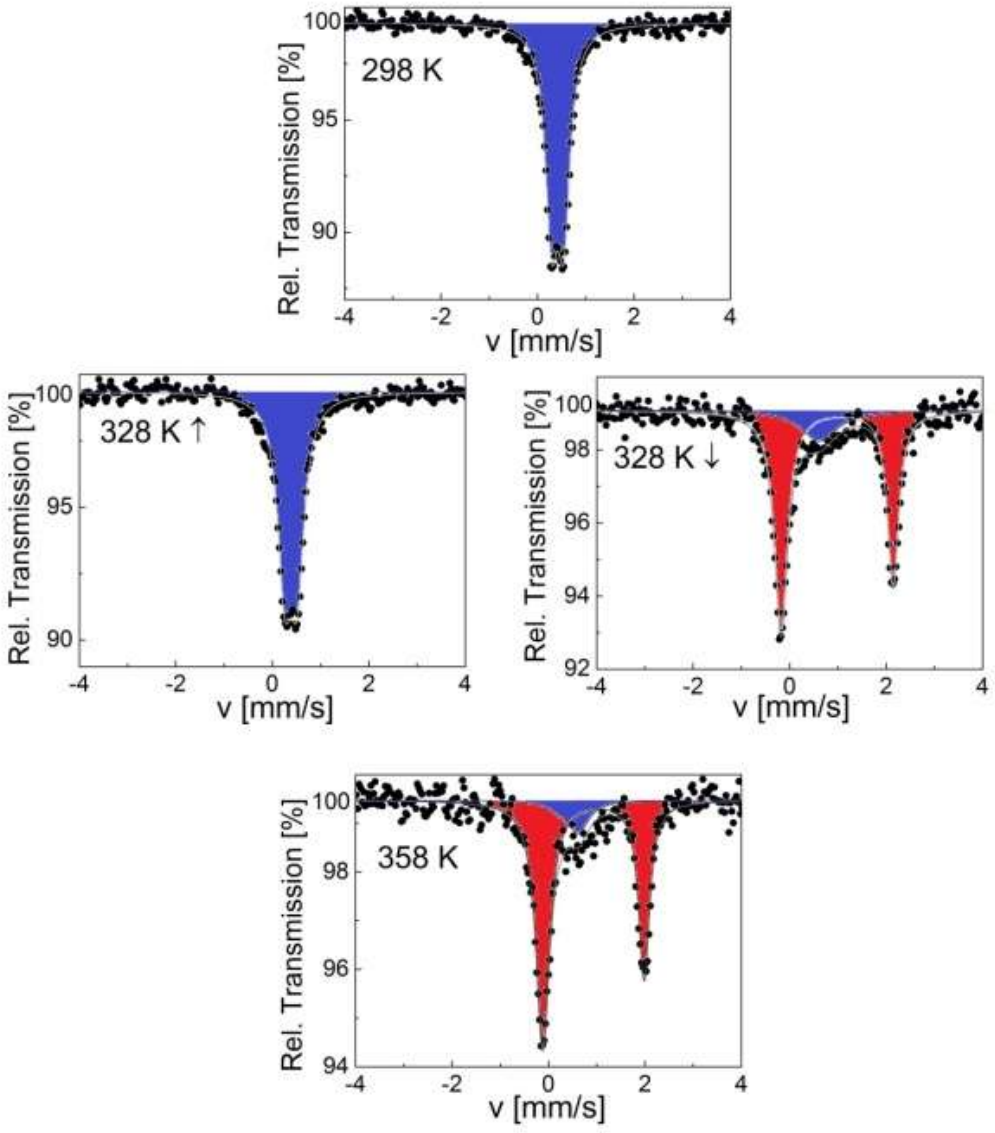

Figure 4.11. Selected 57Fe Mössbauer spectra of SCO-1@MCM; blue and red colours correspond to LS and HS doublets, respectively.

SCO2-@MCM was investigated over the range 78-358 K by Mössbauer spectroscopy. The spectrum at 78 K shows one quadrupole doublet attributed to LS Fe^{II} ions (δ^{LS} = 0.42(1) mm s^{-1} and ΔE_Q^{LS}= 0.23(1) mm s^{-1}) (Figure 4.13). At room temperature, the hyperfine parameters of the

LS state (Table 4.6) are in exact agreement with the ones of the pure material with (δ^{LS} = 0.43(1) mm s^{-1} and ΔE_Q^{LS}= 0.29(1) mm s^{-1}),[293] thus indicating that the inclusion of [Fe(Htrz)$_2$trz](BF$_4$) in the MCM matrix neither changed its microstructure nor resulted in an oxidation. However, the spin state population is modified because 11% of HS ions detected at room temperature for SCO-2 are now switched to the LS state in the composite. Usually, this fraction of HS ions in the HS state is attributed to end of chains, i.e. the formation of short chains which ends with a few percent of remaining water molecules.[318] Thus the coordination polymerization would tend to proceed completely within the matrix. Another explanation could be the remaining paramagnetic Fe spins having a FeN$_6$ environment within the matrix would switch to the LS state due to a local pressure effect caused by the matrix. In both cases, a matrix influence is therefore identified.

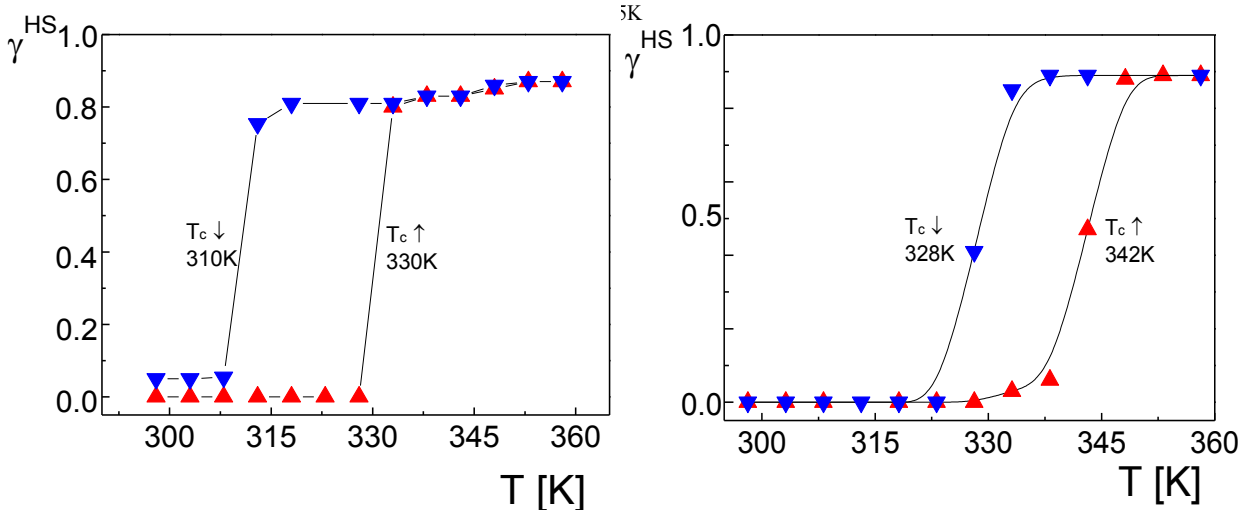

Figure 4.12. Temperature dependence of the HS molar fraction deduced from ^{57}Fe Mössbauer spectroscopy over the temperature range 298-360 K for SCO-1@MCM (Left) and for SCO-2@MCM (right).

On warming up to 338 K, the composite remains in the LS state where a second doublet attributed to HS Fe^{II} ions grows slightly in intensity (7%), δ^{HS} = 0.98(1) mm s^{-1} and ΔE_Q^{HS}= 2.53(1) mm s^{-1} (Figure 4.13). This behaviour indicates the onset of a SCO behaviour, a spin situation which differs from the pure material which only switches below 380 K,[293] confirming a matrix influence on the spin state. On warming further, the HS signal (δ^{HS} = 0.95(1) mms^{-1} and ΔE_Q^{HS}= 2.21(1) mms^{-1}) increases, revealing an asymmetric character, to reach 85% at 358 K. Worthwhile to note that the fraction of LS ions in the HS state is dramatically increased in the

composite (Table 4.6) compared to the 3% detected in the pure material.[293]

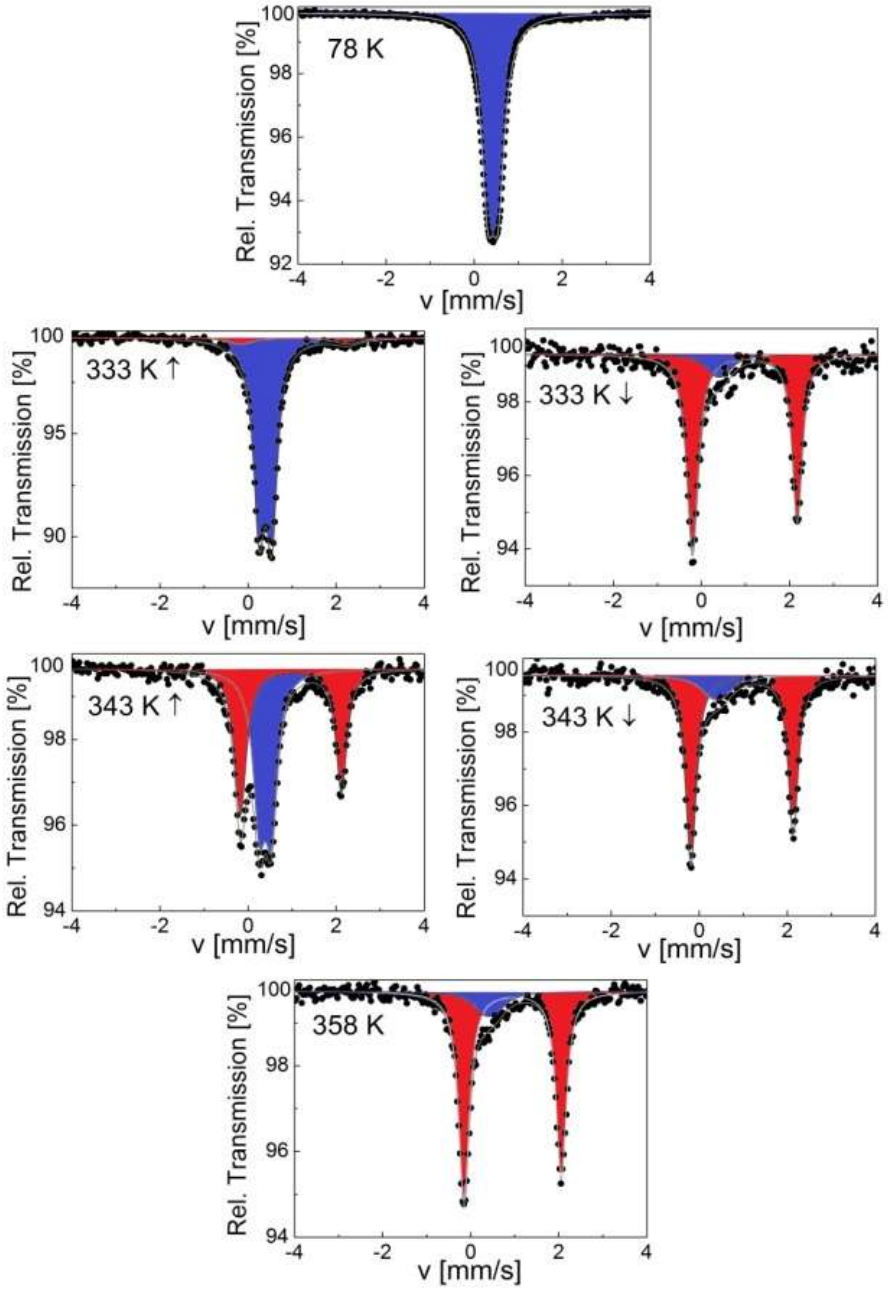

Figure 4.13. Selected ^{57}Fe Mössbauer spectra of SCO-2@MCM; red and blue colours correspond to HS and LS doublets, respectively.

On cooling, hysteresis behaviour is detected for the composite as seen in Figure 4.13. The temperature dependence of the HS molar fraction shown in Figure 4.12 allows to determine the width of the hysteresis loop ΔT = 14 K as well as the transition temperatures ($T_c^{\uparrow}$ = 342 K and $T_c^{\downarrow}$ = 328 K) which differ from the ones of the pure material ($T_c^{\uparrow}$ = 380 K and $T_c^{\downarrow}$ = 344 K) recorded

by Mössbauer spectroscopy.[293] Thus the hysteresis width is considerably reduced compared to the genuine material. In addition, the sharpness of the ST is also affected indicating a loss of cooperativity, and the hysteresis loop is shifted downwards. Given the difference with the transition temperatures obtained with DC magnetic measurements (see below), dehydration of the sample (*i.e.*, a sample containing water molecules was studied, not SCO-2@MCM but SCO-2·xH_2O@MCM) cannot be excluded.

3.4.2. DC magnetic measurements

The magnetic properties of both composite materials are presented for comparison in Figure 4.14. For SCO-1@MCM, the first cycle reveals an abrupt hysteresis loop as large as 49K, with $T_c^{\uparrow}$=389K and $T_c^{\downarrow}$=340K. This hysteresis is not stable, due to the expected water release on warming. Therefore, for the second cycle, the hysteresis falls down to 31 K and is fully reversible, with $T_c^{\uparrow}$ = 371K and $T_c^{\downarrow}$ = 340 K. Compared to the magnetic data recorded on the pure material in the crystalline state, a clear shift of the ST upwards is observed. Indeed, $[Fe(Htrz)_3](BF_4)_2 \cdot H_2O$ (SCO-1) displays a sharp ST at $T_c^{\uparrow}$ = 345 K and $T_c^{\downarrow}$ = 323 K while a lower hysteresis width is obtained for the dehydrated material with $T_c^{\uparrow}$ = 282 K and $T_c^{\downarrow}$ = 276 K.[293]

The transition temperatures recorded for the Mössbauer studies of SCO-1@MCM show a hysteresis loop shifted downwards compared to SCO-1@MCM recorded by DC magnetic measurements which is expected due the time necessary to record each Mössbauer spectrum (one or two days in air atmosphere) which is enough to slowly dehydrate the material. As a result the hysteresis loop width decrease to 20 K, with transition temperatures $T_c^{\uparrow}$ = 330 K and $T_c^{\downarrow}$ = 310 K (Figure 4.12).

The SCO-2 MCM nanocomposite shows a fully reversible hysteresis loop of width 35 K, with $T_c^{\uparrow}$ = 381 K and $T_c^{\downarrow}$ = 346 K. Compared to the magnetic properties of the pure material, a slight shift downwards of the ST curve along with an hysteresis width decrease is noticed ($T_c^{\uparrow}$ = 385 K and $T_c^{\downarrow}$ = 345 K).[293]

This is result is consistent with theoretical predictions about a hysteresis reduction with particle size lowering.[319] The shift was more pronounced for the ST of nanoparticles of SCO-2 coated with gold recorded by DC magnetic measurements with $T_c^{\uparrow}$ = 373 K and $T_c^{\downarrow}$ = 344 K.[320,321] These two results however contradict earlier literature reports which indicate that the ST

properties of this material are not modified when prepared as nanoparticles.[301]

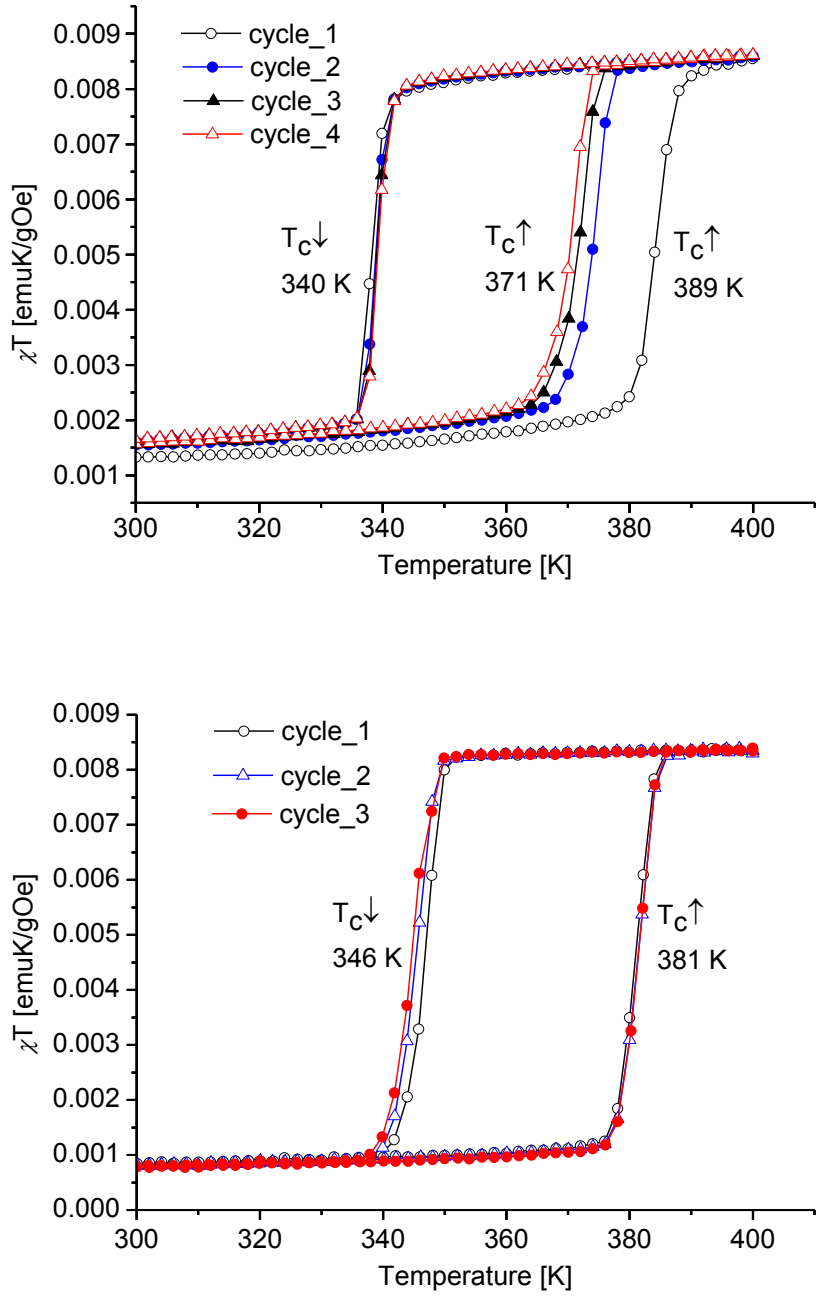

Figure 4.14. Temperature-variable magnetic curves for SCO-1@MCM (Top) and SCO-2@MCM (Bottom).

3.4.3. Optical reflectivity measurements

The SCO of iron(II) complexes with azole based ligands is usually accompanied by a color change from purple in the LS state (lower temperature) to white in the HS state (higher

temperature) (*cf*. Figure 4.1). Hence, the change in spin state can also be followed by optical reflectance measurements in the solid state.[322,323] The spin transitions of the SCO@MCM composites were studied optically under a nitrogen atmosphere to exclude any potential oxidation of the samples in air. The reflectance measurements were carried out using an optical disk cryostat mounted on the stage of a fluorescence microscope linked to a CCD camera. Before each set of measurements, the cryostat was purged for 2h at 10°C.

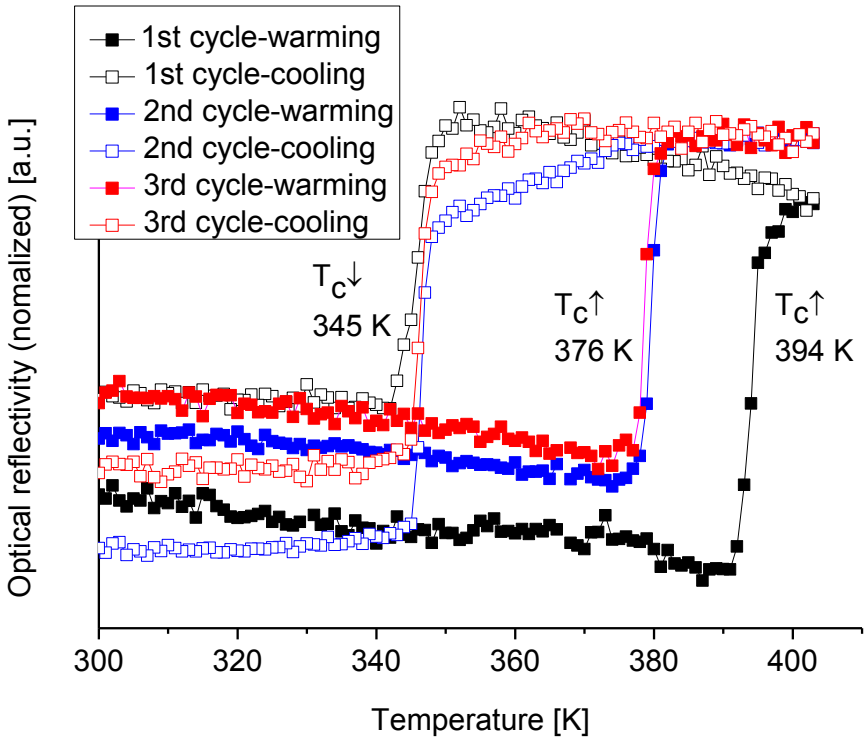

Figure 4.15. Thermal dependence of the normalized optical reflectivity of SCO-1@MCM at a scan rate of 2K/min. The transition temperatures recorded in warming and cooling modes are indicated.

The first cycle recorded on SCO-1@MCM reveals an abrupt transition upon heating and cooling with a hysteresis as large as 49K (black curve in Figure 4.15). However, the hysteresis loop is reduced to 31K in the next cycles (blue and red curves in Figure 4.15), most presumably due to dehydration. These results are consistent with literature data reporting a large hysteresis loop for the hydrated SCO-1 phase ($T_c^{\uparrow}$=336 K and $T_c^{\downarrow}$=323 K) and a narrow one for the dehydrated phase, $T_c^{\uparrow}$=291 K and $T_c^{\downarrow}$ = 286 K).[293] For the SCO-1@MCM material, a hydration/dehydration phenomenon was observed in this work (see also below). Whereas the

alpha or beta phase interconversion for bulk SCO-1[293] was not found. In the previous literature on SCO-1[293] the hydration/dehydration might have been ascribed to an alpha/beta phase transition. Compared to the literature data on optical reflectivity for the free SCO-1 compound, the transition temperatures for SCO-1@MCM are shifted upwards with $T_c^{\uparrow}$=376K and $T_c^{\downarrow}$= 345 K,[293] which suggests a significant matrix effect.

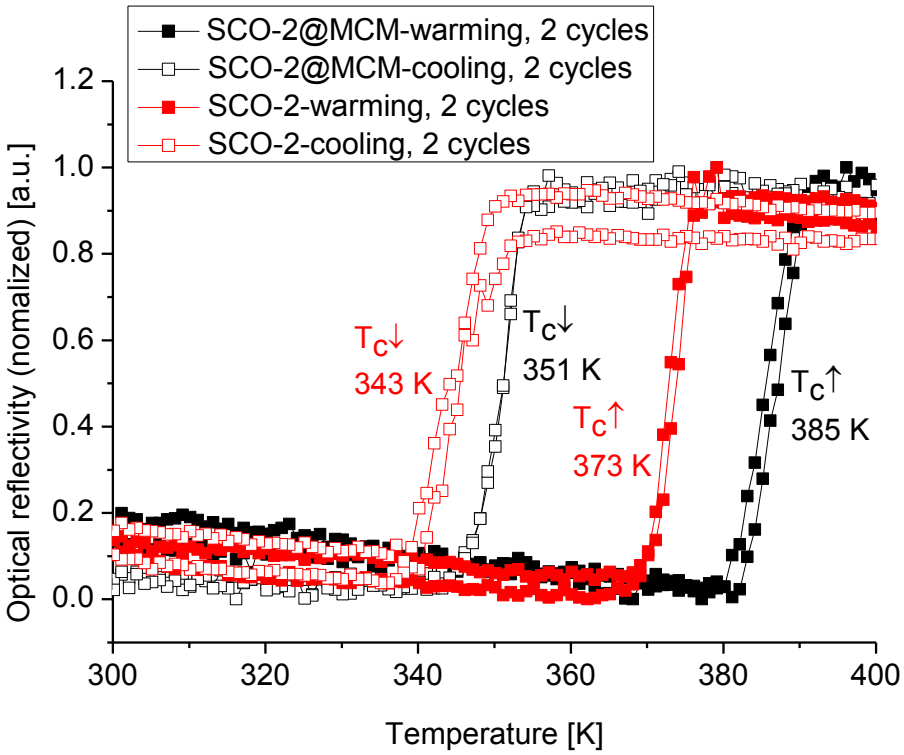

Figure 4.16. Thermal dependence of the normalized optical reflectivity recorded at 2 K/min on both SCO-2@MCM and SCO-2 prepared as nanoparticles using the reverse micelles method. The transition temperatures in the warming and cooling modes are given.

Optical reflectance measurements were recorded here for the first time on SCO-2 prepared as nanoparticles in the liquid state thanks to the reverse micelles method.[301] A hysteresis loop with $T_c^{\uparrow}$= 373 K and $T_c^{\downarrow}$ = 343 K was observed, which differs for the transition temperature in the heating mode compared to previous reflectivity measurements in the bulk sample (not in a nano-form) in the crystalline state $T_c^{\uparrow}$= 381 K and $T_c^{\downarrow}$ = 347 K.[293]

The SCO-2 compound embedded in the MCM matrix shows a ST at $T_c^{\uparrow}$= 385K and $T_c^{\downarrow}$=351K with a hysteresis of about 35K, hence of the same width as the bulk sample but shifted upwards. This behaviour is consistent with what was observed in the case of SCO-1@MCM, presenting the

same kind of matrix effect.

We could attribute this shift to the compound being embedded between the pore walls. The HS state has elongated Fe-Ligand bond lengths (Fe-N ≈ 2.1-2.2 Å) compared to the LS state (Fe-N ≈ 1.9-2.0 Å) thereby requiring more space. Thus, the ST has to operate against the higher pressure exerted by the pore walls of the MCM matrix. In other words, higher external pressure favours the LS state so that the LS→HS transition occurs at higher energy, *i.e.*, temperature.

Table 4.4 provides a summarizing overview of the spin transition temperatures for the SCO and SCO@MCM materials from the different methods.

Table 4.4. Summary of transition temperatures (Tc in Kelvin).

Material	^{57}Fe Mössbauer (Hysteresis)		Magnetic (Hysteresis)		Optical reflect. (Hysteresis)		Ref.
	$T_c^{\uparrow}$	$T_c^{\downarrow}$	$T_c^{\uparrow}$	$T_c^{\downarrow}$	$T_c^{\uparrow}$	$T_c^{\downarrow}$	
Free SCO-1	n.a.[a]	n.a.[a]	345[b] (22)	323[b]	336[b] (13)	323[b]	293
			282[c] (6)	276[c]	291[c] (5)	286[c]	
SCO-1@MCM	330 (20)	310	389[d] (49)	340[d]	394[d] (49)	345[d]	This work
			371[e] (31)	340[e]	376[e] (31)	345[e]	
Free SCO-2	380 (36)	344	385 (40)	345	373[f] (30)	343[f]	293, this work
SCO-2@MCM	342 (14)	328	381 (35)	346	385 (34)	351	This work

[a] n.a.= not available. [b] Hydrated material, $[Fe(Htrz)_3](BF_4)_2 \cdot H_2O$. [c] Dehydrated material. [d] First heating and cooling cycle on hydrated material. [e] Second to fourth cycle on dehydrated material. [f] Optical reflectance measurements were recorded in this work on SCO-2 prepared as nanoparticles in the liquid state according to Ref. 301

It is worth to notice that, after Mössbauer measurements, DC magnetic measurements and optical reflectivity measurements, the strong "matrix effect" is found only for SCO-1@MCM, whereas "matrix effect" for SCO-2@MCM is much weaker (compared to SCO-1@MCM). We trace this to the hydration of SCO-1, which contains crystal water (Figure 4.17) and suggest that water is important as a "pressure mediator" for delivering the "hydrostatic pressure" to induce a significant matrix effect. However, the specific reasons of the action of crystal water still need

further investigation. The crystal water in SCO-1@MCM is partly lost upon heating to 127 °C (400 K) (cf. Figure 4.17) which explains the shifts from the first to the second cycle in the warming temperatures ($T_c^{\uparrow}$) in Figure 4.14 and Figure 4.15.

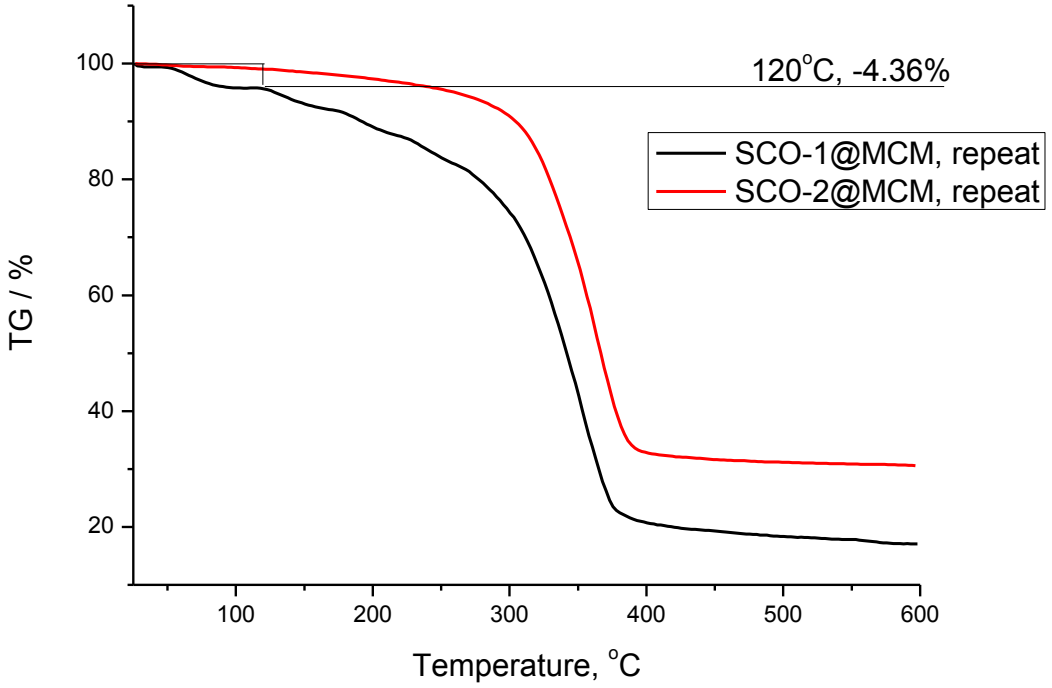

Figure 4.17. TG curves of the SCO@MCM materials.

Thermogravimetric analysis (TGA) shows that SCO-1@MCM possesses one water molecule per each unit, whereas SCO-2@MCM nearly does not contain solvent. Each sample was heated up to 600 °C with a rate of 5 °C/min. Up to 120 °C, 4.36 and 0.95 wt.% are lost for SCO-1 and SCO-2@MCM, respectively (Figure 4.17).

Table 4.5. Overview of ^{57}Fe Mössbauer parameters for SCO-1@MCM.[a]

T [K]	δ [mm/s]	ΔE_Q [mm/s]	$\Gamma/2$ [mm/s]	Relative Area [%]	Sites
78	0.43(1)	0.26(2)	0.13(1)	100	LS
298↑	0.42(1)	0.26(1)	0.15(1)	100	LS
303↑	0.41(1)	0.26(1)	0.16(1)	100	LS
308 ↑					

	0.40(1)	0.26(1)	0.16(1)	100	LS
313 ↑	0.40(1)	0.26(1)	0.16(1)	100	LS
318 ↑	0.39(1)	0.25(1)	0.17(1)	100	LS
323 ↑	0.38(1)	0.26(1)	0.17(1)	100	LS
328 ↑	0.38(1)	0.26(1)	0.18(1)	100	LS
333↑	0.97(1) 0.46(1)	2.30(1) 0.28(1)	0.13(1) 0.29(1)	80.0 20.0	HS LS
338 ↑	0.96(1) 0.45(1)	2.25(1) 0.28(1)	0.13(1) 0.26(1)	83.0 17.0	HS LS
343 ↑	0.95(1) 0.45(1)	2.21(1) 0.34(1)	0.13(1) 0.31*	83.0 17.0	HS LS
348 ↑	0.94(1) 0.44(1)	2.18(1) 0.34*	0.14(1) 0.31*	85.0 15.0	HS LS
353 ↑	0.93(1) 0.43*	2.15(1) 0.36(2)	0.13(1) 0.28(1)	87.0 13.0	HS LS
358	0.93(1) 0.43(1)	2.10(1) 0.38*	0.13(1) 0.26*	87.0 13.0	HS LS
353↓	0.94(1) 0.43(1)	2.14(1) 0.35*	0.14(1) 0.32(1)	87.0 13.0	HS LS
348↓	0.94(1) 0.44(1)	2.13(1) 0.38(1)	0.14(1) 0.33(1)	87.0 13.0	HS LS
343↓	0.95(1) 0.45*	2.21(1) 0.34*	0.13(1) 0.34(1)	83.0 17.0	HS LS
338↓	0.96(1) 0.45(1)	2.25(1) 0.32*	0.14(1) 0.46(1)	83.0 17.0	HS LS
333↓	0.97(1) 0.46(1)	2.29(1) 0.35*	0.16(1) 0.44(1)	82.0 18.0	HS LS
328↓	0.98(1) 0.47(1)	2.32(1) 0.30*	0.14(1) 0.45(1)	82.0 18.0	HS LS
318↓	0.99(1) 0.49(1)	2.39(1) 0.35*	0.14(1) 0.31(1)	81.0 19.0	HS LS
313↓	0.99(1) 0.54(1)	2.42(1) 0.47(1)	0.14(1) 0.26(1)	75.0 25.0	HS LS
308↓	0.99(1) 0.50(1)	2.42(1) 0.31(1)	0.15(1) 0.16(1)	5.0 95.0	HS LS
303↓	0.99(1) 0.50(1)	2.40(1) 0.30(1)	0.14(1) 0.16(1)	5.0 95.0	HS LS
298↓	1.07(1) 0.49(1)	2.63(1) 0.30(1)	0.16(1) 0.16(1)	5.0 95.0	HS LS

[a] ↑ indicates warming and ↓ indicates cooling; δ = isomer shift relative to α-iron, ΔE_Q = quadrupole splitting, Γ/2 = half width at half maximum, *Fixed parameter.

Table 4.6. Overview of ^{57}Fe Mössbauer parameters for SCO-2@MCM.[a]

T [K]	δ [mm/s]	ΔE_Q [mm/s]	$\Gamma/2$ [mm/s]	Relative Area [%]	Sites
78	0.42(1)	0.23(1)	0.18(1)	100	LS
298↑	0.43(1)	0.28(1)	0.14(1)	100	LS
303↑	0.42(1)	0.29(1)	0.14(1)	100	LS
308↑	0.42(1)	0.29(1)	0.14(1)	100	LS
318↑	0.42(1)	0.29(1)	0.14(1)	100	LS
323↑	0.42(1)	0.29(1)	0.14(1)	100	LS
328↑	0.41(1)	0.29(1)	0.14(1)	100	LS
333↑	0.40(1)	0.29(1)	0.15(1)	100	LS
338↑	0.98(1) 0.39(1)	2.53(1) 0.29(1)	0.19* 0.15(1)	7.0 93.0	HS LS
343↑	0.97(1) 0.39(1)	2.29(1) 0.27(1)	0.15(1) 0.16(1)	47.0 53.0	HS LS
348↑	0.96(1) 0.41(1)	2.27(1) 0.29*	0.14(1) 0.37(1)	86.0 14.0	HS LS
353↑	0.96(1) 0.41(1)	2.25(1) 0.28*	0.15(1) 0.41(1)	86.0 14.0	HS LS
358↑	0.95(1) 0.41(1)	2.21(1) 0.28(3)	0.14(1) 0.32(2)	85.0 14.0	HS LS
343↓	0.97(1) 0.41(1)	2.32(1) 0.28*	0.14(1) 0.32(1)	85.0 14.0	HS LS
338↓	0.97(1) 0.41(1)	2.35(1) 0.28*	0.15(1) 0.32*	85.0 14.0	HS LS
333↓	0.98(1) 0.42(1)	2.37(1) 0.30*	0.14(1) 0.32*	85.0 15.0	HS LS
328↓	0.99(1) 0.40(1)	2.41(1) 0.30(1)	0.14(1) 0.16(1)	41.0 59.0	HS LS
323↓	0.44(1)	0.27(1)	0.11(1)	100	LS
318↓					

	0.42(1)	0.30(1)	0.14(1)	100	LS
313↓	0.43(1)	0.29(1)	0.12(1)	100	LS
308↓	0.43(1)	0.29(1)	0.13(1)	100	LS
303↓	0.41(1)	0.31(1)	0.16(1)	100	LS
298↓	0.41(1)	0.31(1)	0.16(1)	100	LS

[a] ↑ indicates warming and ↓ indicates cooling; δ = isomer shift relative to α-iron, ΔE_Q = quadrupole splitting, Γ/2 = half width at half maximum, *Fixed parameter.

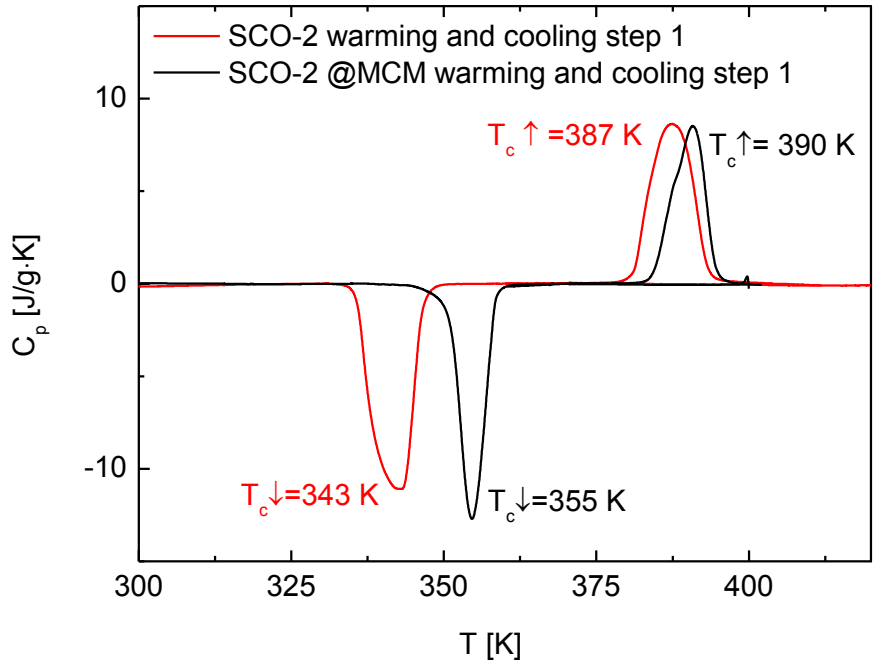

Figure 4.18 Heat capacity vs T for SCO-2 and SCO-2@MCM recorded by differential scanning calorimetry at 10 K/min

DSC measurements of SCO-2 reveal a qharp endothermic peak in warming and an exothermic peak on cooling at $T_{max}^{\uparrow}$= 387 K and$T_c^{\downarrow}$ = 343K respectively. SCO-2@MCM reveals a similar pattern with a shift in temperature upwards at $T_{max}^{\uparrow}$= 390 K and$T_c^{\downarrow}$ = 355K, both at 10 K/min (Figure 4.18).

4. Conclusion

Composite materials made of MCM-41 and of two 1D SCO compounds, namely $[Fe(Htrz)_3](BF_4)_2 \cdot H_2O$ (SCO-1)and $[Fe(Htrz)_2trz]BF_4$ (SCO-2)were successfully prepared with the identification of nanoobjects of ~2nm size. Although location of the 1D chain is remote from the walls of the host matrix, as concluded from temperature variable ^{57}Fe Mössbauer spectroscopy, a pressure effectwas identified for SCO-1@MCM by temperature variable magnetic and optical reflectance measurements, enabling the spin transition to be shifted to higher temperatures, compared to the bulk material. For SCO-1@MCM the LS→HS transition ($T_c^{\uparrow}$) was increased by 44-58 K and the HS→LS transition ($T_c^{\downarrow}$) by 17-22 K in comparison to bulk SCO-1 during the first warming-cooling cycle. During the first warming to about 400 K partial dehydration occurs. For the partially dehydrated SCO-1@MCM material this shift was even more pronounced with $T_c^{\uparrow}$ increased by 85-89 K and $T_c^{\downarrow}$ increased by 59-64 K relative to bulk SCO-1. The range given reflects the values from two different methods (temperature variable magnetic and optical reflectance measurements). Also, the hysteresis between $T_c^{\uparrow}$ and $T_c^{\downarrow}$ increases by 26-33 K when placing SCO-1 into the MCM-41 matrix. In the case of SCO-2@MCM this pressure or matrix effect only becomes evident upon comparison to a nanoSCO-2 material which was done by the optical reflectance measurements. The significant difference in matrix effect on the SCO behavior of the similar materials SCO-1 and SCO-2 is traced to the hydration of the SCO-1 and SCO-1@MCM material. This hydration is only partially lost during the first heating cycle. Water is apparently crucial in exerting a confinement pressure or matrix effect on the spin transition.

Acknowledgment

Prof. Christoph Janiak and Dr. Ishtvan Boldog are gratefully acknowledged for the guidance of SCO@MCM composites work in this chapter. Prof. Yann Garcia and Dr. Marinela M. Dîrtu are gratefully acknowledged for Mössbauer characterization. Dr. Laure Cuignet and Dr. Aurelian Rotaru are acknowledged for optical reflectivity measurements. Prof. Vojislav Spasojevic is thanked for DC magnetic measurements. Dr. Mariusz Wolff is thanked for preparation of nanoparticles of SCO-2 in this chapter.

Chapter 5

Coordination polymers and MOFs based on carboxyphenyladamantanes

1. Introduction

In the past two decades, metal–organic frameworks (MOFs) become the most attractive porous materials known today,[324] exhibiting outstanding high surface areas, flexible structures, adjustable surface functionality, tuneable pore sizes and shapes, and the broad application potential. Thus, it is always interested to obtain new structure MOFs for the scientists.

Recently, three Zr(IV)/Hf(IV) based MOFs, which combined with linear 2,6-naphtalene dicarboxylate, have hexanuclear eight-connected clusters involving carboxylates were reported.[325] Another two stable, non-interpenetrated Zr/Hf MOFs based on a rigid tetrahedral ligand were easily synthesized and provide a systematic way of constructing non-interpenetrated MOFs with high porosity (BET surface area up to 3411 m^2/g).[326] Thus, combination of these eight connected clusters with the tetrahedral four-connected node associated with $Ad(PhCOO)_4$ (Ad = adamantine, Ph = phenyl) might lead to formation of new porous MOFs. Tris-carboxyphenyladamantane ligand-analogue can be used for construction of a porous coordination polymer with a FeS_2 topology based on a $Zn_6(\mu\text{-}O_6)$ cluster.[327] So, $Ad(PhCOO)_3$ ligand is a potential candidate to form porous structure.

In this chapter, three carboxyphenyladamantanes ligands $Ad(PhCOO)_4$, $Ad(PhCOO)_3$ and $Ad(PhCOO)_2$ (Ad = adamantine, Ph = phenyl) were used to synthesize new MOFs. The standard crystallization was usually conducted under a mild solvothermal condition. Suitable single crystals were carefully selected under a polarizing microscope and sent to do single-XRD measurement. Here four new coordination polymers and MOFs were successfully synthesized based on above three ligands. All of them were uniformed crystals and their structures were determined by single-crystal X-ray diffraction analysis.

The three carboxyphenyladamantanes ligands (Scheme 5.1) which used in this chapter were

synthesized and obtained from Dr. Ishtvan Boldog. The analysis and purification of ligands were also conducted by Dr. Ishtvan Boldog. My work was mainly focus on the possible syntheses for new structure MOFs, hence, the synthesis procedure and analytical data of ligands were not involved in this thesis.

Scheme 5.1. Schematic drawings of $Ad(PhCOOH)_X$ ligands.

2. Experimental

2.1. Materials

All the chemicals were purchased from the following distributors (Table 5.1) and used without further purification.

Table 5.1. The information of chemicals which used in this chapter.

Reagent	Purity, % / Grade	Commercial Source
Manganese(II) chloride tetrahydrate	⩾98%	Sigma-Aldrich
Cobalt(II) chloride hexahydrate	98%	Sigma-Aldrich
Cadmium chloride hemi(pentahydrate)	⩾98%	Sigma-Aldrich
N, N-Dimethylformamide	99.9 %	VWR
Ethanol	99.9 %	Merck

2.2. Synthesis

2.2.1. Synthesis of $\{Co[Ad(COOH)_2(COO)_2]\}\cdot xDMF\cdot yH_2O$ (compound 1)

A mixture of the 4,4',4",4"'-(adamantane-1,3,5,7-tetrayl) tetrabenzoic acid ($Ad(PhCOOH)_4$)

ligand (30.8 mg, 0.05 mmol) and $CoCl_2 \cdot 6H_2O$ (13 mg, 0.1 mmol) were dissolved in 2 mL N,N-Dimethylformamide (DMF) and sealed in a Pyrex glass tube (i.d. 8 mm/o.d. 10 mm). The tube was placed in an oven and heating at 80 °C for 72 h, then it was cooled to ambient temperature at a rate of 0.1 °C/min.

The resulting blue-violet crystals were washed with DMF several times to give pure $\{Co[Ad(COOH)_2(COO)_2]\} \cdot nDMF$ (Figure 5.1).

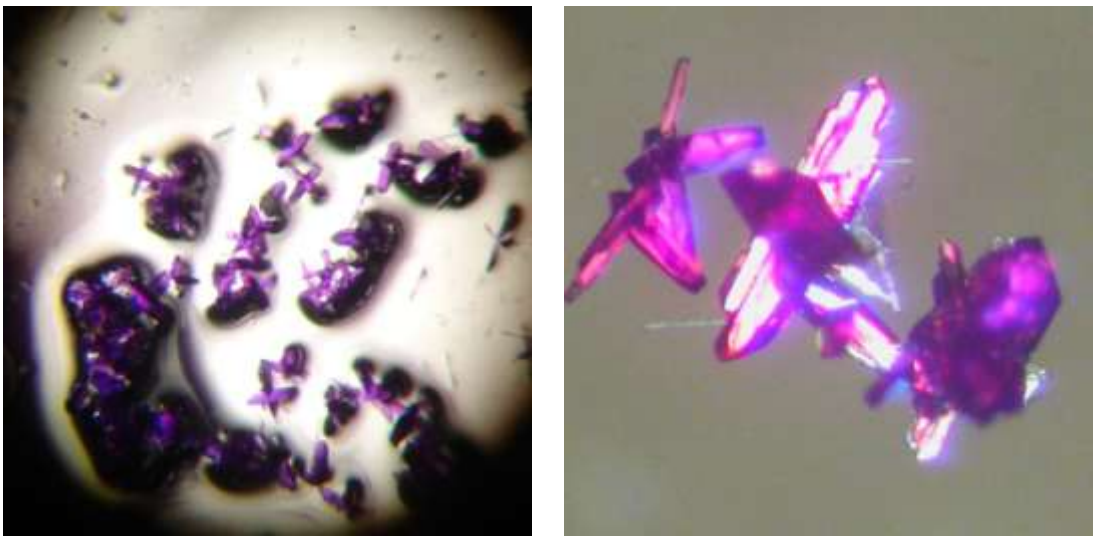

Figure 5.1. $\{Co[Ad(COOH)_2(COO)_2]\} \cdot xDMF \cdot yH_2O$ violet cross needle crystals observed under a microscope. Bulk crystals on the left were placed in paraffin oil.

2.2.2. Synthesis of $Mn[Ad(PhCOO)_4] \cdot xDMF \cdot yH_2O$ (compound 2)

A mixture of the 4,4',4",4"'-(adamantane-1,3,5,7-tetrayl) tetrabenzoic acid ($Ad(PhCOOH)_4$) ligand (30.8 mg, 0.05 mmol) and $MnCl_2 \cdot 4H_2O$ (20 mg, 0.1 mmol) were dissolved in 2 mL N,N-Dimethylformamide (DMF) and sealed in a Pyrex glass tube (i.d. 8 mm/o.d. 10 mm). The tube was placed in an oven and heating at 100 °C for 72 h, then it was cooled to ambient temperature at a rate of 0.1 °C/min.

The resulting colorless crystals were washed with DMF several times to give pure $Mn[Ad(PhCOO)_4] \cdot nDMF$ (Figure 5.2).

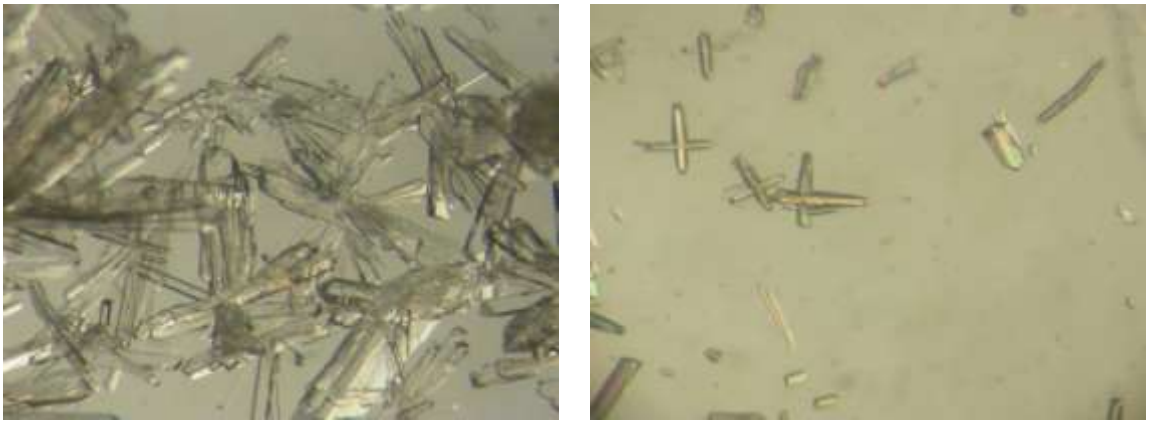

Figure 5.2. $Mn[Ad(PhCOO)_4]\cdot nDMF$ colorless cross needle crystals observed under a microscope. Bulk crystals on the left were placed in paraffin oil.

2.2.3. Synthesis of $Mn[Ad(PhCOO)_2\cdot DMF]$ (compound 3)

A mixture of the 4,4'-((1s,3s,5r,7r)-adamantane-1,3-diyl)dibenzoic acid ($Ad(PhCOOH)_2$) ligand (18.8 mg, 0.05 mmol) and $MnCl_2\cdot 4H_2O$ (20 mg, 0.1 mmol) were dissolved in 1 mL N,N-Dimethylformamide (DMF) and sealed in a Pyrex glass tube (i.d. 8 mm/o.d. 10 mm). The tube was placed in an oven and heating at 140 °C for 72 h, then it was cooled to ambient temperature at a rate of 0.1 °C/min.

The resulting colorless crystals were washed with DMF three times to give pure $Mn[Ad(PhCOO)_2\cdot DMF]$ (Figure 5.3).

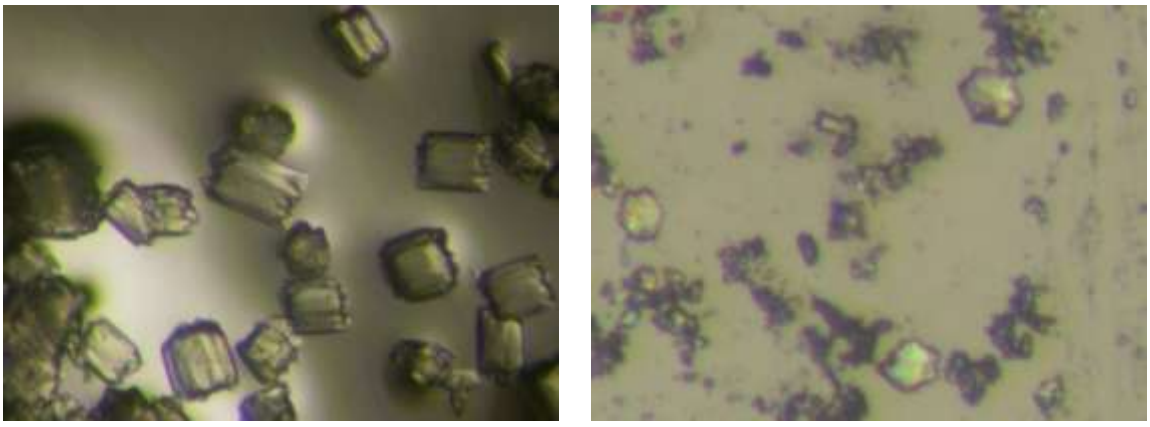

Figure 5.3. $Mn[Ad(PhCOO)_2\cdot DMF]$ colorless crystals observed under a microscope. Bulk crystals on the left were placed in paraffin oil.

2.2.4. Synthesis of $\{Cd[Ad(PhCOO)_3\cdot xDMF\cdot yH_2O]\}\cdot mH_2O\cdot nDMF$ (compound 4)

A mixture of the 4,4',4''-((1s,3s,5s)-adamantane-1,3,5-triyl)tribenzoic acid ($Ad(PhCOOH)_3$) ligand (12.4 mg, 0.025 mmol) and $CdCl_2 \cdot 2{,}5H_2O$ (11.4 mg, 0.05 mmol) were dissolved in 1 mL N,N-Dimethylformamide (DMF) and sealed in a Pyrex glass tube (i.d. 8 mm/o.d. 10 mm). The tube was placed in an oven and heating at 130 °C for 72 h, then it was cooled to ambient temperature at a rate of 0.1°C/min.

The resulting colorless crystals were washed with DMF three times to give pure $Cd[Ad(PhCOO)_3 \cdot xDMF \cdot yH_2O]$ (Figure 5.4).

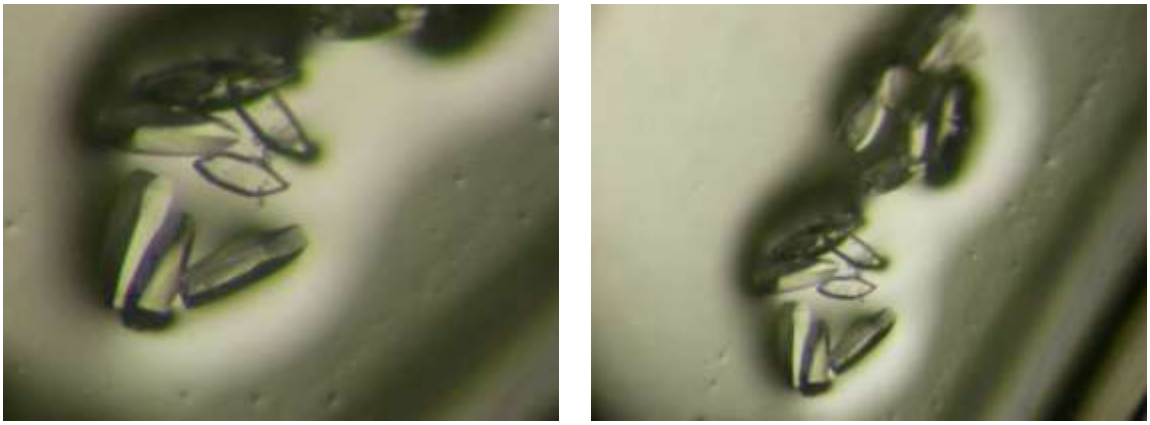

Figure 5.4. $Cd[Ad(PhCOO)_3 \cdot xDMF \cdot yH_2O]$ colorless crystals observed under a microscope. Bulk crystals were placed in paraffin oil.

2.3. Characterization

X-ray diffraction analyses were carried out on a PANalytical X'Pert PRO diffractometer using Cu $K\alpha_1/\alpha_2$ radiation with λ = 1.5418 Å and a Ni-foil as K_β-filter. Suitable single crystals were carefully selected under a polarizing microscope. The structure was solved by direct methods using SHELXS-97; refinement was done by full-matrix least squares on F^2 using the SHELXL-97 program suite.[328] The data were collected on a PANalytical X'Pert PRO X-ray diffractometer and obtained by Rietveld refinement.[329]

Powder X-ray diffraction (PXRD) measurements were carried out at Univ. Düsseldorf on samples at ambient temperature with a Bruker D2 Phaser using a flat silicon, low background sample holder and Cu-K_α radiation (λ = 1.54184 Å) at 30 kV and 0.04°/s. Simulated PXRD patterns were calculated from single-crystal data using the MERCURY 3.0.1 software suite from CCDC.

The N_2 adsorption/desorption measurements from which the BET surface area is obtained were performed on a Quantachrome NOVA 4000 instrument at 77K. Normally, the samples were degassed under high vacuum (10^{-5} Torr) at 200°C for at least 2 h, prior to each measurement.

Thermogravimetric analysis (TGA) was performed with a Netzsch TG209 F3 Tarsus instrument.

FT-IR measurements were carried out on a Bruker TENSOR 37 IR spectrometer at ambient temperature in the range of 4000 to 500 cm−1 either in a KBr pellett or with an ATR unit (Platinum ATR-QL, Diamond).

Elemental (CHN) analyses were carried out on a Perkin Elmer CHN 2400.

3. Results and Discussion

3.1. {Co[Ad(COOH)$_2$(COO)$_2$]}·xDMF·yH$_2$O (compound 1)

Solvothermal reaction of cobalt(II) chloride with 4,4',4",4'"-(adamantane-1,3,5,7-tetrayl) tetrabenzoic acid (Ad(PhCOOH)$_4$) yields small blue-violet crystals of cross needle shape (Figure 5.1). Blue-violet crystals of dimensions 0.87×0.17×0.08 mm for compound **1** was used for structural determinations. The crystal system of compound 1 is orthorhombic, each Co bridges four carboxylate of the ligands formed Co(μ_8-O) node, each Ad(PhCOOH)$_4$ ligand bridges four Co(μ_8-O) cluster (Figure 5.5 a). Figure 5.5 b showed the section of crystal packing diagram of compound **1**, four carboxylate groups span the four edges of the Co(μ_8-O) secondary building unit, a polyhedral Co(μ_8-O) node fashion to yield the three-dimensional primitive tetrahedral framework shown here as ball-and-stick and as space-filling representation. The yellow sphere with a radius of 7 Å takes into account the van-der-Waals radii of the framework walls. The tunnels with the dimensions 8.6×8.6 Å^2 can be seen from c direction (Figure 5.5 c).

After evaluated the structure of compound **1**, it is quite curious that, the ligand of Ad(PhCOOH)$_4$ is doubly deprotonated. That means compound 1 is not very stable upon removal of solvent molecules. The consequent TG analysis curve was showed in Figure 5.6. There are two weight-loss steps can be observed: the first step, corresponding to 32%, occurs from 25 °C to 200 °C relates to the loss of gust molecules (water and DMF); the second step, corresponding to 43%, is due to the decomposition of the organic moieties and framework between 200 °C and 450 °C. Thus, compound **1** is thermal stable until 200 °C.

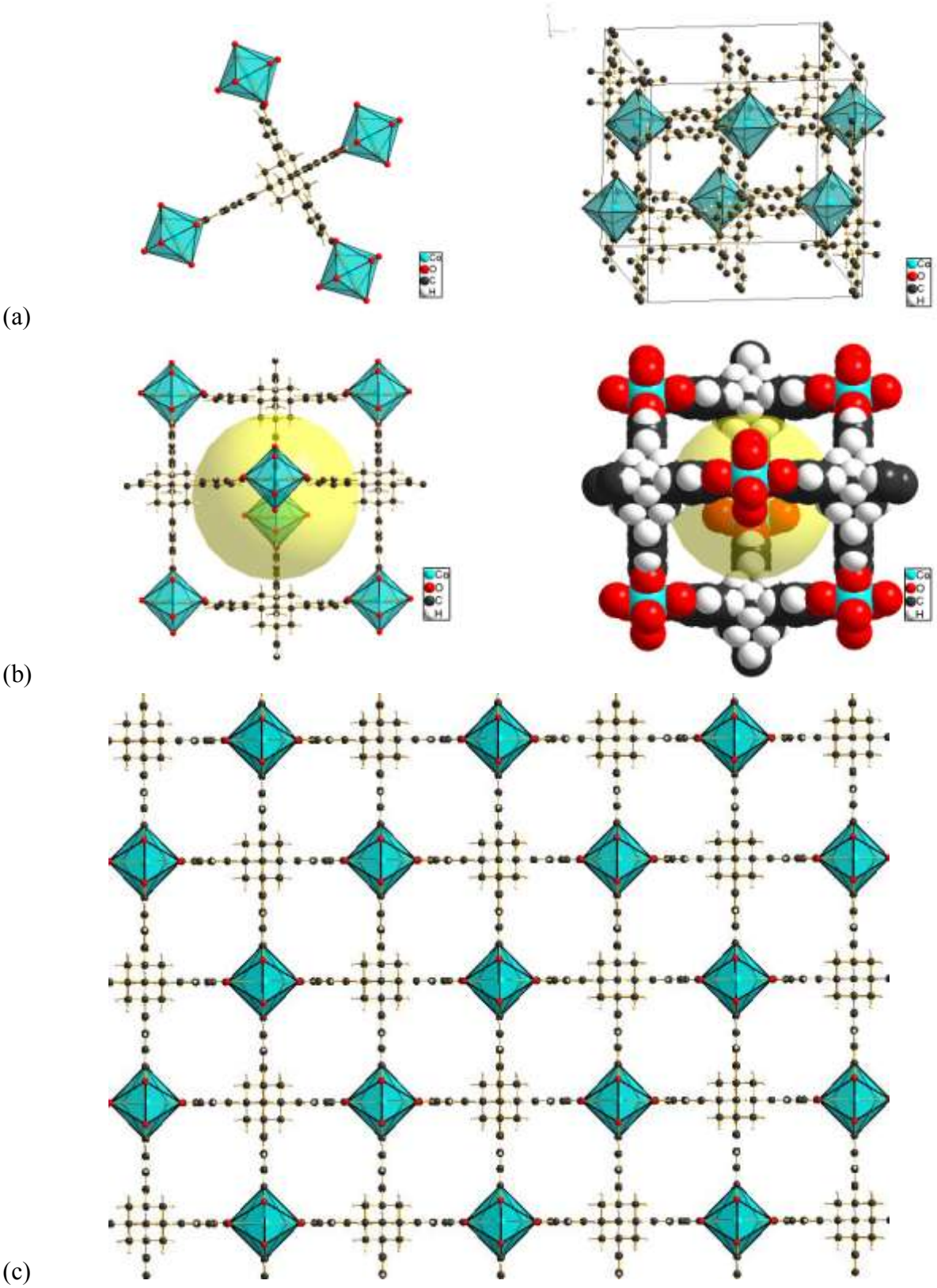

Figure 5.5. Co(μ_8-O) building unit and cell unit of compound **1**(a), ball-and-stick and space-filling plot of tetrahedral cavity of compound **1** (b), framework along c direction (c). (water/DMF-guest molecules are not shown). The different objects in this figure are not drawn to scale.

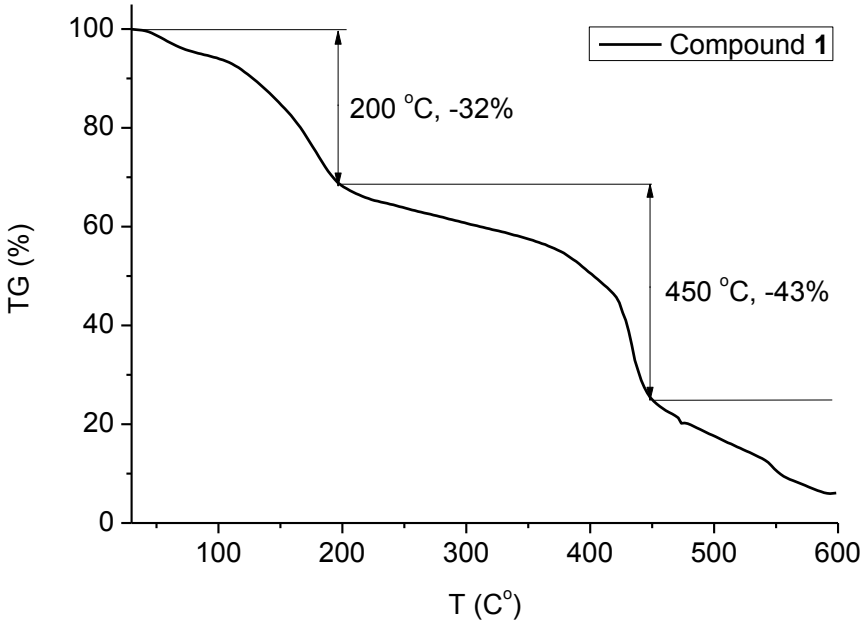

Figure 5.6. The TG curve of $\{Co[Ad(COOH)_2(COO)_2]\}\cdot xDMF\cdot yH_2O$ (compound **1**).

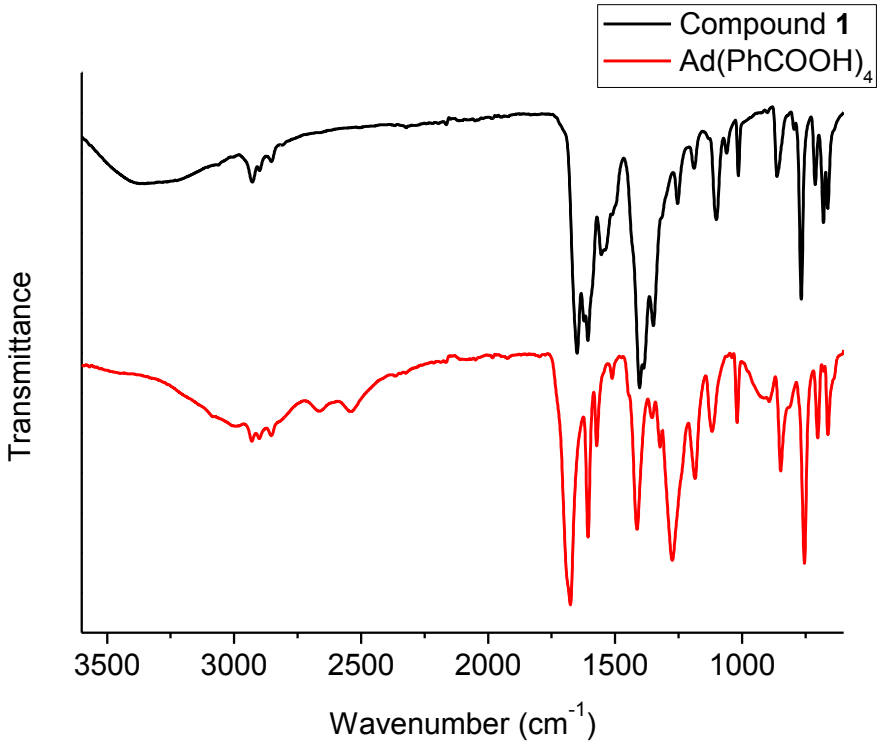

Figure 5.7. IR spectra of compound **1** in comparison to the bulk ligand $Ad(PhCOOH)_4$.

FT-IR spectra were recorded both on compound **1** and ligand $Ad(COOH)_4$ (Figure 5.7). The IR

spectra of $Ad(COOH)_4$ showed that the C=O stretch of carboxylate at 1675 cm^{-1}, whereas in compound **1**, this stretching frequency is shifted to lower value at 1650 cm^{-1}. The new peak at 1400cm^{-1} in the spectra of compound 1 indicated the C-N stretch of DMF.

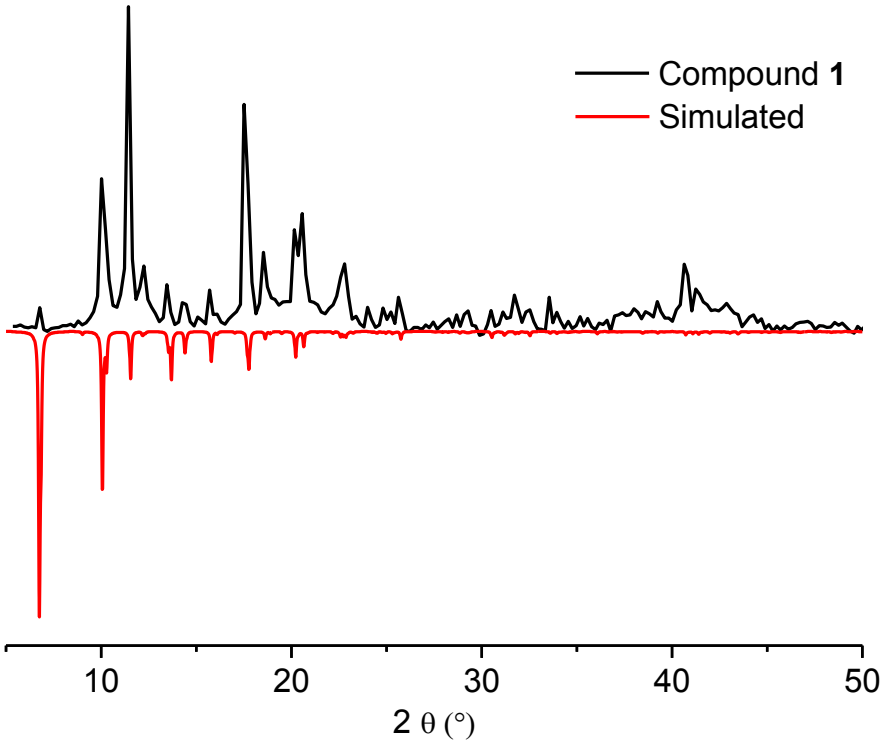

Figure 5.8. Powder X-Ray diffraction pattern of compound **1** in comparison to the simulated pattern (simulated pattern was obtained from single crystal measurement by program Mercury).

Matching powder X-ray diffractogram of compound **1** and the simulated pattern, we could found that, in the range of $5° < 2\theta < 25°$, all reflections of simulated pattern can be seen in the diffractogram of compound **1** (Figure 5.8). While the disordered reflections between 25° and 50° ascribed to the unreacted ligands and solvent molecules (like DMF). The high absorption coefficient of Co atoms limited the 2θ angle to 80° for Cu-Kα radiation and the data set quality.

According to the X-ray structure (Figure 5.5), the pore openings in the structural compounds **1** is not very large. And compound **1** is not very stable at high temperature, due to the ligand of $Ad(PhCOOH)_4$ is not fully deprotonated. Hence, the crystallinity of the compound **1** strongly depends on the duration of the heat treatment. Before the N_2 adsorption/desorption measurement,

the crystals of compound **1** were soaked in CH_2Cl_2 at 40 °C for one week in a sealed glass tube as solvent exchange. Then the sample was took out, washed with CH_2Cl_2 for several time and placed at room temperature for at least one day. Then this sample was degassed at 80°C for 2 h, prior to N_2 adsorption/desorption measurement start. The nitrogen sorption isotherms of compound **1** is given in Figure 5.9, with 423 m^2/g of BET surface area and 611 m^2/g of Langmuir surface area respectively.

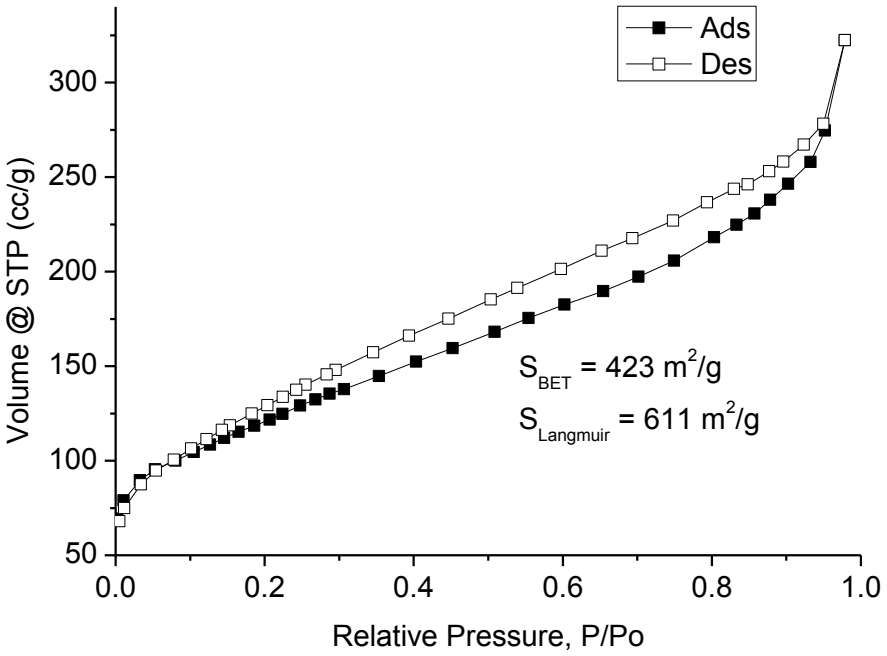

Figure 5.9. N_2 sorption isotherms of compound **1** (BET surface area was calculated in the pressure range 0.05 $< p/p_0 <$ 0.2 from N_2 sorption isotherm at 77 K with an estimated standard deviation of ± 50 m^2/g).

The N_2 sorption isotherm of compound **1** follows a type II isotherm, but with a hysteresis loop, which is associated with mesopores or macropores. The DFT calculation also gave a wide pore diameter distribution from 20 Å to 80 Å (Figure 5.10 A). That's probably the part crystallinity of the compound **1** was damaged in the degassing procedure of N_2 sorption measurement. The comparison of powder X-ray pattern confirmed that, after degassing the crystallinity structure of compound **1** was partly damaged, which can produce the mesopores or macroporous (Figure 5.10 B).

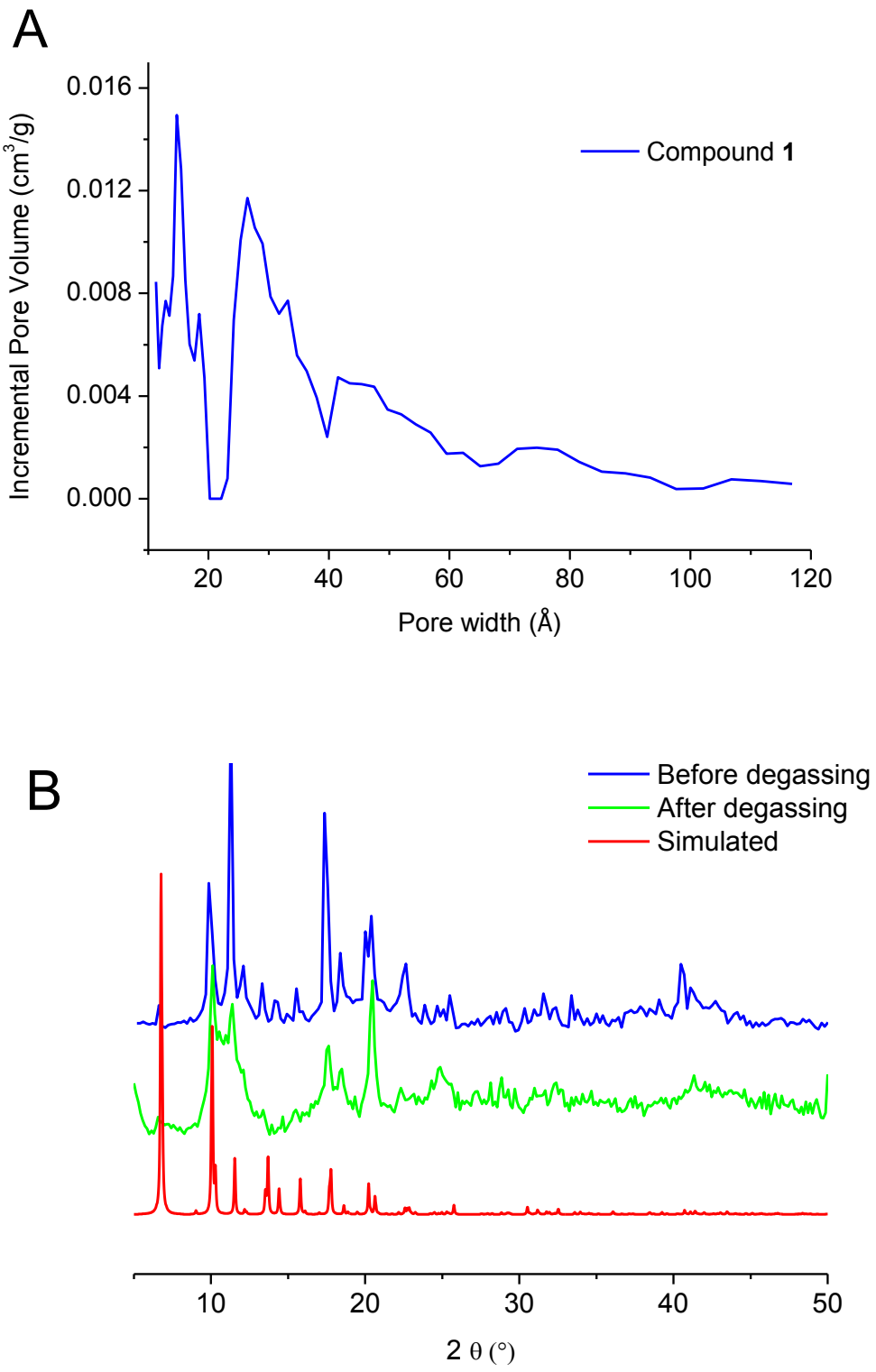

Figure 5.10. Pore size distribution of compound **1** from N_2 adsorption isotherm (at 77 K) analysis (A). Powder X-ray diffractograms of compound **1**, before and after degassing procedure in N_2 sorption measurement respectively (B).

Table 5.2. Crystal data and structure refinement for compound **1**.

Conpound	**{Co[Ad(COOH)$_2$(COO)$_2$]}·xDMF·yH$_2$O**
Empirical formula	$C_{44}H_{56}CoN_2O_{16}$
Formula weight (g/mol)	1121.23
Crystal size (mm)	0.87×0.17×0.08
2θ range (°)	1.56 - 25.16
h; k; l; range	-20<=h<=20; -20<=k<=20; -19<=l<=19
Crystal system	Orthorhombic
Space group	Imma (no. 74)
a (Å)	17.1936(15)
b (Å)	17.5541(14)
c (Å)	19.5950(16)
V (Å^3)	5914.13(80)
Z	8
D_{calc}(g / cm^3)	0.803373
F (000)	1420
μ(mm^{-1})	0.323
Max/min transmission	0.9756 / 0.7659
Reflection collected (R_{int})	2643 (0.1035)
Data completeness (%)	92.5
Independent reflections	1729
Parameters refined	88
Max/min (Δρ[a] /e Å^{-3})	8.391 / -1.742
R1/wR_2 [I > 2σ(I)][b]	0.3864 / 0.7642
R1/wR_2 (all reflections)[b]	0.4407 / 0.7991
Goodness-of-fit on F^{2c}	4.469

[a] Largest difference peak and hole. [b] $R1 = [\Sigma(\|F_0|-|F_c\|)/\Sigma|F_0|]$; $wR_2 = [\Sigma[w(F_0^2-F_c^2)^2]/\Sigma[w(F_0^2)^2]]^{1/2}$. [c] Goodness-of-fit $= [\Sigma[w(F_0^2-F_c^2)^2]/(n-p)]^{1/2}$.

The crystal solvent in the voids of compound **1** was found to be highly disordered and could not be properly defined. Thus, the option SQUEEZE in PLATON for Windows was used to refine the framework structure without the disordered electron density in the voids.[330] For compound **1**, a total of 1057 electrons per 3445 $Å^3$ was squeezed, which corresponds to ~132 electrons per $C_{38}H_{30}CoO_8$ formula unit (Z = 8). PLATON calculates a total potential solvent area volume of 3511 Å3 per unit cell volume of 5914.13 $Å^3$ (59.3 %). So the empirical formula of compound **1** is $\{Co[Ad(COOH)_2(COO)_2]\}\cdot 6DMF\cdot 2H_2O$ ($C_{44}H_{56}CoN_2O_{16}$). Calcd for $C_{44}H_{56}CoN_2O_{16}$: C 59.96; H 6.08; N 3.02. Found: C 56.14; H 6.15; N 3.83. Crystal data and details on the structure refinement are given in Table 5.2.

3.2. $Mn[Ad(PhCOO)_4]\cdot xDMF\cdot yH_2O$ (compound 2)

Solvothermal reaction of manganese(II) chloride with 4,4',4",4'"-(adamantane-1,3,5,7-tetrayl) tetrabenzoic acid ($Ad(PhCOOH)_4$) would yields a colorless crystals with cross needle shape (Figure 5.2). Colorless crystals of dimensions 0.50×0.15×0.15 mm for compound **2** was used for structural determinations. Similar to compound **1**, each Mn bridges four carboxylate of the ligands formed Mn(μ_8-O) node, each $Ad(PhCOOH)_4$ ligand bridges four Mn(μ_8-O) cluster (Figure 5.11 a). But the crystal system of compound **2** is triclinic, that is different from compound 1 (Figure 5.11 a). As we all known, the coordination chemistry of manganese(II) is dominated by four- and six-coordinate metal ions (five- and seven-coordination are also exist but no frequently seen), while coordination numbers higher than seven are seldom encountered in discrete molecules.[331] That because the formation of the eight-coordination manganese(II) complex is highly dependent on the type of ligand used in the synthesis. In fact, early in 1999, two eight-coordinate manganese(II) complexes based on nitrate ligands and the Schiff bases (N,N'-bis[1-(pyridin-2-yl)ethylidene]ethane-1,2-diamine and N,N'-bis[1-(pyridin-2-yl) benzylidene]ethane-1,2-diamine) had already reported.[332] Thus, it is not very surprise we get a eight-coordinated manganese(II) complex. The section of crystal packing diagram of compound **2** showed that, four carboxylate groups span the four edges of the Mn(μ_8-O) secondary building unit, a polyhedral Mn(μ_8-O) node fashion to yield the three-dimensional tetrahedral framework shown here as ball-and-stick and as space-filling representation (Figure 5.11b). The yellow sphere

(a)

(b)

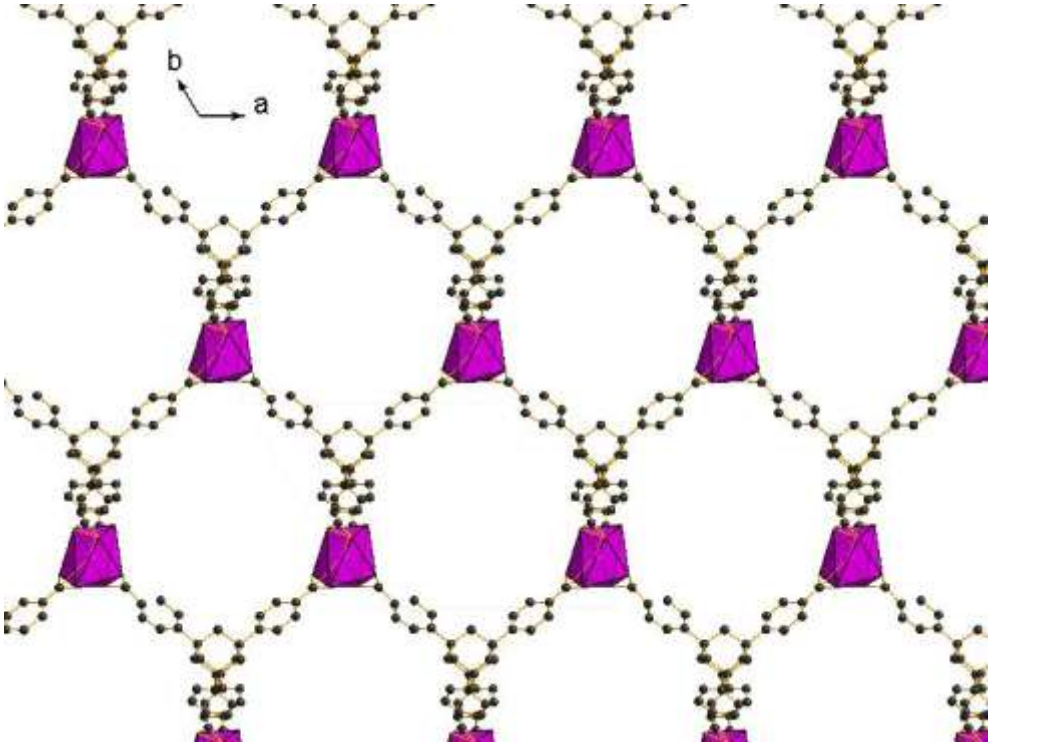

(c)

Figure 5.11. Mn(μ_8-O) building unit and cell unit of compound **2** (a), ball-and-stick and space-filling plot of tetrahedral cavity of compound **2** (b), framework along c direction (c). (water/DMF-guest molecules are not shown). The different objects in this figure are not drawn to scale.

with a radius of 7 Å takes into account the van-der-Waals radii of the framework walls. Along the c direction of the framework, the tunnels with the dimensions 12.1×16.2 $Å^2$ can be seen (Figure 5.11 c).

Unlike compound **1**, the ligand of compound **2** is fully deprotonated. The TG analysis curve of compound **2** was showed in Figure 5.12. There are also two weight-loss steps can be observed: the first step, corresponding to 37%, occurs from 25 °C to 200 °C relates to the loss of gust molecules (water and DMF); the second step, corresponding to 35%, is due to the decomposition of the organic moieties and framework between 200 °C and 520 °C.

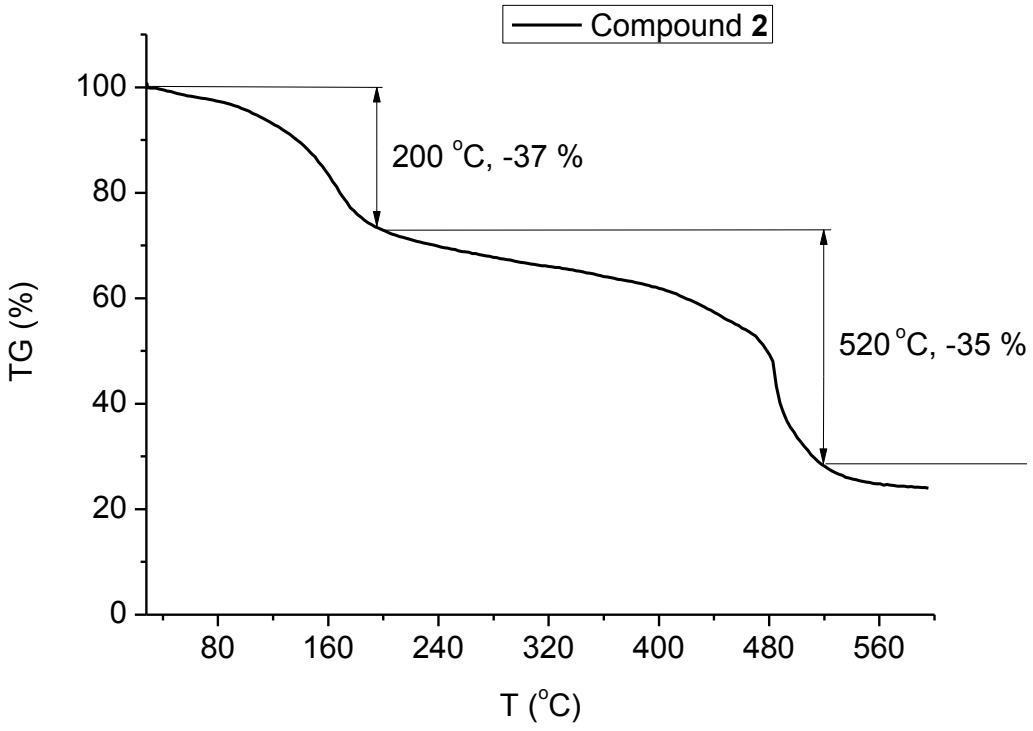

Figure 5.12. The TG curve of $Mn[Ad(PhCOO)_4]\cdot xDMF\cdot yH_2O$ (compound **2**).

FT-IR spectra were recorded both on compound **2** and ligand $Ad(COOH)_4$ (Figure 5.13). In spectra the C=O stretch of carboxylate of $Ad(COOH)_4$ is at 1675 cm^{-1}, whereas in compound **2**, this stretching frequency is also shifted to lower value at 1650 cm^{-1}, which highly agree with the observed result in compound **1**. The new peak at 1400cm^{-1} in the spectra of compound **2** indicated the C-N stretch of DMF solvent which trapped in void of framework.

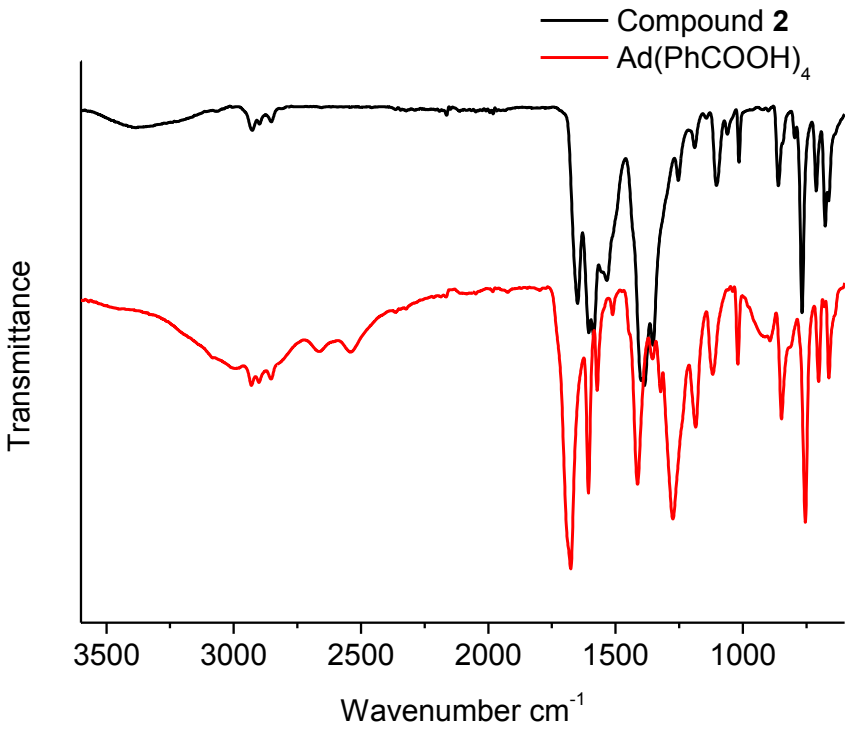

Figure 5.13. IR spectra of compound **2** in comparison to the bulk ligand $Ad(PhCOOH)_4$.

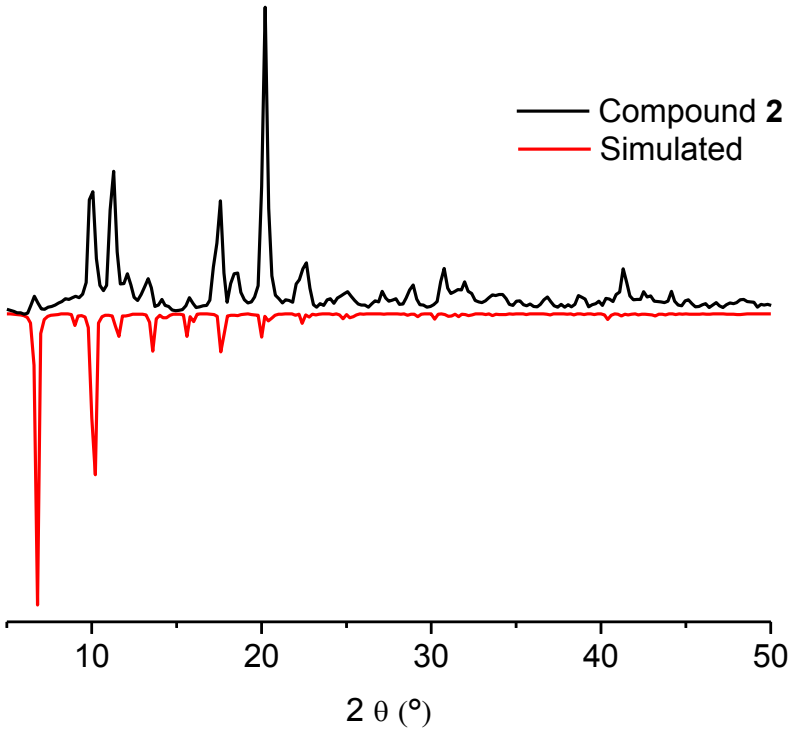

Figure 5.14. Powder X-Ray diffraction pattern of compound **2** in comparison to the simulated pattern (simulated pattern was obtained from single crystal measurement by program Mercury).

The PXRD pattern of compound **2** is generally agree with the simulated pattern (Figure 5.14). Nearly all the main reflections of simulated pattern can be found in the Powder X-ray diffractogram of compound **2**. But for compound **2**, several additional reflections came out, which probably ascribed to the unreacted ligands and solvent molecules.

According to the X-ray structure (Figure 5.11), compound **2** should also be porous. And before N_2 sorption measurement start, the solvent exchange with CH_2Cl_2 is necessary. The solvent exchange procedure is the same as compound **1**. The nitrogen sorption isotherms of compound **2** is given in Figure 5.15, with 289 m^2/g of BET surface area and 409 m^2/g of Langmuir surface area respectively. The surface areas of compound **2** is a bit lower than that of compound **1**.

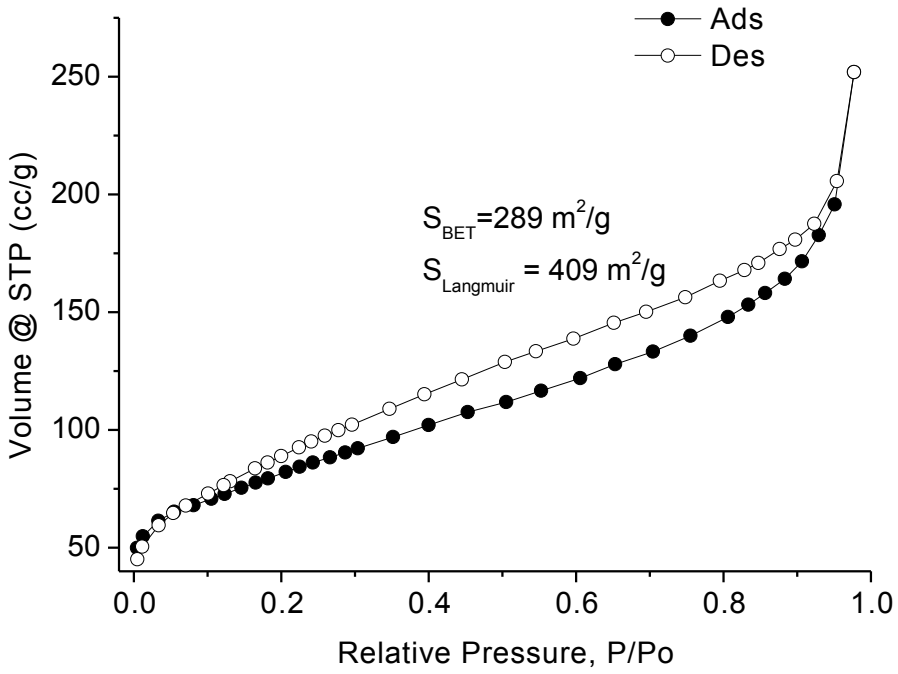

Figure 5.15. N_2 sorption isotherms of compound **2** (BET surface area was calculated in the pressure range 0.05 $< p/p_0 <$ 0.2 from N_2 sorption isotherm at 77 K with an estimated standard deviation of ± 50 m^2/g).

The surface areas of compound **2** is a bit lower than that of compound **1**, but the N_2 sorption isotherms has the same characteristic. The latter also follows a type II isotherm and possesses a hysteresis loop. The DFT calculation give a wide pore diameter distribution from 20 Å to 80 Å (Figure 5.16 Top), which confirms the mesopores and macropores in compound **2**. The reason is

probably due to that, the crystallinity structure of compound **2** is also not very stable with heating and high vacuum conditions. Thus, in the process of degassing of nitrogen sorption measurement, the structure of compound **2** was partly damaged. We could see the obvious difference via compare the PXRD patterns of compound **2** which corresponding to before and after degassing procedure (Figure 5.16 Bottom).

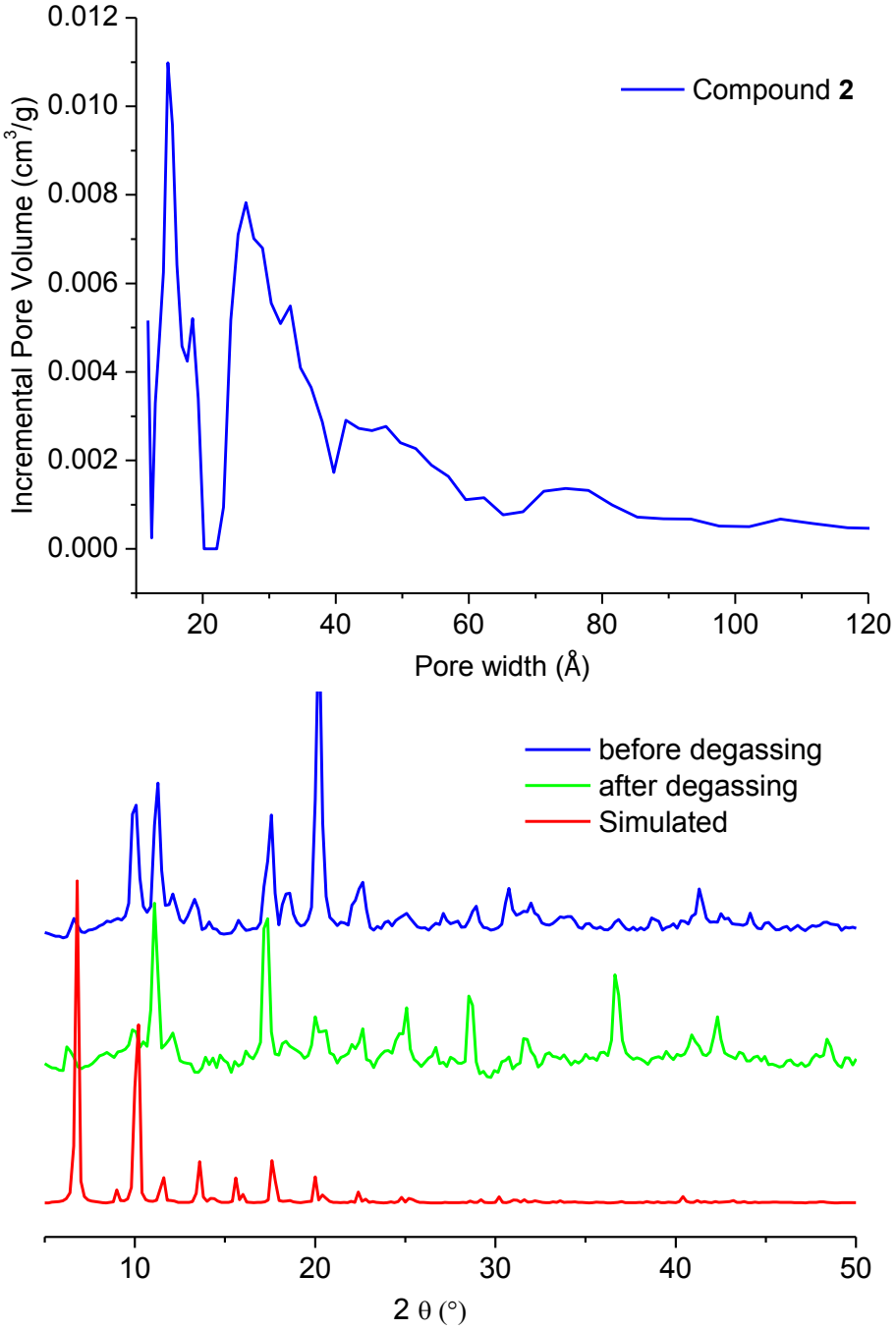

Figure 5.16. Pore size distribution of compound **2** from N_2 adsorption isotherm (at 77 K) analysis (Top). PXRD patterns of compound **2** corresponding to before and after degassing procedure (Bottom).

Table 5.3. Crystal data and structure refinement for compound **2**.

Conpound	**$Mn[Ad(PhCOO)_4]\cdot xDMF\cdot yH_2O$**
Empirical formula	$C_{53}H_{73}Mn\ N_5O_{18}$
Formula weight (g/mol)	1122.43
Crystal size (mm)	0.50×0.15×0.15
2θ range (°)	1.550 - 25.756
h; k; l; range	-19<=h<=17; -19<=k<=17; -19<=l<=19
Crystal system	Triclinic
Space group	P-1 (no. 2)
a (Å)	15.7783(17)
b (Å)	15.7980(17)
c (Å)	15.7985(19)
V ($Å^3$)	3007.47(67)
Z	2
D_{calc}(g / cm^3)	0.738253
F (000)	634
μ(mm^{-1})	0.247
Max/min transmission	0.964 / 0.886
Reflection collected (R_{int})	9693 (0.0725)
Data completeness (%)	97.9
Independent reflections	2983
Parameters refined	376
Max/min ($\Delta\rho^a$ /e $Å^{-3}$)	0.524 / -0.375
$R1/wR_2$ [$I > 2\sigma(I)$][b]	0.1498 / 0.3597
$R1/wR_2$ (all reflections)[b]	0.2294 / 0.3722
Goodness-of-fit on F^{2c}	1.426

[a] Largest difference peak and hole. [b] $R1 = [\Sigma(\|F_0\|-\|F_c\|)/\Sigma|F_0|]$; $wR_2 = [\Sigma[w(F_0^2-F_c^2)^2]/\Sigma[w(F_0^2)^2]]^{1/2}$. [c] Goodness-of-fit $= [\Sigma[w(F_0^2-F_c^2)^2]/(n-p)]^{1/2}$.

For compound **2**, a total of 377 electrons per 1840 $Å^3$ was squeezed, which corresponds to ~189 electrons per $C_{38}H_{28}MnO_8$ formula unit (Z = 2). PLATON calculates a total potential solvent area volume of 1858 $Å^3$ per unit cell volume of 3007.47 $Å^3$ (61.8 %). So the empirical formula of compound 2 is $Mn[Ad(PhCOO)_4]\cdot 5DMF\cdot 5H_2O$ ($C_{53}H_{73}MnN_5O_{18}$). Calcd for $C_{53}H_{73}MnN_5O_{18}$: C 56.68; H 6.55; N 6.24. Found: C 54.94; H 6.07; N 6.59. Crystal data and details on the structure refinement are given in Table 5.3.

3.3. Mn[Ad(PhCOO)$_2$·DMF] (compound 3)

Solvothermal reaction of manganese(II) chloride with 4,4'-((1s,3s,5r,7r)-adamantane-1,3-diyl) dibenzoic acid ($Ad(PhCOOH)_2$) would yields a colorless crystals (Figure 5.3). Colorless crystals of dimensions 0.10×0.10×0.02 mm for compound **3** was used for structural determinations. The crystal system of compound **3** is monoclinic; it contains $\{Mn_2\}$ units coordinated by four carboxylate groups in the well-known paddle-wheel structure of copper acetate. And each Mn atom coordinated a DMF molecule in this structure (Figure 5.17 a). Each $Ad(PhCOOH)_2$ ligand possesses two carboxylate which combined two $\{Mn_2\}$ units to form a two dimensional network structure (Figure 5.17 b). Along the c direction of the network, the tunnels with the dimensions 10.2×14.4 $Å^2$ can be seen (Figure 5.17 b).

Thermogravimetric analysis (TGA) shows that compound **3** only contain small amount of free solvent molecules (Figure 5.18). Up to 300 °C, 19 wt% are lost, which are corresponding to the crystal DMF in the structure. Then an addition lost of 48 wt% between 300 °C and 530 °C are due to the decomposition of the organic moieties and network. Thus, the thermal stability of compound **3** could up to 300 °C, which is higher than compound 1 and 2.

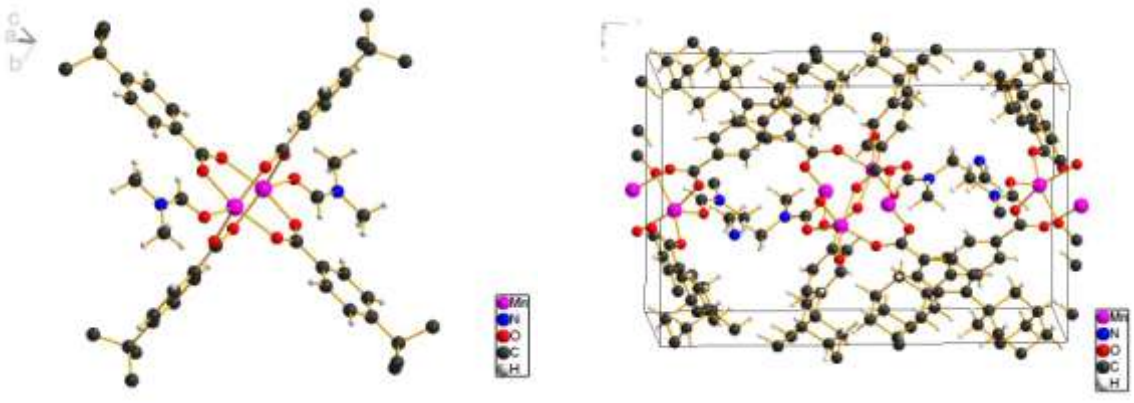

(a)

(b)

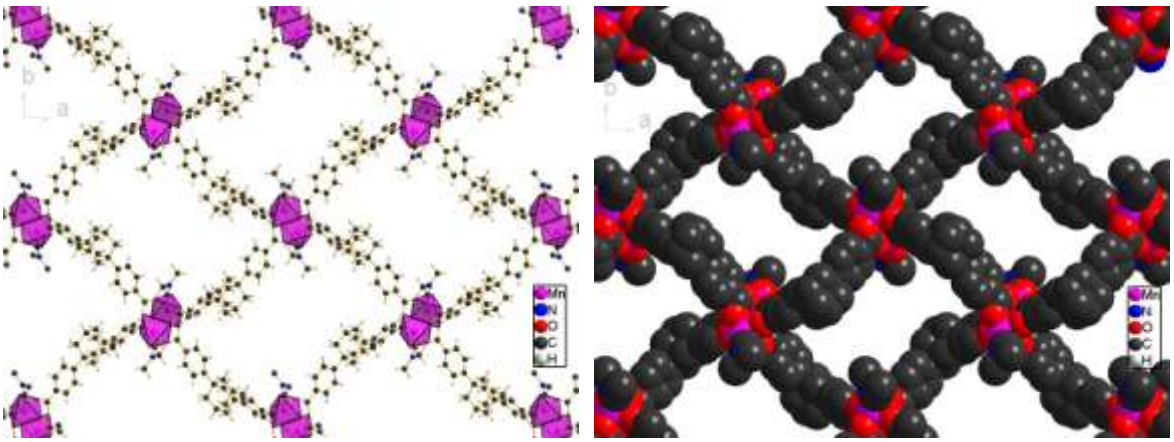

Figure 5.17. $\{Mn_2(\mu_4\text{-}O)\cdot 2DMF\}$ building unit and cell unit of compound **3** (a), the network along c direction with ball-and-stick model and as space-filling model respectively (b). The different objects in this figure are not drawn to scale.

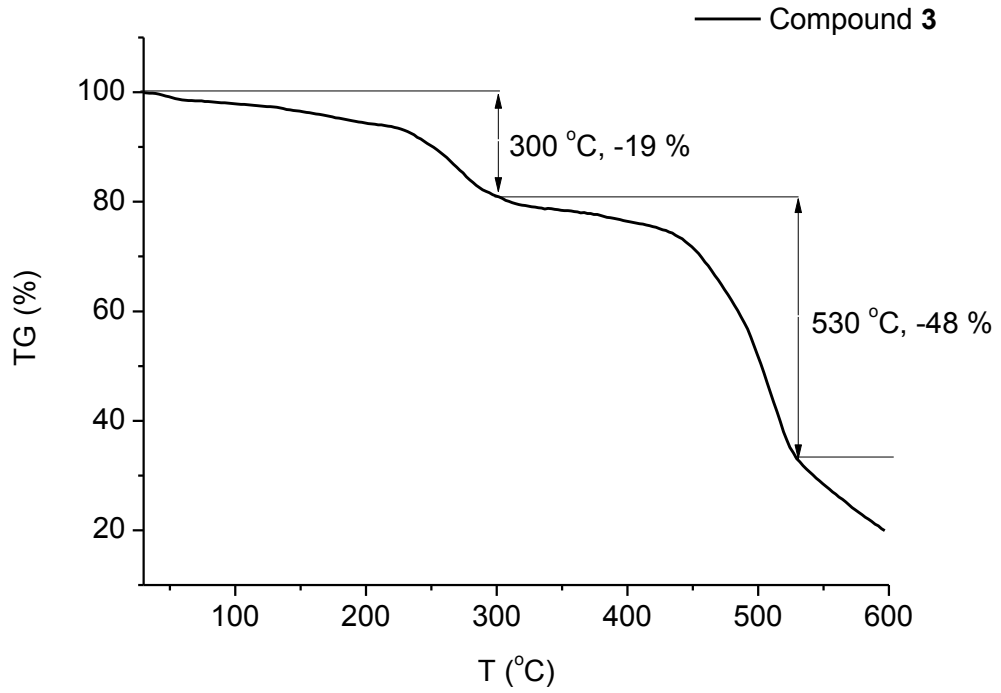

Figure 5.18. The TG curve of $Mn[Ad(PhCOO)_2\cdot DMF]$ (compound 3).

FT-IR spectra were recorded both on compound **3** and ligand $Ad(COOH)_2$ (Figure 5.19). The IR spectra of $Ad(COOH)_2$ showed that the C=O stretch of carboxylate at 1680 cm^{-1} (this value is a little higher than that of $Ad(COOH)_4$, v.s. 1675 cm^{-1}), whereas in compound **3**, this stretching frequency is shifted to lower value at 1660 cm^{-1}. The new peak at 1400cm^{-1} in the spectra of compound **3** is corresponding to the C-N stretch of crystal DMF.

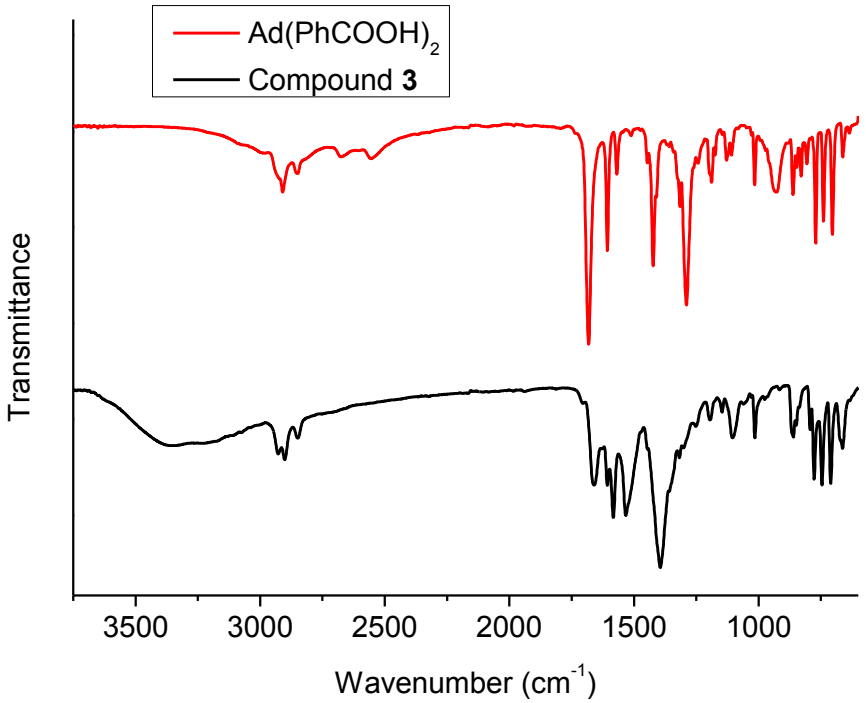

Figure 5.19. IR spectra of compound **3** in comparison to the bulk ligand $Ad(PhCOOH)_2$.

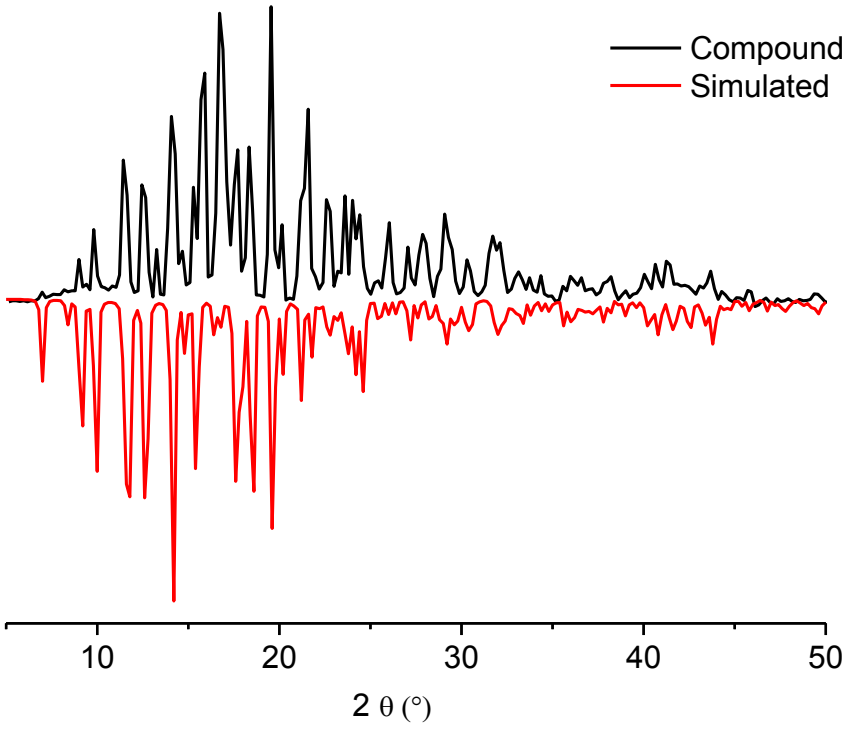

Figure 5.20. Powder X-Ray diffraction pattern of compound **3** in comparison to the simulated pattern (simulated pattern was obtained from single crystal measurement by program Mercury).

The powder X-ray diffractogram of compound **3** matched the simulated pattern very well (Figure 5.20). All the reflections of simulated pattern can be found in the powder X-ray diffraction pattern of compound **3**.

N_2 sorption measurement result showed that the BET surface area of compound **3** is zero, so this 2D-network complex doesn't have porosity.

The empirical formula of compound **3** is Mn[Ad(PhCOO)$_2$·DMF] ($C_{27}H_{29}MnNO_5$). Calcd for $C_{27}H_{29}MnNO_5$: C 64.54; H 5.82; N 2.79. Found: C 61.45; H 5.57; N 3.02. Crystal data and details on the structure refinement are given in Table 5.4.

Table 5.4. Crystal data and structure refinement for compound **3**.

Conpound	**Mn[Ad(PhCOO)$_2$·DMF]**
Empirical formula	$C_{27}H_{29}MnNO_5$
Formula weight (g/mol)	502.14
Crystal size (mm)	0.10×0.10×0.02
2θ range (°)	1.63 – 27.70
h; k; l; range	-16<=h<=16; -23<=k<=25; -7<=l<=12
Crystal system	Monoclinic
Space group	P 2_1/c (no. 14)
a (Å)	12.5159(10)
b (Å)	19.1864(14)
c (Å)	9.9596(8)
V (Å^3)	2383.78(30)
Z	4
D_{calc}(g / cm^3)	1.39994
F (000)	1052
μ(mm^{-1})	0.592
Max/min transmission	0.9882 / 0.9431
Reflection collected (R_{int})	5561 (0.0605)
Data completeness (%)	99.8

Independent reflections	3876
Parameters refined	309
Max/min ($\Delta\rho^a$ /e Å^{-3})	0.295 / -0.212
R1/wR_2 [I > 2σ(I)]^b	0.0408 / 0.0951
R1/wR_2 (all reflections)^b	0.0704 / 0.1124
Goodness-of-fit on F^{2c}	0.901

[a] Largest difference peak and hole. [b] $R1 = [\Sigma(\|F_0\|-\|F_c\|)/\Sigma|F_0|]$; $wR_2 = [\Sigma[w(F_0^2-F_c^2)^2]/\Sigma[w(F_0^2)^2]]^{1/2}$. [c] Goodness-of-fit = $[\Sigma[w(F_0^2-F_c^2)^2]/(n-p)]^{1/2}$.

3.4. {Cd[Ad(PhCOO)$_3$·xDMF·yH_2O]}·mH_2O·nDMF (compound 4)

Solvothermal reaction of cadmium chloride with 4,4',4''-((1s,3s,5s)-adamantane-1,3,5-triyl) tribenzoic acid (Ad(PhCOOH)$_3$) would yields a colorless crystals (Figure 5.4). Colorless crystals of dimensions 0.10×0.10×0.10 mm for compound **4** was used for structural determinations. The crystal system of compound **4** is triclinic; it contains two kinds of building unit, The {Cd(μ_6-O)·DMF} and {Cd(μ_6-O) ·H_2O} (Figure 5.21 a). In {Cd(μ_6-O)·DMF} building unit, the Cd atom coordinated by three carboxylate groups which come from three different Ad(PhCOOH)$_3$ ligand and a DMF molecule. {Cd(μ_6-O)·H_2O} unit is isostructural as {Cd(μ_6-O)·DMF} but with the coordination of water molecules instead. These units would form a 2D network structure. The layers of network are close; the two {Cd} units from different layers would form a double building unit structure (Figure 5.21 b, here we defined one of {Cd} units coordinated with DMF, the other coordinated with water). The double building unit structure spread and forms a two layers network (Figure 5.21 c). Each layer possesses hexagonal grids with the dimensions 17×17 Å^2 along the top view (Figure 5.21 c). From single crystal analysis, it is impossible to define the specific Cd atom coordinated with DMF or water molecule. Thus, the option SQUEEZE in PLATON for Windows was used to refine the network structure without the disordered electron density in the voids. For compound **4**, a total of 23 electrons per 72 Å^3 was squeezed, which corresponds to ~23 electrons per $C_{31}H_{25}CdO_6$ formula unit (Z = 1). Hence, the probability of Cd atom coordinated with DMF or water is the same (0.5 vs. 0.5). Compound **4** with a empirical formula {$C_{31}H_{25}CdO_6$·0.5DMF·0.5H_2O}·2H_2O·DMF, Calcd for: C 55.94; H 5.32; N 2.75. Found: C 56.41; H 5.08; N 2.45. Crystal data and details on the structure refinement

are given in Table 5.5.

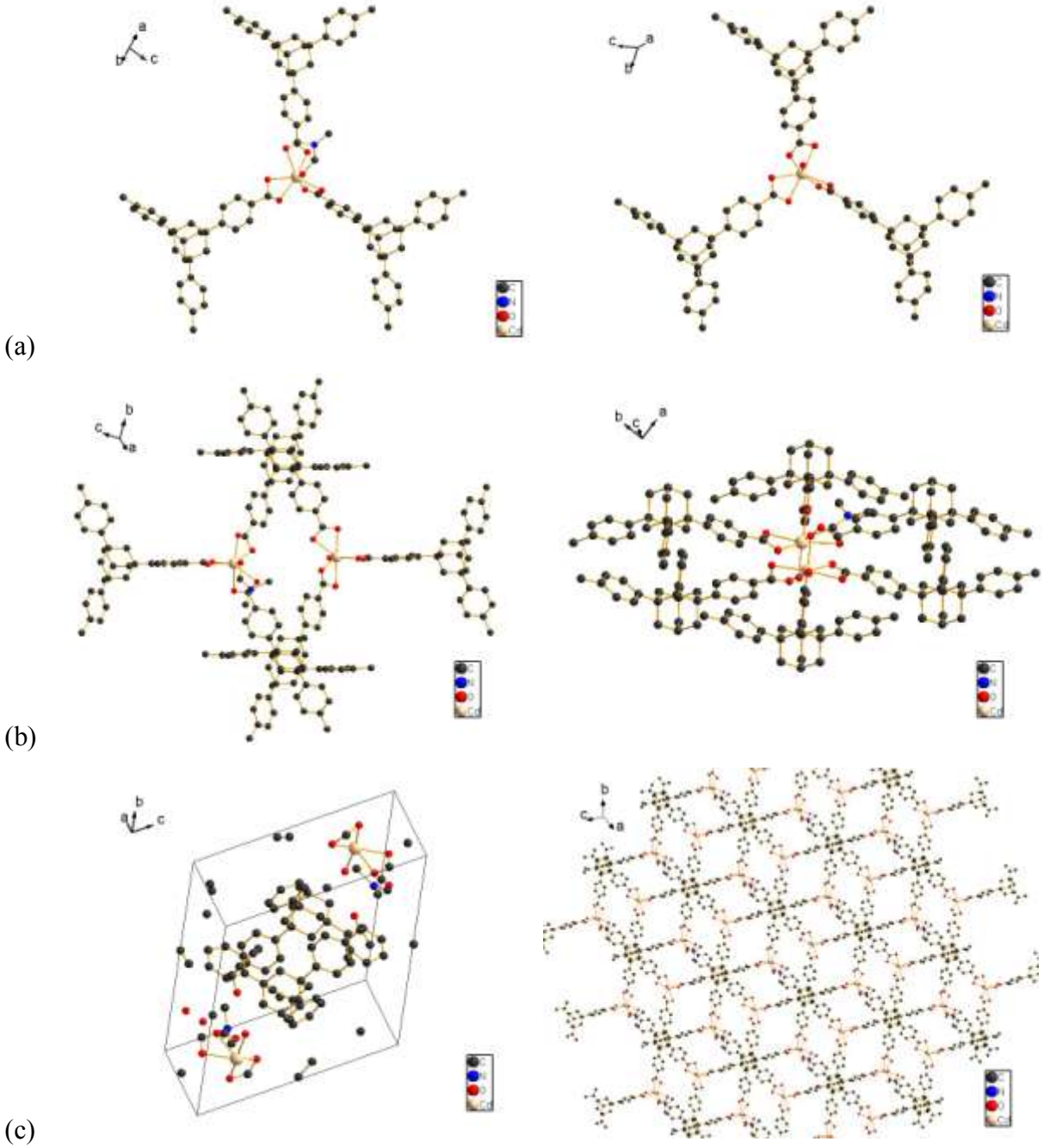

Figure 5.21. The {Cd(μ_6-O)·DMF} and {Cd(μ_6-O)·H_2O} building unit (a), two views of the packing diagram of double building unit structure (b), cell unit of compound **4** and two layers network based on double building unit structure (c). (Hydrogen atoms and water/DMF-guest molecules are not shown). The different objects in this figure are not drawn to scale.

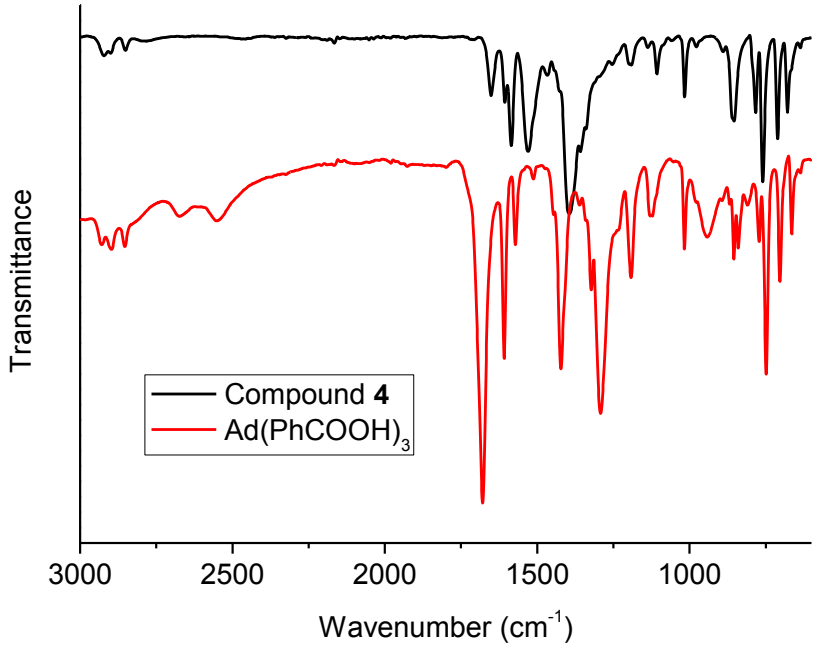

Figure 5.22. IR spectra of compound **4** in comparison to the bulk ligand $Ad(PhCOOH)_3$.

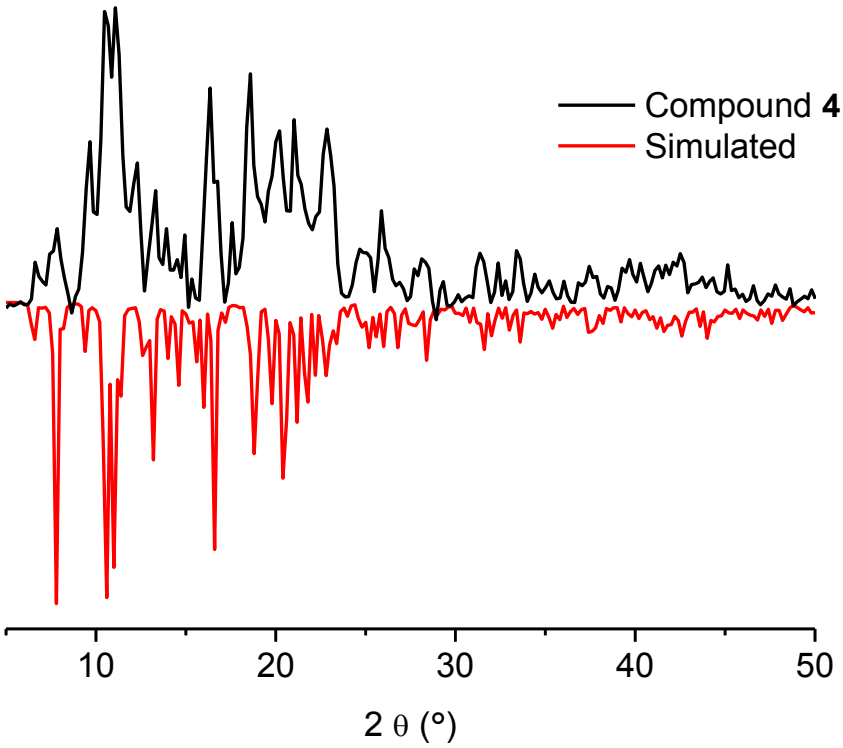

Figure 5.23. Powder X-Ray diffraction pattern of compound **4** in comparison to the simulated pattern (simulated pattern was obtained from single crystal measurement by program Mercury).

FT-IR spectra were recorded both on compound **4** and ligand $Ad(COOH)_3$ (Figure 5.22). The IR spectra of $Ad(COOH)_3$ showed that the C=O stretch of carboxylate at 1680 cm^{-1} (this value is also a little higher than that of $Ad(COOH)_4$, v.s. 1675 cm^{-1}), whereas in compound **4**, this stretching frequency is shifted to lower value at 1650 cm^{-1}. The new peak at 1400cm^{-1} in the spectra of compound **3** is corresponding to the C-N stretch of crystal DMF.

The PXRD pattern of compound **4** is generally agree with the simulated pattern (Figure 5.23). Nearly all the main reflections of simulated pattern can be found in the Powder X-ray diffractogram of compound **4**.

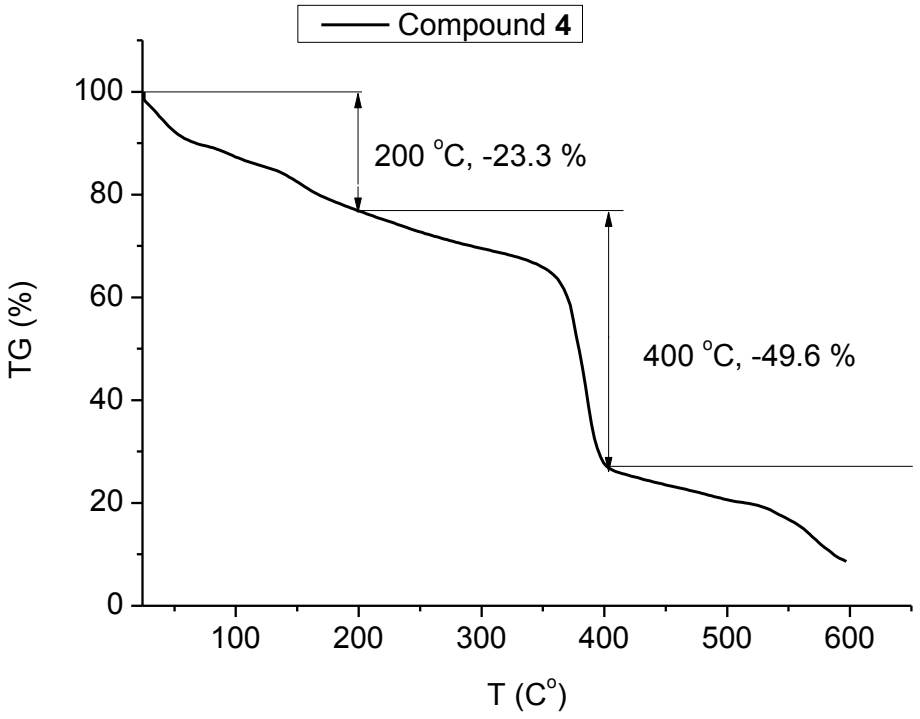

Figure 5.24. The TG curve of $\{Cd[Ad(PhCOO)_3 \cdot xDMF \cdot yH_2O]\} \cdot mH_2O \cdot nDMF$ (compound **4**).

Thermogravimetric analysis (TGA) shows that compound **4** contain significant amount of solvent molecules, which is reflected by weight loss at low temperatures (<200°C, lost 23.3 wt%). Between 200 °C and 400 °C, it lost additional 49.6 wt% of weight, which is due to the decomposition of the organic moieties and network (Figure 5.24).

Though the compound **4** is 2D network structure, it contains a lot of solvent molecules which indicate that it is probably porous. Compound **4** shows a relatively good chemical and thermal

stability compare to compound **1** and **2**. Thus, compound **4** was washed with ethanol for several times and degassed under high vacuum (10^{-3} Torr) at 200 °C for at least 2 h, prior to N_2 sorption measurement. The nitrogen sorption isotherms of compound **4** is given in Figure 5.25, with 196 m^2/g of BET surface area and 268 m^2/g of Langmuir surface area respectively. Although the value of surface areas are not high, compound **4** is comfirmed to be a porous material. This porous property perhaps due to the void between the layers of compound **4**, and the hysteresis loop of the nitrogen sorption isotherm revealed mesoporous.

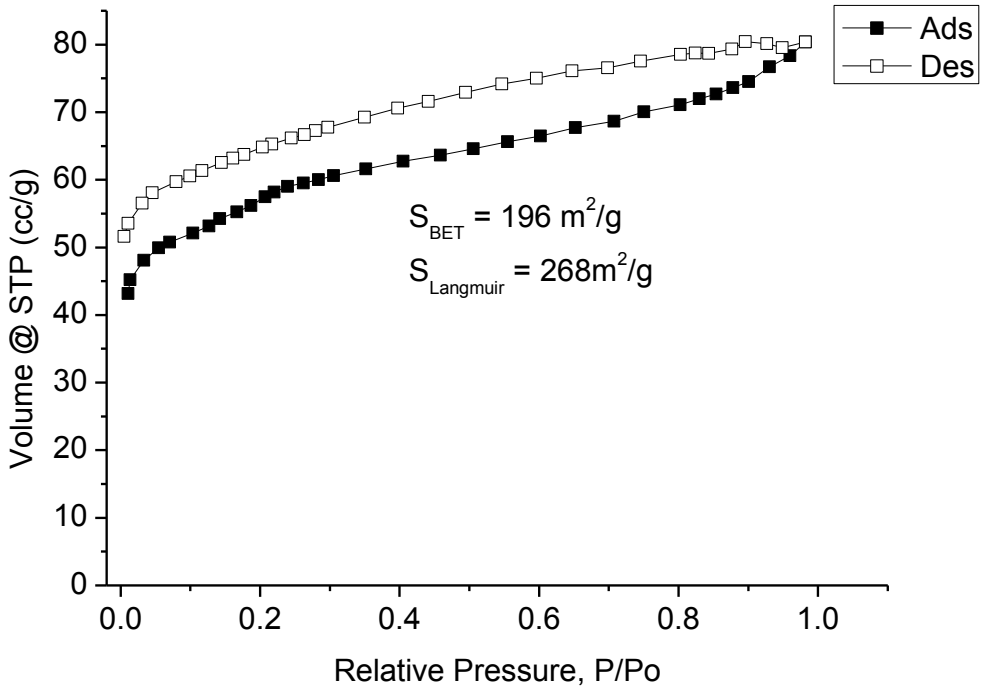

Figure 5.25. N_2 sorption isotherms of compound **4** (BET surface area was calculated in the pressure range 0.05 $< p/p_0 <$ 0.2 from N_2 sorption isotherm at 77 K with an estimated standard deviation of ± 50 m^2/g).

Table 5.5. Crystal data and structure refinement for compound **4**.

Conpound	**{Cd[Ad(PhCOO)$_3$·xDMF·yH$_2$O]}·mH2O·nDMF**
Empirical formula	$C_{31}H_{25}CdO_6$·0.5DMF·0.5H_2O
Formula weight (g/mol)	652.6
Crystal size (mm)	0.10×0.10×0.10

2θ range (°)	1.50 – 26.57
h; k; l; range	-13<=h<=13; -16<=k<=16; -18<=l<=18
Crystal system	Triclinic
Space group	P 1 (no. 1)
a (Å)	11.0682(4)
b (Å)	13.5036(5)
c (Å)	14.6691(5)
V ($Å^3$)	2024.37(13)
Z	1
D_{calc}(g / cm^3)	1.24162
F (000)	632
μ(mm^{-1})	0.571
Max/min transmission	0.945 / 0.945
Reflection collected (R_{int})	14146 (0.0305)
Data completeness (%)	99.2
Independent reflections	11125
Parameters refined	703
Max/min ($\Delta\rho^a$ /e $Å^{-3}$)	1.610 / -0.618
R1/wR_2 [I > 2σ(I)][b]	0.0451 / 0.1203
R1/wR_2 (all reflections)[b]	0.0586 / 0.1294
Goodness-of-fit on F^{2c}	0.862

[a] Largest difference peak and hole. [b] $R1 = [\Sigma(\|\|F_0|-|F_c\|\|)/\Sigma|F_0|]$; $wR_2 = [\Sigma[w(F_0^2-F_c^2)^2]/\Sigma[w(F_0^2)^2]]^{1/2}$. [c] Goodness-of-fit = $[\Sigma[w(F_0^2-F_c^2)^2]/(n-p)]^{1/2}$.

4. Conclusion

In this chapter four Coordination polymers/MOFs based on carboxyphenyladamantanes ligands have been presented. Compound **1** and **2** are 3D framework based on {M(μ_8-O)} nodes (M=Co, Mn) with combining ligand $Ad(PhCOOH)_4$. The ligands of compound **1** are not completely deprotonated, thus, it is not stable in water or under high temperature. The ligands of compound **2** are completely deprotonated, so its stability is better than compound **1** but not that

much. Both compound **1** and **2** are porous materials, with 423 and 289 m^2/g of BET surface area respectively. Compound **3** is a 2D network based on paddle wheel $\{Mn_2(\mu_4\text{-}O)\cdot 2DMF\}$ nodes with the coordination of $Ad(PhCOO)_2$ ligand. It is nonporous material, but with higher chemical and thermal stability than compound **1** and **2**. Compound **3** can remain its structure up to 200°C. Compound **4** is also a 2D network based on $\{Cd(\mu_6\text{-}O)\cdot DMF\}$ and $\{Cd(\mu_6\text{-}O)\cdot H_2O\}$ nodes with the coordination of $Ad(PhCOO)_3$ ligand. Unlike compound **3**, compound **4** is porous, with 196 m^2/g of BET surface area. Its thermal stability can up to 300°C.

Acknowledgment

Dr. Ishtvan Boldog is gratefully acknowledged for the guidance of coordination polymer synthesis and the offering of ligands in this chapter. Dr. Christian Heering is gratefully acknowledged for single crystal measurement and structure analysis.

Reference

1. C. Janiak, *Dalton Trans.*, 2003, 2781–2804.
2. The lecture of 'Advanced materials' in Heinrich-Heine-Universität Düsseldorf, Christoph Janiak, 2013.
3. The first use of the term "coordination polymer" may be traced to J. C. Bailar, Jr., *Preparative Inorganic Reactions*, ed. W. L. Jolly, Interscience, New York, 1964, vol. 1, pp. 1–25.
4. O. M. Yaghi, G. Li and H. Li, *Nature*, 1995, **378**, 703-706;
5. O. M. Yaghi and H. Li, *J. Am. Chem. Soc.*, 1995, **117**, 10401-10402.
6. S. R. Batten, N. R. Champness, X.-M. Chen, J. Garcia-Martinez, S. Kitagawa, L. Öhrström, M. O'Keeffe, M. P. Suh, J. Reedijk, *CrystEngComm*, 2012, **14**, 3001–3004.
7. S. R. Batten, N. R. Champness, X.-M. Chen, J. Garcia-Martinez, S. Kitagawa, L. Öhrström, M. O'Keeffe, M. P. Suh, J. Reedijk, *Pure Appl. Chem.*, 2013, **85**, 1715–1724.
8. G. Férey, *J. Solid State Chem.*, 2000, **152**, 37-48.
9. S. Surble, F. Millange, C. Serre, G. Fe´rey and R. I. Walton, *Chem. Commun.*, 2006, 1518-1520.
10. S. Kitagawa, R. Kitaura, and S. Noro, *Angew. Chem. Int. Ed.*, 2004, **43**, 2334–2375.
11. K. S. Park, Z. Ni, A. P. Côté, J. Y. Choi, R. Huang, F. J. Uribe-Romo, H. K. Chae, M. O'Keeffe, and O. M. Yaghi, *PNAS*, 2006, **103**, 10186-10191.
12. S. S.-Y. Chui, S. M.-F. Lo, J. P. H. Charmant, A. G. Orpen and I. D. Williams, *Science*, 1999, **283**, 1148-1150.
13. M. K. Kim, V. Jo, D. W. Lee, I.-W. Shim and K. M. Ok, *CrystEngComm*, 2010, **12**, 1481–1484.
14. O. K. Farha, A. Ö. Yazaydın, I. Eryazici, C. D. Malliakas, B. G. Hauser, M. G. Kanatzidis, S. T. Nguyen, R. Q. Snurr and J. T. Hupp, *Nat. Chem.*, 2010, **2**, 944–948.
15. N. Klein, I. Senkovska, K. Gedrich, U. Stoeck, A. Henschel, U. Mueller, S. Kaskel, *Angew. Chem. Int. Ed.,* 2009, **48**, 9954–9957.
16. M. J. Katz, Z. J. Brown, Y. J. Colón, P. W. Siu, K. A. Scheidt, R. Q. Snurr, J. T. Hupp and O. K. Farha, *Chem. Commun.,* 2013, **49**, 9449—9451.
17. R. I. Walton, Chem. *Soc. Rev.*, 2002, **31**, 230–238.
18. B. Wisser, A.-C. Chamayou, R. Miller, W. Scherer and C. Janiak, *CrystEngComm*, 2008, **10**,

461–466.

19. H. Thakuria, B. M. Borah and G. Das, *Eur. J. Inorg. Chem.*, 2007, 524–529.
20. C.-Y. Sun, S. Gao and L.-P. Jin, *Eur. J. Inorg. Chem.*, 2006, 2411–2421.
21. C. N. R. Rao, S. Natarajan and R. Vaidhyanathan, *Angew. Chem. Int. Ed.*, 2004, **43**, 1466–1496.
22. A. Carton, A. Mesbah, L. Perrin and M. Francois, *Acta Crystallogr.*, Sect. E: Struct. Rep. Online, 2007, **63**, m948–m958.
23. S. C. Manna, E. Zangrando, J. Ribas and N. R. Chaudjuri, *Dalton Trans.*, 2007, 1383–1391.
24. S. Banerjee, P.-G. Lassahn, C. Janiak and A. Ghosh, *Polyhedron*, 2005, **24**, 2963–2971.
25. B. Moulton, J. Lu, A. Mondal and M. J. Zaworotko, *Chem. Commun.*, 2001, 863–864.
26. H. Abourahma, A. W. Coleman, B. Moulton, B. Rather, P. Shahgaldian and M. J. Zaworotko, *Chem. Commun.*, 2001, 2380–2381.
27. H. Abourahma, G. J. Bodwell, J. Lu, B. Moulton, I. R. Pottie, R. B. Walsh and M. J. Zaworotko, *Cryst. Growth Des.*, 2003, **3**, 513–519.
28. A. Majumder, S. Shit, C. R. Choudhury, S. R. Batten, G. Pilet, D. Luneau, N. Daro, J.-P. Sutter, N. Chattopadhyay and S. Mitra, *Inorg. Chim. Acta*, 2005, **358**, 3855–3864.
29. M. J. Plater, M. R. St. J. Foreman, R. A. Howie, J. M. S. Skakle, E. Coronado, C. J. Gomez-Garcia, T. Gelbrich and M. B. Hursthouse, *Inorg. Chim. Acta*, 2001, **319**, 159–175.
30. M. J. Plater, M. R. St. J. Foreman, E. Coronado, C. J. Gomez-Garcia and A. M. Z. Slawin, J. Chem. Soc., *Dalton Trans.*, 1999, 4209–4216.
31. Q. Wang, M.-J. Wu, X.-G. Wang and X.-J. Zhao, *Acta Crystallogr., Sect. E: Struct. Rep. Online*, 2006, **62**, m2496–m2498.
32. H. X. Zhang, B.-S. Kang, A.-W. Xu, Z.-N. Chen, Z.-Y. Zhou, A. S. C. Chan, K.-B. Yu and C. Ren, *J. Chem. Soc., Dalton Trans.*, 2001, 2559-2566.
33. K.-Y. Choi, K.-M. Chun, K.-C. Lee and J. Kim, *Polyhedron*, 2002, **21**, 1913-1920.
34. B.-L. Chen, K.-F. Mok, S.-C. Ng and M. G. B. Drew, *New J. Chem.*, 1999, **23**, 877-883.
35. H. K. Fun, S. S. S. Raj, R. G. Xiong, J. L. Zuo, Z. Yu and X. Z. You, *J. Chem. Soc., Dalton Trans.*, 1999, 1915-1916.
36. J. Cano, G. D. Munno, J. L. Sanz, R. Ruiz, J. Faus, F. Lloret, M. Julve and A. Caneschi, *J.*

Chem. Soc., Dalton Trans., 1997, 1915-1924.

37. S. A. Bourne, J. Lu, A. Mondal, B. Moulton and M. J. Zaworotko, *Angew. Chem., Int. Ed.*, 2001, **40**, 2111–2113.

38. B. Moulton, H. Abourahma, M. W. Bradner, J. Lu, G. J. McManus and M. J. Zaworotko, *Chem. Commun.*, 2003, 1342–1343.

39. Y.-F. Zhou, F.-L. Jiang, D.-Q. Yuan, B.-L. Wu, R.-H. Wang, Z.-Z. Lin and M.-C. Hong, *Angew. Chem., Int. Ed.*, 2004, **43**, 5665–5668

40. P. Wang, C. N. Moorefield, M. Panzer and G. R. Newkome, *Chem. Commun.*, 2005, 465–467.

41. P.-K. Chen, Y.-X. Che and J.-M. Zheng, *Jiegou Huaxue*, 2006, **25**, 1427–1430.

42. X. Shi, G. Zhu, Q. Fang, G. Wu, Ge Tian, R. Wang, D. Zhang, M. Xue and S. Qiu, *Eur. J. Inorg. Chem.*, 2004, 185–191.

43. C. Daiguebonne, A. Deluzet, M. Camara, K. Boubekeur, N. Audebrand, Y. Gerault, C. Baux and O. Guillou, *Cryst. Growth Des.*, 2003, **3**, 1015–1020.

44. G. Smith, A. N. Reddy, K. A. Byriel and C. H. L. Kennard, *J. Chem. Soc., Dalton Trans.*, 1995, 3565–3570.

45. B. Gomez-Lor, E. Gutierrez-Puebla, M. Iglesias, M. A. Monge, C. Ruiz-Valero and N. Snejko, *Chem. Mater.*, 2005, **17**, 2568–2573.

46. B. Moulton and M. J. Zaworotko, *Chem. Rev.*, 2001, **101**, 1629-1658.

47. S. Banfi, L. Carlucci, E. Caruso, G. Ciani and D. M. Proserpio, *J. Chem. Soc., Dalton Trans.*, 2002, 2714-2721.

48. D. M. Curtin, Y.-B. Dong, M. D. Smith, T. Barclay and H.-C. zur Loye, *Inorg. Chem.*, 2001, **40**, 2825-2834.

49. B.-L. Fei, W.-Y. Sun, K.-B. Yu and W.-X. Tang, *J. Chem. Soc., Dalton Trans.*, 2000, 805-811.

50. M. Kondo, M. Shimamura, S.-I. Noro, T. Yoshitomi, S. Minakoshi and S. Kitagawa, *Chem. Lett.*, 1999, 285-286.

51. E. J. Cussen, J. B. Claridge, M. J. Rosseinsky and C. J. Kepert, *J. Am. Chem. Soc.*, 2002, **124**, 9575-9581.

52. L.-M. Zheng, P. Yin and X.-Q. Xin, *Inorg. Chem.*, 2002, **41**, 4084-4086.

53. H. Li, M. Eddaoudi, T. L. Groy, M. O'Keeffe and O. M. Yaghi, *Nature*, 1999, **402**, 276-279.

54. M. Dincă and J. R. Long, *Angew. Chem., Int. Ed.*, 2008, **47**, 6766–6779.

55. R. E. Morris and P. S. Wheatley, *Angew. Chem., Int. Ed.*, 2008, **47**, 4966–4981.

56. X. Lin, J. Jia, P. Hubberstey, M. Schro¨ der and N. R. Champness, *CrystEngComm*, 2007, **9**, 438–448.

57. D. J. Collins and H.-C. Zhou, *J. Mater. Chem.*, 2007, **17**, 3154–3160.

58. S. Ma, D. Sun, M. Ambrogio, J. A. Fillinger, S. Parkin and H. C. Zhou, *J. Am. Chem. Soc.*, 2007, **129**, 1858-1859.

59. P. Horcajada, C. Serre, M. Vallet-Regí, M. Sebban, F. Taulelle and G. Férey, *Angew. Chem., Int. Ed.*, 2006, **45**, 5974–5978.

60. M. Vallet-Regi, F. Balas and D. Arcos, *Angew. Chem., Int. Ed.*, 2007, **46**, 7548-7558.

61. D. Farrusseng, S. Aguado and C. Pinel, *Angew. Chem., Int. Ed.*, 2009, **48**, 7502–7513.

62. S. Hasegawa, S. Horike, R. Matsuda, S. Furukawa, K. Mochizuki, Y. Kinoshita and S. Kitagawa, *J. Am. Chem. Soc.*, 2007, **129**, 2607-2614.

63. U. Ravon, M. E. Domine, C. Gaudille` re, A. Desmartin-Chomel and D. Farusseng, *New J. Chem.*, 2008, **32**, 937–940.

64. B. Gómez-Lor, E. Gutiérrez-Puebla, M. Iglesias, M. A. Monge, C. Ruiz-Valero and N. Snejko, *Chem. Mater.*, 2005, **17**, 2568–2573.

65. J. Perles, M. Iglesias, M.-A. Martín-Luengo, M. A. Monge, C. Ruiz-Valero and N. Snejko, *Chem. Mater.*, 2005, **17**, 5837–5842.

66. F. Schröder, D. Esken, M. Cokoja, M. W. E. Van den Berg, O. I. Lebedev, G. Van Tendeloo, B. Walaszek, G. Buntkowsky, H.-H. Limbach, B. Chaudret and R. A. Fischer, *J. Am. Chem. Soc.*, 2008, **130**, 6119–6130.

67. M. Müller, S. Hermes, K. Kähler, M. W. E. van den Berg, M. Muhler and R. A. Fischer, *Chem. Mater.*, 2008, **20**, 4576–4587.

68. T. Uemura, N. Yanai and S. Kitagawa, *Chem. Soc. Rev.*, 2009, **38**, 1228–1236.

69. T. Uemura, K. Kitagawa, S. Horike, T. Kawamura, S. Kitagawa, M. Mizuno and K. Endo, *Chem. Commun.*, 2005, 5968–5970.

70. T. Uemura, R. Kitaura, Y. Ohta, M. Nagaoka and S. Kitagawa, *Angew. Chem., Int. Ed.*, 2006, **45**, 4112–4116.

71. M. D. Allendorf, C. A. Bauer, R. K. Bhakta and R. J. T. Houk, *Chem. Soc. Rev.*, 2009, **38**, 1330–1352

72. H. A. Habib, A. Hoffmann, H. A. Ho¨ ppe, G. Steinfeld and C. Janiak, *Inorg. Chem.*, 2009, **48**, 2166–2180.

73. H. A. Habib, J. Sanchiz and C. Janiak, *Dalton Trans.*, 2008, 1734–1744.

74. H. A. Habib, J. Sanchiz and C. Janiak, *Inorg. Chim. Acta*, 2009, 362, 2452–2460.

75. S. S.-Y. Chui, S. M.-F. Lo, J. P. H. Charmant, A. G. Orpen and I. D. Williams, *Science*, 1999, **283**, 1148-1150.

76. G. Majano and J. Perez-Ramirez, *Adv. Mater.*, 2013, 25, 1052–1057.

77. M. O'Keeffe, *Chem. Soc. Rev.*, 2009, **38**, 1215–1217.

78. K. Schlichte, T. Kratzke and S. Kaskel, *Micropor. Mesopor. Mater.*, 2004, **73**, 81-88.

79. M. Eddaoudi, J. Kim, N. Rosi, D. Vodak, J. Wachter, M. O'Keeffe and O. M. Yaghi, *Science*, 2002, **295**, 469-472.

80. J. A. Greathouse and M. D. Allendorf, *J. Am. Chem. Soc.,* 2006, **128**, 10678-10679.

81. J. Yang, A. Grzech, F. M. Mulder and T. J. Dingemans, *Chem. Commun.,* 2011, **47**, 5244–5246.

82. C. Serre, F. Millange, S. Surble and G. Férey, *Angew. Chem., Int. Ed.*, 2004, **43**, 6285-6289.

83. C. Serre, F. Millange, C. Thouvenot, M. Nogues, G. Marsolier, D. Louer and G. Férey, *J. Am. Chem. Soc., 2002*, **124**, 13519-13526.

84. F. Millange, N. Guillou, R. I. Walton, J.-M. Greneche, I. Margiolaki and G. Férey, *Chem. Commun.*, 2008, 4732-4734.

85. S. Bauer, C. Serre, T. Devic, P. Horcajada, J. Marrot, G. Férey and N. Stock, *Inorg. Chem.*, 2008, **47**, 7568-7576.

86. L. Alaerts, M. Maes, L. Giebeler, P. A. Jacobs, J. A. Martens, J. F. M. Denayer, C. E. A. Kirschhock and D. E. De Vos, *J. Am. Chem. Soc.*, 2008, **130**, 14170-14178.

87. T. Loiseau, C. Serre, C. Huguenard, G. Fink, F. Taulelle, M. Henry, T. Bataille, and G. Férey, *Chem. Eur. J.*, 2004, **10**, 1373-1382.

88. P. Horcajada, S. Surblé, C. Serre, D.-Y. Hong, Y.-K. Seo, J.-S. Chang, J.-M. Grenèche, I.

Margiolaki and G. Férey, *Chem. Commun.*, 2007, 2820–2822.

89. P. L. Llewellyn, S. Bourrelly, C. Serre, A. Vimont, M. Daturi, L. Hamon, G. De Weireld, J.-S. Chang, D.-Y. Hong, Y. Kyu Hwang, S. Hwa Jhung and G. Férey, *Langmuir*, 2008, **24**, 7245–7250.
90. L. Hamon, C. Serre, T. Devic, T. Loiseau, F. Millange, G. Férey and G. De Weireld, *J. Am. Chem. Soc.*, 2009, **131**, 8775–8777.
91. A. Vimont, J.-M. Goupil, J.-C. Lavalley, M. Daturi, S. Surbl_e, C. Serre, F. Millange, G. Férey and N. Audebrand, *J. Am. Chem. Soc.*, 2006, **128**, 3218–3227.
92. A. Lieb, H. Leclerc, T. Devic, C. Serre, I. Margiolaki, F. Mahjoubi, J. S. Lee, A. Vimont, M. Daturi, J.-S. Chang, *Micropor. Mesopor. Mater.*, 2012, **157**, 18–23.
93. M. N. Timofeeva, V. N. Panchenko, A. A. Abel, N. A. Khan, I. Ahmed, A. B. Ayupov, K. P. Volcho, S. H. Jhung, *J. Catal.*, 2014, **311**, 114–120.
94. J. H. Cavka, S. Jakobsen, U. Olsbye, N. Guillou, C. Lamberti, S. Bordiga and K. P. Lillerud, J. *Am. Chem. Soc.*, 2008, **130**, 13850–13851.
95. X.-C. Huang, Y.-Y. Lin, J.-P. Zhang and X.-M. Chen, *Angew. Chem., Int. Ed.*, 2006, **45**, 1557–1559
96. J. R. Long and O. M. Yaghi, *Chem. Soc. Rev.*, 2009, **38**, 1213–1214.
97. C. Janiak and J. K. Vieth, *New J. Chem.*, 2010, **34**, 2366–2388.
98. M. Fujita, Y. Kwon, S. Washizu and K. Ogura, *J. Am. Chem. Soc.*, 1994, **116**, 1151-1152.
99. O. R. Evans, H. L. Ngo and W. Lin, *J. Am. Chem. Soc.*, 2001, **123**, 10395- 10396.
100. R. Tannenbaum, *Chem. Mater.*, 1994, **6**, 550-555.
101. J. M. Tanski and P. T. Wolczanski, *Inorg. Chem.*, 2001, **40**, 2026-2033.
102. C. Janiak, *Angew. Chem., Int. Ed. Engl.*, 1997, **36**, 1431-1434.
103. M. A. Withersby, A. J. Blake, N. R. Champness, P. Hubberstey, W.-S. Li and M. Schröder, *Angew. Chem., Int. Ed. Engl.*, 1997, **36**, 2327-2329.
104. A. J. Blake, N. R. Champness, A. N. Khlobystov, S. Parsons and M. Schröder, *Angew. Chem., Int. Ed. Engl.*, 2000, **39**, 2317-2320.
105. F. Bodar-Houillon, T. Humbert, A. Marsura, J.-B. Regnouf de Vains, O. Dusausoy, N. Bouhmaida, N. E. Ghermani and Y. Dusausoy, *Inorg. Chem.*, 1995, **34**, 5205-5209.
106. Y.-B. Dong, G.-X. Jin, M. D. Smith, R.-Q. Huang, B. Tang and H.-C. zur Loye, *Inorg.*

Chem., 2002, **41**, 4909-4914.

107. Z. Hu, G. Huang, W. P. Lustig, F. Wang, H. Wang, S. J. Teat, D. Banerjee, D. Zhang and J. Li, *Chem. Commun.,* 2015, **51**, 3045—3048.
108. G. E. Gomez, M. C. Bernini, E. V. Brusau, G. E. Narda, D. Vega, A. M. Kaczmarek, R. Van Deun and M. Nazzarro, *Dalton Trans.*, 2015, **44**, 3417–3429.
109. Y. Lu and B. Yan, *Chem. Commun.,* 2014, **50**, 15443—15446.
110. C.-T. Chen and K. S. Suslick, *Coord. Chem. Rev.*, 1993, **128**, 293-322.
111. O. Kahn, *Molecular Magnetism*, VCH, Weinheim, 1993.
112. K. Drabent, Z. Ciunik and A. Ozarowski, *Inorg. Chem*., 2008, **47**, 3358-3365.
113. H. A. Habib, J. Sanchiz and C. Janiak, *Dalton Trans.*, 2008, 4877–4884.
114. B. G.-Hernández, J. K. Maclaren, H. A. Höppe, J. Pasán, J. Sanchiz and C. Janiak, *CrystEngComm*, 2012, **14**, 2635–2644.
115. P. G. Lacroix, *Eur. J. Inorg. Chem.*, 2001, 339-348.
116. H. Zhang, X. Wang, K. Zhang and B. K. Teo, *J. Solid State Chem.*, 2000, **152**, 191-198.
117. H. Hou, Y. Wei, Y. Fan, C. Du, Y. Zhu, Y. Song, Y. Niu and X. Xin, *Inorg. Chim. Acta*, 2001, **319**, 212-218.
118. H. Hou, Y. Song, Y. Fan, L. Zhang, C. Du and Y. Zhu, *Inorg. Chim. Acta*, 2001, **316**, 140-144.
119. P. Horcajada, T. Chalati, C. Serre, B. Gillet, C. Sebrie, T. Baati, J. F. Eubank, D. Heurtaux, P. Clayette, C. Kreuz, J.-S. Chang, Y. K. Hwang, V. Marsaud, P.-N. Bories, L. Cynober, S.Gil, G. Férey, P. Couvreur and R. Gref, *Nat. Mater.*, 2010, **9**, 172-178.
120. S. K. Bhatia and A. L. Myers, Langmuir, 2006, **22**, 1688–1700.
121. D. Britt, H. Furukawa, B. Wang, T. G. Glover and O. M. Yaghi, *Proc. Natl. Acad. Sci. U. S. A*., 2009, **106**, 20637–20640.
122. S. Noro, S. Kitagawa, M. Kondo and K. Seki, *Angew. Chem., Int. Ed.*, 2000, **39**, 2082-2084.
123. J. S. Beck, J. C. Vartuli, W. J. Roth, M. E. Leonowicz, C. T. Kresge, K. D. Schmitt, C. T.-W. Chu, D. H. Olson, E. W. Sheppard, S. B. McCullen, J. B. Higgins, J. L. Schlenker, *J. Am. Chem. Soc.*, 1992. **114**, 10834-10843.
124. C. T. Kresge , M. E. Leonowicz, W. J. Roth, J. C. Vartuli and J. S. Beck, *Nature*, 1992, **359**, 710-712.

125. M. Lindén, S. Schacht, F. Schüth, A. Steel, K. K. Unger, *J. Porous Mater.*, 1998, **5**, 177-193.

126. P. Selvam, S. K. Bhatia, C. G. Sonwane, *Ind. Eng. Chem. Res.,* 2001, **40**, 3237-3261.

127. B. Muñoz , A. Rámila , J. Pérez-Pariente , I. Díaz and M. Vallet-Regí, *Chem. Mater.*, 2003, **15**(2), 500–503.

128. M. Manzano, V. Aina, C. O. Arean, F. Balas, V. Cauda, M. Colilla, M. R. Delgado and M. Vallet-RegÌ, *Chem. Eng. J.*, 2008, 137, 30–37.

129. J. Li, M. Huang, X. Liu, H. Wei, Y. Xu, G. Xu and E. Wang, *Analyst*, 2007, **132**, 687–691.

130. Y. Li, X. Zeng, X. Liu, X. Liu, W. Wei and S. Luo, *Colloids Surf.*, B, 2010, **79**, 241–245.

131. Y. Wang, L. Sun, T. Jiang, J. Zhang, C. Zhang, C. Sun, Y. Deng, J. Sun and S. Wang, *Drug Dev Ind Pharm*, 2014, **40**(6), 819-828.

132. A. Benhamou, M. Baudu, Z. Derriche and J. P. Basly, *J. Hazard Mater*, 2009, **171**, 1001–1008.

133. S . Nazzal, N . Guven, I. K. Reddy and M. A. Khan, *Drug Dev Ind Pharm*, 2002, **28**, 49–57.

134. D. Halamová and V. Zeleňák, *J Incl Phenom Macro.*, 2012, **72**, 15–23.

135. Y. Wang, L. Sun1, T. Jiang1, J. Zhang, C. Zhang, C. Sun1, Y. Deng, J. Sun and S. Wang, *Drug Dev Ind Pharm*, 2014, **40**(6), 819–828.

136. M. Abdollahi-Alibeik and M. Pouriayevali, *React. Kinet., Mech. Catal.*, 2011, **104**, 235–248.

137. J. C. Juan, J. Zhang and M. A. Yarmo, *J. Mol. Catal. A: Chem.*, 2007, **267**, 265–271.

138. A. Sayari, *Chem. Mater.*, 1996, **8**, 1840–1852.

139. Y. X. Jiang, W. B. Song, Y. Liu, B. Wei, X. C. Cao and H. D. Xu, Mater. *Chem. Phys.*, 2000, **62**, 109–114.

140. P. Carraro, V. Elias, A. Garcia Blanco, K. Sapag, S. Moreno, M. Oliva and G. Eimer, *Micropor. Mesopor. Mater.*, 2014, **191**, 103–111

141. J. Rathousky, A. Zukai, O. Franke and G. Schulz-Ekloff, *J. Chem. Soc., Faraday Trans.*, 1995, **91**, 937–940.

142. A. J. Palace Carvalho, T. Ferreira, A. J. Estêvão Candeias, J. P. Prates Ramalho, *J. Mol. Struct., THEOCHEM*, 2005, **729**, 65–69

143. J. Li, M. Huang, X. Liu, H. Wei, Y. Xu, G. Xu and E. Wang, *Analyst*, 2007, **132**, 687–691.

144. H. Guo, N. He, S. Ge, D. Yang and J. Zhang, *Talanta*, 2005, **68**, 61–66.
145. F. Wang, J. Yang and K. Wu, *Anal. Chim. Acta*, 2009, **638**, 23–28.
146. S. Wua, J. Wang, G. Liu, Y. Yang and J. Lu, *J. Membr. Sci.*, 2012, **390– 391**, 175– 181.
147. S. Hamoudi and K. Belkacemi, *J. Porous Mater.*, 2004, **11**, 47-54.
148. Q. Huo, D. I. Margolese, U. Ciesla, D. G. Denuth, P. Feng, T. E. Gier, P. Sieger, A. Firouzi, B. F. Chmelka, F. Schuth and G. D. Stucky, *Chem. Mater.*, 1994, **6**, 1176-1191.
149. J. H. Kim, R. D. Burnett and A. Gabriel, *J Biomed Nanotech*, 2012, **8**, 432–438.
150. J. Choma, S. Pikus and M. Jaroniec, *Appl. Surf. Sci.*, 2005, **252**, 562-569.
151. L. Cambi and A. Cagnasso, Atti. Accad. Naz. Lincei, *CI. Sci. Fis., Mat. Nut., Rend.*, 1931, **13**, 809–813.
152. L. Cambi and L. Szego, *Ber. Dtsch. Chem. Ges. B*, 1931, **64**, 2591–2598.
153. W. A. Baker Jr. and H. M. Bobonich, *Inorg. Chem.*, 1964, **3**, 1184–1188.
154. S. Brooker, *Chem. Soc. Rev.,* 2015, **44**, 2880—2892.
155. Y. Zhang, *J. Chem. Phys.,* 2014, **141**, 214703.
156. C.-F. Wang, R.-F. Li, X.-Y. Chen, R.-J. Wei, L.-S. Zheng and J. Tao, *Angew. Chem. Int. Ed.,* 2015, **54**, 1574 –1577.
157. L. J. Kershaw Cook, H. J. Shepherd, T. P. Comyn, C. Bald, O. Cespedes, G. Chastanet and M. A. Halcrow, *Chem. Eur. J.*, 2015, **21**, 4805-4816.
158. S. Vela, J. J. Novoa and J. Ribas-Arino, Phys. *Chem. Chem. Phys.,* 2014, **16**, 27012-27024.
159. I. Nemec, R. Herchel and Z. Trávníček, *Dalton Trans.*, 2015, **44**, 4474–4484.
160. S. Zheng, M. A. Siegler, O. Roubeau and S. Bonnet, *Inorg. Chem.*, 2014, **53**, 13162−13173.
161. T. Buchen, P. Gu¨tlich, K. H. Sugiyarto and H. A. Goodwin, *Chem. Eur. J.*, 1996, **9**, 1134–1138.
162. K. Nakano, N. Suemura, K. Yoneda, S. Kawata and S. Kaizaki, *Dalton Trans.*, 2005, 740–743.
163. D.-Y. Hong, Y. K. Hwang, C. Serre, G. Férey, and J. –S. Chang, *Adv. Funct. Mater.*, 2009, **19**, 1537–1552.
164. G. Férey, C. Mellot-Draznieks, C. Serre, F.Millange, J. Dutour, S. Surble and I. Margiolaki, *Science*, 2005, **309**, 2040–2042.
165. Y. K. Hwang, D.-Y. Hong, J.-S. Chang, H. Seo, M. Yoon, J. Kim, S. H. Jhung, C. Serre, G. Férey, *Appl. Catal. A: General,* 2009, **358**, 249–253.

166. C. M. Granadeiro, A. D. S. Barbosa, P. Silva, F. A. Almeida Paz, V. K. Saini, J. Pires, B. de Castro, S. S. Balula, L. Cunha-Silva, *Appl. Catal. A: General*, 2013, **453**, 316–326.
167. N. V. Maksimchuk, K. A. Kovalenko, S. S. Arzumanov, Y. A. Chesalov, M. S. Melgunov, A. G. Stepanov, V. P. Fedin and O. A. Kholdeeva, *Inorg. Chem.*, 2010, **49**, 2920–2930.
168. A. Henschel, K. Gedrich, R. Kraehnert and S. Kaskel, *Chem. Commun.*, 2008, 4192–4194.
169. D. Julião, A. C. Gomes, M. Pillinger, L. Cunha-Silva, B. de Castro, I. S. Gonçalves, S. S. Balula, *Fuel Process. Technol*. 2015, **131**, 78–86.
170. Y. K. Hwang, D.-Y.Hong, J.-S.Chang, S. H. Jhung, Y.-K.Seo, J. Kim, A. Vimont, M. Daturi, C. Serre, and G. Férey, *Angew. Chem. Int. Ed.*, 2008, **47**, 4144-4148.
171. M. Wen, K. Mori, T. Kamegawa and H. Yamashita, *Chem. Commun.,* 2014, **50**, 11645—11648.
172. F. Wu, L. –G. Qiu, F. Ke, X. Jiang, *Inorg. Chem. Commum.*, 2013, **32**, 5 – 8.
173. M. Saikia, D. Bhuyan and L. Saikia, *New J. Chem.,* 2015, **39**, 64—67.
174. C. M. Granadeiro, M. Karmaoui, E. Correia, D. Julião, V. S. Amaral, N. J. O. Silva, L. Cunha-Silva and S. S. Balula, *RSC Adv.*, 2015, **5**, 4175–4183.
175. L. Bromberg, T. A. Hatton, *ACS Appl. Mater. Interfaces*, 2011, **3**, 4756–4764.
176. F. Yang, C.-X. Yang, X.-P. Yan, *Talanta*, 2015, **137**, 136–142.
177. S. Xian, Y. Yu, J. Xiao, Z. Zhang, Q. Xia, H. Wang and Z. Li, *RSC Adv.*, 2015, **5**, 1827–1834.
178. H. B. TanhJeazet, C. Staudt and C. Janiak, *Chem. Commun.*, 2012, **48**, 2140-2142.
179. H. B. TanhJeazet, T. Koschine, C. Staudt, K. Raetzke and C. Janiak, *Membranes*, 2013, **3**, 331-353
180. S. Bernt, V. Guillerm, C. Serreb and N. Stock, *Chem. Commun.*, 2011, **47**, 2838–2840.
181. S. M. Cohen, Chem. Sci., 2010, **1**, 32-36.
182. M. Kim; S. M. Cohen, *CrystEngComm*, 2012, **14**, 4096-4104.
183. A. Khutia, H. U. Rammelberg, T. Schmidt, S. Henninger and C. Janiak, *Chem. Mater.*, 2013, **25**, 790-798.
184. M. Lammert, S. Bernt, F. Vermoortele, D. E. De Vos and N. Stock, *Inorg. Chem.*, 2013, **52**, 8521-8528.
185. M. Yamashita, M. Suzuki, H. Hirai, H Kajigaya, *Care Med.,* 2001, **29** (8): 1575–1578.
186. D. Jiang, A. D. Burrows and K. J. Edler, *CrystEngComm*, 2011, **13**, 6916–6919.
187. J. Zhou, K. Liu, C. Kong, and L. Chen, Bull. *Korean Chem. Soc.*, 2013, **34**(6), 1625-1631.

188. T. Shen, J. Luo, S. Zhang and X. Luo, *J. Environ. Chem. Eng.*, 2015, 3, 1372–1383.
189. M. Jacoby, *Chem. & Eng. News*, 2008, **86**, 13-16.
190. Chemistry World, 2009 (February), 49; http://www.rsc.org/images/MOF_tcm18142948.pdf.
191. N. Stock and S. Biswas, *Chem. Rev.*, 2012, **112**, 933–969.
192. P. Á. Szilágyi, E. Callini, A. Anastasopol, C. Kwakernaak, S. Sachdeva, R. van de Krol, H. Geerlings, A. Borgschulte, A. Züttelc and B. Damb. *Phys. Chem. Chem. Phys.*, 2014, **16**, 5803—5809.
193. N. Cao, J. Su, W. Luo, G. Cheng. *Int. J. Hydrogen Energy*, 2014, **39**, 9726-9734.
194. X. Zhou, W. Huang, J. Shi, Z. Zhao, Q. Xia, Y. Li, H. Wang and Z. Li, *J. Mater. Chem. A*, 2014, **2**, 4722–4730.
195. J. Pires, M. L. Pinto, C. M. Granadeiro, A. D. S. Barbosa, L. Cunha-Silva, S. S. Balula, V. K. Saini. *Adsorption*, 2014, **20**, 533–543.
196. Y. Li, R. T. Yang, *AIChE J.*, 2008, **54**, 269-279.
197. L. H. Wee, F. Bonino, C. Lamberti, S. Bordigab and J. A. Martensa. *Green Chem.*, 2014, **16**, 1351–1357.
198. W. Salomon, F.-J. Yazigi, C. Roch-Marchal, P. Mialane, P. Horcajada, C. Serre, M. Haouas, F. Taulelle and A. Dolbecq, *Dalton Trans.*, 2014, **43**, 12698–12705.
199 K. Sumida, D. L. Rogow, J. A. Mason, T. M. McDonald, E. D. Bloch, Z. R. Herm, T. H. Bae, J. R. Long, *Chem. Rev.*, 2012, **112**, 724-781.
200. N. A. Khan, I. J. Kang, H. Y. Seok, S. H. Jhung. *Chem. Engin. J.*, 2011, **166**, 1152–1157.
201. L. Bromberg, Y. Diao, H. Wu, S. A. Speakman, and T. A. Hatton. *Chem. Mater.*, 2012, **24**, 1664−1675.
202. S.-N. Kim, S.-T. Yang, J. Kim, J.-E. Park and W.-S. Ahn. *CrystEngComm*, 2012, **14**, 4142–4147.
203. I. Senkovska, S. Kaskel. *Micropor. Mesopor. Mater.*, 2008, **112**, 108–115.
204. N. V. Maksimchuk, M. N. Timofeeva, M. S. Melgunov, A. N. Shmakov, Yu. A. Chesalov, D. N. Dybtsev, V. P. Fedin O. A. Kholdeeva. *J. Catal.*, 2008, **257**, 315–323.
205. Y. Pan, B. Yuan, Y. Li and D. He, *Chem. Commun.*, 2010, **46**, 2280 -2282.
206. J. Ehrenmann, S. K. Henninger and C. Janiak, *Eur. J. Inorg. Chem.,* 2011, 471–474.
207. M. Wickenheisser, C. Janiak, *Micropor. Mesopor. Mater.*, 2015, **204**, 242-250.
208. M. Wickenheisser, A. Herbst, R. Tannert, B. Milow, C. Janiak, Micropor. Mesopor. Mater. 2015, in press. http://dx.doi.org/10.1016/j.micromeso.2015.05.017.

209. A. Herbst, A. Khutia, C. Janiak, *Inorg. Chem.*, 2014, **53**, 7319−7333.

210. B. B. Saha, I. I. El-Sharkawy, T. Miyazaki, S. Koyama, S. K. Henninger, A. Herbst, C. Janiak, *Energy,* 2015, **79**, 363-370.

211. L. D Gelb, K. E. Gubbins, R. Radhakrsihan, M. Sliwinska-Bartowiak, *Rep. Prog. Phys.*, 1999, **62**, 1573–1659.

212. N. A. Sedron, J. P. R. B. Walton, N. Quirke, *Carbon*, 1989, **27**, 853–861.

213. A. Vishnyakov, P. Ravikovitch, A.V. Neimark, *Langmuir*, 2000, **16,** 2311–2320.

214. T. Loiseau, G. Férey, *J. Fluorine Chem.*, 2007, **128**, 413-422.

215. K. S. W. Sing, D. H. Everett, R. A. W. Haul, L. Moscou, R. A. Pierotti, J. Rouquero and T. Siemieniewska, *Pure & Appl. Chem.*, 1985, **57**(4), 603—619.

216. X. X. Huang, L. G. Qiu, W. Zhang, Y. P. Yuan, X. Jiang, A. J. Xie, Y. H. Shen and J. F. Zhu. *CrystEngComm*, 2012, **14**, 1613-1617.

217. F. Yin, G. Li, H.Wang, *Catal. Commun.*, 2014, **54**, 17–21.

218. Z. Rui, Q. Li, Q. Cui, H. Wang, H. Chen and H. Yao, *Chin. J. Chem. Eng.*, 2014, **22**(5), 570—575.

219. S. Wang, L. Bromberg, H. Schreuder-Gibson, and T. A. Hatton. *ACS Appl. Mater. Interfaces*, 2013, **5**, 1269−1278.

220. J. Yang, Q. Zhao, J. Li, J. Dong. *Micropor. Mesopor. Mater.*, 2010, **130**, 174–179.

221. E. V. Ramos-Fernandez, M. Garcia-Domingos, J. Juan-Alcañiz, J. Gascon, F. Kapteijn. *Appl. Catal., A: General*, 2011, **391**, 261–267.

222. C. X. Yang and X. P. Yan. *Anal. Chem.*, 2011, **83**, 7144–7150.

223. S. H. Jhung, J.-H. Lee, J. W. Yoon, C. Serre, G. Férey, and J.-S. Chang. *Adv. Mater.*, 2007, **19**, 121–124.

224. H. Dai, J. Su, K. Hua, W. Luo, G. Cheng. *Int. J. Hydrogen Energy*, 2014, **39**, 4947-4953.

225. G. Wißmann, A. Schaate, S. Lilienthal, I. Bremer, A. M. Schneider and P. Behrens, *Micropor. Mesopor. Mater.*, 2012, **152**, 64-70.

226. A. Schaate, P. Roy, A. Godt, J. Lippke, F. Waltz, M. Wiebcke, P. Behrens, *Chem. Eur. J.*, 2011, **17**, 6643–6651.

227. Eds.: P. Gütlich, H. A. Goodwin, *Top. Curr. Chem.*, 2004, 233–235.

228. O. Kahn and C. J. Martinez, *Science*, 1998, **279**, 44 – 48.

229. J. A.Wolnya, H. Paulsenb, A. X. Trautweinb, V. Schünemann, *Coord. Chem. Rev.*, 2009, **253**, 2423–2431.

230. H.-Z. Ye, C. Sun and H. Jiang, *Phys. Chem. Chem. Phys.,* 2015, **17**, 6801—6808.

231. M. Cavallini, I. Bergenti, S. Milita, G. Ruani, I. Salitros, Z.-R. Qu, R. Chandrasekar, and M. Ruben, *Angew. Chem. Int. Ed.*, 2008, **47**, 8596 –8600.

232. M. Kepenekian, J. S. Costa, B. L. Guennic, P. Maldivi, S. Bonnet, J. Reedijk, P. Gamez and V. Robert, *Inorg. Chem.*, 2010, **49**, 11057–11061.

233. D. Chiruta, J. Linares, P. R. Dahoo, M. Dimian, *Physica B*, 2014, **435**, 76–79.

234. A. L.-Fernández, M. P. Cuéllar, J. M. Herrera, A. S.-Castillo, M. C. Pegalajar, S. T.-Padilla, E.Colacioc and L. F. C.-Vallveya, *J. Mater. Chem. C*, 2014, **2**, 7292-7303.

235. M. P. Cuéllara, A. L.-Fernándezb, J. M. Herrerac, A. S.-Castillob, M. C. Pegalajara, S. T.-Padillac, E. Colacioc, L. F. C.-Vallvey, *Sens. Actuators, B*, 2015, **208**,180–187.

236. A. Atitoaie, R. Tanasa, A. Stancu, C. Enachescu, *J. Magn. Magn. Mater.*, 2014, **368**, 12–18.

237. C.-M. Jureschi, I. Rusu, E. Codjovi, J. Linares, Y. Garcia, *A. Rotaru, Physica B*, 2014, **449**, 47–51.

238. M. M. Dîrtu, F. Schmit, A. D. Naik, A. Rotaru, J. M.-Brynaert and Y. Garcia, *Int. J. Mol. Sci.*, 2011, **12**, 5339-5351.

239. O. Roubeau, J. G. Haasnoot, E. Codjovi, F. Varret and J. Reedijk, *Chem. Mater.,* 2002, **14**, 2559-2566.

240. D. Qiu, L. Gu, X.-L. Sun, D.-H. Ren, Z.-G. Gu and Z. Li, *RSC Adv.*, 2014, **4**, 61313–61319.

241. P. Gütlich, A. B. Gaspar and Y. Garcia, *Beilstein J. Org. Chem.,*2013**, 9***,* 342–391.

242. M. Mikolasek, G. Félix, G. Molnár, F. Terki, W. Nicolazzi and A. Bousseksou, *Phys. Rev. B*, 2014, **90**, 075402.

243. G. Molnár, L. Salmon, W. Nicolazzi, F. Terkib and A. Bousseksou, *J. Mater. Chem. C*, 2014, **2**, 1360–1366.

244. G. Félix, W. Nicolazzi, L. Salmon, G. Molnár, M. Perrier, G. Maurin, *Phys. Rev. Lett.*, 2013, **110**, 235-701.

245. H. J. Shepherd, G. Molnár, W. Nicolazzi, L. Salmon and A. Bousseksou, *Eur. J. Inorg. Chem.,* 2013, 653–661.

246. A. Tissot, L. Rechignat, A. Bousseksoub and M.-L. Boillot, *J. Mater. Chem.*, 2012, **22**, 3411–3419

247. A. Tokarev, J. Long, Y. Guari, J. Larionova, F. Quignard, P. Agulhon, M. Robitzer, G. Molnár, L. Salmonc and A. Bousseksou, *New J. Chem.,* 2013, **37**, 3420—3432.

248. D. Qiu, D.-H. Ren, L. Gu, X.-L. Sun, T.-T. Qu, Z.-G. Gu and Z. Lia, *RSC Adv.*, 2014, **4**, 31323–31327.
249. E. C. Ellingsworth, B. Turner and G. Szulczewski, *RSC Adv.*, 2013, **3**, 3745–3754.
250. S. Basak, P. Hui, and R. Chandrasekar, *Chem. Mater.*, 2013, **25**, 3408−3413.
251. J. Dugay , M. G.-Marqués , T. Kozlova , H. W. Zandbergen , E. Coronado and H. S. J. van der Zant, *Adv. Mater.*, 2015, **27**, 1288–1293.
252. C. Volkringer, D. Popov, T. Loiseau, G. Férey, M. Burghammer, C. Riekel, M. Haouas, and F. Taulelle, *Chem. Mater.*, 2009, **21**, 5695–5697.
253. P. Serra-Crespo, E. V. Ramos-Fernandez, J. Gascon and F. Kapteijn, *Chem. Mater.*, 2011, **23**, 2565–2572.
254. S. Trofimenko, *J. Am. Chem. Soc.*, 1967, **89(13)**, 3170-3177.
255. S. Proch, J. Herrmannsdçrfer, R. Kempe, C. Kern, A. Jess, L. Seyfarth, J. Senker, *Chem. Eur. J.*, 2008, **14**, 8204 – 8212
256. S. Hermes, M.-K. Schröter, R. Schmid, L. Khodeir, M. Muhler, A. Tissler, R. W. Fischer, R. A. Fischer, *Angew. Chem. Int. Ed.*, 2005, **44**, 6237–6241.
257. M. Meilikhov, K. Yusenko, D. Esken, S. Turner, G.-V. Tendeloo, R. A. Fischer, *Eur. J. Inorg. Chem.*, 2010, 3701–3714
258. M. S. Al-Shall, V. Abdelsayed, A. E. R. S. Khder, H. M. A. Hassan, H. M. El-Kaderi, T. E. Reich, *J. Mater. Chem.*, 2009, **19**, 7625–7631.
259. H. Yang, J. Li, H. Zhang, Y. Lv, S. Gao, *Micropor. Mesopor. Mater.*,2014, **195**, 87–91.
260. Z. Guo, M. V. Reddy, B. M. Goh, A. K. P. San, Q. Bao, K. P. Loh, *RSC Adv.*, 2013, **3**, 19051–19056.
261. M. Hartmann and M. Fischer, *Micropor. Mesopor. Mater.*, 2012, **164**, 38–43
262. C. Janiak, Angewandte Chemie, International Edition (2000), **39(14)**, 2559.
263. L. Salmon, G. Molnár, S. Cobo, P. Oulié, M. Etienne, T. Mahfoud, P. Demont, A. Eguchi, H. Watanabe, K. Tanaka and A. Bousseksou, *New J. Chem.*, 2009, **33**, 1283–1289.
264. A. I. Kitaigorodskii, Molecular Crystals and Molecules, Academic Press, New York, 1973.
265. B. Seoane, C. Téllez, J. Coronas and C. Staudt, *Sep. Purif. Technol.*, 2013, **111**, 72–81.
266. J.-H. Moon, Y.-S. Bae, S.-H. Hyun and C.-H. Lee, *J. Membr. Sci.*, 2006, **285**, 343-352.
267. B. Hutchinson, L. Daniels, E. Henderson, P. Neill, G. J. Long and L. W. Becker, J. Chem. Soc., Chem. Commun., 1979, 1003-1004.
268. F. Grandjean, G. J. Long, B. B. Hutchinson, L. Ohlhausen, P. Neill and J. D. Holcomb,

Inorg. Chem., 1989, **28**, 4406-4414.

269. T. Delgado, A. Tissot, C. Besnard, L. Guénée, P. Pattison and A. Hauser, Chem. Eur. J. 2015, **21**, 3664 – 3670.
270. H. Naggert, A. Bannwarth, S. Chemnitz, T. von Hofe, E. Quandt and F. Tuczek, *Dalton Trans.*, 2011, **40**, 6364–6366.
271. C. Göbel, T. Palamarciuc, C. Lochenie and B. Weber, Chem. Asian J. 2014, **9**, 2232-2238.
272. M. C. Muñoz, J. A. Real, *Coord. Chem. Rev.*, 2011, **255**, 2068–2093.
273. G. Levchenko, A. Khristov, V. Kuznetsova, V. Shelest, *J. Phys. Chem. Solids*, 2014, **75**, 966–971.
274. M. B. Duriska, S. M. Neville, B. Moubaraki, J. D. Cashion, G. J. Halder, K. W. Chapman, C. Balde, J.-F. Létard, K. S. Murray, C. J. Kepert, S. R. Batten, *Angew. Chem.*, 2009, **121**, 2587–2590.
275. N. Moliner, L. Salmon, L. Capes, M. C. Muñoz, J.-F. Létard, A. Bousseksou, J.-P. Tuchagues, J. J. McGarvey, A. C. Dennis, M. Castro, R. Burriel, J. A. Real, *J. Phys. Chem. B*, 2002, **106**, 4276-4283.
276. A. Galet, A. B. Gaspar, G. Agusti, M. C. Muñoz, G. Levchenko, J. A. Real, *Eur. J. Inorg. Chem.*, 2006, 3571–3573.
277. P. Gütlich, A. Hauser, H. Spiering, *Angew. Chem. Int. Ed. Engl.*, 1994, **33**, 2024-2054.
278. P. Gütlich, A. Hauser, *Coord. Chem. Rev.*, 1990, **97**, 1-22.
279. H. Toftlund, *Coord. Chem. Rev.*, 1989, **94**, 67-108.
280. C. Janiak, T. G. Scharmann, J. C. Green, R. P. G. Parkin, M. J. Kolm, E. Riedel, W. Mickler, J. Elguero, R. M. Claramunt, D. Sanz, *Chem. Eur. J.*, 1996, **2**, 992-1000.
281. P. Gütlich, Struct. *Bonding (Berlin)*, 1981, **44**, 83-195.
282. H. A. Goodwin, *Coord. Chem. Rev.*, 1976, **18**, 293-325.
283. C. Janiak, T. G. Scharmann, T. Bräuniger, J. Holubová, M. Nádvornik, *Z. Anorg. Allg. Chem.* 1998, **624**, 769-774.
284. M. Rubio, R. Hernández, A. Nogales, A. Roigand D. López, *Eur. Polym. J.*, 2011, **47**, 52–60.
285. J. Panda, S. Chattopadhyay and T. K. Nath, *Thin Solid Films*, 2013, **546**, 211–218.
286. A. Tissot, J.-F. Bardeau, E. Rivière, F. Brisseta and M.-L.Boillot, *Dalton Trans.*, 2010, **39**, 7806–7812.
287. Y. Raza, F. Volatron, S. Moldovan, O. Ersen, V. Huc, C. Martini, F. Brisset, A. Gloter, O. Stephan, A. Bousseksou, L. Catala and T. Mallah, *Chem. Commun.*, 2011, **47**, 11501–11503.

288. E. Codjovi, N. Menéndez, J. Jeftic and F. Varret, *C. R. Acad. Sci. Paris, Chimie / Chemistry*, 2001, **4**, 181–188.

289. B. L. Guennic, S. Borshch and V. Robert, *Inorg. Chem.*, 2007, **46**, 11106-11111.

290. D. Chiruta, J. Linares, M. Dimian, Y. Alayli and Y. Garcia, *Eur. J. Inorg. Chem.*, 2013, 5086–5093.

291. L. Stoleriu, P. Chakraborty, A. Hauser, A. Stancu and C. Enachescu, *Phys. Rev. B*, 2011, **84**, 134102.

292. L. G. Lavrenova, V. N. Ikorskii, V. A. Varnek, I. M. Oglezneva and S. V. Larionov, *Koord. Khim.*,1990, **16**, 654-661.

293. J. Kröber, J.–P. Audière, R. Claude, E. Codjovi, O. Kahn, J. G. Haasnoot, D. Grolière, C. Jay and A. Gonthier-Vassal, *Chem. Mater.*, 1994, **6**, 1404-1412.

294. K. H Sugiyarto and H. A. Goodwin, *Aust. J. Chem.*, 1994, **47**, 263-277.

295. C. Faulmann, J. Chahine, I. Malfant, D. de Caro, B. Cormary, L. Valade, *Dalton Trans.*, 2011, **40**, 2480.

296. P. Durand, S. Pillet, E.-E. Bendeif, C. Carteret, M. Bouazaoui, H. El Hamzaoui, B. Capoen, L. Salmon, S. Hebert, J. Ghanbaja, L. Aranda and D. Schaniel, *J. Mater. Chem. C*, 2013, **1**, 1933-1942.

297. D. Qiu, D.-H. Ren, L. Gu, X.-L. Sun, T.–T. Qu, Z.-G. Gu and Z. Li, *RSC Advances*, 2014, **4**, 31321-31327.

298. I. Suleimanov, J. Sanchez Costa, G. Molnar, L. Salmon and A. Bousseksou, *Chem. Commun.*, 2014, **50**, 13015-13018.

299. A. Stein, B. H. Melde and R. C. Schroden, *Adv. Mater.*, 2000, **12**, 1403-1419.

300. J. Kröber; J. –P. Audière; R. Claude; E. Codjovi; O. Kahn; J. G. Haasnoot; D. Grolière; C. Jay; A. Gonthier-Vassal, *Chem. Mater.,*1994, **6**, 1404-1412.

301. E. Coronado, J. R. Galán-Mascarós, M. Monrabal-Capilla, J.García-Martínez and P. Pardo-Ibáñez, *Adv. Mater.*, 2007, **19**, 1359-1361.

302. K. Lagarec, D. G. Rancourt: Mössbauer Spectral Analysis Software for Windows 1.0, Department of Physics, University of Ottawa, Canada, 1998.

303. K. H. Breuer and W. Eysel. *Thermochim. Acta*, 1982, **57**, 317-329.

304. M. GomesSpeziali, A. G. Marques da Silva, D. M. Vaz de Miranda, A. Lisboa Monteiro, P. A. Robles-Dutenhefner, *Appl. Catal., A*, 2013, **462– 463**, 39–45.

305. R. Huang, B. Lan, Z. Chen, H. Yan, Q. Zhang, J. Bing, L. Li, *Chem. Engin. J.*, 2012, **180**,

19–24.
306. Z. Obalı, N. A. Sezgi, T. Dŏgu. *Chem. Engin. J.*, 2011, **176–177**, 202–210.
307. A. J. Palace Carvalho, T. Ferreirab, A. J. Estêvão Candeiasa, J. P. Prates Ramalho. *J. Mol. Struct.: THEOCHEM*, 2005, **729**, 65–69.
308. H. Wu, X. Li, Y. Li, S. Wang, R. Guo, Z. Jiang, C. Wu, Q. Xin, X. Lu, *J. Membr. Sci.*, 2014, **465**, 78–90.
309. P. Carraro, V. Elías, A. G. Blanco, K. Sapag, S. Moreno, M. Oliva, G. Eimer, *Micropo. Mesopor. Mater.*, 2014, **191**, 103–111.
310. Y. Wang, L. Sun, T. Jiang, J. Zhang, C. Zhang, C. Sun, Y. Deng, J. Sun, S. Wang, *Drug Dev Ind Pharm*, 2014, **40**(6), 819–828.
311. F. Rodriguez-Reinoso and A. Linares-Solano, in Chemistry and Physics of Carbon, **Vol. 21** (P. A. Thrower, Ed.) Marcel Dekker, New York, 1988.
312. J. Garrido, A. Linares-Solano, J. M. Martin-Martinez, M. Molina-Sabio, F. Rodriguez-Reinoso and R. Torregosa, *Langmuir*, 1987, **3**, 76-81.
313 D. Cazorla-Amoros, J. Alcaniz-Monje and A. Linares-Solano, *Langmuir*, 1996, **12**, 2820-2824.
314 J. Garcia-Martinez and D. Cazorla-Amoros, A. Linares-Solano, in Characterization of PorousSolids V (K. K. Unger, G. Kreysa and J. P. Baselt, Eds.) Elsevier, Amsterdam, 2000, pp. 485-494.
315. Quantachrome Instruments (1900 Corporate Drive, Boynton Beach, FL 33426 USA, www.quantachrome.com) Powder Tech Note 35.
316. A. Bhunia, I. Boldog, A. Möller and C. Janiak. *J. Mater. Chem. A*, 2013,**1**, 14990-14999.
317. Y. Garcia, V. Ksenofontov and P. Gütlich, *C. R. Acad. Sci.*, 2001, **IIc**, 227-233.
318. Y. Garcia, P. J. van Koningsbruggen, R. Lapouyade, L. Fournès, L. Rabardel, O. Kahn, V. Ksenofontov, G. Levchenko and P. Gütlich, *Chem. Mater.*,1998, **10**, 2426-2433.
319. T. Kawamoto and S. Abe, *Chem. Commun.*, 2005, 3933-3935.
320. Y. A. Tobon, C. Etrillard, O. Nguyen, J.-F. Létard, V. Faramarzi, J.-F. Dayen, B. Doudin, D. M. Bassani, and F. Guillaume. *Eur. J. Inorg. Chem.*, 2012, 5837–5842.
321. In ref. 320, the experimental section mentions that magnetic properties were recorded on nanoparticles of [Fe(Htrz)2trz]BF4 whereas the caption to figure3 refers to the monohydrate material.
322. V. Martínez, A. B. Gaspar, M. C. Muñoz, G. V. Bukin, G. G. Levchenko and J. A. Real, *Chem.*

Eur. J., 2009, **15**, 10960–10971.

323. G. Levchenko, G. V. Bukin, S. A. Terekhov, A. B. Gaspar, V. Martinez, M. C. Muñoz and J. A. Real, *J. Phys. Chem.B*, 2011, **115**, 8176–8182.
324. A. Carné-Sánchez, I. Imaz, K. C. Stylianou and D. Maspoch, *Chem. Eur. J.*, 2014, **20**, 5192 – 5201.
325. V. Bon, I. Senkovska, M. S. Weiss and S. Kaskel, *CrystEngComm*, 2013, **15**, 9572–9577.
326. M. Zhang, Y.-P. Chen, M. Bosch, T. Gentle III, K. Wang, D. Feng, Z. U. Wang and H.-C. Zhou, *Angew. Chem. Int. Ed.*, 2014, **53**, 815 –818.
327. J. Cui, Z. Lu, Y. Li, Z. Guo and H. Zheng, *Chem. Commun.*, 2012, **48**, 7967–7969.
328. G. M. Sheldrick, *Acta Crystallogr. A*, 2008, **64**, 112–122.
329. C. Montoro, F. Linares, E. Quartapelle Procopio, I. Senkovska, S. Kaskel, S. Galli, N. Masciocchi, E. Barea and J. A. R. Navarro, *J. Am. Chem. Soc.*, 2011, **133**, 11888–11891.
330. A. L. Spek, J. Appl. Crystallogr., 2003, **36**, 7–13; PLATON – A Multipurpose Crystallographic Tool, Utrecht University, Utrecht, The Netherlands, A. L. Spek, 2008; Windows implementation: L. J. Farrugia, University of Glasgow, Scotland, Version 40608, 2008.
331. B. Chiswell, E.D. McKenzie, L.F. Lindoy, in: G. Wilkinson, R.D. Gillard, J.A. McCleverty *(*Eds.*)*, Comprehensive Coordination Chemistry, vol. 4, Pergamon, Oxford, 1987, Ch. 41, pp. 1–122.
332. M. Louloudi, V. Nastopoulos, S. Gourbatsis, S. P. Perlepes b, Nick. Hadjiliadis, *Inorg. Chem. Commun.*, 1999, **2**, 479–483.